SPACOMM 2015

The Seventh International Conference on Advances in Satellite and Space Communications

ISBN: 978-1-61208-397-1

RESENS 2015

The International Symposium on Advances in Remote Sensing Technologies and Computation

April 19 - 24, 2015

Barcelona, Spain

SPACOMM 2015 Editors

Timothy Pham, Jet Propulsion Laboratory, USA
Joseph C. Casas, Missions Formulation Manager, Science and Space Technology Projects Office, NASA MSFC, Huntsville, Alabama, USA
Claus-Peter Rückemann, WWU Münster and Leibniz Universität Hannover and HLRN, Germany

SPACOMM 2015

Foreword

The Seventh International Conference on Advances in Satellite and Space Communications (SPACOMM 2015), held between April 19th-24th, 2015 in Barcelona, Spain, continued a series of events attempting to evaluate the state of the art in academia and industry on the satellite, radar, and antennas based communications bringing together scientists and practitioners with challenging issues, achievements, and lessons learnt.

Significant efforts have been allotted to design and deploy global navigation satellite communications systems. Satellite navigation technologies, applications, and services still experience challenges related to signal processing, security, performance, and accuracy. Theories and practices on system-in-package RF design techniques, filters, passive circuits, microwaves, frequency handling, radars, antennas, and radio communications and radio waves propagation have been implemented. Services based on their use are now available, especially those for global positioning and navigation. For example, it is critical to identify the location of targets or the direction of arrival of any signal for civilians or on-purpose applications; smarts antennas and advanced active filters are playing a crucial role. Also progress has been made for transmission strategies; multiantenna systems can be used to increase the transmission speed without need for more bandwidth or power. Special techniques and strategies have been developed and implemented in electronic warfare target location systems.

SPACOMM 2015 also featured the following Symposium:

- RESENS 2015: The International Symposium on Advances in Remote Sensing Technologies and Computation

We take here the opportunity to warmly thank all the members of the SPACOMM 2015 Technical Program Committee, as well as the numerous reviewers. The creation of such a high quality conference program would not have been possible without their involvement. We also kindly thank all the authors who dedicated much of their time and efforts to contribute to SPACOMM 2015. We truly believe that, thanks to all these efforts, the final conference program consisted of top quality contributions.

Also, this event could not have been a reality without the support of many individuals, organizations, and sponsors. We are grateful to the members of the SPACOMM 2015 organizing committee for their help in handling the logistics and for their work to make this professional meeting a success.

We hope that SPACOMM 2015 was a successful international forum for the exchange of ideas and results between academia and industry and for the promotion of progress in the field of satellite and space communications.

We hope Barcelona provided a pleasant environment during the conference and everyone saved some time for exploring this beautiful city.

SPACOMM 2015 Advisory Committee:

Stelios Papaharalabos, ISARS/National Observatory of Athens, and Athens Information Technology (AIT), Greece
Piotr Tyczka, Poznan University of Technology, Poland

Michael Sauer, Corning Cable Systems, USA
Ling Pei, Finnish Geodetic Institute, Finland

SPACOMM 2015

Committee

SPACOMM Advisory Committee

Stelios Papaharalabos, ISARS/National Observatory of Athens, and Athens Information Technology (AIT), Greece
Piotr Tyczka, Poznan University of Technology, Poland
Michael Sauer, Corning Cable Systems, USA
Ling Pei, Finnish Geodetic Institute, Finland

SPACOMM 2015 Technical Program Committee

Ashfaq Ahmed, Politecnico di Torino, Italy
Ayman Mahmoud Ahmed, NARSS-Cairo, Egypt
Mohamed Al-Mosawi, University of Portsmouth, UK
Markos P. Anastasopoulos, National Technical University of Athens, Greece
Iva Bačić, Rochester Institute of Technology, Croatia
Marco Baldi, Università Politecnica delle Marche - Ancona, Italy
Mark Bentum, University of Twente & ASTRON, The Netherlands
Igor Bisio, University of Genoa - Italy, Italy
Pierre Borne, Ecole Centrale de Lille, France
Shkelzen Cakaj, Telecom of Kosovo / Prishtina University, Kosovo
Enzo Alberto Candreva, University of Bologna, Italy
Joseph C. Casas, NASA, USA
Emmanuel Chaput, IRIT-CNRS, France
Bruno Checcucci, Perugia University, Italy
Vittorio Dainelli, Rheinmetall Italia S.p.A. - Rome, Italy
Leonardo Dagui de Oliveira, Escola Politécnica da Universidade de Sao Paulo, Brazil
Francescantonio Della Rosa, Tampere University of Technology, Finland
Felix Flentge, ESA/ESOC HSO-GIB - Darmstadt, Germany
Thierry Gayraud, LAAS-CNRS, Université de Toulouse, France
Mathieu Gineste, Thales Alenia Space, France
Tzung-Pei Hong, National University of Kaohsiung, Taiwan
Suk-seung Hwang, Chosun University, Republic of Korea
Konstantinos Kontis, The University of Manchester, UK
Otto Koudelka, TU Graz, Austria
Anirban Kundu, Netaji Subhash Engineering College, India
Massimiliano Laddomada, Texas A&M University - Texarkana, USA
Haibin Liu, China Aerospace Engineering Consultation Center, China
Simona Lohan, Department of Electronics and Communications Engineering, Tampere University of Technology, Finland
Krešimir Malaric, University of Zagreb, Croatia
Herwig Mannaert, University of Antwerp, Belgium

Emmanouel T. Michailidis, University of Piraeus, Greece
Marina Mondin, Politecnico di Torino, Italy
Brian Niehoefer, Viadee Business Consultancy, Germany
Nele Noels, University of Gent, Belgium
Stelios Papaharalabos, ISARS/National Observatory of Athens, and Athens Information Technology (AIT), Greece
Ling Pei, Shanghai Jiao Tong University, China
Cathryn Peoples, University of Ulster - Coleraine, UK
Dionysia K. Petraki, National Technical University of Athens, Greece
Timothy Pham, Jet Propulsion Laboratory / California Institute of Technology, USA
Prashant Pillai, University of Bradford, UK
Luigi Portinale, Università del Piemonte Orientale "A. Avogadro" - Alessandria, Italy
Ronald Raulefs, German Aerospace Center, Germany
Vincent Roca, INRIA Rhone-Alpes, France
Pedro Agustín Roncagliolo, University of La Plata, Argentina
Alexandru Rusu-Casandra, Politehnica University of Bucharest, Romania
Heung-Gyoon Ryu, Chungbuk National University, Republic of Korea
Michael Sauer, Corning Cable Systems, USA
Ana Maria Sierra Diaz, Telefónica I+D - Madrid, Spain
Yosef Gavriel Tirat-Gefen, Castel Research Inc., USA
Piotr Tyczka, Poznan University of Technology, Poland
Huiyu Zhou, Queen's University Belfast, UK
Zhiwen Zhu, Communications Research Centre Canada, Canada

RESENSE 2015 Technical Program Committee

Agnes Begue, UMR-TETIS, France
Jean-Marc Delvit, CNES, France
Ronan Fablet, Institut Telecom/Telecom Bretagne, France
Feng Gao, USDA-ARS Hydrology & Remote Sensing Lab, USA
Olaf Hellwich, Technische Universität Berlin, Germany
Keith Morrison, Cranfield University, UK
Giorgio Pasquettaz, CRF, Italy
Irina Sergievskaya, Institute of Applied Physics of Russian Academy of Sciences, Russia
Zhengwei Yang, National Agricultural Statistics Service - United States Department of Agriculture, USA

Copyright Information

For your reference, this is the text governing the copyright release for material published by IARIA.

The copyright release is a transfer of publication rights, which allows IARIA and its partners to drive the dissemination of the published material. This allows IARIA to give articles increased visibility via distribution, inclusion in libraries, and arrangements for submission to indexes.

I, the undersigned, declare that the article is original, and that I represent the authors of this article in the copyright release matters. If this work has been done as work-for-hire, I have obtained all necessary clearances to execute a copyright release. I hereby irrevocably transfer exclusive copyright for this material to IARIA. I give IARIA permission or reproduce the work in any media format such as, but not limited to, print, digital, or electronic. I give IARIA permission to distribute the materials without restriction to any institutions or individuals. I give IARIA permission to submit the work for inclusion in article repositories as IARIA sees fit.

I, the undersigned, declare that to the best of my knowledge, the article is does not contain libelous or otherwise unlawful contents or invading the right of privacy or infringing on a proprietary right.

Following the copyright release, any circulated version of the article must bear the copyright notice and any header and footer information that IARIA applies to the published article.

IARIA grants royalty-free permission to the authors to disseminate the work, under the above provisions, for any academic, commercial, or industrial use. IARIA grants royalty-free permission to any individuals or institutions to make the article available electronically, online, or in print.

IARIA acknowledges that rights to any algorithm, process, procedure, apparatus, or articles of manufacture remain with the authors and their employers.

I, the undersigned, understand that IARIA will not be liable, in contract, tort (including, without limitation, negligence), pre-contract or other representations (other than fraudulent misrepresentations) or otherwise in connection with the publication of my work.

Exception to the above is made for work-for-hire performed while employed by the government. In that case, copyright to the material remains with the said government. The rightful owners (authors and government entity) grant unlimited and unrestricted permission to IARIA, IARIA's contractors, and IARIA's partners to further distribute the work.

Table of Contents

SC-FDMA Waveform Enabling Frequency Holes in a Shared Spectrum Context

Benjamin Ros, Sonia Cazalens, Christelle Boustie
Satellite telecommunications systems department
CNES (French Space Agency)
Toulouse, France
e-mail: benjamin.ros@cnes.fr

Xavier Fouchet
SILICOM
Toulouse, France
e-mail: xfouchet@silicom.fr

***Abstract*—Single-Carrier Frequency Division Multiple Access (SC-FDMA) is a well suited waveform for satellite link thanks to its low Peak-to-Average Power Ratio (PAPR) level, compared to Orthogonal Frequency Division Multiple Access (OFDMA). Moreover, it allows a frequency access which is very attractive given the growing interest in integrated satellite-terrestrial system and dynamic use of the spectrum. The purpose of this article is to prove that doing frequency holes to enable the dynamic use of the spectrum don't degrade so much waveform envelope fluctuations while enabling efficient transmission.**

Keywords— shared spectrum; integrated satellite terrestrial system; OFDM; SC-FDMA; (EW)-SC-FDMA; satellite payload impairments; carrier to intermodulation ratio.

I. INTRODUCTION

For spectral resource optimization in a dynamic spectral resource sharing context, a waveform which seems to be promising for the satellite is the Single-Carrier Frequency Division Multiple Access (SC-FDMA). Its interest has already been demonstrated in the Digital Video Broadcasting (DVB) - Next Generation broadcasting system to Handheld (NGH) [1] standardization process in an S-band mobile system. This waveform is also recommended in an International Telecommunication Union (ITU) working group [5] for satellite International Mobile Telecommunications-Advanced (IMT-advanced) systems. More recently, interest of this waveform raised in European Telecommunications Standards Institute - Satellite Communication and Navigation (ETSI-SCN) and DVB - Second Generation Satellite Extensions (S2x) standardization process applicable to higher frequency bands (Ku, Ka).

Besides, the 5G Infrastructure Public-Private Partnership (5G PPP) consortium [6] targets for new systems a dynamic sharing of existing frequency bands (Cognitive Radio) and the emergence of integrated satellite terrestrial systems. Integration of satellite will allow delivering 5G services in areas of low population density and to ensure communications everywhere in case of a disaster.

Multi-carrier waveform is not the historical waveform used on satellites. But, as European Union is promoting through incoming 5G the integration of satellite and terrestrial components [6], paradigm is currently being modified. Indeed, to make easier spectrum scalability, satellite should be able to choose sub-bands it uses depending on existing terrestrial systems. Moreover, in the case of integrated systems specifically, to encourage mass market terminal deployment, terminal should be able to receive the satellite signal or terrestrial one with the same chipset. This emphasizes the need for satellite to use a multi-carrier granular access, as it is already the case in terrestrial systems. If Orthogonal Frequency Division Multiple Access (OFDMA) first appears as obvious solution, it should be mentioned that this waveform has a high crest factor, which does not allow optimizing the efficiency of satellite amplifiers. An intermediate solution is the use of SC-FDMA, keeping the granular access in frequency, but severely limiting the envelope fluctuations, it becomes even more attractive to the satellite. This is why this waveform has been chosen here to address this problem.

One example of such integrated system (the spectrum of the terrestrial and satellite components is managed by the same company) is given hereafter. It provides a service to nomadic or mobile devices. To optimize the spectrum use according to the traffic, the scheduler decides if a part of the band is allocated to either satellite component or terrestrial one, as it is depicted in Figure 1.

In section II, description of the waveform enabling frequency holes is done. In section III, satellite payload impairments are discussed and then in section IV, methodology used to analyze results obtained is introduced. Finally, in section V, simulations results are presented, comparing OFDMA, SC-FDMA and Extended-and-Weighted SC-FDMA (EW-SC-FDMA) performances over non-linear channel, and considering frequency holes.

II. SC-FDMA WAVEFORM MODELIZATION WITH FREQUENCY HOLES

A. Basic SC-FDMA modeling

Because there have been several studies on SC-FDMA waveform [3][4], modeling will not be strictly detailed. However, differences with OFDMA transceiver architecture will be emphasized. General SC-FDMA transceiver is summarized in Figure 3, and is described hereafter.

Firstly, interleaved and coded bits b_n are mapped into symbols c_i, $i \in [0 \dots M-1]$. Spreading operation, specific to SC-FDMA transmission, is then done by applying an M–Discrete Fourier Transform (DFT) to the c_i symbols to get C_k symbols, $k \in [-\frac{M}{2} \dots \frac{M}{2} - 1]$:

$$C_k = \frac{1}{\sqrt{M}} \sum_{i=0}^{i=M-1} c_i \, e^{-j\frac{2\pi ki}{M}}. \quad (1)$$

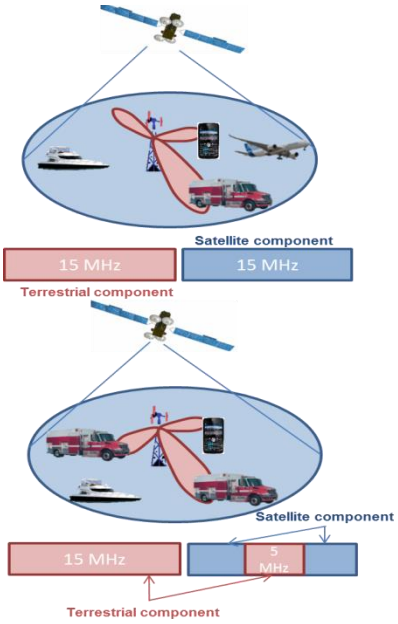

Figure 1. Example of integrated system managing efficiently its spectrum.

In case of Extended-and-Weighted SC-FDMA (EW-SC-FDMA), as it can be seen in Figure 2, some of the edge C_k symbols are duplicated and put at the opposite side edge in the guard band. Main sizing parameter here is α, called the roll off factor. Extension process outputs M', equals to (1+α)M, complex symbols $C_{k'}$. Weighting process is finally applied over these subcarriers in order to have a square root raised cosine shaping [3]. It multiplies term by term $H_{SRC}(k')$ with $C_{k'}$ to get $S_{k'}$. Note that $H_{SRC}(k')$, $k' \in \left[-\frac{M'}{2}; +\frac{M'}{2}-1\right]$, is the frequency response of the square root raised cosine filter, given by:

$$H_{SRC}(k') = \begin{cases} 1, & 0 \le |k'| < \frac{(1-\alpha)}{2}M \\ \cos\left[\frac{\pi}{2\alpha M}\left(|k'| - \frac{(1-\alpha)}{2}M\right)\right], & \frac{(1-\alpha)}{2}M \le |k'| < \frac{(1+\alpha)}{2}M \end{cases} \quad (2)$$

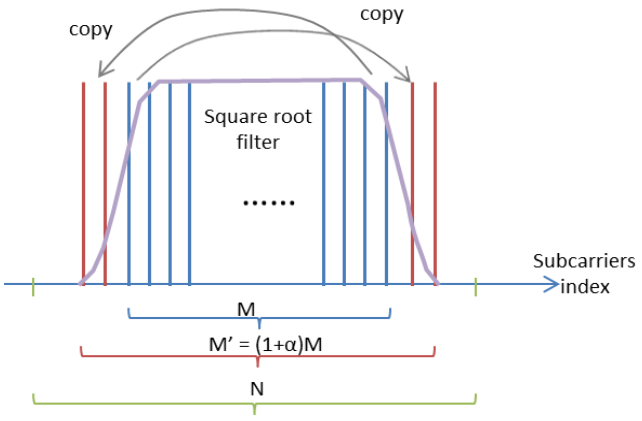

Figure 2. Extension and weighting process.

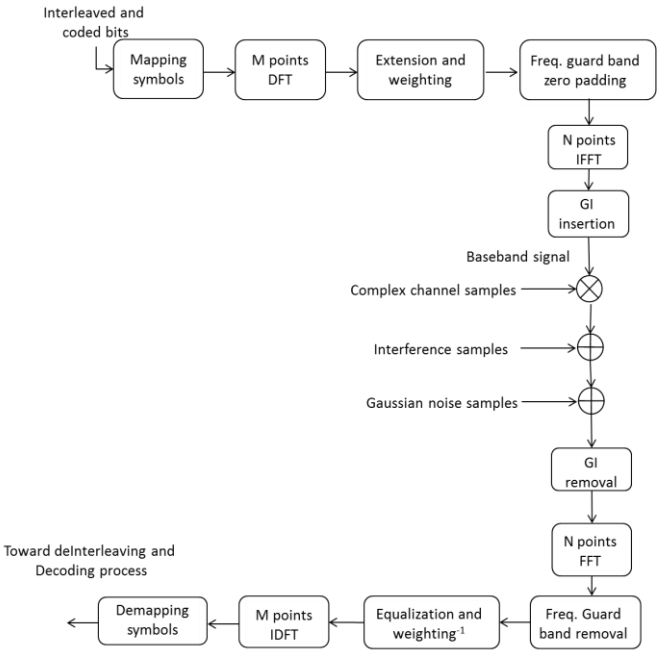

Figure 3. SC-FDMA transceiver architecture

It can be pointed out that when α equals to 0, process is strictly equivalent to SC-FDMA process. Next, unused subcarriers in the guard band are filled by zero, exactly N - (1+α)M, to get a vector owning N complex symbols, $S_{k''}$. Note that to be compliant with OFDMA process, N should be a power of 2, that is not the case for M. Lastly, OFDMA modulation process can be done by applying a N-Inverse Fast Fourier Transform (IFFT) and inserting guard interval, getting baseband signal s_n.

For receiver considerations, the equalization should use a Minimum Mean Square Error (MMSE) frequency domain algorithm [3][4], working subcarrier by subcarrier. Furthermore, a slightly difference which can be observed with SC-FDMA receiver compared to OFDMA one, is the way to compute the Log Likelihood Ratio (LLR) metrics at the demapping symbols step. Classic LLR formulation is reminded here:

$$LLR(b_i) = ln \frac{\Sigma_{x \in c_i^1} exp\left(-\frac{|I-\rho_I I_x|^2 + |Q-\rho_Q Q_x|^2}{2\sigma^2}\right)}{\Sigma_{x \in c_i^0} exp\left(-\frac{|I-\rho_I I_x|^2 + |Q-\rho_Q Q_x|^2}{2\sigma^2}\right)}, \quad (3)$$

where x is a symbol of the Quadrature amplitude modulation (QAM) constellation, c_i^j represents the symbols of the constellation carrying the bit b_i when b_i is equal to *j*, I and Q are the in phase and quadrature components of the received signal, $\rho_{I/Q}$ is the fading on the I or Q component, $2\sigma^2$ is the Additive White Gaussian Noise (AWGN) variance, I_x and Q_x denote the reference symbols of the QAM constellation. In SC-FDMA receiver, because of the despreading process, i.e., there is a M points Inverse-DFT between equalization and demapping process, it is assumed that $\rho_{I/Q}$ can be

approximated to the mean square of the frequency channel response of the corresponding OFDMA symbol over the active subcarriers $H_c(k')$:

$$\rho_{I/Q} \approx \sqrt{\frac{\sum_{k'=-M'/2}^{\frac{M'}{2}-1} |H_C(k').H_{SRC}(k')|^2}{M}}. \quad (4)$$

B. *Frequency holes insertion*

Frequency holes are inserted inside useful signal at the spreading process level. In fact, spreading applies a L<M DFT over the incoming c_i symbols before filling M-L other symbols with zero, as it is drawn in Figure 4.

Some vocabulary is necessary to define where frequency hole is located. β is defined as the relative bandwidth occupied by frequency holes over maximum achievable useful bandwidth:

$$\beta = \frac{M-L}{M}. \quad (5)$$

Δ is the relative shift of the frequency hole center relatively to the bandwidth center. To clarify these notations, an example is given in Figure 5.

C. *Interference model*

The interferer location is defined as it is done for the frequency holes, with β and Δ parameters. Generative model is quite simple: complex symbols are generated according to a normal law $\mathcal{N}(0;\beta)$, supposing power of the useful signal as unitary power when occupying all possible subcarriers. Interference symbols are applied to subcarriers as if it was an OFDMA signal. When frequency holes are defined, interference is added exactly at the hole location.

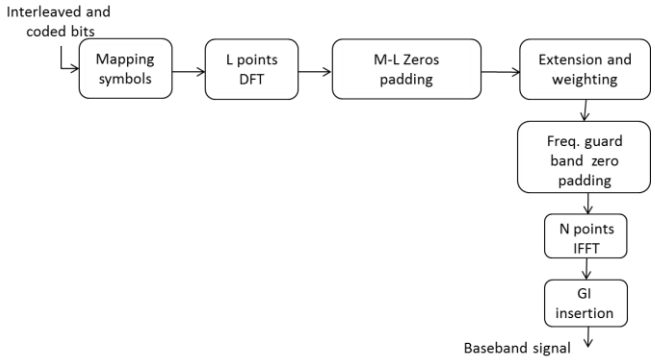

Figure 4. SC-FDMA transceiver architecture enabling frequency holes

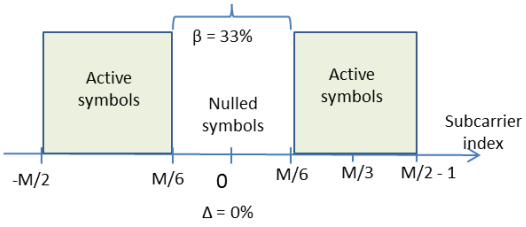

Figure 5. Position and size example of a frequency hole

III. SATELLITE PAYLOAD IMPAIRMENTS

In the literature, satellite payload impairments models usually include three main origins: nonlinear amplifier, selective input filters and phase noise [2]. For the current work, it is assumed that only non-linearity effects are considered. Phase noise is not considered because it is well known that effect is very weak over a Quadrature Phase Shift Keying (QPSK) modulation combined with current stability specifications over satellite local oscillators. Input filters distortion may have an effect over the performances, but as the three studied waveforms (OFDMA, SC-FDMA, EW-SC-FDMA) have a subcarrier equalization process, it can be predicted that the effect would be quite closed to each other, while not negligible. This is the reason why it was decided to focus on non-linearity effects only, knowing there are envelope fluctuations differences between waveforms. A typical un-linearized model is chosen, giving Output Back Off (OBO) [dB] as a function of Input Back Off (IBO) [dB], and giving phase slope Kp [degrees/dB] as a function of IBO:

$$OBO = \sqrt{U} - \sqrt{U + V.IBO^2}, \quad (6)$$

$$Kp = \begin{cases} 0 \; when \; IBO \in [-\infty; -15 \; dB] \\ 0.2 \; when \; IBO \in]-15 \; dB; \; -9 \; dB], \\ 2 \; when \; IBO \in]-9 \; dB; \; +5 \; dB] \end{cases} \quad (7)$$

Where U=24.29 and V=1.28. Typical representation is given in Figure 6.

Nonlinear conversion is applied to complex baseband signal as a look-up table, before entering to propagation channel process, as it is shown in Figure 7.

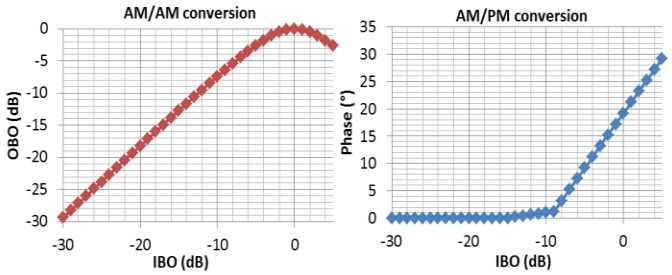

Figure 6. Non linearity conversion curve

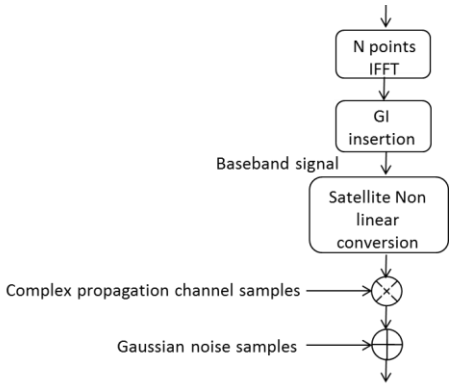

Figure 7. Insertion of non-linearity conversion in the transceiver

Note that the output of the satellite non-linear block delivers unitary power.

IV. COMPARATIVE METHOD ANALYSIS

We are about to compare different waveforms enabling creation of a frequency hole inside their spectrum. Here is proposed a method to compare waveforms, considering power loss, signal quality loss, and Carrier over Intermodulation ratio. Power loss is corresponding to OBO value, and signal quality loss equals to the performance gap considering non-linearity sub-block or not. Total loss metric is then defined as:

$$Total\ loss = signal\ quality\ loss + power\ loss$$

$$\begin{cases} power\ loss = |OBO| \\ signal\ quality\ loss = \frac{C'+I_m}{N}_{BER=10^{-5}} - \frac{C}{N}_{BER=10^{-5}} \end{cases}, \quad (10)$$

Where $\frac{C}{N}_{BER=10^{-5}}$ is the required signal to noise ratio in dB with ideal amplifier response at bit error rate (BER) 10^{-5}, and $\frac{C'+I_m}{N}_{BER=10^{-5}}$ is the required amplified signal power (pure signal plus intermodulated part) to noise ratio in dB at bit error rate 10^{-5}. Both metrics are given at the receiver input location. Assuming that I_m has a Gaussian behavior, pure Signal over Intermodulation power ratio $\left(\frac{C'}{I_m}\right)$ can be derived (linear form):

$$\left(\frac{C'}{I_m}\right) = \frac{1+\left(\frac{C'+I_m}{N}\right)_{BER=10^{-5}}}{\left(\frac{C}{N}\right)^{-1}_{BER=10^{-5}} * \left(\frac{C'+I_m}{N}\right)^{-1}_{BER=10^{-5}} - 1}. \quad (11)$$

Signal over Intermodulation power ratio is also an important criterion according to satellite operators, because it demonstrates the ability of the payload to work with any spectral efficiency. As a result, performances of the waveforms will be compared at equal $\left(\frac{C'}{I_m}\right)$ ratio. It shall be pointed out that for a same spectral efficiency, $\left(\frac{C'}{I_m}\right)$ is directly linked to signal quality loss considering (10) and (11). Thus, judicious representation may be, for each waveform, required |OBO| to get BER $= 10^{-5}$ vs $\left(\frac{C'}{I_m}\right)$ representation.

V. SIMULATIONS

A. Parameters and simulation chain

Simulations are performed by using a DVB-NGH like transceiver chain [1]. DVB-NGH specifications enable SC-FDMA utilization without extension and weighting functionality. Besides, frequency hole, interferences and on-board nonlinear amplifier had to be considered as it is depicted in Figure 8. A significant importance should be given to the way signal over noise ratios are computed when dealing with frequency holes. As power at output of the amplifier is unitary in simulations, it was chosen to get noise power considering the maximum achievable band for useful signal, independently from the frequency hole width. This choice may appear unsuitable for conventional multi-carrier receiver, which may be able to ignore the subcarriers carrying only noise. However, for results comparison, it enables to avoid any surboosting effect because of both frequency holes and unitary power: waveforms are compared at same E_S/N_0. Lastly, simulation parameters are summarized in Tab. I.

B. Enveloppe fluctuations

Because dealing with non-linearity effects, the study of envelope fluctuations for each waveform may help to understand further results. This is why complementary cumulated distribution function for instantaneous power is given for each studied waveform in Figure 9.

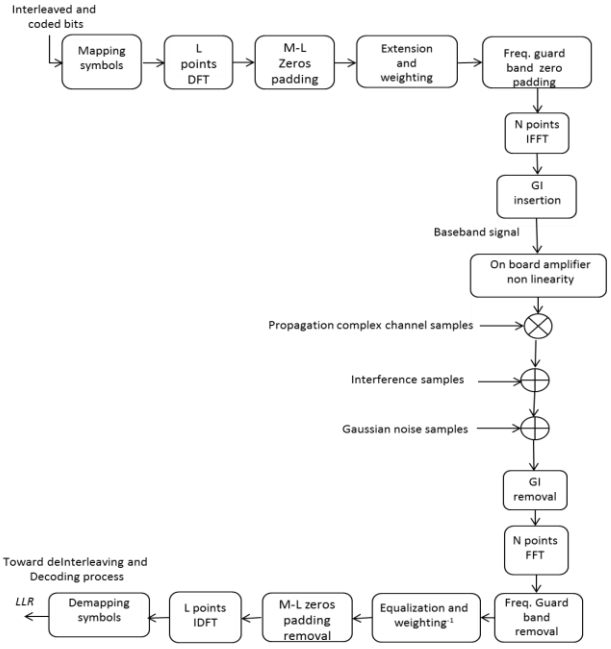

Figure 8. Simulation Chain, including SC-FDMA, frequency hole, interference and non linearity functionalities

TABLE I. MAIN PARAMETERS FOR PERFORMED SIMULATIONS

Parameter name	Value
Satellite signal Bandwidth	15 MHz
Sampling frequency	120/7 MHz
Modulation and coding	QPSK ½ (real coder efficiency 4/9) LDPC + BCH encoder 16200 bits codeword
Max active subcarriers (M)	426
OFDM FFT size (N)	512
OFDM Guard interval	1/16
Total OFDM symbol duration	31.73 µs
SC-FDMA	α = 0 (SC-FDMA) or α = 5% (EW-SC-FDMA)
Frequency hole insertion	Δ=0, β=33% when activated
Interference insertion	Δ=0, β=33% when activated
Satellite RF model	Typical Voltera model for un-linearized TWTA when activated
Propagation channel	Ideal (AWGN) in this study

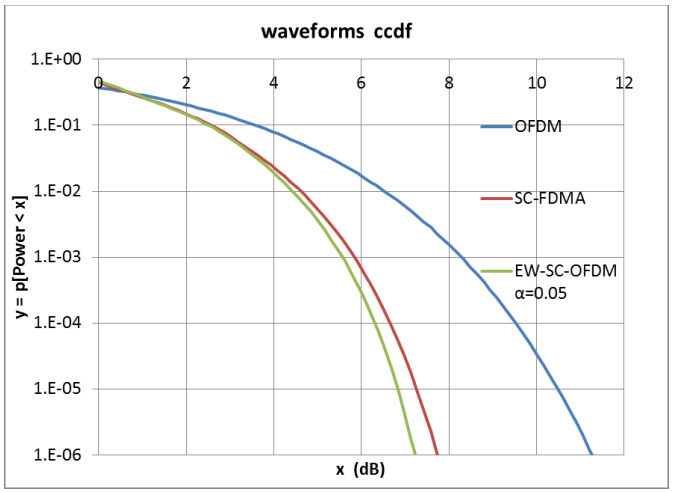

Figure 9. Comparison of waveforms power fluctuation

As it can be found in literature, SC-FDMA waveform performs better than OFDMA one. Using extension can help to better decrease fluctuations, but in this paper 5% roll off factor was chosen, that explains the small difference with SC-FDMA. However, one shall note that this comparison is considering waveforms without frequency holes insertion.

C. *Results without frequency holes*

As a reference, BER simulations have been performed according to the method described in chapter IV. For a wide range of C/I_m, it appears in Figure 10 that SC-FDMA like waveforms outperform OFDMA, gap increasing when C/I_m is growing. These results emphasize the fact that when no interferer is present, SC-FDMA is a good choice to be compatible from terrestrial multi-carrier legacy and to enjoy efficient use of the satellite payloads.

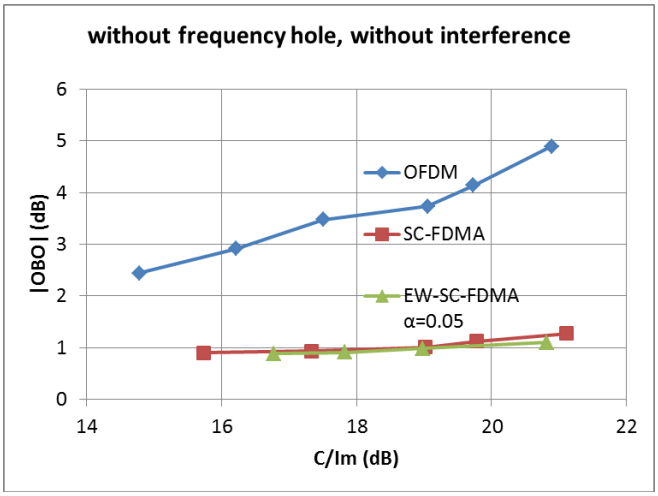

Figure 10. Comparison of waveforms when no frequency holes are inserted and without interference

D. *Results with frequency holes*

Here, frequency hole was inserted with $\Delta=0$ and $\beta=33\%$ parameters. Especially for single carrier waveforms, inserting a such wide hole inside useful bandwidth may modify its fluctuations behavior. But, as it is depicted in Figure 11, single carrier waveforms performances are not so much degraded by the hole insertion, and remain quite competitive compared to OFDMA, despite the large width of the hole.

E. *Results with interferences*

Interferences are inserted with $\Delta=0$ and $\beta=33\%$ parameter. I_0, the power spectrum density of interferer is the same as C_0, the power spectrum density of the signal. That leads to relatively weak level of interferers but with quite large bandwidth (1/3 of achievable useful bandwidth). With no real surprise, it is first checked that inserting hole in any of the three waveforms results in a negligible degradation (see it in Figures 12, 13, and 14), because only secondary lobes of active useful subcarriers capture interferences when frequency hole is inserted.

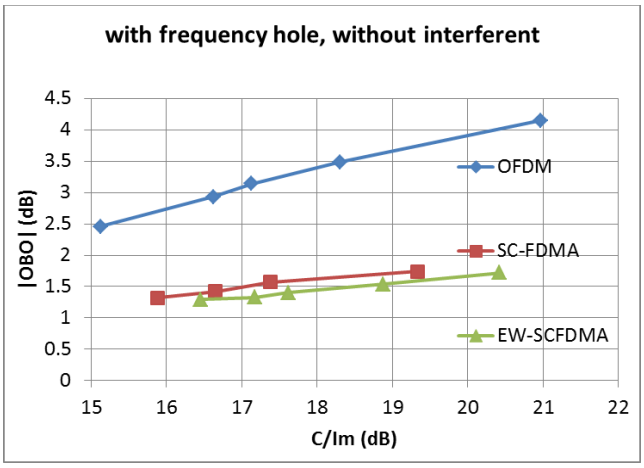

Figure 11. Comparison of waveforms when frequency holes are inserted and without interference

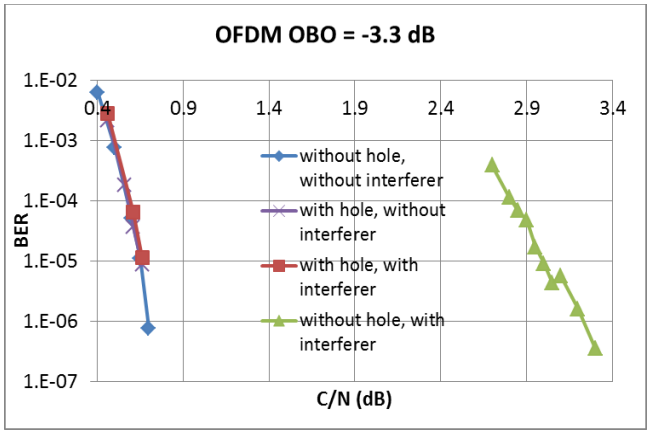

Figure 12. OFDM behaviour with weak interferent

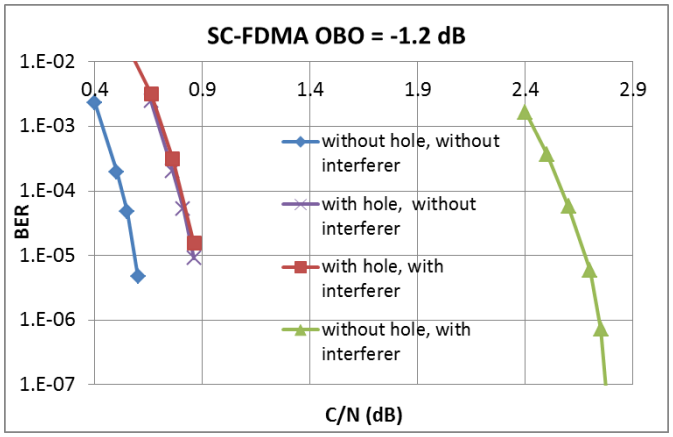

Figure 13. SC-FDMA behaviour with weak interferent

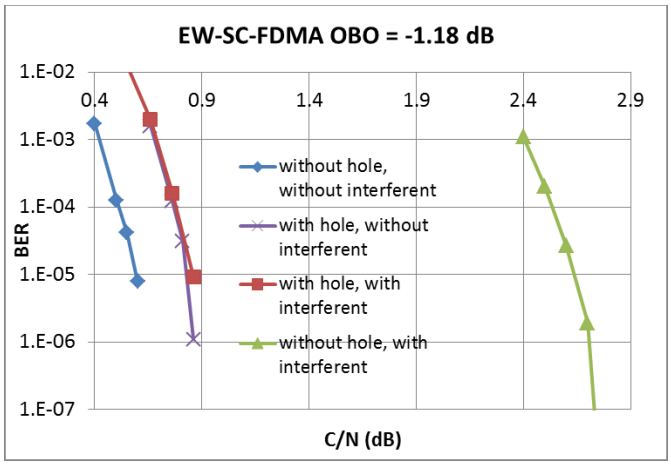

Figure 14. EW-SC-FDMA behaviour with weak interferent

Besides, no creating hole when interferer is present is showing quite degraded results, even if the interferer has a weak level. Reader shall point out that weak interferer was chosen to visualize the degradation on the same curve. But, from a system point of view, power spectrum density of a terrestrial interferer would be greater than satellite useful signal one, and would emphasize the need for such frequency hole in the waveform.

VI. CONCLUSION

At a time where, on one hand, historical satellite chipset manufacturers are working to enlarge their modulated carriers bandwidths to maximize the payload efficiency, and on the other hand there is a need to make easier spectrum scalability, a SC-FDMA based solution was introduced to address this issue. In this paper, it has been shown that SC-FDMA waveform fluctuations enable using payload in an efficient way, and that creating frequency hole do not degrade so much envelope fluctuations; SC-FDMA waveform remains in all cases relevant compared to OFDMA. Thus, using this waveform would take advantage of both frequency scalability and payload efficiency, while offering a solution at physical layer level for dynamic spectral resource sharing systems.

For further work, a study case with several powers and bandwidths for the interferer should be done to better demonstrate the need for inserting frequency hole. Moreover, total achievable bit rate should be considered: by using the spectrum compression effect when creating frequency hole, spectral efficiency could be improved and may balance the lack of spectrum.

ACKNOWLEDGMENT

The authors thank the Satellite Mobile Innovative Laboratory and Engineering project of French Space Agency allowing this kind of applicative research.

REFERENCES

[1] ETSI, “Digital Video Broadcasting (DVB); Next Generation broadcasting system to Handheld, physical layer specification (DVB-NGH)”, EN 303 105 V1.1.1, May 2013.

[2] ETSI, “DVB-SH implementations Guidelines”, TS 102 584 V1.3.1, Nov 2011. [Online]. Available from: http://www.etsi.org/deliver/etsi_ts/102500_102599/102584/01.03.01_60/ts_102584v010301p.pdf [retrieved: April, 2015].

[3] S. Okuyama, K. Takeda, and F. Adashi, “MMSE frequency-domain equalization using spectrum combining for Nyquist filtered broadband”, VTC spring conference, Taipei, Taiwan, May 2010, pp. 1-5.

[4] H. Kobayashi, T. Fukuharal, H. Yuant, and Y. Takeuchi, “Proposal of single carrier OFDM technique with adaptive modulation method”, VTC spring conference, April 2003, pp. 1915-1919 vol. 3.

[5] ITU-R, Recommendation M.2047-0, “Detailed specifications of the satellite radio interfaces of International Mobile Telecommunications-Advanced (IMT-advanced)”, December 2013. [Online]. Available from: http://www.itu.int/dms_pubrec/itu-r/rec/m/R-REC-M.2047-0-201312-I!!PDF-E.pdf [retrieved: April, 2015].

[6] 5G-Private Public Partnership project homepage. [Online]. Available from: http://5g-ppp.eu/etp/ [retrieved: April, 2015].

 ISBN: 978-1-61208-397-1

Application of Knife-Edge Diffraction Theory to Optimize Radio Frequency Compatibility On-board a Satellite

Jens Timmermann
Electrical Systems (TSPET32)
Airbus DS GmbH
Friedrichshafen, Germany
email: Jens.Timmermann@astrium.eads.net

Christian Imhof
Electrical Systems (TSPET32)
Airbus DS GmbH
Friedrichshafen, Germany
email: Christian.Imhof@astrium.eads.net

Dieter Lebherz
Electrical Systems (TSPET32)
Airbus DS GmbH
Friedrichshafen, Germany
email: Dieter.Lebherz@astrium.eads.net

Jörg Lange
Electrical Systems (TSPET32)
Airbus DS GmbH
Friedrichshafen, Germany
email: Joerg.Lange@astrium.eads.net

***Abstract*— Modern Earth observation satellites accommodate manifold combinations of Radio Frequency (RF) transmitters and receivers located at various positions on-board the satellite. To minimize the field strength generated by the Tx at the Rx position, one method is to shade the line of sight path by a metallic baffle leading to signal attenuation. This contribution shows the achievable attenuation in practical satellite design and compares the results obtained by field simulations to those obtained by a simplified model (knife-edge diffraction theory). Hereby, knife-edge theory has been expanded by inclusion of angle-dependent antenna gain. Due to the good agreement of the results, knife-edge theory can be used for first-order assessments and parameter studies. This approach minimizes the overall computation time and is currently used to optimize Radio Frequency Compatibility (RFC) on-board the future MetOp Second Generation (MetOp-SG) satellites.**

Keywords- Radio Frequency Compatibility; knife-edge diffraction; baffle attenuation; satellite performance.

I. INTRODUCTION

The European MetOp meteorological satellites currenty in orbit will be replaced after 2020 by follow-on satellites with advanced instrumentation. The MetOp-SG will ensure observations until approximately 2040 [1].

After successful finalization of ESA Phase A/B1 study by Airbus Defence and Space, the company has been nominated by EUMETSAT / ESA as prime contractor for the provision of the space segment of MetOp-SG. For this purpose, two satellites (Satellite A and Satellite B) with different scientific instruments are currently developed. Each satellite houses a variety of transmitters (Tx) and instrument receivers (Rx) being sensitive in the RF frequency range. The purpose of the transmitters is to transmit data towards the Earth while ensuring that the instrument receivers are not distorted by the emissions. Although the on-board transmitters are designed to radiate towards the Earth, the field strength around the transmitters is not negligible potentially leading to interference seen by the on-board receivers [2]. Limiting this effect is key to proper performance of the receivers. Reduction of unintended interference power can be achieved by, e.g., sufficiently large distances among transmitters and receivers, optimization of antenna patterns and inclusion of additional baffles to generate a No-Line-of-Sight between Tx and Rx. Figure 1 shows a preliminary model of "Satellite A" together with the positions of an exemplary transmitter radiating in the X-Band towards the Earth, the Microwave Sounder (MWS) instrument receiver, a baffle and the Nadir direction (towards the Earth during flight).

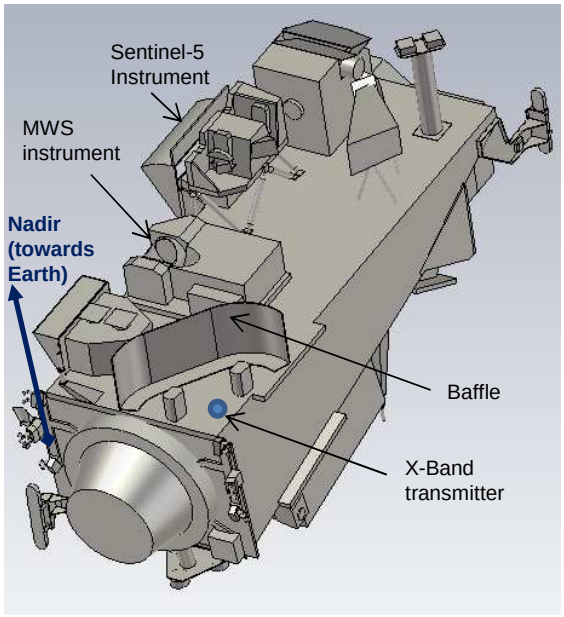

Figure 1. Model of "Satellite A" being part of MetOp Second Generation: Exemplary transmitter and instrument receiver positions

This paper investigates the effect of the baffle on the field strength at the MWS. Hereby, section II presents two general approaches (field simulation and knife-edge diffraction theory) to determine the baffle attenuation. Section III shows an expansion of knife-edge diffraction theory by inclusion of angle-dependent antenna gain and compares the obtained results for the two approaches. Conclusions are given in section IV.

 ISBN: 978-1-61208-397-1

II. APPROACH TO DETERMINE BAFFLE INFLUENCE

This section assumes a metallic baffle (e.g., wall) between a Tx and a victim Rx to limit undesired signals at the Rx position. The physics of electromagnetic wave propagation at RF frequencies is the reason for an undesired signal still present at the Rx position, albeit strongly attenuated: Signal paths originating from diffraction at the baffle can travel towards the Rx as a result of Huygen's principle. In addition, further signal contributions may originate from reflections or scattering at objects in the vicinity of the Tx and Rx. The principle of this multipath propagation is visualized in Figure 2. Hereby, the shown diffracted path interacts with the baffle directly above the hypothetical Line of Sight path. In general, further diffracted paths are possible with interaction points along the top of the baffle.

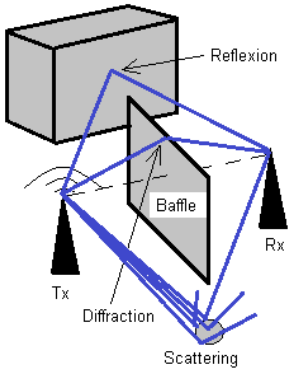

Figure 2. Multipath propagation

Since reflected and scattered paths can carry significant power levels, these contributions should be avoided by a proper design of the baffle (e.g., by an adequate height and an adequate length around the surrounding objects). In this case, the dominant contribution at Rx side only results from the diffraction at the baffle. Due to the physics of diffraction, the interfering signal decreases with steeper diffraction angle (e.g., increased baffle height) and frequency.

The influence of a baffle on the received signal can be determined either by:

- A simplified wave propagation model, e.g., theory of knife-edge diffraction.
- 3D field simulations: A simulation tool solves the corresponding electromagnetic field equations and determines the received field strength at the Rx. This method implicitly takes into account diffraction, reflection and scattering.

A. *Analytical Approach by Knife-edge Diffraction*

The scenario related to "knife-edge diffraction" is visualized in Figure 3: It assumes a "knife-edge" obstacle between Tx and Rx and shows the diffracted path between Tx and Rx. Hereby, the obstacle subdivides the distance between Tx and Rx into d_1 and d_2. Two cases are possible: In case 1, the upper edge of the obstacle appears at a height $h > 0$ w.r.t. the Line of Sight (LOS). This leads to a "No Line of Sight" (NLOS) scenario. In case 2, the upper edge of the obstacle appears at a height $h < 0$ w.r.t. LOS. This leads to a LOS scenario.

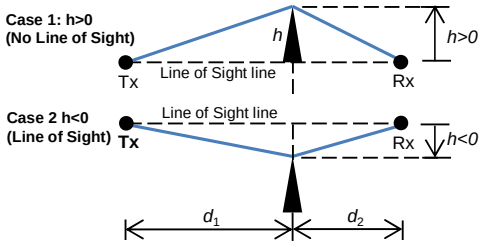

Figure 3. Diffraction at a "knife-edge" for two cases: "No Line of Sight" and "Line of Sight"

According to [3] and [6], the loss induced by the baffle (diffraction loss) is

$$L_{dB} = -20 \cdot \log_{10} \left| F(v) \right| \tag{1}$$

with the Fresnel integral

$$F(v) = \frac{1+j}{2} \cdot \int_{v}^{\infty} e^{-j\pi t^2/2} dt \tag{2}$$

and

$$v = h \cdot \sqrt{\frac{2}{\lambda} \cdot \left(\frac{1}{d_1} + \frac{1}{d_2} \right)} \tag{3}$$

where v is the Fresnel-Kirchhoff diffraction parameter and $\lambda = c_0 / f$ is the wavelength of the considered signal. The resulting diffraction loss ("baffle attenuation") as a function of v is plotted below for v = [-5 .. 5] as per [4]:

Figure 4. Diffraction loss of a "knife-edge" versus parameter v [4]

The figure shows the level of the diffracted path in dB relative to freespace which is negative for $v > -0.7$. Hereby, a level of "- x dB" corresponds to an attenuation of "x dB". According to (3), v and h are proportional, hence, $h > 0$ (NLOS) is associated with $v > 0$, yielding a baffle attenuation of at least 6 dB (see graph).

The above graph can be approximated, e.g., by the following piecewise function [5]:

$$L_{dB} = \begin{cases} -(6 + 9 \cdot v - 1.27v^2) & \text{if } 0 \le v \le 2.4 \\ -(13 + 20 \cdot \log_{10}(v)) & \text{if } v > 2.4 \end{cases} \quad (4)$$

Note that above equation is the good one compared to a sign error related to $1.27v^2$ in [5].

To quickly determine the "baffle attenuation", the approach is to determine v by (3) and then to apply (4) for the obtained v. Example: For d_1 = 1.5 m, d_2 = 1.5 m and f = 8.2 GHz (X-Band), Figure 5 visualizes the "baffle attenuation" as a function of h.

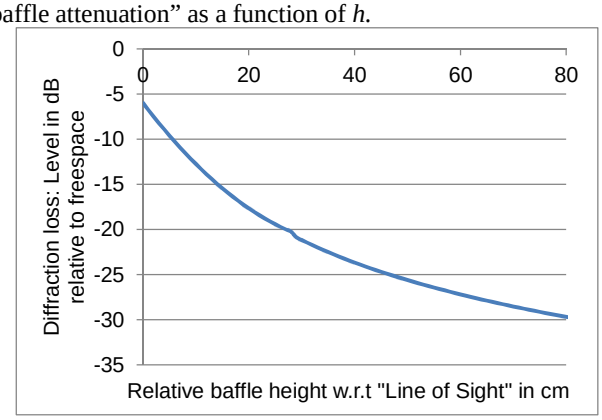

Figure 5. Diffraction loss of a "knife-edge" versus h assuming d_1 = 1.5 m, d_2 = 1.5 m and f = 8.2 GHz

The result reveals that the attenuation is very sensitive to the height. This behavior is due to the small wavelength which is only 3.7 cm in the considered case.

The other way around, the theory of knife-edge diffraction reveals that the baffle attenuation in X-Band frequency range can be improved significantly by only slightly increasing the baffle height. In practice, constraints on the height are given by the required field of views of the transmitters and instruments.

B. Simulation based approach (CST field simulation)

An approach based on solving electromagnetic field equations has the following advantages:

- Result available for any baffle geometry (not only for simple objects like a "knife-edge")
- All wave propagation phenomena implicitly taken into account (e.g., also reflection and scattering), not only diffraction as in the "knife-edge model"
- Environment (surrounding structure) can be taken into account

A well suited approach for satellite engineering is to use the simulation software "Microwave Studio" from the company CST. This tool has, e.g., also been used by Airbus Defence and Space to assess EMC/RFC for MTG satellites.

To determine the baffle attenuation, a dipole antenna is placed at the transmitter position and oriented in a way that the radiation towards the receiver position is maximized. The electric field strength in dB(mV/m) at a victim receiver is first simulated without baffle (reference, including Line of Sight path) and then with baffle. In both cases, the surrounding satellite structure is taken into account. The difference of the electric field strength in dB(mV/m) corresponds to the baffle attenuation in dB.

To obtain the simulation results reported in this paper, the integral equal solver based on Multi Level Fast Multipole Method (MLFMM) has been used. MLFMM is a technique based on the same principles as the traditional "Method of Moments" (MoM), but applicable to models of significantly larger electrical size. Given the geometrical dimensions of typical Earth observation satellites, simulations at frequencies as high as (roughly) 30 GHz can be performed applying this numerical technique. Higher frequencies (smaller wavelengths) require a mesh size which results in increased memory demand and simulation time. Should the need arise to overcome that constraint for practical limitations (e.g., memory size), the satellite structure can be restricted to a representative volume encompassing the Tx and Rx positions.

III. COMPARISON OF FIELD SIMULATIONS W.R.T. KNIFE-EDGE THEORY

On Satellite A, the radiation of the X-Band transmitter towards the MWS instrument is reduced by a baffle. Figure 6 visualizes a part of the satellite structure including the phase center of the transmitter (modeled as a dipole) radiating at 8.2 GHz, the baffle as well as the MWS victim receiver. Hereby, two Rx positions ("Position 1", "Position 2") are considered, where "Position 2" corresponds to the center of the MWS reflector plate. The figure also shows the position of the Sentinel-5 instrument.

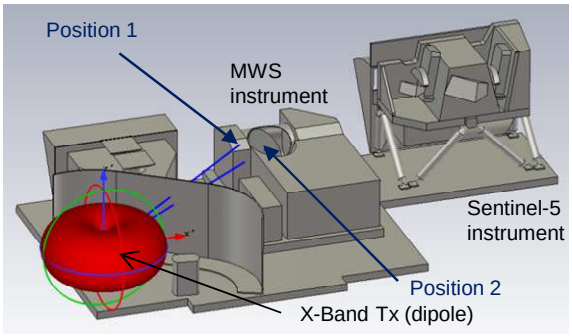

Figure 6. Part of the structure of Satellite A (dipole Tx)

The figure also indicates the LOS directions between Tx and the two Rx positions. The electric field strengths are simulated with the CST software for two scenarios:

- "without baffle"

 ISBN: 978-1-61208-397-1

- "with baffle".

Results are presented below:

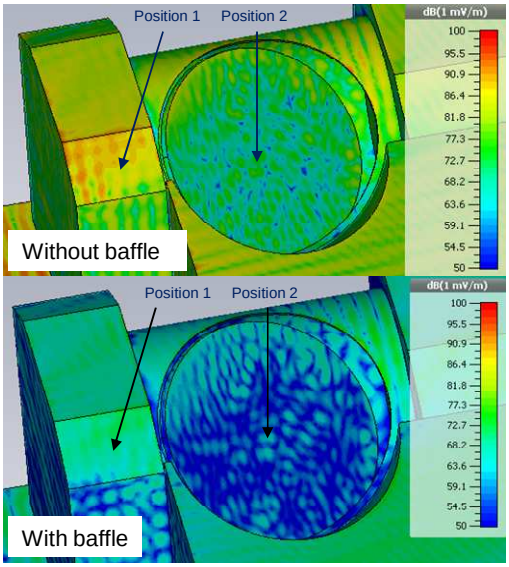

Figure 7. Simulated field strength at MWS assuming radiating dipole; f=8.2 GHz

Observation:
Position 1: The case "Without baffle" reveals a field strength of 90 ± 1 dBmV/m". The case "With baffle" reveals 72 ± 1 dBmV/m. Hence, the difference is 18 dB.
Position 2: The case "Without baffle" reveals a field strength of ≈ 77 dBmV/m". The case "With baffle" reveals ≈ 64 dBmV/m. Hence, the difference is 13 dB.

In a second step, the attenuation is estimated by applying the theory of knife-edge diffraction. As explained in the section on knife-edge theory, the baffle subdivides the theoretical LOS path into two distances (d_1, d_2) and a relative height h of the baffle.
For "Position 1", the values are: d_1 = 1.07 m, d_2 = 1.08 m, h = 0.16 m. Assessment at f = 8.2 GHz yields an expected baffle attenuation of 17.2 dB while 18 dB has been simulated by CST software according to the previous figure. This shows a good agreement between simplified theory and CST simulations. Assessment for "Position 2" (d_1 = 1.05 m, d_2 = 1.43 m, h = 0.218 m) at f = 8.2 GHz yields an expected baffle attenuation of 18 dB while 13 dB has been simulated by CST software. This behavior can be explained as follows: In contrast to "Position 1", "Position 2" does not enable a path directly diffracted at the baffle towards the receiver position. The signal can arrive at "Position 2" only via multiple interactions, hence, the knife-edge diffraction theory based on a single baffle is not applicable.

Next, the radiation pattern of the transmit antenna is replaced by the measured characteristics of the physical X-Band antenna which is a helix antenna. Figure 8 visualizes the 3D pattern as well as the antenna gain as a function of elevation angle Θ.

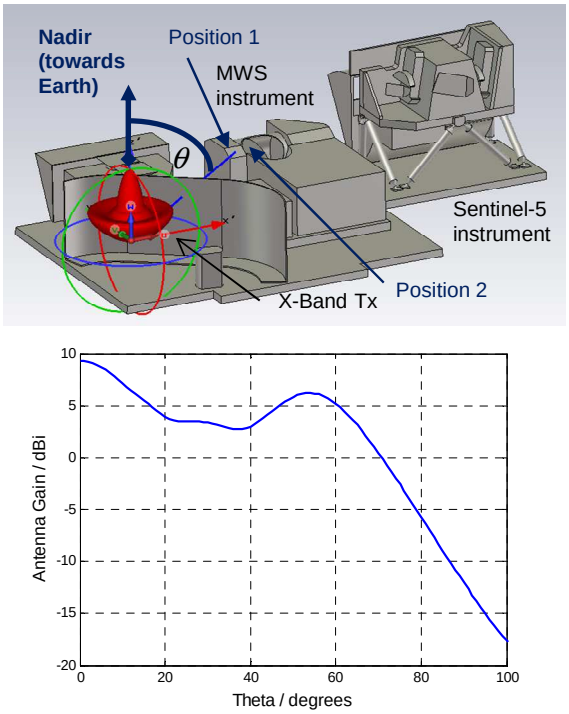

Figure 8. Scenario involving real antenna pattern

For the analysis, "Position 1" is considered. The CST simulation as per Figure 9 reveals: The case "Without baffle" leads to a field strength of 80.8 ± 1 dBmV/m" while "With baffle" leads to 70.8 ± 1 dBmV/m. Hence, the difference caused by the baffle is 10 dB.

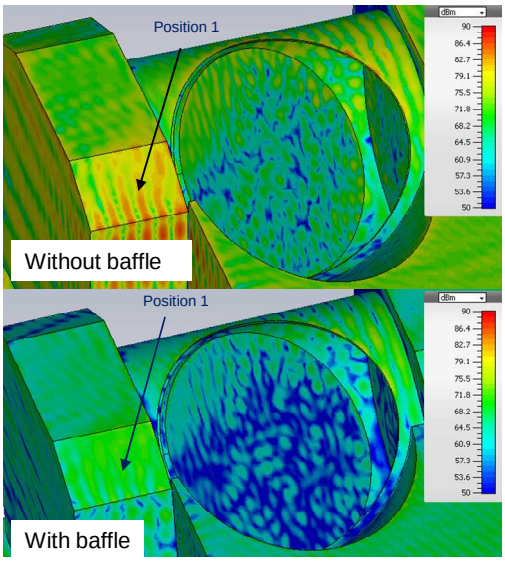

Figure 9. Simulated field strength at MWS assuming real antenna pattern; f=8.2 GHz

The question arises if this value of 10 dB attenuation can be predicted by the knife-edge diffraction theory. To do so, the angle-dependent antenna data has been incorporated into the knife-edge diffraction theory. The approach is described hereafter:

First, the elevation angle is determined under which a propagation path leaves the transmitter. Figure 10 shows the principal scenario:

- A dotted line indicates the propagation path in LOS direction which is present in absence of the baffle. The associated elevation angle is Θ_1.
- In presence of a baffle, a path originating from diffraction appears at an angle $\Theta_2 < \Theta_1$. Hereby, the interaction point with the baffle is inside the plane defined by the Nadir direction and the LOS direction.

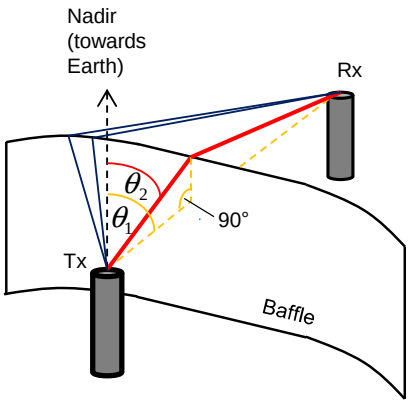

Figure 10. Principal scenario involving diffracted paths

For "Position 1", the elevation angles and the associated antenna gain according to Figure 8 are:

- Θ_1 = 89.9 deg, associated with a gain of -12.5 dBi.
- Θ_2 = 82.4 deg, associated with a gain of -7.3 dBi.

Hence, the diffracted path runs along a direction with higher gain when compared to the LOS direction. Therefore, it is expected that the influence of the baffle is lower compared to the dipole case. The expected attenuation by insertion of the baffle corresponds to the result of the dipole, corrected by the delta antenna gain, hence, the expected value is 17.2 dB – ((-7.3) - (-12.5)) dB = 12 dB.

For comparison, 10 dB attenuation has been determined using the CST simulation software. Limited differences in the result can be explained, e.g., by

- Multipath propagation:
  While above consideration assumes only one diffracted path, further diffracted paths are possible along the top of the baffle. These additional paths occur out of the plane which is defined by Nadir direction and LOS direction. Possible additional paths are already visualized in the left part of Figure 10. In principle, all paths have to be weighted by the angle-dependent antenna gain and then summed up. As the knife-edge theory does not predict multiple paths and the associated elevation angles, only weighting of the diffracted path "in-plane" is possible. A more complex channel model which predicts multiple paths and allows for insertion of an angle dependent antenna gain is Ray-tracing [7]. A disadvantage of this technique is however increased computational time.
- Baffle geometry:
  The baffle geometry differs from the ideal "knife-edge theory" as the baffle is bended and the distance between Tx and baffle differs along the baffle.
- Approximation of Fresnel integral :
  Equation (4) is only an approximation of (1).

To verify the effect of baffles on-board the MetOp-SG satellites prior to launch, early measurements are envisaged in the frame of ground testing. These so-called mock-up tests will use transmitters and receivers with representative antenna pattern as well as a relevant part of the satellite structure.

A similar approach using an adapted knife-edge model is shown in [8] which considers the channel between a train and a satellite including a knife-edge obstacle that models structural elements on the roof of the train. In [8], classical knife-edge theory is expanded by only one antenna gain (the "train antenna gain") whereas the present contribution takes into account both the characteristics of the transmitter and the receiver.

Finally, a general remark is given w.r.t. field predictions when involving antenna patterns: The radiation pattern of a transmit antenna differs between the near-field and the far field where far field conditions are achieved at distances of $d > d_{min} = 2\ D^2 / \lambda$ (D = antenna dimension). When using a far field antenna pattern in above approach, the distance between the transmit antenna and the baffle has to be at least d_{min} (fulfilled in above consideration).

IV. CONCLUSIONS

On-board a satellite, strong decoupling between a transmitter and a victim receiver can be achieved by a baffle of adequate height and length so that the strongest propagation path results from diffraction at the top of the baffle.

The height of the baffle shall be large enough to

- realize NLOS between Tx and Rx (and hence, a diffracted path towards the Rx)

 ISBN: 978-1-61208-397-1

- avoid reflexions at, e.g., high objects in the vicinity of Tx and Rx

The length of the baffle shall be large enough to avoid reflexions at objects next to the baffle which could carry significant power towards the Rx.

To determine the baffle attenuation for such a properly designed baffle, two methods have been studied: 3D field simulations and knife-edge diffraction theory (based on a single baffle), expanded by information on antenna gain. It has been shown that the results agree well when the diffracted path can travel directly into the Rx as per Figure 10 (no multiple diffraction). Hence, the simplified theory helps to quickly assess the baffle influence prior to starting time-consuming simulations. This approach is currently applied by Airbus Defence and Space to ensure radio frequency compatibility on the future MetOp-SG satellites.

REFERENCES

[1] Statement Of Work for MetOp Second Generation (MetOp-SG) Phase B2/C/D/E, ESA UNCLASSIFIED – For Official Use, MOS-SOW-ESA-SYS-0494, issue 1, 09/09/2013.

[2] J.A. Miller and A.R. Horne, "Radio frequency compatibility design and testing on the polar platform spacecraft," Electromagnetic Compatibility, 10th International Conference on Electromagnetic Compatibility (Conf. Publ. No. 445), vol., no., pp.35,40, 1-3 Sep 1997.

[3] K. Du and M. Swamy, Wireless Communication Systems: From RF Subsystems to 4G Enabling Technologies. Cambridge University Press, 2010.

[4] http://www.mike-willis.com/Tutorial/PF7.htm [retrieved: Feb., 2015]

[5] www.wirelesscommunication.nl/reference/chaptr03/diffrac.htm [retrieved: Feb., 2015]

[6] C. Hasslet, Essentials of Radio Wave Propagation. Cambridge Wireless Essentials Series, Cambridge University Press, 2008.

[7] J. Timmermann, M. Porebska, C. Sturm, and W. Wiesbeck, “Investigating the Influence of the Antennas on UWB System Impulse Response in Indoor Environments”, 37th European Microwave Week (EuMW), Oct. 2007, pp. 1562-1565.

[8] Scalise, S., Ernst, H. and Harles, G. “Measurements and modeling of the land mobile satellite channel at Ku-Band.” IEEE Transactions on Vehicular Technology, 57 (2), pp. 693-703, March 2008.

 ISBN: 978-1-61208-397-1

On the Observability in Switched Ethernet Networks in the Next Generation of Space Launchers: Problem, Challenges and Recommendations

Jérémy Robert, Jean-Philippe Georges, Thierry Divoux
Université de Lorraine, CRAN, UMR 7039,
Vandœuvre-lès-Nancy, France
CNRS, CRAN, UMR7039, France
firstname.name@univ-lorraine.fr

Philippe Miramont, Badr Rmili
CNES - Direction Des Lanceurs
Paris, France
firstname.name@cnes.fr

***Abstract*—Nowadays, many embedded systems use specific data buses to ensure the exchange of data. To reduce the financial cost, the mass and to increase performance in keeping at least the same reliability, a solution is to rely on a components off-the-shelf (COTS) technology. As switched Ethernet is a well-known solution and widely implemented, this technology is studied for the next generation of space launchers. In this paper, we focus on the observability issue defined as, not simply network management system techniques, but as the ability to monitor the satisfaction of the application quality of performance (especially in terms of time constraints and frames sequence). It consists to obtain a real picture of the communications at any given time and location. In a conventional communication technology (i.e., specific buses), it is easy to collect all exchanges on the physical wire with a dedicated device. But, it is not possible anymore on a switched network. Many monitors are therefore implemented and have to be synchronized. Hence, this paper aims at highlighting the implementation challenges that we have faced in our experimental test bench mainly in coping with online synchronization. Some recommendations on synchronisation and multi-monitoring issues are therefore submitted for the future developments.**

Keywords-Ethernet networks; observability; time synchronization; real-time.

I. INTRODUCTION

Traffic monitoring can be the cornerstone for understanding communication networks. The monitoring activity aims at collecting from the various network devices a set of relevant data. This enables to characterize the network state and therefore to identify unusual network behavior. According to the application domain, the purposes of the monitoring can also be different like network management [1], network security [2], network performance analysis [3], etc. The monitoring mechanisms depend directly on the intended application and also on the nature of the observed system.

In the paper, the system to monitor is the switched Ethernet network (as shown in Figure 1), which could be embedded into the next-generation of the space launchers ([4]). This component off-the-shelf (COTS) technology is aimed at replacing the current MIL-STD-1553B [5] (for control traffic) and Controller Area Network (CAN, for telemetry traffic) buses embedded in the european (unmanned) launchers. Figure 1 gathers terminal nodes to be used in a scenario where control and telemetry traffics are performed on a single network. In this application, relevant data is (at least) the full packet capture. In general, a new technology is only considered in many applications such as space [6] or automotive [7] if (and only if) this monitoring feature is satisfied. This study is led in the framework of a ”CNES french Research & Technology (R&T) activity”.

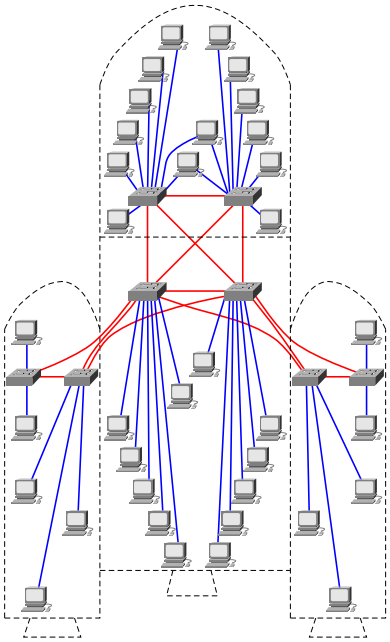

Figure 1. Switched Ethernet Architecture suggested in [4] for the next-generation of space launcher

In space applications (aircrafts, satellites, launchers), conventional communication technologies rely mainly on a specific bus, which is a unique physical medium (potentially redundant for the reliability [8]). As all end-nodes are connected to the same physical wire, each frame is observable to each of them. This is an important ability since a single dedicated device, a so called monitor, enables therefore to collect all exchanges along with a timestamp and to writte them into a trace (a real picture of the

 ISBN: 978-1-61208-397-1

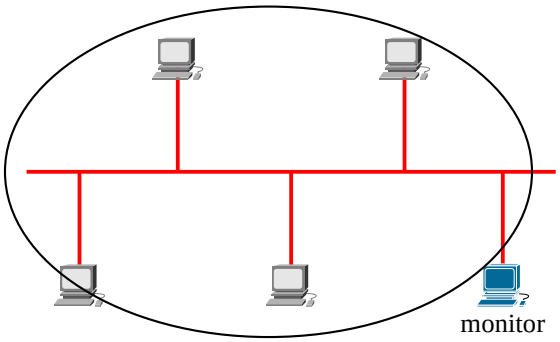

Figure 2. Global monitoring domain based on a unique observation point

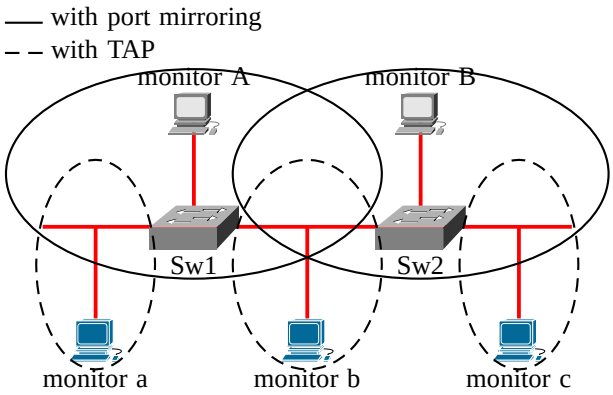

Figure 3. Distributed monitoring architecture based on multiple local monitoring domains

communications at any given time). This device constitutes a unique observation point of the network, which is necessary and sufficient to meet the monitoring traffic requirement for space applications. Accordingly, the monitoring domain covers the whole entire architecture as shown in Figure 2.

In a switched network, all end-nodes are inter-connected with several switches. Regarding the switch operating, the traffic is confined to different segments (to each link between switches) and eventually forwarded. As a consequence, to obtain a real picture of the communications as previously (on a shared medium), many monitors have to be implemented. A distributed monitoring architecture is therefore needed to cover the whole network (cf. Figure 3). Each monitor (the number and the location of these devices is discussed hereafter) generates locally a trace. The issue of distributed (monitoring) applications is to retrieve location and ordering of events (e.g., emission/reception of a frame on a device before an other one), which happens on the network architecture. Indeed, different messages in the traces have to be linked with a strict ordering relationship. However, the clocks in each monitor are initially running asynchronously and may produce significant offsets. To merge all the local traces, it needs a global reference time with synchronisation offsets have to be as small as possible. The underlying question is therefore the time synchronization method [9].

Let us remember that the objective is to obtain the highest fidelity picture of the communications in order to analyze the real network behavior. The analysis is performed offline, after tracing is finished. The aim of the paper is to highlight the implementation challenges that we face in our switched Ethernet experimental test bench and the consequences for the next generation of space launchers.

The remainder of the paper continues as follows: the section II reviews the related work and the problem overview. This is followed by a description of the proposed monitoring architecture and implementation challenges in Section III. Discussions and recommendations are given in Section IV. Section V presents the challenges to pass from the traffic monitoring to the control state observability. Finally, in section VI some conclusions and future work are given.

II. Related work and Problem overview

In a switched Ethernet network, the monitoring architecture is distributed. The number and the location of the monitors depend on the selected concepts (and also application requirements). Indeed, there exist several different techniques to capture network traffic. A point-to-point link can be splitted with a special device, named network Test Access Point (TAP) which enables to connect a monitor on this particular link. The traffic is also copied to this monitor in a passive way. Many manufacturers suggests this type of products as NetOptics®[10] or Fluke Networks[11]. A second method, called port mirroring, consists of using a special switches function (available on the most of commercial switches), which enables to copy all traffic coming from all or part of ports to a dedicated port. Figure 3 shows these different methods on a simple example where the dashed lines represent the observation domains for the TAP technique and the solid lines those for port mirroring technique.

Whatever is the solution retained for traffic monitoring, all monitors must have the same reference time to be able to make conclusions and recommendations on the network behavior (usual and unusual events). However, the clocks of each monitor produce time-varying offsets (because of clock drift), which are different from one another. This clock drift can be limited by using a synchronisation protocol as Network Time Protocol (NTP) or IEEE1588 - Precision Time Protocol (PTP). Some work (mainly, in a operating system tracing) suggest to rely on offline synchronisation by using a post-processing algorithm. These algorithms are mainly based on regression analysis (linear, least-squares, convex hull, etc.) [12] or linear programming [13]. The choice of the concept depends on the required performance which will be discussed in the following.

 ISBN: 978-1-61208-397-1

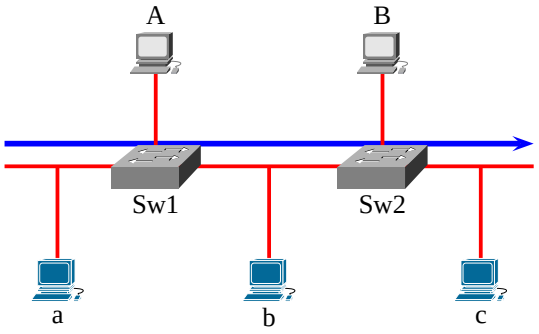

Figure 4. Illustration of synchronisation constraints

Let us remember that the ordering of events have to be retrieved from the analysis of traces. For example, Figure 4 shows a flow crossing respectively two switches Sw1 and Sw2. The flow must be captured on the monitor A (or a) before being it on the monitor B (or b and c) in the case of port mirroring technique (or in the TAP technique). As a consequence, a synchronisation performance constraint has to be defined in order to be sure that this ordering relationship can be observed. This constraint corresponds to the maximum offset between two monitors off_{max} (A and B, or a and b or b and c) and depends on the network parameters: the transmission time τ and the propagation delay δ (which can be negligible on the short Ethernet links). It can be expressed as $off_{max} < \tau + \delta$ with $\tau = \frac{min(L_{frame})}{C}$ where C corresponds to the link capacity and L_{frame} to the length of the Ethernet frames. The impact of the network parameters is discussed hereafter.

III. Monitoring Architectures and Implementation Issues

Our research laboratory collaborates closely with the CNES to lead R&T activities. In this framework, a certain level maturity of switched Ethernet technology has to be reached for the next generation of space launchers. This level can be assessed according to the Technology Readiness Level (TRL) [14]. In this collaboration, the objective is to reach the TRL4. Here, the aim is to constitute a ”proof-of-concept” on the ability to monitor all traffic.

For this purpose, an experimental test bench has been implemented in a laboratory environment (i.e., without being in an operational environment and without space components, but with a set of launcher representative data) as shown in Figure 5. It is composed of 8 switches Cisco IE3000 [15] and 100 Raspberry PI as end-nodes. On this topology, it has been deployed our monitoring architecture consisting of 8 computers (1 per switch) with Linux as operating system. Each monitor implements a special hardware card for time synchronisation: a Meinberg PTP card (PTP 270 PEX model) [16] . This card has been designed to add precise timestamping capabilities to data acquisition and

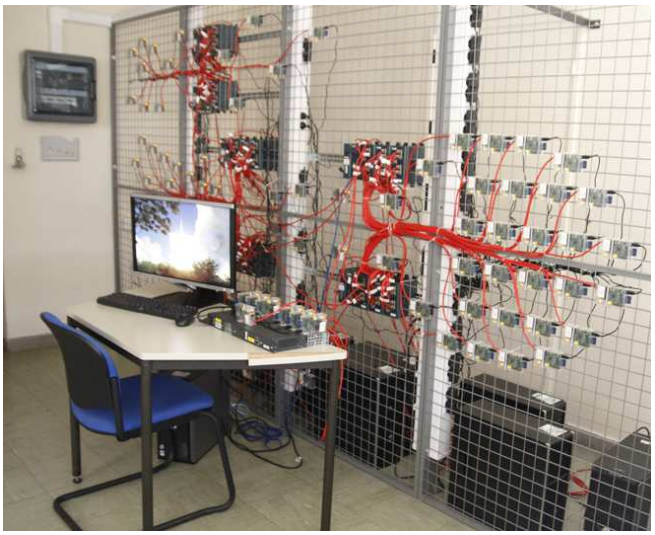

Figure 5. Our experimental test bench

measurement applications. The trafic is captured using the tcpdump[17] library. And the port mirroring technique has been chosen to minimize the number of additional devices.

In this framework, we face in many technical constraints to implement the monitoring architecture. The first one is that the PTP card can not be used as a standard network interface card. As a consequence, a second Ethernet link has to be used to monitor the traffic sent by the switch (via the port mirroring). On the other hand, the port mirroring can transmit only the copies of sent and received traffic for all monitored source ports. It therefore could not have been used to synchronise the monitor. The monitors are connected to a switch by two Ethernet links.

The second constraint concerns the timestamping of the captured frames. Indeed, the timestamping uses the date of the kernel clock and not the one of the PTP card (cf. tcpdump operation) as shown in Figure 6. As a consequence, a local synchronization is needed to enables to synchronize

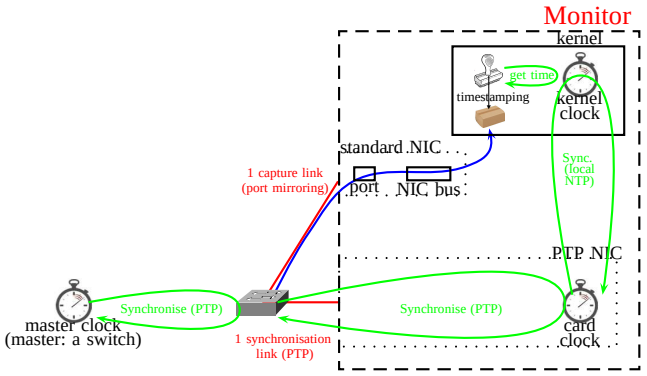

Figure 6. Experimental timestamping mechanism

 ISBN: 978-1-61208-397-1

the kernel clock with the PTP card. To do that, NTP at stratum 0 is therefore used (to our knowledge, PTP can not be implemented locally yet). NTP is a protocol initially suggested by [18] for synchronizing the clocks of computer systems over packet-switched data network. It is based on a client-server model. To synchronize its clock with a server, the client computes the round-trip time and the offset from several measured timestamps (server's/client's timestamps of request/response packet transmission and reception). The timestamping remains on NTP at the high level. Hence, it is not related to specific hardwares like in PTP. The performances of the two control loops (as shown in Figure 6) have been measured on each monitor. Figures 7 and 8 represent the variation of the offset from master measured on a given day (without experimentations) for the PTP and NTP loop.

In brief, the PTP offsets are ranged between $-300\ ns$ and $300\ ns$ and those of NTP between $-40\ \mu s$ and $40\ \mu s$. These graphs highlight that the offsets of NTP are greater than those of PTP. For NTP, the variations are all the more important as the Central Processing Unit (CPU) load increases (e.g., when tcpdump is used).

In this network, all links are configured with a $100\ Mbits/s$ capacity. As a consequence, to be sure to detect the ordering of events with a minimum Ethernet frame ($72\ octets$), the offset between two monitors must be inferior to $5.76\ \mu s$. In our case, the offsets between two monitors can be $80\ \mu s$ at worst ($40\ \mu s$ from the master for monitor 1 and $-40\ \mu s$ from the master for monitor 2). As a consequence, it is clear that this is not possible to detect the ordering of events in a consistent manner. However, some temporal results have already been achieved with this monitoring architecture. Indeed, if the observation of events are not linked to many monitors, then this monitoring architecture is suitable for that. For exemple, the temporal respect of the events sequence (to a single destination and crossing a unique switch) has been verified.

Although this study shows that this implementation is not currently and directly applicable to traffic monitoring in space applications (because of NTP loop only), it is nevertheless possible to submit many recommendations to the future developments.

IV. Discussions / Recommendations

In this work, the set of tools are turnkey solutions, this means that no specific development have been done. A monitor and the function "port mirroring" in the switch constitutes here a prototype of the function "trafic monitoring".

The aim of this section is therefore to present some possible evolutions and/or recommendations for the future development.

To validate in a definitive manner our "proof-of-concept", here are some obvious evolutions, which could be applied in our experimental test bench:

- other type of switch with timestamping capabilities (at the mirroring port) could also be used (e.g., Cisco Nexus). At the time of the choice, these devices were not available yet.
- to avoid the NTP loop on each monitor, a homemade tcpdump could be developed to timestamp directly all collected frames with the PTP card clock. It is important to note that this solution is really feasible.

The devices used in the experimental test bench will be not embedded as is in the space launcher. But, if we look at the space news, we can see that many Ethernet switches begin to be used in space program (e.g., Hewlett Packard switches on-board ISS (International Space Station) [19]) or begin to be rugged for space environment in the launch vehicle (e.g., Cisco IE 3000 switches for the Atlas and Delta IV [20]). All devices are based on COTS, and industrials refer to a R-COTS (Rugged-COTS) or M-COTS (Modified-COTS).

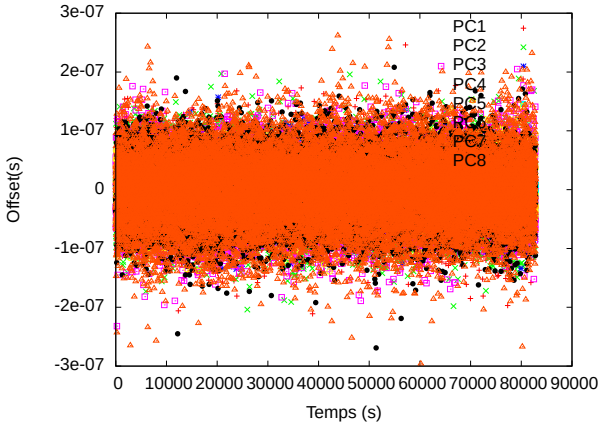

Figure 7. *Offsets* PTP measured on a day

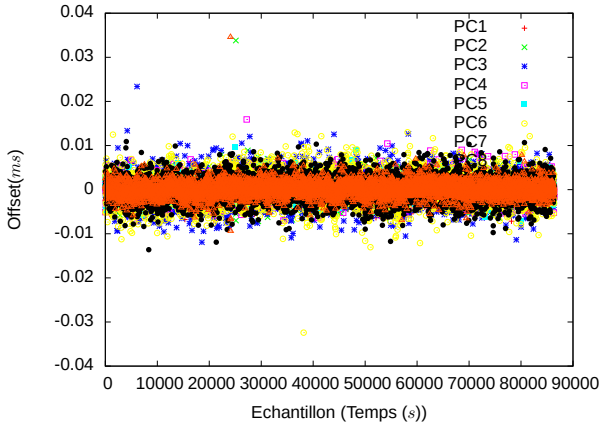

Figure 8. *Offsets* NTP measured on a day

In any case, it seems that all switches still implement the port mirroring function (e.g., TTEthernet switches, Aitech S750 Radiation Tolerant switches, etc.). Developing a homemade switch rather than relying on commercial products might be long and expensive, especially regarding memories for mechanisms like mirroring. For instance, it takes 3 years for HP to develop new switches for the International Space Station.

As a consequence, in a short term, it is clear that it will be interesting to develop quickly a solution for timestamping directly the frame with the PTP card clock. Then, in design phase, it will be necessary to study the total quantity of traffic which is copied from all monitored source ports to the port mirroring. Indeed, the bandwidth of this port is limited and it can become congested.

On the other hand, we can see that the synchronisation constraint is all the more when the network capacity increases. Consequently, it is possible that the mere use of synchronisation to satisfy the trafic monitoring requirement is not sufficient. Others methods need to be designed to face this limitation. A track will be to consider offline synchronization by using the knowledge of network events (since that space applications are often deterministic).

V. From network traffic monitoring to the control state observability: challenges

With traditional buses for launchers, the network testing mainly relies on traffic monitoring. It mainly consists in capturing all frames from a single capture point. It is useful to check if packets losses occur (network QoS) and also to know the current static launcher control state (application quality of performance like the information promptness and the arrival ordering). The on-board controller manages this control state by sending specific data, called *control words*, to the sensors/actuators. By analyzing the content of the packet, it is hence possible to retrieve the *control word* values measured by the sensors and those sent by the controller to the actuators. Hence, the network acts as an observer of the control state.

All those control words are related to the different dynamics of the launcher control. A control step is defined by a sequence $\mathcal{S}$ of application control words w_i with $\mathcal{S} = \{w_1, w_2 \dots w_n\}$. The key point is now to develop strategies to monitor how a given sequence (and not only a frame) will be served in time by the next generation of networks. For each word w_i, the control application will define a target sending date t_i (relative to a reference time) with a tolerance δ_i. From the network point of view, each word corresponds to a single frame that has to be sent to a destination (not necessary the same for all words even if several may belong to the same transfert). The departure time of these frames may also be not periodic. Hence, the traffic monitoring should be able to observe these times and next, to check that all these requirements (order and tolerance) are satisfied. Next generation network, and in particular, switched Ethernet network, may however face two important issues:

Compared to buses, switched architectures do not permit anymore to capture from one single point the whole traffic (see Figure 3). To achieve this objective, it requires to add several capture points (based on TAP on each link or on port mirroring mechanisms on each switch). The synchronisation of these multiple captures have to be solved in order to test if the application sequence order and tolerance are satisfied. This first issue only deals for switched Ethernet network (like in native IEEE 802.1D or AFDX) and may not occur for Ethernet protocols that will be used on a bus.

The second issue that Ethernet protocols may introduce is related to the medium access policy. Even if at the MAC level, IEEE 802.3 defines a specific method, a lot of solutions add a middleware that change the access. For instance, with Modbus/TCP, it may corresponds to a Master/Slaves policy where only one frame is sent at a given time on the network. For legacy switched architectures, it means that several frames may be simultaneously forwarded around the network. As a consequence, the frames order may change and a given frame may be captured at different dates and locations by several monitors.

We define here the observability as the ability to determine dynamically how the sequence requirements are satisfied. A question might be *is the word w_j successfully forwarded by the network at the time $t_j \pm \delta_j$*. Even if multiple (network) observers are used, a centralized overview of the current frames exchanged by the network has to be determined (this centralized overview is important for launchers where the control state information have to be transmitted to the ground via the telemetry channel). In the following, we will develop such challenges for two example of space solutions: AFDX [21] and TTEthernet [22].

Avionics Full-Duplex Switched Ethernet (AFDX) relies on the exact bandwidth regulated traffic control to guarantee a determinist service. Thanks to the notion of Virtual Links (ARINC 664, part 7), a channel is opened between a source and a destination and is characterized by a minimal time between two consecutive frames (Bandwidth Allocation Gap). As the name suggests, this technology relies on a switched topology. As a consequence, AFDX solution has to face to the synchronisation issue of the multiple captures (obtained on several monitors) as seen previously. On the other hand, many frames may be sent on the network on the same time. The middleware enables to guarantee only the bandwidth for a given flow and not its order relatively to an other.

TTEthernet is a time-triggered Ethernet solution. It relies on time division multiple access (TDMA) for time-triggered communication (according to SAE AS 6802). The aim is to ensure predictable transmission delays without queuing, and therefore low latency and jitter. In this way, a unique

 ISBN: 978-1-61208-397-1

frame is a priori on the network at a given time. However, this frame will be captured by several monitors at different dates as the topology is a switched one. Although the TDMA mechanism may guarantee the order (if these traffic flows are considered as time-triggered communication), it will be important to check the respect of tolerance. Indeed, as the target sending date is calculated during the flight (relatively to several events), it is possible that a sender has no access to the medium at this date (slot allocated to an other sender) and has to wait the next cycle. On the other hand, TTEthernet enables to use two others traffic classes: rate-constrained (ARINC 664, part 7), and COTS Ethernet (IEEE 802.3) traffic flows. Some sequences could be sent by using several frames belonging to these others traffic classes. As a consequence, no guarantees are given by the middleware and the same previous issues remain to handle.

VI. Conclusion

In this work, we face implementation issue in terms of synchronisation. However, the paper highlights that it is possible to lead quickly a proof-of-concept of traffic monitoring in switched Ethernet networks in the next generation of space launchers.

It is also important to note that the presented problem will be the same for any switched Ethernet technology (TTEthernet, AFDX, etc.), which could be retained for the next generation of space launchers. As a consequence, all solutions could benefit from the recommendations established in this paper.

References

[1] K. G. Anagnostakis, S. Ioannidis, S. Miltchev, M. Greenwald, J. M. Smith, and J. Ioannidis, “Efficient packet monitoring for network management,” IEEE/IFIP Network Operations and Management Symposium (NOMS), 2002, pp. 423–436.

[2] R. Bejtlich, “The Practice of Network Security Monitoring: Understanding Incident Detection and Response,“ No Starch Press, 2013.

[3] R. Hofstede, I. Drago, A. Sperotto, and A. Pras, “Flow monitoring experiences at the ethernet-layer,” EUNICE Workshop on Energy-Aware Communications, 2011, pp. 129–140.

[4] J. Robert, J.-P. Georges, T. Divoux , P. Miramont, B. Rmili, “Toward self-reconfiguration of switched ethernet architectures in the next generation of space launchers,” International Conference on Advances in Satellite and Space Communications (SPACOMM), 2013, pp. 17–22.

[5] Department of Defense, “Military standard aircraft internal time division command/response multiplex data bus,” MIL-STD 1553B, 1978.

[6] J. Robert, J. Georges, T. Divoux, P. Miramont, B. Rmili, “Ethernet networks for real-time systems: application to launchers,” International Space System Engineering Conference (DASIA), 2011.

[7] A. Kern, H. Zhang, T. Streichert, and J. Teich, “Testing switched ethernet networks in automotive embedded systems,” IEEE International Symposium on Industrial Embedded Systems (SIES), 2011, pp. 150–155.

[8] D. Monchaux, P. Gast, and J. Sangare, “Avionic-x: A demonstrator for the next generation launcher avionics,” Embedded Real-Time Software and Systems (ERTS), 2012.

[9] L. Lamport, “Time, clocks, and the ordering of events in a distributed system,” Communications of the ACM, vol. 21, no. 7, 1978, pp. 558–565.

[10] http://www.netoptics.com, 2015.

[11] http://www.flukenetworks.com, 2015.

[12] A. Duda, G. Harrus, Y. Haddad, and G. Bernard, “Estimating global time in distributed systems.” International Conference on Distributed Computing Systems (ICDCS), vol. 87, 1987, pp. 299–306.

[13] S. B. Moon, P. Skelly, and D. Towsley, “Estimation and removal of clock skew from network delay measurements,” Eighteenth Annual Joint Conference of the IEEE Computer and Communications Societies. Proceedings. IEEE, vol. 1., 1999, pp. 227–234.

[14] “Iso/fdis 16290 - space systems – definition of the technology readiness levels (trls) and their criteria of assessment.”

[15] http://www.cisco.com/c/en/us/products/switches/industrial-ethernet-3000-series-switches/index.html, 2015.

[16] https://www.meinbergglobal.com/english/products/pci-express-ieee-1588-ptp-slave.htm, 2015.

[17] http://www.tcpdump.org, 2015.

[18] D. L. Mills, “Internet time synchronization: the network time protocol,” IEEE Transactions on Communications, vol. 39, no. 10, 1991, pp. 1482–1493.

[19] R. Schmidhuber, “International space station welcomes aboard procurve networking,”EADS Astrium Space Transportation White Paper, 2008.

[20] “Curtiss-wright awarded contract by united launch alliance,” Press-releases, April 10, 2014.

[21] “Arinc 664, aircraft data network, part 7: Deterministic networks.” 2003.

[22] “SAE AS6802: Time-triggered ethernet,” 2011.

 ISBN: 978-1-61208-397-1

Enhanced HARQ for Delay Tolerant Services in Mobile Satellite Communications

Rami Ali Ahmad, Jérôme Lacan
University of Toulouse, ISAE/DMIA & TéSA
Toulouse, France
Email: rami.aliahmad@isae.fr, jerome.lacan@isae.fr

Fabrice Arnal, Mathieu Gineste
Thales Alenia Space
Toulouse, France
Email: fabrice.arnal@thalesaleniaspace.com, mathieu.gineste@thalesaleniaspace.com

Laurence Clarac
CNES
Toulouse, France
Email: laurence.clarac@cnes.fr

***Abstract*—The objective of our paper is to improve efficiency (in terms of throughput or system capacity) for mobile satellite communications. In this context, we propose an enhanced Hybrid Automatic Repeat reQuest (HARQ) for delay tolerant services. Our proposal uses the estimation of the mutual information. We evaluate the performance of the proposed method for a land mobile satellite channel by means of simulations. Results are compared with those obtained with a classical incremental redundancy (IR) HARQ scheme. The technique we propose, shows a better performance in terms of efficiency while maintaining an acceptable delay for services.**

***Keywords*—Hybrid ARQ; Satellite Communications; Land Mobile Satellite (LMS) Channel; Delay; Efficiency.**

I. INTRODUCTION

For many years, mobile satellite communications services are challenging and very costly. Land mobile satellite (LMS) channels are highly affected by important propagation impairments (time-selective channel) and inter/intra system interference, that both cause unstable and low signal to noise ratio (SNR), which the receivers have to cope with. This usually implies strong limitations on the delivered service throughput, whatever the considered satellite frequency band.

Our objective is to propose a mechanism, which improves the efficiency of link usage while providing an appropriate service to applications. The targeted services (data transfer from sensors, messages for aeronautical services, etc.) are assumed to be tolerant to delay. For example some aeronautical services define delay requirement for the delivery of 95% of messages [1].

To deal with problems caused by link characteristics in mobile satellite communications, there are many solutions. One of these solutions is to use pure Forward Error Correction (FEC), which can makes the message very robust. However using FEC is not sufficient sometimes, due to the highly varying channel, where its quality changes dramatically. This make it difficult sometimes to decode the message, even if the used code is very robust. Alternatively, Automatic Repeat reQuest (ARQ) can be used as a solution to deal with channel variations, where transmitter attempts many retransmissions in case of unsuccessful decoding. ARQ messages without FEC, are not so robust to ensure a reliable communication.

Hybrid ARQ (HARQ) protocols are used in most of recent terrestrial wireless communication systems. Worldwide interoperability for microwave access (WIMAX) and long term evolution (LTE) are examples of these systems that use HARQ [2]. There are many types of HARQ techniques. HARQ type I is called chase combining (CC). The receiver asks the transmitter for the transmission of the same packet of coded data. At the receiver, the decoder combines the multiple copies of the transmitted packet weighted by the SNR received. HARQ type II, is also called incremental redundancy (IR). Unlike the previous method, which transmits simple repetitions of the same encoded packets, IR technique transmits additional redundant information in an incremental way if the decoding does not succeed from the first transmission. If each retransmission packet is self-decodable this scheme is called type III HARQ [3]. Classical IR HARQ, which transmits a fixed number of bits at each transmission, is not optimal from the efficiency point of view even if it can improve the decoding delay especially for high values of SNR. However, choosing optimal values for number of bits to be sent at each transmission can improve the system performance and throughput level. Many papers has proposed methods to choose an optimal number of bits at each transmission, a theoretical basis for a parity bits selection by means of a risk-sensitive optimal control is established in [4]. The idea of random transmission assignments of the mother code bits was introduced in [5]. An optimized IR HARQ schemes based on punctured LDPC codes over the BEC was proposed in [6].

Contrarily to classical IR HARQ scheme, the main idea of our enhanced HARQ technique is to estimate the average number of bits to be transmitted at each transmission to decode the codeword with a targeted probability. This probability depends on the application/service (delay constraints). This technique uses the mutual information to predict the mean number of bits needed for each transmission. It uses the knowledge of the statistical distribution of the channel attenuation. Our enhanced HARQ transmission proposal is simulated in a satellite communications environment, where an LMS channel and a long Round-Trip time are considered.

The remainder of this paper is organised as follows. Section II describes the channel capacity and the LMS channel model.

 ISBN: 978-1-61208-397-1

We present classical IR HARQ in Section III. In Section IV, we propose an enhanced HARQ model for delay tolerant services in mobile communications. We present the results of simulations and we compare the performance of both techniques (classical IR and enhanced HARQ) in Section V. We conclude our study in Section VI.

II. Channel Modelling

In our study on mobile satellite communications, we considered an LMS channel to model this environment [7] [8]. In the following, we explain how to compute the capacity of this channel.

A. Channel capacity and Mutual Information

Channel capacity C quantifies the maximum achievable transmission rate of a system communicating over a band-limited channel, while maintaining an arbitrarily low error probability. It corresponds to the maximum of the mutual information between the input and output of the channel, where the maximization is done with respect to the input distribution. Mutual information (MI) measures the information that input of the channel (X) and output of the channel (Y) share. It is a key parameter in our approach, as it will be used to calculate the mean number of bits needed to decode a message at each transmission with a given probability.

Given the channel input symbol x_i, its energy E_{si}, a realisation of noise n_i (which has a Gaussian distribution with variance $\frac{N_0}{2}$) and the channel attenuation ρ_i, the channel output symbol y_i can be written as:

$$y_i = \rho_i \sqrt{E_{si}} x_i + n_i. \tag{1}$$

For an equally distributed input probability, the MI corresponds to the capacity of the channel, which is AWGN, can be calculated by the following equation [9]:

$$MI\left(\frac{E_s}{N_0}\right) = \log_2(M) - \frac{1}{M(\sqrt{\pi})^N} \times \sum_{m=1}^{M} \underbrace{\int_{-\infty}^{+\infty} \cdots \int_{-\infty}^{+\infty}}_{\text{N times}} \exp(-|t|^2) \times \log_2 \left[\sum_{i=1}^{M} \exp(-2t.d_{mi} - |d_{mi}|^2) \right] dt, \tag{2}$$

where:

- M is the modulation order;
- N is the space dimension that depends on the used modulation ($N = 2$ for any PSK-based modulation with more than 2 states);
- t is the integration variable of dimension N ($t = (t[1], ..., t[N])$);

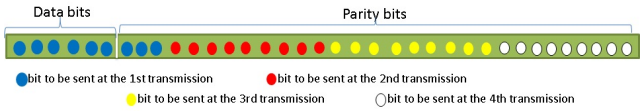

Figure 1. Example of the transmission technique considered in our simulations (Code rate 1/6, with a maximum of 4 retransmissions).

- $d_{mi} = \sqrt{\frac{E_s}{N_0}}(x_m - x_i)$ (x_i it is an input symbol).

For the rest of the paper, we define MI_{req} as the average MI per bit required to decode a codeword at a given probability expressed in Word Error Rate (WER). MI_{req} can be calculated using the mutual information function (2) and the performance curves giving the WER versus E_s/N_0 of the used modulation/coding scheme [10]. By using these performance curves, we can deduce the E_s/N_0 necessary to obtain a given WER. Then we use this value of E_s/N_0 in the mutual information function (2) to obtain the mutual information required to decode a codeword at this given WER. The prediction of performance of the WER based on MI is quite classical, and has been described and validated in [11].

From now on, to compute the mutual information we use (2), $\frac{E_s}{N_0}$ is replaced by $\rho_i^2 \frac{E_s}{N_0}$, where $\frac{E_s}{N_0}$ is the average energy per symbol.

B. LMS Channel

One of the reference propagation models for LMS channel is a statistical model based on a three state Markov chain [7]. This model considers that the received signal originates from the sum of two components: the direct signal and the diffuse multipath. The direct signal is assumed to be log-normally distributed with mean α (decibel relative to LOS (Line Of Sight)) and standard deviation Ψ (dB), while the multipath component follows a Rayleigh distribution characterized by its average power, MP (decibel relative to LOS). This model is called Loo distribution [8] [12]. For the modelling of the LMS channel in our simulations, we use attenuation time series using a propagation simulator based on the three state channel [7] [8] provided by CNES. Using this tool we calculate the distribution of the probability to obtain an attenuation in the channel for a given environment.

III. Incremental Redundancy HARQ

IR HARQ can be described as follows. The sender transmits a number of bits that correspond to a given codeword. After receiving the feedback (ACK/NACK) from the receiver, the transmitter decides to no longer send bits corresponding to this codeword if an ACK is received, or to send more parity bits if a NACK is received. The number of bits to be sent in the next retransmission is fixed at each transmission. These numbers of bits are chosen without any knowledge about the channel quality or the global channel characteristics. If the cumulative received sequence can not be decoded after a maximum number of bits transmitted, the transmitter stops sending bits that correspond to this codeword. The parity bits

 ISBN: 978-1-61208-397-1

are generated according to a coding scheme with a code rate corresponding to the maximum number of bits that can be transmitted per codeword. Bits to be sent at each transmission are part of the original codeword (mother code), leading to a different code rate at each transmission (see Figure 1). This technique of transmission is somehow similar to puncturing. Data bits of each codeword must be kept at the buffer of the sender as long as the codeword is still not decoded or the transmitter has not decided to end the transmission. At the receiver side, the LLRs (Log Likelihood Ratio) of the received symbols of each codeword are kept in the buffer as long as the codeword is not decoded or the transmission of the corresponding bits has not ended. An overview of ARQ and HARQ mechanisms implemented or proposed in beyond 3rd generation systems was presented in [2].

IV. Enhanced HARQ for delay tolerant services in mobile satellite communications

In this section, we propose an enhanced HARQ model using mutual information. In our scheme, the computation of the numbers of bits to be transmitted at each transmission is done in a way that insures the decoding with a probability. These probabilities are predefined for each transmission and chosen according to delay constraints of the application.

In the following, we explain how to proceed to compute the number of bits required to decode a codeword with a predefined probability, supposing the knowledge of the global statistics of the channel.

A. Enhanced HARQ Model

Our proposal uses the MI to compute the number of bits to be transmitted at each transmission. After transmitting some bits of a given codeword, this codeword accumulates some mutual information. This mutual information can be computed knowing the number of bits transmitted and the attenuation coefficient affecting the transmitted bits. In this model we consider a reference E_s/N_0, which is a fixed value of E_s/N_0 in clear sky (for a given terminal and without attenuation). The model assumes that the channel is stationary for the transmission time of the bits, at a given transmission for a given codeword. The MI obtained at the j^{th} transmission for a given codeword can be computed as:

$$MI^{(j)} = N_{sent}^{(j)}.MI((\rho^{(j)})^2.\frac{E_s}{N_0}), \quad (3)$$

where:

- $\rho^{(j)}$ is the attenuation coefficient affecting bits transmitted at the j^{th} transmission for a given codeword;
- $N_{sent}^{(j)}$ is the number of bits transmitted at the j^{th} transmission;
- $MI(\cdot)$ is the function giving the value of mutual information for a given E_s/N_0 on a gaussian channel.

The MI per bit accumulated for a given codeword, from the beginning of transmission until the j^{th} transmission, can be computed as:

$$MI_{acc}^{(j)} = \frac{N^{(j-1)}MI_{acc}^{(j-1)} + MI^{(j)}}{N^{(j)}}, \quad (4)$$

where:

- $N^{(j)}$ is the total number of bits transmitted for a codeword up to the j^{th} transmission;
- $MI_{acc}^{(0)}$=0.

Note that $\rho^{(j)}$ is unknown in our model, thus $MI_{acc}^{(j)}$ is also unknown.

Let us consider $MI_{needed}^{(j+1)}$ the minimum MI per bit needed to decode the codeword at the $(j+1)^{th}$ transmission with a predefined decoding probability.

Let $N_{needed}^{(j+1)}$ be the number of bits to be transmitted at the $(j+1)^{th}$ transmission, we have:

$$N_{bits}MI_{req} = N^{(j)}MI_{acc}^{(j)} + N_{needed}^{(j+1)}MI_{needed}^{(j+1)}, \quad (5)$$

where N_{bits} is the maximum number of bits that can be transmitted for a codeword in total.

Finally $N_{needed}^{(j+1)}$ is given by:

$$N_{needed}^{(j+1)} = \frac{N_{bits}MI_{req} - N^{(j)}MI_{acc}^{(j)}}{MI_{needed}^{(j+1)}}. \quad (6)$$

$MI_{needed}^{(j+1)}$ and $MI_{acc}^{(j)}$ are the key parameters for the computation of the number of bits to be sent at the $(j+1)^{th}$ transmission. In the following, we explain in detail how to proceed to calculate these two values at each transmission according to the predefined decoding probabilities.

B. Computation of $MI_{needed}^{(j+1)}$ and $MI_{acc}^{(j)}$

In a first step, we will explain how to calculate $MI_{needed}^{(j+1)}$, then we finish by explaining the way we compute $MI_{acc}^{(j)}$.

We use the knowledge of the statistical distribution of the channel attenuation to control the probability of decoding a codeword at each transmission.

The idea is to define at the beginning of the communication, a table containing the probability of decoding at each transmission. The decoding probability and the efficiency of the link usage are related, the sender can transmit a large number of bits at the first transmission, which increases the decoding probability but the efficiency will decrease and vice versa. So, we have to improve efficiency while respecting delay constraints for services. In addition the sender may also want to limit the number of transmission attempts for a given codeword.

In the rest of this paper, we will consider P_j the probability of decoding at the j^{th} transmission conditioned on the fact that decoding at earlier transmissions was impossible, where $P = \sum_j P_j$ is the percentage of decoded codewords over all the transmitted codewords and is equal to 1.

 ISBN: 978-1-61208-397-1

To target a decoding probability P_j at the j^{th} transmission, we have to find the corresponding $MI^{(j)}_{needed}$ necessary to calculate the number of bits $N^{(j)}_{needed}$ to be transmitted (6). For this, we define $\rho^{(j)}_{needed}$ as the minimum successive attenuation coefficient (threshold) that provides a MI greater than $MI^{(j)}_{needed}$. This threshold is the minimum attenuation needed to obtain the decoding probability at the j^{th} transmission. $\rho^{(j)}_{needed}$ depends not only on the j^{th} element in the probability decoding table but also on $\sum_{k=1}^{j-1} P_k$ as we will see later in (8). $MI^{(j)}_{needed}$ is given by:

$$MI^{(j)}_{needed} = MI((\rho^{(j)}_{needed})^2 . \frac{E_s}{N_0}), \tag{7}$$

Where $MI(\cdot)$ is defined in (2), that takes as input $(\rho^{(j)}_{needed})^2 . \frac{E_s}{N_0}$.

We assume that the reference E_s/N_0 fixed for a given terminal (only ρ^2 change over the time). $MI^{(j)}_{needed}$ depends only on the channel attenuation threshold $\rho^{(j)}_{needed}$. Since decoding probabilities at each transmission are predefined, $\rho^{(j)}_{needed}$ is pre-computed. $MI(\cdot)$ is a strictly increasing function (as a function of ρ). Then any attenuation coefficient greater than $\rho^{(j)}_{needed}$ will lead to a successful decoding. To determine $\rho^{(j)}_{needed}$ leading to P_j, we use the cumulative distribution function (CDF) of the attenuations of LMS Channel.

To simplify our calculation, we consider these two events:

- A_j: Successful decoding at the j^{th} transmission;
- B_{j-1}: Not decoding at the $(j-1)^{th}$ transmission.

P_j can be defined as $p(A_j \cap B_{j-1})$ and p_j is $p(A_j)$. Since A_j and B_{j-1} are independent (according to the channel modelling),

$$\begin{aligned} P_j &= p_j(1 - \sum_{k=1}^{j-1} P_k), \\ p_j &= \frac{P_j}{(1 - \sum_{k=1}^{j-1} P_k)} . \end{aligned} \tag{8}$$

CDF of the channel gives us $P(\rho \leq \rho^{(j)}_{needed})$, while p_j corresponds to $P(\rho \geq \rho^{(j)}_{needed})$ (successful decoding).

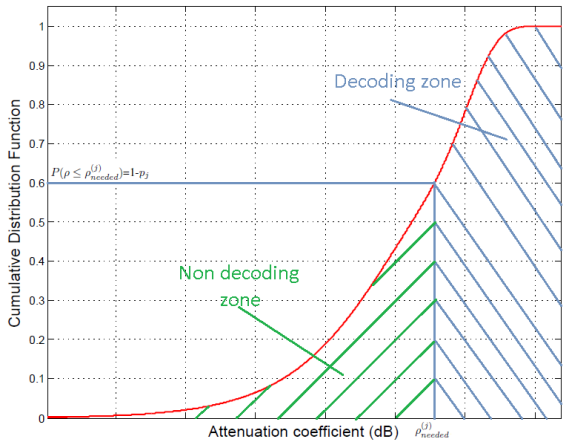

Figure 2. CDF of the attenuation coefficients in the LMS channel.

Transmission	1	2	3
Probability	0.5	0.3	0.2

$p_1 = 0.5$ $\quad p_2 = \frac{0.3}{1-0.5} = 0.6$ $\quad p_3 = \frac{0.2}{1-0.8} = 1$ Using (8)

Using CDF (Figure 2)

$\rho^{(1)}_{needed}$= - 4.1861 $\quad \rho^{(2)}_{needed}$= -5.9094 $\quad \rho^{(3)}_{needed}$= -19.4783

$MI^{(1)}_{needed}$= 1. 9764 $\quad MI^{(2)}_{needed}$= 1.9070 $\quad MI^{(3)}_{needed}$= 0.2925

$N^{(1)}_{needed} = \frac{N_{bits} MI_{req} - N^{(0)} MI^{(0)}_{acc}}{MI^{(1)}_{needed}} = \frac{21761-0}{1.9764} = 11010$ bits Using (6)

$MI^{(1)}_{acc} = \sum_i p_{wi}\, MI((\rho_i)^2 \frac{E_s}{N_0}) = 1.4104 \;/\; (\rho_i < -4.1861)$ Using (9)

$N^{(2)}_{needed} = \frac{N_{bits} MI_{req} - N^{(1)} MI^{(1)}_{acc}}{MI^{(2)}_{needed}} = \frac{21761-11010*1.4104}{19070} = 3268$ bits

$MI^{(2)}_{acc} = \sum_i p_{wi}\, MI((\rho_i)^2 \frac{E_s}{N_0}) = 0.8353 \;/\; (\rho_i < -5.9094)$

$N^{(3)}_{needed} = \frac{N_{bits} MI_{req} - N^{(2)} MI^{(2)}_{acc}}{MI^{(3)}_{needed}} = \frac{21761-14278*0.8353}{0.2925} = 33623$ bits

Figure 3. Numerical example for the computation of number of bits to be transmitted at each transmission ($E_s/N_0 = 13\,dB$, code (8920,1/6), three transmissions).

Therefore, $\rho^{(j)}_{needed}$ on the CDF graph is given by 1-p_j (See Figure 2).

Once we found $\rho^{(j)}_{needed}$ leading to P_j, we use it in (7) to calculate $MI^{(j)}_{needed}$.

At the $(j-1)^{th}$ transmission, only codewords affected by attenuation coefficients greater than $\rho^{(j-1)}_{needed}$ are decoded. $MI^{(j-1)}_{acc}$ represents the average mutual information per bit of all codewords that have not been decoded at the $(j-1)^{th}$ transmission, affected by attenuation coefficients less than $\rho^{(j-1)}_{needed}$. $MI^{(j-1)}_{acc}$ is the sum of all mutual informations weighted by their probabilities in the non decoding zone (see Figure 2). For this, we use the CDF and the PDF (probability density function) of the channel. $MI^{(j-1)}_{acc}$ can be calculated by:

$$MI^{(j-1)}_{acc} = \sum_i p_{wi} MI((\rho_i)^2 . \frac{E_s}{N_0}), \tag{9}$$

where:

- ρ_i belongs to the ensemble of attenuation coefficients, which are less than $\rho^{(j-1)}_{needed}$;
- p_{wi} is the weighted probability, defined as the probability to obtain ρ_i in the non decoding zone.

Finally, to calculate $N^{(j)}_{needed}$ we use $MI^{(j)}_{needed}$ and $MI^{(j-1)}_{acc}$ in (6). Where $N^{(j-1)}$ is the sum of all numbers of bits already calculated for the previous transmissions.

Figure 3 represents a numerical example for computation of the numbers of bits to be transmitted at each transmission, showing different steps for the calculation of all parameters in our model.

 ISBN: 978-1-61208-397-1

V. SIMULATIONS AND RESULTS

The system parameters that we will consider for all simulations are:

- Satellite Orbit: Geostationary (GEO)
- Round Trip Time: 500 ms
- Band: S
- Land mobile satellite channel , Intermediate Tree Shadowed Environment (ITS)
- Speed: 60 Km/h
- Distance: 10 Km
- Mother FEC code, CCSDS Turbo Codes 1/6
- Codeword length: 53520 bits (Data bits : 8920 bits)
- Modulation: QPSK
- Symbol time : 4.10^{-6} seconds, bit rate (Rb): 500 Kbps

Our simulations are about 10 minutes of communication between the transmitter and the receiver (about 300 Mb transmitted). In our simulations, we consider a targeted WER of 10^{-4}, and we use the actual performances of CCSDS Turbo codes (8920,$\frac{1}{6}$) as presented in [10]. Attenuations in ITS environment are very high, which makes difficult the decoding of 100% of codewords in the range of reference E_s/N_0 considered (7 to 13 dB) with code rates greater than $\frac{1}{6}$. Hence the choice of code rate $\frac{1}{6}$. We suppose that the synchronisation is never lost. The transmitted codewords are identified with a sequence number that is never lost. We suppose also that the return channel does not introduce errors and the feedback can be transmitted immediately (no congestion problem on the reverse link).

A calibration phase is required in the simulations, that take into account the actual numerical performances of the targeted FEC code(s). This allows to avoid implementing a real decoder in the simulation chain, while assuring a very good accuracy of the representation [11]. We use the MI to decide if the codeword is decoded or not using this formula:

$$N^{(j)} MI_{acc}^{(j)} \geq N_{bits} MI_{req} \,. \tag{10}$$

Simulations of classical IR and proposed enhanced HARQ

We present results obtained by implementing both schemes (classical IR and proposed enhanced HARQ) described in previous sections, and we compare these results.

We define a set of precomputed decoding probabilities, that provide for each retransmission a precomputed number of parity bits to send. We are interested to improve the efficiency while maintaining an acceptable delay for services.

We define the efficiency, E (bits/symbol), as follows:

$$E = \frac{N_{data\ bits} N_{decoded\ words}}{N_{total}}, \tag{11}$$

where:

- $N_{data\ bits}$ is the number of data bits (useful bits) per codeword considered in our coding scheme;
- $N_{decoded\ words}$ is the total number of decoded codewords during the communication;
- N_{total} is the total number of symbols transmitted during the communication.

The delay for decoded codewords (at the receiver) can be expressed in terms of number of transmissions (N_{trans}), bit rate (R_b), number of bits sent (N) and propagation delay (T_{propag}), assuming a negligible access delay:

$$Delay = \frac{N}{R_b} + 2(N_{trans} - 1)T_{propag} + T_{propag}\ \ (s)\,. \tag{12}$$

The efficiency and the delay are positively related. To improve the efficiency we can increase the delay while respecting the delay constraints for services. This delay is controlled by the predefined decoding probabilities, which will be quasi constant along all the values of reference E_s/N_0. In the following, we have considered three different tables of decoding probabilities. Fixed decoding probabilities at each transmission considered in our simulations are given in Table I, where the maximum number of transmissions for a given codeword is four. Case 1 corresponds to a service accepting the delivery of 80% of the messages at the first two transmissions and 20% at the last two retransmissions. Case 2 corresponds to a service accepting the delivery of 95% of the messages at the first two transmissions and 5% at the last two retransmissions. Case 3 corresponds to a service accepting the delivery of 45% of the messages at the first two transmissions and 55% at the last two retransmissions.

TABLE I. PREDEFINED DECODING PROBABILITY TABLE FOR THE 3 CONSIDERED CASES

Transmission	1^{st}	2^{nd}	3^{rd}	4^{th}
$P_i(case1)$	0.5	0.3	0.15	0.04999
$P_i(case2)$	0.75	0.2	0.03	0.01999
$P_i(case3)$	0.4	0.05	0.45	0.0999

The number of bits to be transmitted at each transmission for the classical IR HARQ scheme (Section III) can follow several strategies. As a simple case, we consider an equally shared repartition of the data+parity bits among the transmissions, as shown in Table II.

TABLE II. NUMBER OF BITS TO BE TRANSMITTED AT EACH TRANSMISSION FOR CLASSICAL IR HARQ MODEL

Transmission	1^{st}	2^{nd}	3^{rd}	4^{th}
$N_{sent}^{j}(bits)$	13380	13380	13380	13380

After simulating first (classical IR HARQ) and second (enhanced approach with three cases mentioned above) schemes, under the same conditions, we figure out the efficiency and the delay obtained for both schemes and compare them.

Figure 4 shows the average delay, required to decode codewords, obtained with both models (by means of simulations). The mean delay is computed by averaging delays obtained for decoded codewords calculated using (12). As we can see, the values obtained for each case of the proposed model are approximately the same. The delay remains stable and

 ISBN: 978-1-61208-397-1

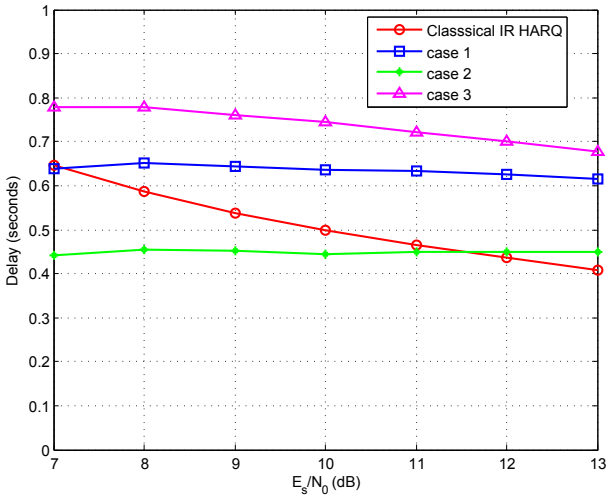

Figure 4. Delay obtained for both models for different values of reference $(E_s/N_0)_{dB}$.

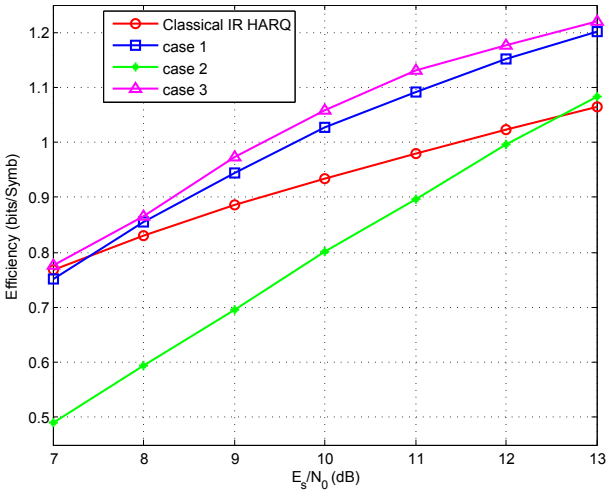

Figure 5. Efficiency obtained for both models for different values of reference $(E_s/N_0)_{dB}$.

controlled by the decoding probability, globally constant. It changes a little, from a reference E_s/N_0 to another, according to the number of bits transmitted and the values of decoding probabilities.

Figure 5 compares the efficiency obtained with both models in the same conditions. We can see that even if we loose in delay, the proposed model in cases 1 and 2, outperforms the classical one especially for high values of reference E_s/N_0. The resulting gain can reach 15%. These results validate our proposal, that fixing decoding probabilities at each transmission can improve the efficiency while respecting delay constraints for a given service. These results seem promising, however they have been obtained without any optimization of decoding probability for each transmission step. Therefore, some further improvements could probably be obtained. This clearly calls for an optimization process in further steps of the work.

VI. Conclusion and Future Work

In this paper, we have compared two techniques of HARQ transmission. The first one is a classical IR HARQ scheme, that transmits the same number of bits at each transmission without any knowledge about the global statistics of the channel; the second one is an enhanced HARQ technique, which takes into account the global statistics of the channel. This proposed enhanced technique estimates the number of bits to be transmitted at each transmission to decode a codeword with a given probability. This estimation relies on the mutual information given the decoding probability at each transmission and the knowledge of the distribution of the channel attenuations. Finally, results obtained after simulating both schemes in a mobile satellite communication environment are compared in terms of decoding probability (delay) and efficiency. Results show that enhanced HARQ has better performance in terms of efficiency especially for high values of reference SNR, while maintaining a quasi constant delay acceptable by delay constraints of service. As future work we will modify the proposed method to make it an adaptive model. This model would calculate the number of bits to be transmitted at each transmission according to decoding probabilities and real values of attenuation coefficients obtained. We plan also to consider additional system parameters, such as framing constraints and overhead to evaluate the performance of the mechanism in real systems.

References

[1] M. Gineste and H. Gonzalez Perez, "On the usage of a dedicated data link layer and half duplex terminals in satellite systems for future air traffic management," in *28th AIAA International Communications Satellite Systems Conference*, Anaheim, California, Aug.-Sept. 2010.

[2] A. Cipriano, P. Gagneur, G. Vivier, and S. Sezginer, "Overview of ARQ and HARQ in beyond 3G systems," in *Personal, Indoor and Mobile Radio Communications Workshops (PIMRC Workshops), 2010 IEEE 21st International Symposium on*, Sept 2010, pp. 424–429.

[3] R1-01-0031, "3rd generation partnership project, technical specification group radio access network, proposal of bit mapping for type-III HARQ," Boston, USA, Jan. 2001.

[4] S. Denic, "Robust incremental redundancy hybrid ARQ coding for channels with unknown interference," in *2011 IEEE International Symposium on Information Theory (ISIT)*, July 2011, pp. 1658–1662.

[5] E. Soljanin, R. Liu, and P. Spasojevic, "Hybrid ARQ with random transmission assignments," in *Advances in Network Information Theory*, P. Gupta, G. Kramer, and A. Wijngarden, Eds. DIMACS Series in Discrete Mathematics and Theoretical Computer Science, American Mathematical Society, March 2003, pp. 321–334.

[6] I. Andriyanova and E. Soljanin, "Optimized IR-HARQ schemes based on punctured LDPC codes over the BEC," *Information Theory, IEEE Transactions on*, vol. 58, no. 10, pp. 6433–6445, Oct 2012.

[7] F. Perez-Fontan, M. Vazquez-Castro, S. Buonomo, J. Poiares-Baptista, and B. Arbesser-Rastburg, "S-band LMS propagation channel behaviour for different environments, degrees of shadowing and elevation angles," vol. 44, no. 1, March 1998, pp. 40–76.

[8] F. Perez-Fontan, M. Vazquez-Castro, C. Enjamio-Cabado, J. Pita-Garcia, and E. Kubista, "Statistical modeling of the LMS channel," vol. 50, no. 6, Nov. 2001, pp. 1549–1567.

[9] C. Berrou, *Codes et turbocodes*. Springer, 2007.

[10] S. Dolinar, D. Divsalar, and F. Pollara, "Turbo codes and space communications," in *Space Operations Conference SpaceOp98*.

[11] W. Chauvet, C. Amiot-Bazile, and J. Lacan, "Prediction of performance of the DVB-SH system relying on mutual information," in *Advanced satellite multimedia systems conference (ASMS) and the 11th signal processing for space communications workshop (SPSC)*, Cagliari, Sept. 2010, pp. 413–420.

[12] C. Loo, "A statistical model for a land mobile satellite link," vol. vt-34, no. 3, Aug. 1985, pp. 122–127.

 ISBN: 978-1-61208-397-1

Ka-Band VSAT System Models under Measured DUSA Attenuation

Kamal Harb, Abdulaziz Al-Yami, Samir Abdul-Jauwad, Muhammad Muzammal Naseer
Electrical Engineering Department
KFUPM University, Saudi Arabia
Email: 1- kharb@kfupm.edu.sa; 2- abdulaziz.yami.1@aramco.com

***Abstract*—The satellite industry's need for Ka-band is increasing due to capacity abundance and cost efficiency. The commonly used C-band and Ku-band satellites have a limited number of geosynchronous orbital slots for given frequency bands. Thus, industries are turning to Ka-band satellites. Operating at high frequencies making them vulnerable to atmospheric conditions like rain, scintillation, dust, humidity, etc. Performance analysis of Ka-band Very Small Aperture Terminal (VSAT) system under Dust and Sand (DUSA) storms induced impairments in Dhahran city, Saudi Arabia, is presented in this paper. In this area, DUSA storms are usually observed due to desertification. Satellite communications and microwave networks are among the most commonly utilized means of communication, scattered all over the country. These networks observe radio wave degradations due to the frequently occurring DUSA storms. This study precisely quantifies attenuation due to DUSA based on real time measurements, being observed in the Eastern region of Saudi Arabia. Simulation results of real time measurements based on the level of visibility during DUSA storms are being proposed to counter the impairments in an optimized manner. These results are then analyzed in a digital video broadcasting - satellite - second generation (DVB-S2) VSAT system environment. The mentioned analysis of received signal strength during such anomalous weather conditions can aid in performance optimization by monitoring the received signal and maintaining it within acceptable level.**

***Keywords*—*Broadband services*; *Digital video broadcasting-satellite-second generation*; *Ka-band Very Small Aperture Terminal*; *Signal to Noise Ratio*.**

I. INTRODUCTION

Satellite service suppliers are targeting the consumer market for the provision of broadband access, knowledge of information and communication technologies and other multimedia applications [1]–[3]. The availability of alternative services, such as Digital Subscriber Line (DSL) or cable, is not common in rural and sub-urban areas. Thus, making the delivery of broadband services to customers via Ka-band satellites is more suitable [2]. Ka-band systems do not use the concept of single service area, rather they employ spot beams. Utilization of Ka-band satellites is an immediate consequence of the industry's need to give more satellite services, which would have resulted in higher cost if provided by legacy bands.

Previously, the Very Small Aperture Terminals (VSAT) market has depended upon C and Ku bands [4]–[7]. Therefore, there is a tight number of geosynchronous orbital slots that could be utilized for a given frequency band, and nearly all orbital openings are represented with current and arranged C-band and Ku-band. So, the Ka-band seems to be a definitive answer for any new satellite correspondence framework. Nevertheless, Ka-band has an immense disadvantage in comparison with C-band and Ku-band due to higher frequency range allotment [8]–[14]. Working at high frequencies makes it more prone to indicator quality issue due to climatic conditions incorporating rain blur, Dust and Sand (DUSA) storms, etc. Dissection of such climate induced weakening impairments in the Eastern district of Saudi Arabia is the essential contribution of this paper.

In this research, climatic information for DUSA storms has been gathered from Saudi Arabian sources and used in physical estimations to get precise gauges in the region of interest. In parallel to the focus of this analysis, many researchers have shown great interest in estimating the high frequency wave attenuation due to DUSA particles [2][3][15]–[18]. Very few studies are conducted at the Ka-band. The impacts are analyzed in a digital video broadcasting - satellite - second generation (DVB-S2) VSAT broadband framework, as depicted in Figure 1, with an adaptive scheme to gauge atmospheric attenuation, due to change in DUSA density at any given area with certain propagation angle and operational frequency. In the wake of quantifying such impairments at diverse and remote locations, improved back propagation-learning calculation – by iteratively computing operational frequencies, elevation angles, modulation and coding – is done to improve the Signal to Noise Ratio (SNR).

This paper is described in five sections. Section II describes the DVB-S2 for supporting forward and receive channels in a flexible way. Section III presents the methodology and simulation of DUSA storm. It also describes different research methods for dust storm. Section IV presents analysis and modeling for DUSA attenuation variations with other propagation factors. Consequently, SNR under DUSA storm conditions were calculated. Finally, we conclude this study in Section V.

II. DVB-S2 VSAT SYSTEM

DVB-S2 VSAT system is used to control record readings for weather attenuation. The remote terminal presented in Figure 1 sends data packets to a satellite and receives back an acknowledgement through Indoor Unit (IDU).

In the initial phase, several modern techniques to estimate the effects of DUSA storms on satellite communications were simulated in MATLAB environment for Ka-band frequencies. Later the parameters of DUSA storms relevant to Saudi Arabia were extracted and incorporated in the simulations to estimate their effects on Ka-band VSAT systems.

Furthermore, the estimates of DUSA density existing in air are gathered from various nearby weather stations and incorporated into simulations to quantify their effects in retarding

 ISBN: 978-1-61208-397-1

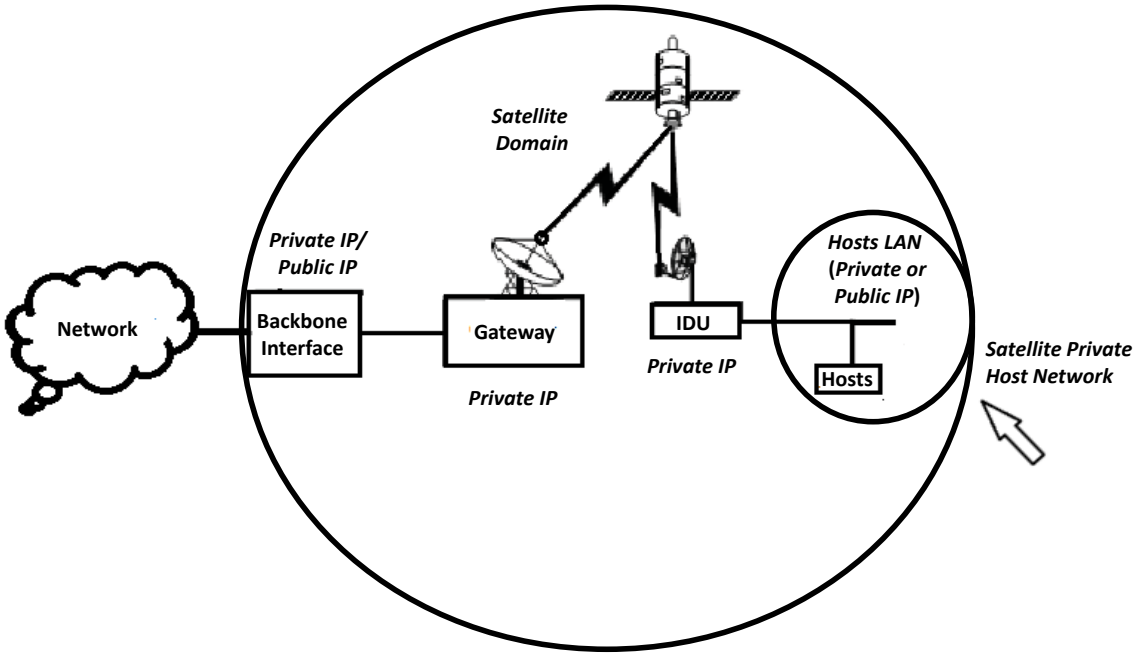

Figure 1. Example of DVB-S2 VSAT Complete Network.

the SNR, as well as Quality of Service (QoS) and therefore effective throughput of VSAT system.

DVB-S2 VSAT system has been modeled in MATLAB to analyze DUSA storms effects related to the concerned region. This system has been simulated in a flexible way such that the primary parameters of VSAT system can be adjusted by changing modulation, coding, transmit power, operating frequency, elevation angle, etc., based on the estimates of DUSA storms, to provide uninterrupted service while optimally managing the radio resources.

The system model is based on DVB-S2 for the forward channel and digital video broadcasting - return channel via satellite (DVB-RCS) for the return channels. DVB-S2 is currently the latest satellite communications standard in production and is commonly used for video based applications. It has the feature of low encoding complexity and also has variable and adaptive coding and modulation modes, which can be used for fluctuating noise conditions. In the forward direction, the system uses DVB-S2 in accordance with the DVB-RCS specification EN 301 790. It offers both QPSK and 8PSK modulation schemes. Figure 2 depicts the E_s/N_0 versus spectral efficiency for the various modulation schemes. While these signal-to-noise ratios are readily achievable for trunking applications between large earth stations, they are not generally available for VSAT networks. On the other hand, DVB-RCS utilized in this study uses the most advanced modulation and coding on the return (remote to gateway) satellite links available in the DVB-RCS specification where Table I

TABLE I. SPECTRAL EFFICIENCY DVB-RCS RETURN LINK.

Channel Spacing Factor = 1.25.	
Turbo Coding (Rate)	Spectral Efficiency (Bits/sec/Hz)
1/3	0.53
2/5	0.64
1/2	0.80
2/3	1.07
3/4	1.20
4/5	1.28
6/7	1.37

the performance of the return link. In the return direction, the system uses QPSK modulation with Turbo coding as per EN 301 790 exclusively. The system offers a variety of Turbo coding rates depending on the nature of encapsulation chosen for the return traffic.

Data traffic in all cases terminates/originates to/from the backbone routers and telephone switches located at the gateway location. This system model supports data communication between a remote in one sub-network and the corporate network, between two remotes in one sub-network and between two remotes in a different sub-network (one remote in sub-network 1 and one remote in sub-network 2). The space segment of the VSAT network consists of two transponders

 ISBN: 978-1-61208-397-1

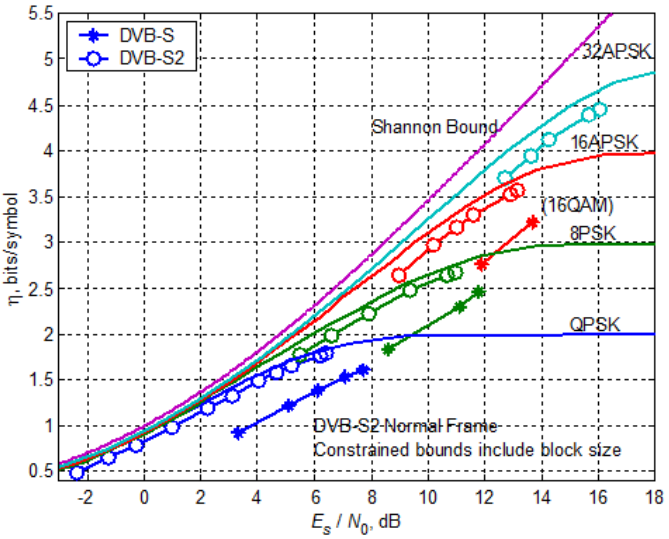

Figure 2. Spectral efficiency of DVB-S2 modulation schemes.

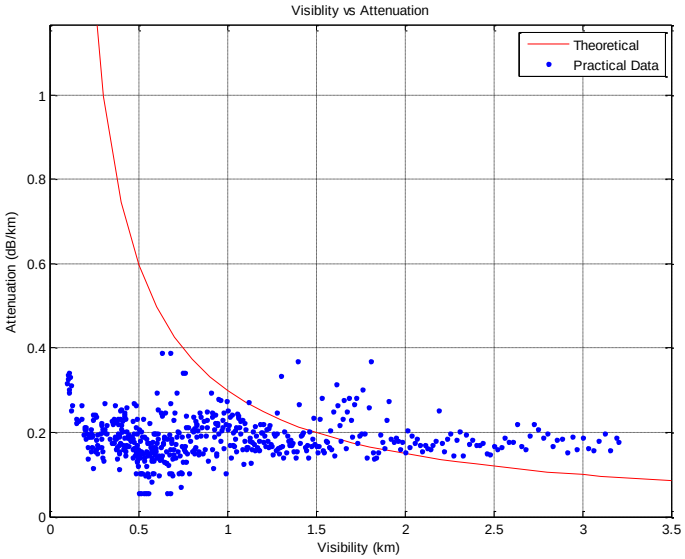

Figure 3. Comparison Uncompensated for Attenuation with Visibility.

on Intelsat 1002.

The test setup mainly consists of a VSAT remote terminal and a visibility sensor both located in Dhahran. The SNR of the transmitted data is physically measured to quantify the effects of such factors on the composite attenuation. Also, the visibility was observed at the same time.

III. METHODOLOGY

This section covers a brief review of different mathematical expressions used in the estimation of DUSA impairments. General formulas for electromagnetic (EM) wave passing through DUSA particles have been implemented in [3] using Rayleigh approximation attenuation and phase shift factors for a VSAT environment where DUSA particles are estimated considering two major components namely visibility and frequency.

A. Rayleigh Approximation

In [3], generic models for DUSA storms affected wave propagation constant based on Rayleigh approximation were developed. The satellite medium parameters experiencing DUSA storms impairment were derived considering location, visibility, frequency, and other factors. These formulas are correlated with the principles by Goldhirshs estimation [19]. By following the analysis for different particles model, the propagation will be:

$$K_{V,H}(\varphi) = k_0 + \frac{2\pi}{k_0} \int_0^{\infty} f_{V,H}(\varphi,\ r)\ N(r)dr \quad (1)$$

where:
k_0: the free-space propagation constant,
φ: the incident radiation propagation angle,
$N(r) = N_0\ P(r)$: DUSA distribution per (cm^3) having radius in the region of $r \rightarrow r + dr$.
$f_{V,H}(\varphi, r)$: the forward scattering amplitude for vertical (V) and horizontal (H) polarizations.

B. Goldhirsh's Formula

Contingent on the Rayleigh approximation, the attenuation model for satellite signal propagation in DUSA storms derived by Goldhirsh is [19]:

$$\alpha = \frac{2.317 \times 10^{-3} \times \varepsilon''}{[(\varepsilon' + 2) + \varepsilon''^2] \times \lambda} \cdot \left(\frac{1}{V_b^{\gamma}}\right) \quad [dB/Km] \quad (2)$$

λ: the wavelength in m,
ε' and ε'': the dielectric constant of the DUSA particles,
γ = 1.07, and V_b visibility in Km is a key component for evaluating of dust induced impairments. Equation (3) presented in [20] shows dependence of visibility and height (h).

$$V = V_0 \left[\frac{h}{h_0}\right]^{0.26}, \quad (3)$$

where V_0 and h_0 are the reference visibility and height, respectively.

C. Ahmed Derivation

Ahmed et al. derived a DUSA storms attenuation model for millimeter-wave based on measured probability density function and Mie theory. The model is expressed by [21]:

$$\alpha = 5.670 \times 10^4 \cdot \left(\frac{1}{V_b}\right) \cdot \left(\frac{r_e}{\lambda}\right) \cdot \frac{\varepsilon''}{[(\varepsilon' + 2) + \varepsilon''^2]} \quad (4)$$

Here, r_e is the effective particle radius in μm.
Similarly, a generic model suitable for different particle sizes

 ISBN: 978-1-61208-397-1

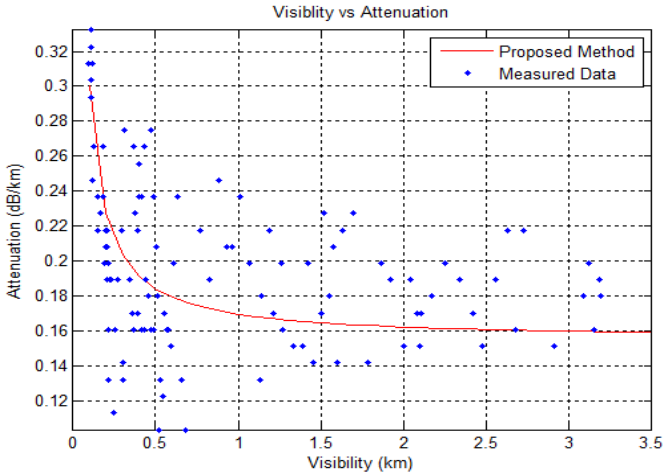

Figure 4. Comparison Compensated for Attenuation with Visibility.

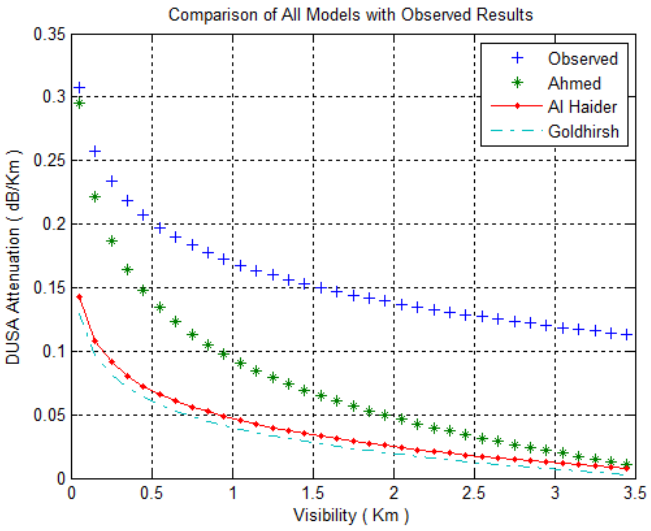

Figure 5. Comparison between different Models.

distributions developed in [21] for microwave propagation in DUSA storms is shown as:

$$\alpha = 0.629 \times 10^{3} \cdot \left(\frac{F \cdot r_e}{V_b}\right) \cdot \left(\frac{\varepsilon''}{[(\varepsilon' + 2) + \varepsilon''^2]}\right) \quad (5)$$

F: the frequency in GHz.

D. Al-Haider derivation

Considering 10 years visibility data and the Rayleigh approximation, Al-Haider developed another attenuation model for microwave propagation in DUSA storms [5] as:

$$\alpha = \frac{0.189}{V_b} \cdot \left(\frac{r}{\lambda}\right) \cdot \left(\frac{3\,\varepsilon''}{[(\varepsilon' + 2) + \varepsilon''^2]}\right) \quad (6)$$

r: the particle radius in m.

The above model is applied to our region of interest in Saudi Arabia. The data pertaining to visibility has been extracted from literature [4]–[12] and is physically measured to quantify the effects of such factors on composite attenuation.

IV. ANALYSIS

The measured data presented in Figure 3 and Figure 4 are used for analyzing DUSA attenuation variations with different values of collected visibility. The uncompensated data for theoretical and practical scenarios presented in Figure 3 show that the theoretical line marginally models the practical data with a higher degree of variations up to approximately 1.25 Km of visibility. This discrepancy at low visibility is due to the lack of appropriate model that match real measurements. It presents a big challenge for researchers and providers as signal could be totally blocked by DUSA storm.

The theoretical line follows a decaying exponential trend, but the recorded data (blue dots) resembles a linear relationship due to outcome discrepancy. It shows that the theoretical line (red) closely models the practical data only around 1.75 Km of visibility and missed it for the rest of data.

The proposed analysis for the compensated data was implemented to get better matching results especially at low visibility by tuning variables presented in (7). This improvement result for attenuation with different visibility is clearly shown in Figure 4. This outcome will lead to an appropriate value for SNR, as well as the overall system's throughput. The practical data (blue dots) follow the trend of recorded data though it is scrambled. However, we see roughly that at a visibility higher than 1.3 Km, the attenuation becomes constant.

DUSA attenuation model for real time measured data compared to other developed models is presented in Figure 4. Note that, the DUSA storms level above the ground, according to Saudi Arabia region, ranges between 4 Km to 6 Km for maximum.

According to numerical methods used for estimations presented in Figure 4, we present a model for DUSA point attenuation (A_p) as follows:

$$A_p = 2.2909 \times 10^{-16} + \left\{\frac{567}{V r_e^2 \lambda} \times \cdots \right. \\ \left. \cdots \times \frac{\varepsilon''}{\left(\varepsilon' + 9.9595 \times 10^{8}\right)^2 + \varepsilon''^2} \times \sum_{i}^{n} p_i r_i^3 \right\} \; dB/Km \quad (7)$$

where $\sum_i p_i\, r_i^3$ represents the summation of different probabilities of particle sizes multiplied by the dust particle size. V is the visibility. Whereas, the parameters λ, r_e, ε' and ε'' are constant values at various frequencies as defined in Table II. The outcome of (7) represents the compensated expression of DUSA model. The constant value is extracted by inspection using MATLAB tests. This value can be integrated back into the original expression with changing of $(\epsilon' + 2)^2$ to $(\epsilon' + 9.9595 \times 10^{8})^2$.

 ISBN: 978-1-61208-397-1

TABLE II. LISTING OF DIELECTRIC CONSTANTS AT VARIOUS FREQUENCIES MEASURED BY [5][6][19].

Dielectric Constants Values			
Frequency GHz	Soil Type	ε'	ε''
1 - 3	loam	3.5	0.14
3 - 10.5	clay, silt	5.73	0.474
10.5 - 14	sand	3.9	0.62
14 - 24	sad	3.8	0.65
24 - 37	loam	2.88	0.3529

A comparison between the observed attenuation model and others presented in this paper which resulted in deviation between the empirical values and the theoretical models is shown in Figure 5. There are many possible reasons for the deviation. One of the main reasons is that attenuations were simulated at different regions with different DUSA properties.

Thus, the proposed point attenuation along the radio wave path resulted in Figure 6 as a function of frequency and propagation angle with different particular sizes.

A. SNR Calculation

The improvement in SNR, as well as system's throughput based on estimation specific to the region is analyzed in [22][23]. The ratio between signal and noise are presented as:

$$SNR = P_t + G_t - A_t + G_r - T - K - R_s \quad dB, \quad (8)$$

A_t (total attenuation) = $A_{DS} + A_0$,
where the free space loss $A_0 = (4.\pi.d/\lambda)^2$,
d the distance in Km between the transmitter (ground station) and the receiver (satellite),
A_{DS} represents DUSA attenuation.
P_t and P_r represent the transmitter and receiver powers respectively.
G_t and G_r are antenna gains at the transmitter and receiver respectively. R_s is the transmission rate, K represents the Boltzman constant, and T represents the effective noise temperature.

A receive bandwidth (B_r) is considered. Thus, the noise power (N) will be:

$$N = N_0 \cdot B_r = K \cdot T \cdot B_r \quad (9)$$

System preformance of a digital system can be determined using the SNR or vice versa. Thermal noise power spectral density is given by $N_0 = K \,.\, T$, where, $K = 1.38 \times 10^{-23}\ Ws/K = -228.6\ dB\ Ws/K$, $T = T_a + T_r$, with T_a represents the noise temperature of the antenna, and the noise temperature of the receiver is:

$$T_r = \left(10^{\left(N_r/10\right)} - 1\right) \cdot 290 \quad (10)$$

$N_r \approx 0.7 \rightarrow 2$ dB: represents noise figure of low-noise amplifier, and R_s: represents the symbol rate.

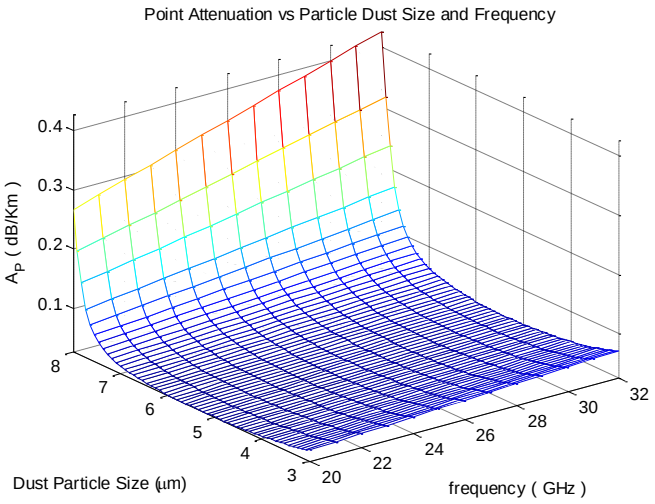

Figure 6. Point Attenuation with Visibility and Frequency under Dusty Weather in Dhahran, Saudi.

Therefore, satellite system performance is improved by providing enhanced estimates for attenuation due to DUSA storms leading to adjustment of SNR output in lieu of a wide range of frequencies, transmitted power, for any specific propagation angle, transmission rate, gain, and location as shown in Figure 7.

After having quantified the effects of DUSA storms in a generic satellite system, the main wave propagation parameters can be mitigated according to these impairments to eventually enhance the SNR and data-rates. Based on achieved analogy for different signal attenuation and SNR, designers are able to build a clear estimation for signal propagation in dusty and sandy weather conditions. Different results for geometries and locations of this technique are investigated. Resulting prototype products can be hardware controllers, which take the values of DUSA storm estimated as explained above, and would give optimal values of output transmit power, modulation, coding, operating frequency, and elevation angle.

Uplink Power Control (UPC) is a technique of adjusting the output power of the uplink with the aim to maintain a constant SNR ratio at a remote terminal, which can be used in our system's model. Adaptive Coding and Modulation (ACM) is used to keep the received signal quality above designers' threshold level in varying SNR levels. The modulation scheme is altered between a high capacity modulation at high SNR to a low capacity robust modulation at low SNR levels. After measuring DUSA storm attenuation, UPC and ACM can be used in the case of rain fade in satellite links.

V. CONCLUSION

Analysis of DUSA storm effects on a generic satellite link was the starting point of the proposed work. A relationship that estimates the DUSA storm effects has been derived for real time data. In this paper, different means for enhancing the throughput of a Ka-band broadband VSAT system were studied. Such systems are much susceptible to weather

 ISBN: 978-1-61208-397-1

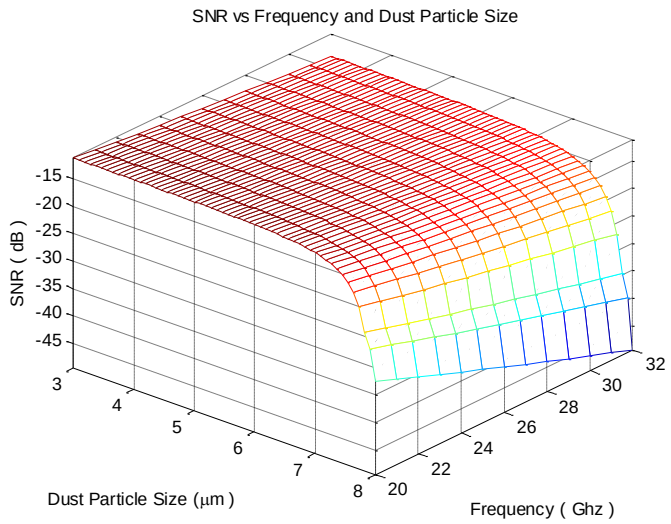

Figure 7. SNR Values vs Frequency and Dust Particle size in Dhahran, Saudi.

effects, in which DUSA storms impact transmitted signal and corresponding data rates are below the desired threshold levels. Hence, the performance of high throughput applications – like transmission of multimedia, interactive voice, etc. – is affected. The quantification of DUSA effects at different geographical locations, with the view to eventually upgrading the system parameters by virtue of an intelligent controller at the hub station. This system can ensure high throughput and reliable data transmission at all times. Estimating the attenuation due to DUSA storm is based on the latest techniques available in literature through incorporated weather data mainly about DUSA storms concentrations. In addition, the data is measured from different VSAT remote sites to achieve more specific physical results. Up to date techniques mitigate these effects and improve data-rates and QoS. The effects are analyzed in a DVB-S2 VSAT broadband system in which an adaptive scheme was used to estimate atmospheric attenuation due to DUSA density changes at any given location, with certain propagation angle and operational frequency.

ACKNOWLEDGMENT

The authors wish to thank the management of Saudi Aramco and King Fahd University of Petroleum & Minerals (KFUPM) and Hafr Al-Batin University, Electrical Engineering department for supporting this project and for facilitating the logistics needed for installing the satellite system and collecting data. This work is supported by Aramco and the Deanship of Scientific Research (DSR) at KFUPM through project No. FT121013.

REFERENCES

[1] Electronic Communications Committee (ECC), The use of the frequency bands 27.5-30.0 GHz AND 17.3-20.2 GHz by satellite networks, Report 152, within the European Conference of Postal and Telecommunications Administrations (CEPT), Sept. 2010.

[2] G. Maral, VSAT Networks. West Sussex, England: Wiley, 1995.

[3] Q. Dong, Y. Li, J. Xu, H. Zhang, and M. Wang, “Effect of sand and dust storms on microwave propagation,” IEEE Transactions Antennas Propagation, Feb. 2013, vol. 61, no. 2, pp. 910–916.

[4] K. Harb, O. Butt, A. Al-Yami, and S. H. Abdul-Jauwad, “Probabilistic dust storm layers impacting satellite communications,” in Proc. of the IEEE International Conference on Space Science and Communication (IconSpace), July 2013, pp. 407–411.

[5] A. Ali, M. A. Alhaider, and A. S. Ahmed, “Airborne dust size analysis for tropospheric propagation of millimetric waves into dust storms,” IEEE Transactions on Geosclencf and Remote Sensing, Sept. 1987, vol. 5, pp. 599–693.

[6] H. Y. Chen, Y. Ze, and C. C. Ku, “Calculation of wave attenuation in sand and dust storms by the fdtd and turning bands methods at 10-100 GHz,” IEEE Transactions on Antennas and Propagation, June 2012, vol. 60, no. 6, pp. 2951–2960.

[7] O. Butt, K. Harb, and S. H. Abdul-Jauwad, “Intelligent decision system for measured dust distributions impairing satellite communications,” in Proc. of the IEEE International Conference on Computational Intelligence and Virtual Environments for Measurement Systems and Applications (SIVEMSA), Ottawa, Ont., Canada, May 2014, pp. 106–111.

[8] K. Harb, B. Omair, S. Abdul-Jauwad, A. Al-Yami, and A. Al-Yami, “A proposed method for dust and sand storms effect on satellite communication networks,” in Innovations on Communication Theory (INCT), Oct. 2012, pp. 33–37.

[9] E. Saleh and I. Abuhdima, “Effect of sand and dust storms on microwave propagation signals in southern Libya,” in 15th IEEE Mediterranean Electrotechnical Conference, Tripoli, Libya, April 2010, pp. 695–698.

[10] P. Estabrook, J. Huang, W. Rafferty, and M. Sue, “A 20/30 GHz personal access satellite system design,” in IEEE International Conference on Communications (ICC), Boston, MA, June 1989, pp. 216–222.

[11] F. Davarian, “Earth-satellite propagation research,” IEEE Communications Magazine, April 1994, vol. 32, pp. 74–79.

[12] L. J. Ippolito and T. A. Russell, “Propagation considerations for emerging satellite communications applications,” Proc. of the IEEE, June 1993, vol. 81, no. 6, pp. 923–929.

[13] L. C. Palmer, E. Laborde, and A. S. amd P. Y. Sohn, “A personal communication network using a Ka-band satellite,” IEEE J. Select. Areas Communication, Feb. 1992, vol. 10, no. 2, pp. 401–417.

[14] M. J. Willis and B. G. Evans, “Fade countermeasures at ka band for olympus,” Int. Journal Satellite Communications, July 1994, vol. 6, no. 3, pp. 301–311.

[15] E. Vilar and M. Filip, “Adaptive modulations as a fade countermeasure: An olympus experiment,” Int. J. Satell. Communication, Feb. 1990, vol. 8, pp. 31–41.

[16] J. Horle, “Up-link power control of satellite earth-stations as a fade countermeasure of 20/30 ghz communications systems,” International Journal of Satellite Communications (ISSN 0737-2884), Sept. 1988, vol. 6, pp. 323–330.

[17] E. R. Berlekamp, R. E. Peile, and S. P. Pope, “The application of error control to communications,” IEEE Communications Magazine, Jan. 1987, vol. 25, no. 4, pp. 44–57.

[18] D. W. Blood and R. K. Crane, Handbook for the estimation of microwave propagation effects-Links calculations for earth-space paths (path loss and noise estimation): NASA Goddard Space Flight Center, 1979.

[19] J. Goldhirsh, “Attenuation and backscatter from a derived two-dimensional duststorm model,” IEEE Transactions Antennas Propagation, Dec. 2001, vol. 49, no. 12, pp. 1703–1711.

[20] E. A. Elsheikh, M. R. Islam, K. Al-Khateeb, A. Z. Alam, and Z. Elshaikh, “A proposed vertical path adjustment factor for dust storm attenuation prediction,” in 4th International Conference on Mechatronics (ICOM), May 2011, pp. 1–3.

[21] A. Ahmed, A. Ali, and M. Alhaider, “Measurement of atmospheric particle size distribution during sand/duststorm in Riyadh, Saudi Arabia,” Atmospheric Environment, 1987, vol. 21, no. 12, pp. 193–196.

[22] E. Lutz, M. Werner, and A. Jahn, Satellite Systems for Personal and Broadband Communications. Springer, New York, 2000.

[23] K. Harb, F. R. Yu, P. Dakhal, and A. Srinivasan, “Performance improvement in satellite networks based on markovian weather prediction,” in Proc. IEEE GlobCom, Miami, Florida, USA, Dec. 2010, pp. 1–5.

 ISBN: 978-1-61208-397-1

Weather-Impacting Link Analysis for New Horizons Data Return

Timothy Pham, Jason Liao
Jet Propulsion Laboratory
California Institute of Technology
Pasadena, California, USA
e-mails: Timothy.Pham@jpl.nasa.gov
Jason.Liao@jpl.nasa.gov

Christopher Deboy
Applied Physics Laboratory
Johns Hopkins University
Laurel, Maryland, USA
e-mail: Christopher.Deboy@apl.jhu.edu

Abstract - **This paper describes a recent effort in characterizing the weather conditions at the Canberra Deep Space Communications Complex of the National Aeronautics and Space Administration (NASA) Deep Space Network (DSN) to assess how they could impact the data return of the New Horizons mission during the Pluto encounter period. The frequency of rain occurrence is quantified based on recent 2014 statistics. The cumulative distribution of the precipitation rate during the rain events and the corresponding signal degradation are studied. The result is then evaluated against the anticipated link margin for two possible tracking configurations: one with a single 70m antenna, the other with an array of a 70m and three 34m antennas. The array offers a more robust link with greater margin, thus, a better protection against possible rain degradation; however, it would negatively impact other missions that require DSN support over the same period. The determination of possible improvement in terms of increased probability of data return offered by the antenna arraying helps selecting a strategy that best balances the benefit to the New Horizons mission and the impact to other missions concurrently supported by the DSN.**

Keywords - DSN; performance analysis; weather statistics; New Horizons

I. INTRODUCTION

The National Aeronautics and Space Administration (NASA) New Horizons mission is preparing for a historic encounter with the dwarf planet Pluto in July 2015. Since this is a once in a lifetime event, the mission design team wants to maximize the success probability of data return. A few weeks prior to the actual encounter on July 14, 2015, there will be several tracking passes that are critical to mission planning. These passes return the optical navigation data on possible hazardous objects around Pluto that are critical to the trajectory design of the flyby. There are also a few tracking passes immediately after the flyby that return the important scientific observation data.

To maximize the probability of data return over the scheduled passes to ensure the timeliness of trajectory design, the New Horizons mission is interested in quantifying if there is sufficient link margin to cover the adverse weather conditions. Rains – particularly the heavy ones – would reduce the received signal quality. In rainy condition, the signal to noise ratio is reduced by simultaneous effects of signal attenuation caused by the absorption and scattering of the raindrops, and of the increase in the ground system noise temperature.

In the previous baseline operation, the New Horizons mission plans to use the 70m antenna for the return of data. To get additional link margin, the mission could request for other 34m antennas to be added for arraying with the 70m. Doing so however would take away the tracking antennas needed by other missions. It is important then to understand if there is significant advantage with the array that would justify the negative impact to other missions.

In this paper, we will address the following questions:

(1) What is the probability of encountering the rain?

(2) In the event of rain, what is the likelihood that the signal degradation would exceed the available link margin?

(3) Would the extra gain from the array significantly improve the probability of a successful data return?

In Section II, we will discuss the available link margin for single antenna and the extra gain provided by the array. We will examine the statistics of events where rains affect the data return and quantify the probability that a pass may encounter rains in Section III. Section IV discusses the relationship between the precipitation rate (which is an indication on the intensity of the rain) and the signal degradation. Section V considers the statistics of precipitation rate observed in past rain events, assesses the probability where the link margin can sustain the signal degradation, and reflects the resulting operational planning under consideration. Conclusions are captured in Section VI.

II. AVAILABLE LINK MARGIN

The DSN has three tracking complexes spread evenly across the Earth longitudes in order to maintain a constant visibility to spacecraft in deep space. The three complexes are known as Goldstone, Canberra and Madrid Deep Space Communications Complexes, based on the its location in the United States, Australia and Spain. Each complex has a 70m antenna, one 34m high efficiency (HEF) antenna and at least two 34m beam-waveguide (BWG) antennas (Goldstone complex has one additional 34m BWG antenna). The distinction of the HEF vs. BWG antennas is due to their design and performance since the two sets of antennas were constructed at different time and with different technology

 ISBN: 978-1-61208-397-1

and operations considerations. The HEF antenna offers a better signal performance because its design is optimized at X-band, but its support is limited to S- and X-band. The BWG design focuses mainly on X- and Ka-band, and offers other operational advantages such as the ease of maintenance and addition of other frequency bands as needed.

For the Pluto flyby operation, the New Horizons mission plans to have a reserved 1.5 dB link margin with the 70m antenna tracking. Arraying the 70m with other 34m antennas would add additional margin. Each 34m antenna has a slightly less than half of the antenna aperture and a higher zenith system noise temperature than that of the 70m antenna. Since the system noise temperature changes as a function of elevation – due to different amount of atmospheric noise contribution resulted from different path length that the signal travels through the Earth atmosphere – the relative performance metric of Gain over Noise Temperature (G/T) between the 34m and the 70m antennas varies over the elevation range of the pass. Table 1 shows the G/T of the 70m, 34m HEF and 34m BWG at some key elevation points.

TABLE I. G/T PERFORMANCE OF VARIOUS DSN ANTENNAS AND CONTRIBUTION OF 3X34M ARRAY TO THE 70M ANTENNA

Elevation	G/T_70-m, dB	G/T_34-m HEF, dB	G/T_34-m BWG, dB	Contribution of 34-m HEF to 70-m	Contribution of 34-m BWG to 70-m	Array Gain with 3x34-m added to 70-m, dB
10	57.6	52.0	51.5	0.28	0.24	2.37
20	60.1	53.6	53.3	0.23	0.21	2.08
30	61.0	54.3	53.9	0.21	0.20	1.96
45	61.3	54.5	54.2	0.21	0.20	1.95
80	61.2	54.8	54.5	0.23	0.21	2.07

At the referenced 45 deg elevation, the 34m antenna G/T is about 20% of the G/T of the 70m antenna. An array of the 70m and three 34m antennas (one HEF and two BWGs) would yield 61% improvement in G/T compared to that of the 70m antenna alone. Allowing for 0.1 dB loss due to imperfect estimation and thus compensation of the relative delays among the input signals to be combined, the array would add 1.95 dB gain to the original 1.5 dB link margin of the 70m antenna. At other elevations, the array gain is higher, extending up to 2.4 dB at the lower elevation of 10 deg. Thus, with the array configuration, the link would have a minimum of 3.4 dB margin.

III. RAIN STATISTICS

In this section, we examine the rain statistics observed at the DSN sites. Among the three sites, Canberra typically has more rain [1]. Thus, assessment on the rain impact is based on Canberra data.

Records of Canberra tracking passes during January – November 2014 indicated that there were 37 events of rain that affect the data return. The majority was associated with data loss; however, some just resulted in signal degradation without data loss. The total data affected was 6871 minutes over a 10-month period, equated to 1.6% of the time. The probability of a tracking pass affected by the rain is thus only 1.6%.

Since the Pluto Flyby will occur on July 14, 2015 and the critical passes under consideration take place in June – July 2015, there is a concern on whether the weather conditions during these two months are different from, or worse than, the average statistics. Table 2 shows the long-term averaged precipitation measured at the nearby Tidbinbilla Reserve [2]. July is typically considered as one of the rainier months.

TABLE II. TYPICAL PRECIPITATION AT TIDBINDILLA NEARBY CANBERRA TRACKING COMPLEX

Tidbinbilla Long-term Averages	Jan	Feb	Mar	Apr	May	Jun	Jul	Aug	Sep	Oct	Nov	Dec	Ann
Mean Max (°C)	26.9	26.1	23.5	19.1	15.2	11.7	10.8	12.6	15.5	18.7	22.0	24.7	***18.7***
Mean Min (°C)	12.1	12.3	10.0	6.7	3.7	1.3	0.1	1.0	3.5	5.8	8.8	10.6	***6.2***
Mean Rain (mm)	83.2	75.3	69.1	65.7	67.7	66.9	83.8	95.8	92.6	89.9	91.7	65.1	***946.1***
Median Rain (mm)	62.9	48.1	43.3	38.2	59.7	54.4	69.5	89.5	86.8	81.2	81.2	54.0	***874.9***
Mean Rain Days	7.9	7.5	7.7	7.8	9.9	12.2	12.1	12.6	11.8	10.6	10.6	8.2	***115.6***

Next we examine at the rain statistics specifically in the past year of 2014 to further validate the long-term averages. Figure 1 shows the actual the day of year when the 37 rain events occurred and their duration in January – November 2014. The rain impact lasted from a few minutes to up to 10 hours, with an average duration of about 3 hours (185 minutes). The data also indicated that June and July were not particularly rainier compared to other months. Instead, the rains seemed to occur throughout the year, although with less rain in March and May.

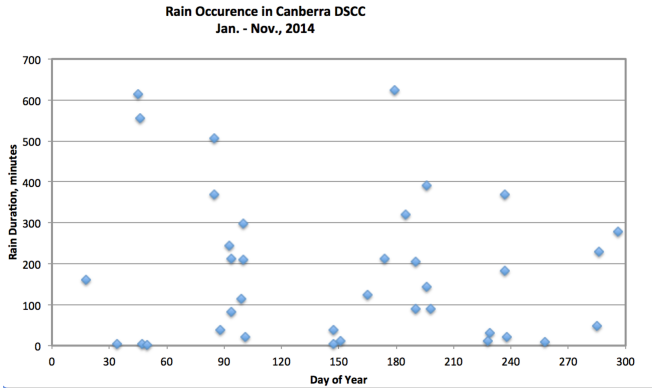

Figure 1. Rain Occurrence at Canberra Complex, January-November 2014

The recent rain observations in 2014 for the month of July is different from the long-term average shown in Table 2. We attribute the difference to be a variation of one specific year from the long-term average.

IV. SIGNAL DEGRADATION MODEL

As indicated in Section III, the chance of having a track coincides with a rain event is rather small (1.6%). However, if the track happens to be on a rainy day, we want to know the probability that the link margin can buffer the negative effect of the rain.

As signal travels through the rain, two effects occur. First, signal is attenuated because of scattering and absorption of signal power by the raindrops. The scattering diffuses the signal power. The absorption - due to a

 ISBN: 978-1-61208-397-1

resonance between the signal waveform and the vibration of water molecules - also draws the power away from the signal and transfers it to the increased motion of the water molecules. These effects become greater as there are more raindrops in heavier rains. Based on the Recommendation ITU-R P.838-3, Specific Attenuation Model for Rain for Use in Prediction Methods [3], the signal specific attenuation – attenuation per unit distance (dB/km) – can be modeled as a power function of the precipitation rate:

$$\gamma(R) = kR^{\alpha} \quad (1)$$

where:

γ is the specific attenuation (dB/km)

R is the precipitation rate (mm/h)

k = 0.0037825 (for circular polarization at X-band)

α = 1.38557 (for circular polarization at X-band)

The total attenuation is equal to the specific attenuation multiplied by the path length that the signal traverses through the rain. Assuming a height of rain cloud of h and a spacecraft line of sight at θ elevation, the signal attenuation path length L can be approximated as:

$$L(R) = \frac{\gamma(R).h}{\sin\theta} \quad (2)$$

In addition to the signal attenuation, the rain also causes an increase in the system noise temperature. This is due to the fact that the temperature of the rain (~300K) is much higher than that of typical cold sky (~25K) and the rain also acts as a lossy waveguide. As shown in [4], the increase in atmospheric noise temperature is:

$$\Delta T = (T_r - T_a)(L - 1)/L \quad (3)$$

where:

ΔT is the increase in atmospheric noise temperature, K.

T_r is the rain physical temperature, ~300K.

T_a is the typical cold sky temperature, ~25K.

L is the rain attenuation.

Figure 2 shows a sample of the rain impact for the case of cloud height $h = 7.5\ km\ and$ spacecraft elevation $\theta = 45$ deg. This elevation is chosen as an example because it is almost the midpoint in the 10-80 deg elevation range expected with New Horizons tracking at Canberra. Individual effects of signal attenuation (given by (2)) and degradation in system noise temperature (given by (3)) are included, as well as the total degradation.

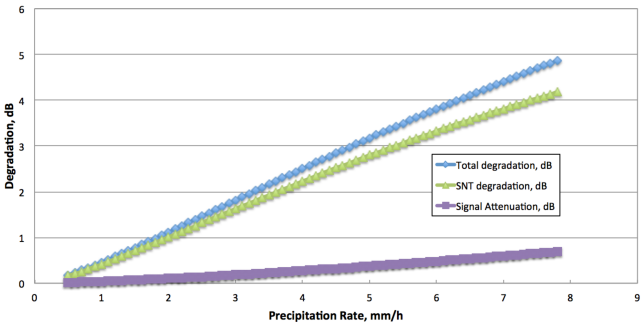

Figure 2. Modeled signal attenuation, system noise temperature degradation and total degradation for various precipitation rates at 45-deg elevation and 7.5 km rain height

V. ASESSMENT

For the particular case of 45-deg elevation and an assumed 7.5 km rain height, the single 70m antenna tracking with a 1.5 dB link margin could tolerate any rain with precipitation rate up to 1.5 mm/h. In contrast, with a 3.4 dB margin from an array of 70m and three 34m antennas, the link can sustain the rains up to 3.1 mm/h.

To determine the probability of occurrence of rain with precipitation rates of 1.5 mm/h and 3.1 mm/h, we examined the precipitation rate of each of the 37 rain events in 2014. The average precipitation rates are plotted in Figure 3. Twenty-five rain events (68%) were found to have precipitation rate below 1.5 mm/h, and 32 events (86%) below 3.1 mm/h.

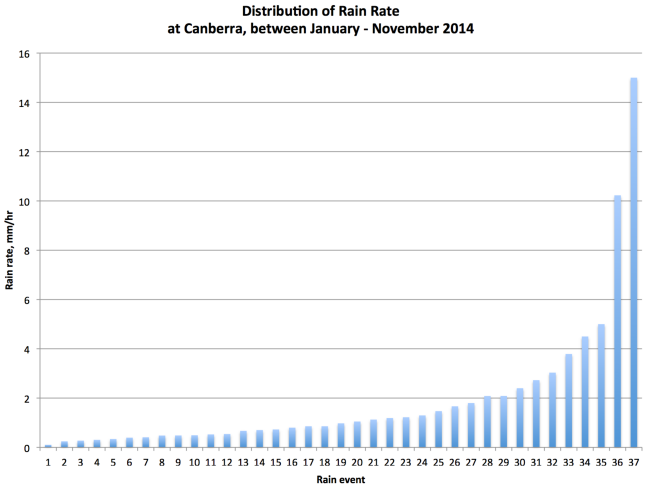

Figure 3. Distribution of precipitation rate from rain events in 2014 at Canberra.

Thus, the probability of sustaining the rain impact with a single 70m antenna tracking is 68%. With an array, that probability increases to 86%.

More general, the probability of successful data return at other elevations (10, 20, 30, 45 and 80 deg) is presented in Figure 4. At lower elevations, the single 70m antenna configuration has lower probability of success because the signal suffers more loss as it travels on a longer path through the rain. In those cases, the benefit of having extra gain provided via the array is more significant. At higher elevations, the single 70m antenna has greater chance to succeed due to smaller impact of the rain over shorter path. Correspondingly, there is a smaller improvement with the arraying.

Note that the New Horizons spacecraft does not spend equal amount of time across the elevation range. Because the spacecraft changes its elevation at a much faster rate during rise and set, the time spent at low elevations (10 – 30 deg) is much less than the time at high elevations (30 – 80 deg). In a typical New Horizons track at Canberra, 75% of the track time is above 30-deg elevation. Thus, in Figure 4, the region of high elevations above 30 degrees is more relevant to the assessment of improvement in the probability of success between the single 70m antenna and the array

 ISBN: 978-1-61208-397-1

configuration. At 30-deg elevation, the array would increase the probability of success from 73% to 89%. At highest elevation, the success probability increases from 86% to 95%.

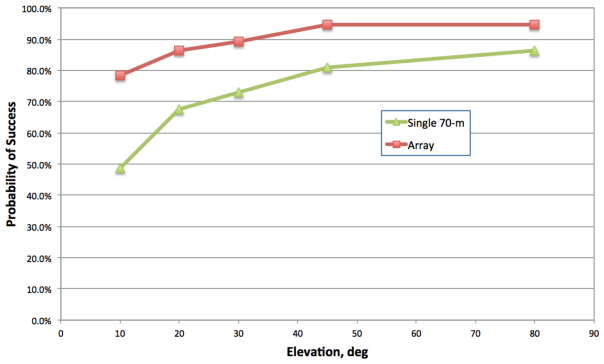

Figure 4. Probability of successful data return in the event of rain for single 70m antenna and array configuration

Given that the probability of success with the single 70m antenna at high elevation is already above 70% and the array only increases the chance by 9% – 16%, the New Horizons mission operations team, at the time of this report, is considering a hybrid approach (subject to the final decision). The mission would stay with the single 70m antenna configuration for these critical passes. That would allow other missions continue to be supported by other 34m antennas in the DSN. In the event of forecasted rain or encountering actual rain during the pass, the New Horizons mission would then request the 34m antennas, if available, to be added to the array to increase the probability of successful data return.

VI. CONCLUSION

In summary, our analysis indicates that the probability that a New Horizons' tracking pass could encounter rain is about 1.6%. When subjected to rain, there is a 73% chance that a New Horizons pass with a single 70m antenna would be able to sustain the rain's impact. If an array of one 70m and three 34m antennas is used, the link margin would increase by 1.95 dB and the success probability of weathering the rain would improve by an additional 9% – 16% at various tracking elevations. This analysis has aided the New Horizons mission planners to design a strategy that would maximize the probability of data return within various operational constraints.

ACKNOWLEDGMENT

The work described in this paper was carried out by the Jet Propulsion Laboratory, California Institute of Technology, under a contract with the National Aeronautics and Space Administration.

REFERENCES

[1] DSN Telecommunications Link Design Handbook, Document No. 810-005, Rev. E, Jet Propulsion Laboratory, Pasadena, California, http://eis.jpl.nasa.gov/deepspace/dsndocs/810-005/, accessed December 20, 2014

[2] Weatherzone, http://www.weatherzone.com.au/climate/station.jsp?lt=site&lc=7031, accessed December 20, 2014

[3] Recommendation ITU-R P.838-3, Specific Attenuation Model for Rain for Use in Prediction Methods, http://www.itu.int/dms_pubrec/itu-r/rec/p/R-REC-P.838-3-200503-I!!PDF-E.pdf, accessed December 20, 2014

[4] R. A. Nelson, "Rain – How it affects the communications link", Via Satellite 2000, http://www.aticourses.com/sampler/Rain_Affect_Communications_Link.pdf, accessed Dec. 20, 2014

 ISBN: 978-1-61208-397-1

Development and Verification Plan of Space Internet Technologies for Korean Lunar Exploration

Jin-Ho Jo, Tae-Cheol Hong, Byoung-Sun Lee, Jae-Young Ahn
Satellite & Wireless Convergence Research Department,
Electronics and Telecommunications Research Institute (ETRI),
Daejeon City, Rep. of Korea
E-mail: jhjo@etri.re.kr, taechori@etri.re.kr, lbs@etri.re.kr, jyahn@etri.re.kr

***Abstract*— The Space Internet, also known as the Interplanetary Internet, is a proposed network intended to connect stations on Earth with others in orbit around and on the surface of other planets and moons in the Solar System. This paper reports on a space Internet development and test plans for Korean lunar exploration program. First, Korean lunar program was reviewed. Then Delay Tolerant Network (DTN) characteristics and DTN protocols used in lunar exploration are reviewed. DTN communication architectures are presented. The Korea lunar exploration program is divided into two phases. In first phase, test lunar Orbiter will be launched without Lander or Rover. So, proposed DTN test architecture is based on Lander and Rover located on earth. In second phase, Lander and Rover will be landed on the moon. The DTN architecture and protocol stacks for second phase are also proposed.**

Keywords-Ionosphere; Delay Tolerant Network(DTN); CCSDS File Delivery Protoclo(CFDP); Bundle Protocol(BP); Licklider Transmission Protocol(LTP); Proximity-1.

I. INTRODUCTION

Korea plans to develop a space vehicle on its own and launch it during the first half of 2020, and send up a lunar orbiter and a lunar lander for itself before the end of the same year. In the longer term, it is planning to explore Mars, asteroids, and deep space to join the ranks of space industry powerhouses [1] [2].

The Korean lunar project is divided into two phases. The goals of the first phase, which continues until 2017, include the completion of the basic technical design of the orbiter and module in cooperation with NASA, and the development of a test orbiter. At the same time, the scientific equipment to be carried in the orbiter and earth-bound control station to be responsible for deep space communication will be built.

The second phase is for the self-production of the orbiter and module and actual launch using a Korea Space Launch Vehicle (KSLV). To this end, 15 government-funded research institutes, such as the Korea Aerospace Research Institute (KARI) have formed a council and conducted 31 research tasks.

Electronics and Telecommunications Research Institute (ETRI) plan to develop space Internet technologies for the lunar communication. During the first phase, space Internet technology developed by ETRI will be tested through test lunar orbiter. If first phase testing is successful, space Internet technologies will be applied to the mission communication in the second phase of lunar exploration.

This paper focused on overview of development and test plan of space Internet technologies for Korea lunar exploration. In this paper, Delay/Disruption Tolerant Network (DTN) is reviewed first in Section 2. The protocols used in DTN communication for Korea lunar exploration is reviewed in Section 3. Architecture for DTN communication is reviewed in Section 4. In this section, DTN architecture for first and second phase is reviewed separately. Finally, research activities and future works are summarized in Section 5.

II. DEAY TOLERANT NETWORK

The Internet has been a great success at interconnecting communication devices across the earth. It has done this by using a homogeneous set of communication protocols, called the TCP/IP protocol suite. All devices on the hundreds of thousands of networks that make up the Internet use these protocols for routing data and insuring the reliability of message exchanges.

Connectivity on the Internet relies primarily on wired links, including the wired telephone network, although wireless technologies such as satellite and short range mobile links are also an essential part of the network. These links, as used on the Internet, are continuously connected in end-to-end, low-delay paths between sources and destinations. They have low error rates and relatively symmetric bidirectional data rates.

The interplanetary network differs from the terrestrial Internet in a number ways as following that might arise individually or collectively.

- Intermittent connectivity: Connectivity may suffer from disruptions leading to link failure and network partitioning, for a large number of reasons like mobility issues, radio issues, and battery issues.
- Delay issues: Links could have a very high propagation delay or have such a highly variable delay that traditional protocol like TCP would fail.
- Asymmetric data rates: Links can suffer from highly asymmetric data rates or can be simply just unidirectional.

 ISBN: 978-1-61208-397-1

- High error rates: Some links may have high error rates. They could require a high level of correction and a large number of retransmissions, leading to the creation of tight bottlenecks [3].

A DTN is a network of smaller networks. It is an overlay on top of special-purpose networks, including the Internet. DTNs support interoperability of other networks by accommodating long disruptions and delays between and within those networks, and by translating between the communication protocols of those networks. In providing these functions, DTNs accommodate the mobility and limited power of evolving wireless communication devices. DTNs were originally developed for interplanetary use, where the speed of light can seem slow and delay-tolerance is the greatest need. However, DTNs may have far more diverse applications on earth, where disruption-tolerance is the greatest need. The potential earth applications span a broad range of commercial, scientific, military, and public-service applications.

The DTN architecture implements store-and-forward message switching by overlaying a new transmission protocol, called the Bundle Protocol (BP), on top of lower-lower protocols, such as the Internet protocols. The bundle protocol ties together the lower protocol layers so that application programs can communicate across the same or different sets of lower-lower protocols under conditions that involve long network delays or disruptions.

The bundle-protocol agent stores and forwards entire bundles (or bundle fragments) between nodes. A single bundle protocol is used throughout a DTN. By contrast, the lower-lower protocols below the bundle protocol are chosen to suit the characteristics of each communication environment.

III. PROTOCOLS USED IN DTN COMMUNICATIONS

The protocols used for DTN communication in Korea lunar exploration are summarized as following.

- CCSDS (Consultative Committee for Space Data Systems) File Delivery Protocol (CFDP): The CFDP [4] is a File Transfer Protocol (FTP)-like protocol for transferring files between two entities separated by interplanetary distances, on the space links that have asymmetric bandwidths. CFDP can be used over a wide range of underlying communication services. It can be configured for either ground station to spacecraft or spacecraft to ground station transfers, apart from other configurations of a network of platforms, such as a spacecraft constellation or a series of planetary landers. The CFDP offers typical file operation commands such as delete, move, and copy that can be used to control a distant file store.
- Bundle Protocol (BP): The Bundle Protocol [5] provides effective mechanisms for communicating in and/or through highly stressed environments such as those with intermittent connectivity, large and/or variable delays, and high bit error rates. For providing its services, BP forms a store-and-forward overlay network by sitting at the application layer2 of some number of constituent Internets. The protocol data unit is called as a bundle and it comprises a sequence of two or more blocks of protocol data, which serve various purposes.
- Licklider Transmission Protocol (LTP): The Licklider Transmission Protocol [6], also known as Long-haul Transmission Protocol [7], is principally aimed at supporting the links, characterized by extremely long message route-trip times and/or frequent interruptions in connectivity. It has emerged as one of the best candidates as a convergence layer protocol in the case of interplanetary space communication. For single hop deep-space RF links, LTP is intended to serve as a retransmission-based reliable mechanism and does ARQ of data transmissions by soliciting selective-acknowledgment reception reports. LTP's design notions are directly descended from the retransmission procedures defined for CFDP.
- Proximity-1: Proximity-1 Space Link Protocol [8] is a short haul delivery communications protocol designed to establish a two-way communications link between a lander and an orbiter, negotiate data rate and communications mode, and reliably deliver data during short orbiter-to-surface contacts. Developed by CCSDS, Proximity-1 is implemented on Mars Exploration Rovers, Mars Odyssey, Mars Reconnaissance Orbiter, and Mars Express as well as on Phoenix Mars Lander. The frequency band used by this protocol is in the 400 MHz band so as to reduce complexity of the ground craft.
- Space Link Extension (SLE): The SLE transfer services [9], developed by the CCSDS, provide a standard method to transport spacecraft forward and return data between various tracking stations, mission operation control centers and data-user facilities. This standardization of the interfaces between the various facilities permits re-use of systems for successive missions and eliminates the development costs of mission-specific implementations. Mission risk is reduced since standard SLE services facilitate the rapid substitution of ground stations in the event of a failure. Since the SLE protocols run over existing communications infrastructure and utilize TCP/IP protocols, they help integrate Space Data Systems into the global communications network.

IV. DTN COMMUNICATION ARCHITECTURE

The DTN architecture for lunar exploration consists of following communication nodes.

- Orbiter: orbiting the moon to perform data relay for the Lander and Rover
- Lander: on a moon surface to perform science mission and data relay for the Rover

 ISBN: 978-1-61208-397-1

- Rover: move on the moon surface to perform science mission
- Ground Station (GS): on earth for communication with the orbiter and lander
- Mission Control Center (MMC): on earth for monitoring and control of the lunar Orbiter
- Lander Control Center (LCC): on earth for monitoring and control of the Lander
- Rover Control Center (RCC): on earth for monitoring and control of the Rover

The communications links between the nodes are shown in Figure 1. The Orbiter can communicate with earth through GS whereas Lander and Rover cannot communicate with earth directly. Lander and Rover can communicate with earth through Orbiter relay.

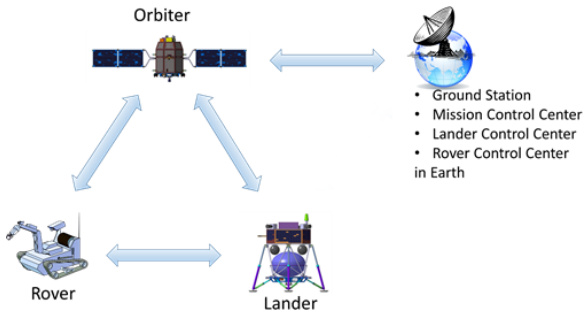

Figure 1. Communication links in lunar exporlation

A. *DTN Architecture for first phase*

In the first phase of lunar exploration, test lunar orbiter called Korea Pathfinder Lunar Orbiter (KPLO) will be launched for the testing purpose. The KPLO mission is to verify Orbiter functionality and to check many parameters to be considered for the second phase of lunar exploration. In the meantime ETRI plan to test DTN technologies through KPLO in the first phase of lunar exploration. The purpose of testing is to verify DTN protocol functionality and performance and also if DTN communication architectures are acceptable for lunar mission communications. Figure 2 shows a DTN configuration in first phase of lunar exploration. Because there are no Lander and Rover on the moon in first phase, ground models of Lander and Rover will be located on earth for the communication testing. RCC is a source of DTN node and Rover is a destination of DTN node. MCC, Lander, KPLO and Cube-sat are DTN nodes which perform, store, and forward bundles between the source and destination. GS is not a DTN node because it just transfers bundles between the MCC and Orbiter. GS, MCC, RCC and Lander ground model are connected together through Internet.

Two kinds of DTN tests will be performed in first phase of lunar exploration. The first test is a DTN round trip test. In this testing, RCC controls Rover on earth through KPLO. RCC send command message or files to Rover in earth through KPLO and receive status telemetry or image files captured by Rover through KPLO also. The signal flow of round trip test is shown in Figure 3. Table 1 shows tentative protocols between the communication links.

The CFDP class 1 will be used for message or file transfer between RCC and Rover. Custody transfer based on store-and-forward mechanism and end-to-end reliability is provided by BP and LTP which are underlying CFDP. The SLE protocol will be used in the link between MCC and GS. This link can be assumed to be continuously available and there seems to be no need to apply the store-and-forward of BP in the GS. Proximity-1 can be used as a radio link between the Orbiter, Lander and Rover. Figure 7 at end of this paper shows a protocol stack for DTN round trip test in first phase.

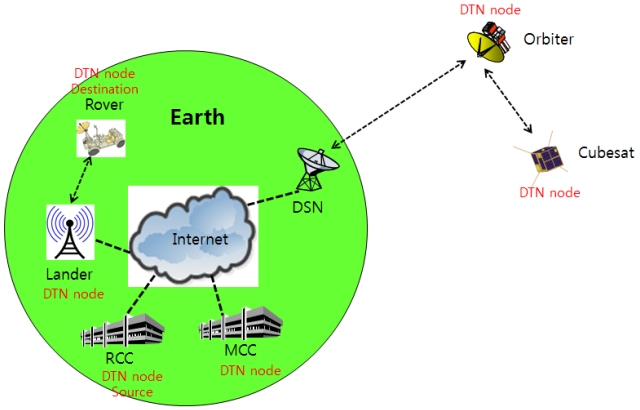

Figure 2. DTN test configuration in first phase

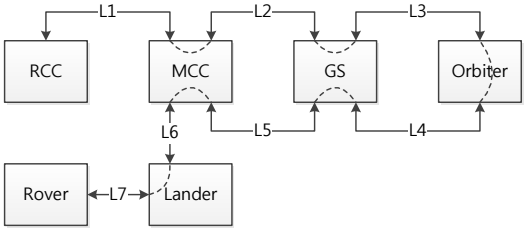

Figure 3. Signal flow of DTN round trip test in first phase

TABLE I. PROTOCOLS USED IN DTN ROUND TRIP TEST

Links	Protocols
L1	CFDP/BP/UDP
L2/L5	CFDP/BP/LTP/SLE
L3/L4	CFDP/BP/LTP/TMTC(AOS)
L6	CFDP/BP/UDP
L7	CFDP/BP/Proximity-1

Second test is a DTN communication test using Cube-sat. Cube-sat is released from the Orbiter when Orbiter is settled down in the orbit. Then, RCC on earth sends command to Cube-sat, and captured image by Cube-sat is transferred to RCC through KPLO relay. Cube-sat mission will continue

 ISBN: 978-1-61208-397-1

until the link between KPLO and Cube-sat is disconnected. The signal flow of Cube-sat communication test is shown in Figure 4 and Table 2 shows tentative protocols between the communication links.

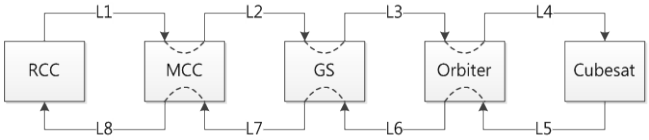

Figure 4. Signal flow of Cube-sat communication test at first phase

TABLE II. PROTOCOLS USED IN CUBE-SAT COMMUNICATION TEST

Links	Protocols
L1/L8	CFDP/BP/UDP
L2/L7	CFDP/BP/LTP/SLE
L3/L6	CFDP/BP/LTP/TMTC(AOS)
L4/L5	CFDP/BP/ Proximity-1 or CFDP/BP/ 802.11

B. *DTN Architecture for second phase*

In the second phase of lunar exploration, self-production of the Orbiter and Lander will be launched using a Korea Space Launch Vehicle (KSLV). The Orbiter is launched first and Lander follows. After Orbiter and Lander are settled down in its lunar orbit, Lander will be landed on the surface of moon. After safe landing, Lander deploys antenna and Rover will be released from the Lander. After safe release, Rover will perform science mission moving around landing area. Figure 5 shows a DTN communication configuration in second phase.

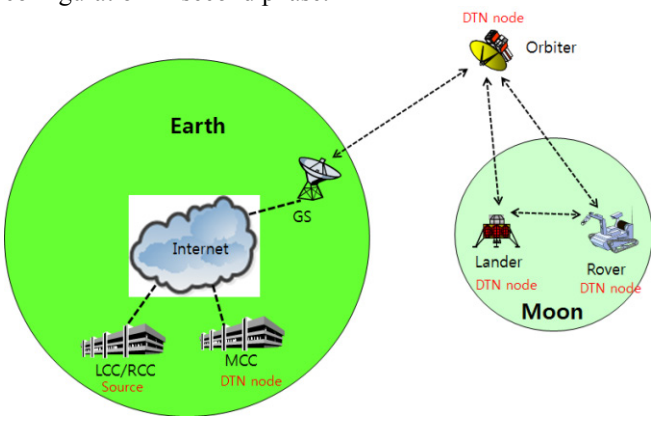

Figure 5. DTN communication configuration in second phase

As in first phase, CFDP class 1 will be used for file and message transfer between the RCC and Rover. The protocols are simular with the first phase. The signal flow of DTN communication in second phase is shown in Figure 6 and Table 3 shows tentative protocols between the communication links in second phase.

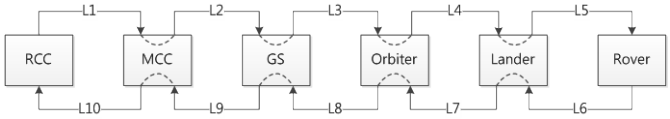

Figure 6. Signal flow of DTN communication at second phase

TABLE III. PROTOCOLS OF CUBE-SAT COMMUNICATION TEST

Links	Protocols
L1/L10	CFDP/BP/UDP
L2/L9	CFDP/BP/LTP/SLE
L3/L8	CFDP/BP/LTP/TMTC(AOS)
L4/L7	CFDP/BP/ Proximity-1
L5/L6	CFDP/BP/ Proximity-1

Figure 8 at end of this paper shows a protocol stacks for DTN communication in second phase.

V. CONCLUSION AND FUTURE WORK

In this paper, we presented a development and test plans of space Internet technologies for Korea lunar exploration. In the first phase of lunar exploration, two kinds of test scenarios are considered now. First scenario is DNT round trip test through KPLO. In this test, RCC controls Rover on earth through KPLO relay. RCC also monitors telemetry from the Rover on earth and also receive images captured by Rover through KPLO relay. Second scenario is DTN communication with Cube-sat. In this test, RCC controls Cube-sat through KPLO, it monitors telemetry from the Cube-sat, and also receives image captured by Cube-sat through KPLO relay. The purpose of DTN testing in first phase is to check and validate that DTN technologies are acceptable for the mission communication in second phase.

In the second phase of lunar exploration, Lander and Rover will be located on the surface of moon. In this phase DTN technologies will be applied to the communications between earth and lunar assets.

At this moment, ETRI installed DTN test-bed for the test of DTN protocols functionality and performance. Also, ETRI have a cooperation plan with NASA in the DTN and Cube-sat development. In near time, ETRI DTN test-bed will be connected to NASA test-bed for inter-operability testing. For the Cube-sat design, we are considering using smart phone as a communication payload for Cube-sat. ETRI also designs Proximity-1 space link modem for the inter spaceship communications. ETRI also participates in CCSDS meeting continuously.

REFERENCES

[1] "National Long-Term Space Development Plan," Ministry of Science, ICT and Future Planning, Nov. 2013.

[2] Receptive Committee of the 18th Presidency, "Administrative Goals," Cheongwadae, Feb. 2013, pp.50.

 ISBN: 978-1-61208-397-1

[3] M. Prathaban, Contribution to the Performance Study of Interplanetary Networks, Doctor of Philosophy in Computer Science, Telecom SudParis, 2010.

[4] CCSDS. File Delivery Protocol (CFDP). Blue Book. Issue 4, URL:http://public.ccsds.org/publications/archive/727x0b4.pdf, Washington, D.C, January 2007.

[5] CCSDS Bundle Protocol Specification, Draft Recommanded Standard, Issue 2, URL://http://public.ccsds.org/sites/cwe/rids/Lists/CCSDS%207342R2/Attachments/734x2r2.pdf, October 2013.

[6] Licklider Transmission Protocol (LTP) for CCSDS, Draft Recommended Standard, Issue 3, URL:http://public.ccsds.org/sites/cwe/rids/Lists/CCSDS%207342R3/Attachments/734x2r3.pdf, July 2014.

[7] F.S. Muhammad, L. Franck, and S. Farrell, "Transmission Protocols for Challenging Networks: LTP and LTP-T," International Workshop on Satellite and Space Communications, September 2007, pp. 145-149.

[8] CCSDS. Proximity-1 Space Link Protocol - Data Link Layer. Blue Book, Issue 5, URL:http://public.ccsds.org/publications/archive/211x0b5.pdfWashington, D.C, December 2013.

[9] Space Link Extension-Return All Frames Service Specification, Recommended Standard, Issue 3, URL:http://public.ccsds.org/publications/archive/911x1b3ec1.pdfJanuary 2010.

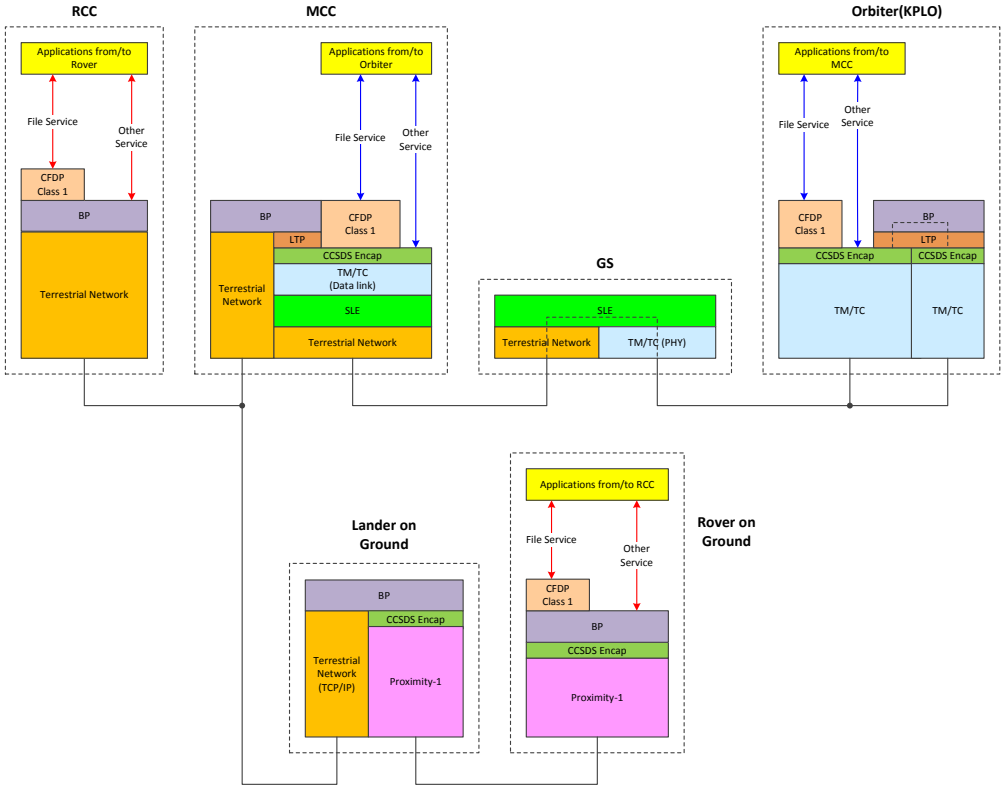

Figure 7. Protocol stacks of DTN round trip test in first phase

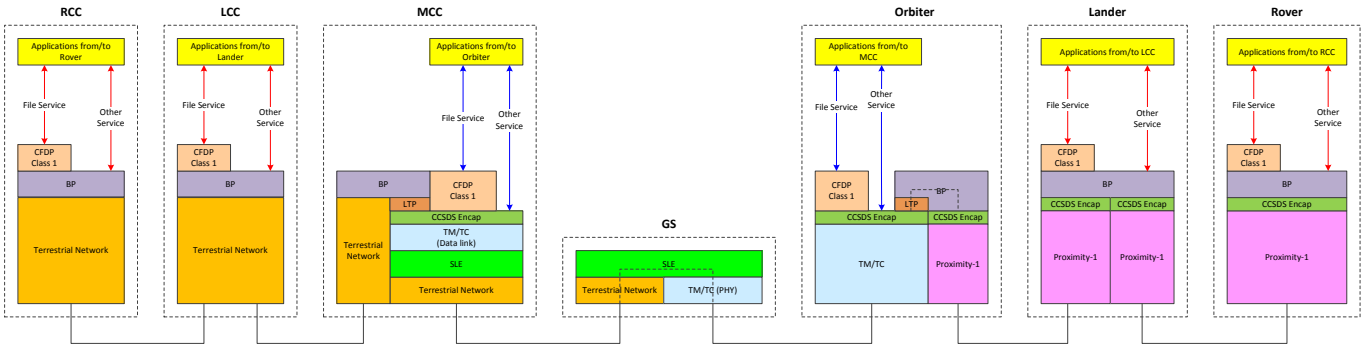

Figure 8. Protocol stacks of DTN communication in second phase

Network Coded Multicast and Multi-unicast over Satellite

Paresh Saxena and M. A. Vázquez-Castro
Dept. of Telecommunications and Systems Engineering.
Universitat Autònoma de Barcelona, Barcelona, Spain
Email: paresh.saxena@uab.es, angeles.vazquez@uab.es

***Abstract*—In this paper, we investigate the use of systematic random network coding (SNC) for multicast and multi-unicast over satellite. In particular, the satellite coverage is over a large geographical area that consists of several users. These users may face different channel conditions and undergo different packet loss rates. In this work, we identify two regions of transmission. The multicast region where all users subscribed to the multicast channel can recover all the data packets and the multi-unicast region where only users with good channel conditions can recover all the data packets but those with bad channel accept transmission losses. For the two regions, we derive theoretically and by simulation the benefits of SNC against state-of-the-art end-to-end coding. Our results show that SNC can achieve up to 26.90% and 24.26% higher maximum achievable rates for multicast and multi-unicast respectively. Further, we show practical architectural and encapsulation feasibility.**

***Index Terms*—Network coding, Multicast, Satellite communication, Achievable rates.**

I. Introduction

SNC [1]-[6] has been studied recently as a practical network coding scheme to increase the achievable rates and reliability of wireless networks. It has been proved that SNC achieves smaller complexity, smaller delay and smaller overhead as compared to previous network coding schemes based on random network coding (RNC) [7] [8]. However, in the current literature, SNC has been investigated mainly in the networks for unicast with a source and a sink connected via several intermediate nodes.

In this paper, we investigate the use of SNC for multicast and multi-unicast over satellite. We identify two regions of transmission, one for multicast and another for multi-unicast with an in-network (re)encoding to increase the achievable rates and the reliability of satellite networks.

We consider a system topology (Figure 1) where a source is connected to all the sinks via an intermediate node. This system topology is a relevant case in satellite systems where there is one intermediate node which could be a gateway (or others) and there can be several sink nodes which are the users distributed in a large geographical area undergoing different packet loss rates. Our theoretical derivations and simulation results on the reliability and the achievable rates show the benefits of network coding with respect to state-of-the-art end-to-end forward erasure codes (FEC) codes like Reed-Solomon (RS) codes for both multicast and multi-unicast.

In this paper, we also explore the benefits of network coding in two different set of layers of a satellite network protocol architecture. These are satellite-independent layers (application, transport and IP layers) and satellite-dependent layers (link and physical layers). In particular, the satellite-independent layers are mainly significant for the application's developer who has access to the data flowing in these layers and the satellite-dependent layers are mainly significant for the system operators. In this paper, first we present the implementation of network coding in the link layer of the satellite systems and second, we focus on the implementation of network coding in the application layer for better internet communication over satellite systems.

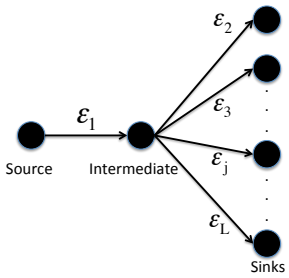

Figure. 1: System model

The rest of the paper is organized as follows. In Section II, we discuss the system model. In Section III, we describe the systematic network coding for multicast and multi-unicast. In Section IV, we present the theoretical analysis and derivation of theoretical expressions for the reliability and the achievable rate. Section V presents the implementation of SNC in the link layer of the protocol stack and Section VI presents the simulation results. In Section VII, we discuss the implementation of SNC in the upper layers of the satellite network protocol stack. Finally, Section VIII concludes this paper.

II. System Model

Consider that a source node has K data packets to send to $L-1$ sink nodes. Each packet is a column vector of length M over a finite field $\mathbb{F}_q$. The set of data packets in matrix notation is $\mathbf{S} = \left[\begin{array}{cccc} \mathbf{s}_1 & \mathbf{s}_2 & . \; . \; . & \mathbf{s}_K \end{array} \right]$, where $\mathbf{s}_t$ is the t^{th} data packet. The source is connected to all the sinks via an intermediate node as shown in Figure 1. All the links are modeled as memoryless erasure channels. There are L links in the network. The erasure probability from the source to the intermediate node is denoted by ϵ_1 and the erasure probability from the intermediate node to the sink node j is denoted by $\epsilon_j, j = 2, .., L$.

We assume there is no feedback from the sinks (or from the intermediate node) due to the inherent large latency of satellite systems. We also assume that packet transmissions occur at discrete time slots such that each node can transmit

 ISBN: 978-1-61208-397-1

one packet per time slot. We will also assume that the coding schemes run for a total of N time slots (N is larger than or equal to K) and every node (except the sinks) transmits a packet in each time slot $t = 1, 2, ..., N$.

III. Systematic network coding for multicast and multi-unicast

A. Encoding at the source node

The SNC encoder sends K data packets in the first K time slots (systematic phase) followed by $N - K$ random linear combinations of data packets in the next $N - K$ time slots (non-systematic phase). Let $\mathbf{X} = \mathbf{SG}$ represent K systematic packets and $N - K$ coded packets transmitted by the SNC encoder during N consecutive time slots. The generator matrix $\mathbf{G} = \begin{bmatrix} \mathbf{I}_K & \mathbf{C} \end{bmatrix}$ consists of the identity matrix $\mathbf{I}_K$ of dimension K and $\mathbf{C} \in \mathbb{F}_q^{K \times N-K}$ with elements chosen randomly from a finite field $\mathbb{F}_q$. The code rate is given by $\rho = \frac{K}{N}$.

B. Re-encoding at the intermediate node

The SNC re-encoder performs re-encoding operations in every time slot and sends N packets to the sink nodes. Let $\mathbf{X}_I = \mathbf{X}\mathbf{D}_1\mathbf{T}$ represent N packets transmitted by the SNC re-encoder during N consecutive time slots where $\mathbf{D}_1 \in \mathbb{F}_q^{N \times N}$ represents erasures from the source node to the intermediate node and $\mathbf{T} \in \mathbb{F}_q^{N \times N}$ represents the re-encoding operations at the intermediate node.

The erasure matrix $\mathbf{D}_1$ is an $N \times N$ diagonal matrix with every diagonal component zero with probability ϵ_1 and one with probability $1 - \epsilon_1$.

The re-encoding matrix $\mathbf{T}$ is modeled as an upper triangular matrix. The non-zero elements of $\mathbf{T}$ are selected as follows. During the systematic phase, if a packet $\mathbf{s}_t$ is lost i.e., $\mathbf{D}_1(t,t) = 0$ then the non-zero elements of the t^{th} column of matrix $\mathbf{T}$ are randomly selected from $\mathbb{F}_q$. This represents that if the systematic packet is lost from the source node to the intermediate node, then the intermediate node transmits a random linear combination of the packets stored in its buffer. If a packet $\mathbf{s}_t$ is not lost, i.e., $\mathbf{D}_1(t,t) = 1$ then the t^{th} column of matrix $\mathbf{T}$ is the same as the t^{th} column of identity matrix $\mathbf{I}_N$. This represents that the intermediate node forwards this systematic packet to the sinks. During the non-systematic phase, the intermediate node sends a random linear combination of the packets stored in its buffer and all the non-zero elements of last $N - K$ columns of $\mathbf{T}$ are chosen randomly from the finite field $\mathbb{F}_q$.

C. Decoding at the sink nodes

Let $\mathbf{Y}_j = \mathbf{X}_I\mathbf{D}_j, j = 2, 3, ..., L$ represents N packets received by the sink node j where $\mathbf{D}_j$ represents erasures from the intermediate node to the sink node j. $\mathbf{D}_j$ is $N \times N$ diagonal matrix of the same type as $\mathbf{D}_1$ but with erasure probability ϵ_j. If the sink node j does not receive any packet in time slot t then the t^{th} column of $\mathbf{Y}_j$ is a zero column.

The overall SNC coding strategy can be expressed using a linear operation channel (LOC) model where the output at the sink node j is $\mathbf{Y}_j = \mathbf{S}\mathbf{G}\mathbf{H}_j$ where $\mathbf{H}_j = \mathbf{D}_1\mathbf{T}\mathbf{D}_j$ represents the transfer matrix from the source to the sink j. We assume that the coding vectors are attached in the packet headers so that the matrix $\mathbf{G}\mathbf{H}_j$ is known at the sink j. However, the overhead, due to the attached coding vectors, is kept low due to the use of systematic coding (coding vectors are not attached with the systematic packets). The decoding is progressive using the Gaussian Jordan algorithm as in [6]. All the K data packets are recovered when K innovative packets are received at the sink j, i.e., $rank(\mathbf{G}\mathbf{H}_j) = K$.

IV. Theoretical Analysis

In this section, we will present the theoretical expressions of the average reliability and the average achievable rate of the considered topology. Let us first define η as the residual erasure rate of any link that could be achieved after the overall coding and decoding operations. The reliability of the link is given by $(1 - \eta)$.

Based on the definitions of the residual erasure rate and the reliability and using the definition of achievable rate from [9], the average achievable rate of the considered topology is given by,

$$R_{av} = \rho\,(1 - \eta_{av}) \tag{1}$$

with,

$$\eta_{av} = \frac{1}{L-1} \sum_{j=2}^{L} [1 - (1 - \eta_1)(1 - \eta_j)] \tag{2}$$

as the average reliability of the considered topology, η_1 is the residual erasure rate from the source node to the intermediate node and η_j is the residual erasure rate from the intermediate node to the sink node j where,

$$\eta_l = \phi_{l1} + \phi_{l2}, l = 1, 2, ..., L \tag{3}$$

The first term represents the residual erasure rate for the case when the correctly received packets are less than K, it is given by,

$$\phi_{l1} = \epsilon_l Pr(A < K - 1) \tag{4}$$

where A is a Binomial random variable, accounting for the Bernoulli nature of the erasures. The second term represents the case of reception of K or more packets but not linearly dependent. It is given by,

$$\phi_{l2} = \epsilon_l Pr(A \geq K - 1) Pr(rank(\mathbf{G}\mathbf{H}_j) < K) \tag{5}$$

Using the results in [10], we obtain the exact expressions of ϕ_{l1} and ϕ_{l2} in (6) and (7), respectively.

V. Implementation in link layer of satellite systems

A. State-of-the-art link layer protocols in satellite systems

The current state-of-the-art link layer protocols in the satellite systems provide efficient encapsulation of network layer (IP) protocol data units (PDUs) over the physical layer

 ISBN: 978-1-61208-397-1

$$\phi_{l1} = \epsilon_l \sum_{i=0}^{K-1} \left(\begin{array}{c} N-1 \\ i \end{array} \right) (1-\epsilon_l)^i \, \epsilon_l^{N-1-i} \tag{6}$$

$$\phi_{l2} = \epsilon_l \sum_{i_1=0}^{K-1} \left(\begin{array}{c} K \\ i_1 \end{array} \right) (1-\epsilon_l)^{i_1} \, \epsilon_l^{K-i_1} \sum_{i_2=K-i_1}^{N-K} \left(\begin{array}{c} N-K \\ i_2 \end{array} \right) (1-\epsilon_l)^{i_2} \, \epsilon_l^{N-K-i_2} \left(1 - \prod_{i_3=0}^{K-i_1-1} \left(1 - q^{i_3-i_2}\right) \right) \tag{7}$$

frames. For example, generic stream encapsulation (GSE) protocol [11] in digital video broadcasting by satellite - second generation (DVB-S2) based systems is used as a link layer protocol to encapsulate network layer IP packets.

The existing link layer forward erasure correction (LL-FEC) frameworks in the satellite systems are mainly based on RS or Raptor codes [12]. However, the main limitation of the existing frameworks is that they operate only in end-to-end fashion and do not utilize the coding opportunities at the intermediate node. In this section, we will present an architectural and encapsulation framework to enable link layer systematic network coding (LL-SNC) at the source and at the intermediate node of the satellite systems.

B. LL-SNC architecture and encapsulation

In Figure 2, we present the complete information flow with LL-SNC architecture and LL-SNC encapsulation where IP packets are transmitted from the source and recovered at the sink. This figure represents the case when there is only one sink in the network. When there are several sinks, the same LL PDUs are transmitted from the intermediate node to all the sink nodes.

At the source, the network layer IP packets are encapsulated into an LL-SNC frame. The LL-SNC frame consists of an application data table (ADT) to store IP PDUs, a network coding data table (NCDT) table to store network coded packets and a coefficient data table (CDT) to store coding coefficients. The data from the LL-SNC frame is then encapsulated into LL PDUs. The LL PDUs are then encapsulated into the physical (PHY) frames.

At the intermediate node, the payload of correctly received LL PDUs is stored in the LL-SNC frame. The IP PDUs are stored in the ADT of the intermediate node. The coded packets and the corresponding coefficients are stored in NCDT and CDT of the intermediate node. When the intermediate node receives LL PDU without error, it sends the LL PDU to the sink node and also stores it in the LL-SNC frame. When the intermediate node receives LL PDU with errors, it discards the LL PDU and generates new coded packet and coding coefficients as explained in Section III. These new coded packets and the corresponding coefficients are stored in NCDT and CDT of the intermediate node.

At the sink node, the correctly received LL PDUs are stored in the LL-SNC frame. The IP PDUs are stored in the ADT of the sink node. The coded packets and the coding coefficients are stored in NCDT and CDT respectively. The progressive decoding is performed and the lost IP PDUs are recovered. These IP PDUs are then passed to the upper layers.

VI. Simulation results

A. Simulation setup

In our simulation setup, we consider realistic satellite transmission scenarios with links having light rainfall (erasure rate of 0.2) and/or heavy rainfall (erasure rate of 0.6) [13]. In each case, we compare LL-SNC with LL-FEC. We assume IP PDUs of length 1500 bytes. Each IP PDU is mapped to a column of the ADTs of consecutive LL-SNC frames. Two LL-SNC frame lengths, $N \in \{50, 256\}$ and several values of code rates are considered for comparison. The size of ADT, i.e., K changes with the code rate. We set the physical layer symbol rate of $B_s = 27.5$ Mbaud/s, $\varsigma = 2$ as the modulation constellation and $r_{phy} = 1/2$ as the physical coding rate such that the bit rate is $B_s \varsigma r_{phy} = 27.5\ Mbps$. The transmission delay is set to be 250 ms. In each case, we average over 1000 experiments for every performance metric. The number of erasures per-frame varies (according to the random erasure rate) between the 1000 experiments.

B. Performance metrics

1) Achievable rates and reliability: The theoretical expressions of the average achievable rate and the average reliability are derived in Section IV. In this section, we will present the simulation results on the average achievable rate and the average reliability. In the results, we also compare the simulation results with the theoretical expressions derived in Section IV.

2) Average delay per-packet: If a packet $\mathbf{s}_t$ is transmitted by the source at time t_j and it is recovered at the sink at time t_r then packet $\mathbf{s}_t$ incurs a delay δ_t where, $\delta_t = t_r - t_j$. For the block of K packets, the average delay per-packet is given as, $\triangle = \frac{\sum_{t=1}^{K} \delta_t}{K}$. Note that the delay is evaluated only for the packets which are recovered at the sink.

C. Results

In Figure 3, we show the results on achievable rates and reliability when there are two sinks in the network. The multicast capacity of the network is limited by one of the links joining the intermediate node to the sink node. We consider the following erasure probabilities: $\epsilon_1 = 0.2$, $\epsilon_2 = 0.2$ and $\epsilon_3 = 0.6$. In Figure 4, we show the results on achievable rates and reliability when there are ten sinks in the network. The multicast capacity of the network is limited by one of the links joining the intermediate node to the sink node. We consider the following erasure probabilities: $\epsilon_1 = 0.2$, $\epsilon_j = 0.2, j = 1, 2, ..., 9$ and $\epsilon_{10} = 0.6$. Furthermore, we present the maximum achievable rates for both multicast and

 ISBN: 978-1-61208-397-1

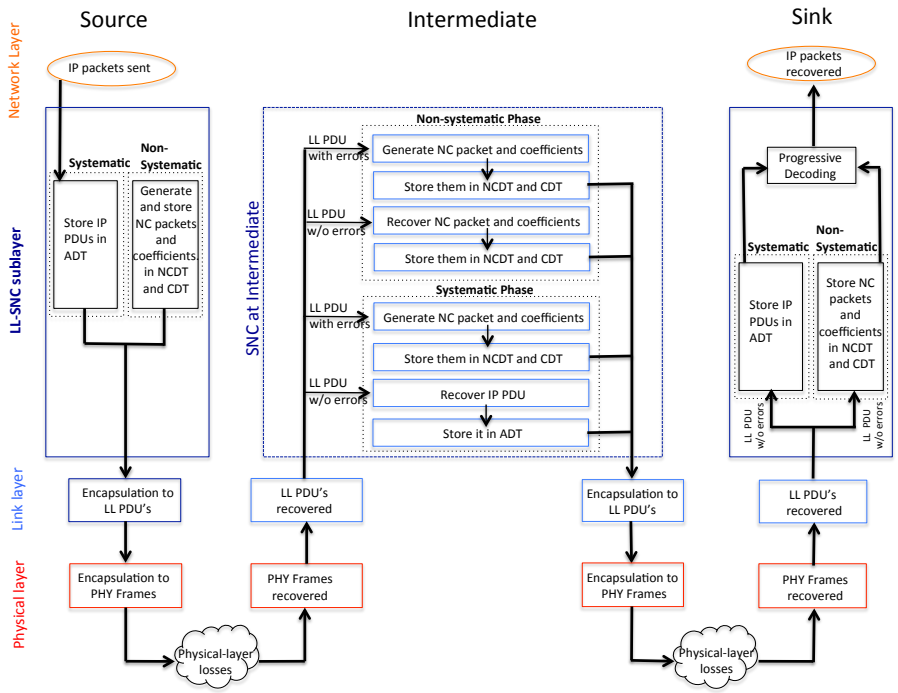

Figure. 2: Flow diagram with LL-SNC architecture and LL-SNC encapsulation in satellite system

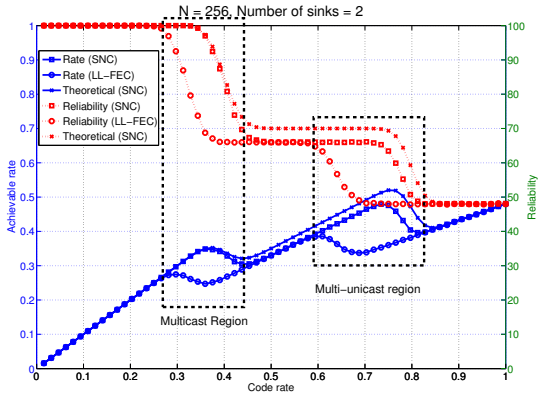

Figure. 3: LL-SNC multicast and multi-unicast region with two sinks

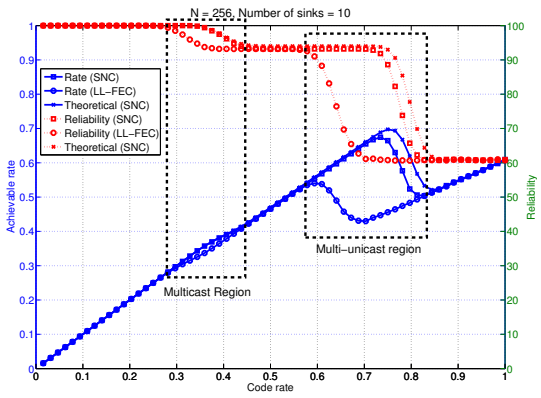

Figure. 4: LL-SNC multicast and multi-unicast region with two sinks

TABLE I: MAXIMUM ACHIEVABLE RATES FOR MUTI-CAST AND MULTI-UNICAST

N	Application	Sinks	LL-SNC	LL-FEC	Gain
256	Multicast	2	0.3486	0.2747	26.90%
256	Multi-unicast	2	0.4794	0.3858	24.26%
256	Multicast	10	0.3575	0.3043	17.48%
256	Multi-unicast	10	0.6745	0.5404	24.81%
50	Multicast	2	0.3035	0.2553	18.88%
50	Multi-unicast	2	0.3852	0.3579	7.63%
50	Multicast	10	0.3107	0.2751	12.94%
50	Multi-unicast	10	0.5406	0.4990	8.34%

multi-unicast in Table I. Following are the key conclusions from these results:

- We have identified two regions in these graphs: one for multicast and the another for multi-unicast (represented by dashed boxes). The region for multicast is corresponding to the case when the average reliability approaches 100%. This would mean that all the sinks in the network are able to recover all the data packets. We have also identified the multi-unicast region where the sinks with better channel recover all the data packets and the sink(s) with bad channel still suffer from some losses. The benefit of multi-unicast over multicast is that one can achieve overall higher transmission rates by not sacrificing the rate due to the bottleneck sink (link with higher erasure rate). Hence, based on the requirements of the users, our results provide optimal usage of available bandwidth for transmission.
- The multicast is feasible only when the code rate is smaller than the capacity of the network which is

 ISBN: 978-1-61208-397-1

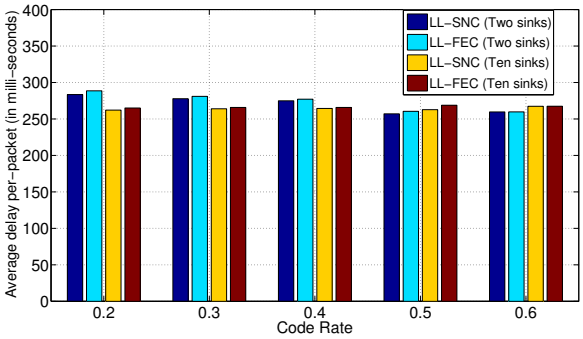

Figure. 5: Average delay per-packet

$\min_j(1-\epsilon_j) = 0.4$. However, when the code rate is higher than the multicast capacity, multi-unicast is feasible. This is because the capacity of the sinks with good channel is different and higher than the capacity of the network (in our example it is 0.8). Therefore, when the code rate is smaller than 0.8, the sinks with good channel can recover all the data packets making multi-unicast feasible.

- LL-SNC provides higher transmission rates and higher reliability than LL-FEC in all the cases. When the number of sink increases, LL-SNC can provide close to 100% reliability in the multi-unicast region itself. This is because there is only one bottleneck link in the network and only one sink suffers from the bad channel. In this case, it would be efficient to transmit in the multi-unicast region such that the higher transmission rates are achieved and almost all the sinks (except the one with the bad channel) are able to recover all the data packets. Furthermore, LL-SNC also provides higher maximum achievable rates than LL-FEC for both multicast and multi-unicast. The maximum achievable rate increases as the frame length increases or the number of sinks increases. Our results (Table I) show that LL-SNC can achieve up to 26.90% and 24.26% higher maximum achievable rates than LL-FEC for multicast and multi-unicast respectively.

In Figure 5, our simulation results also show that LL-SNC provides smaller average delay per-packet than LL-FEC. This is because of the following two reasons. First, the progressive decoding in LL-SNC allows the sinks to start decoding and recovering as soon as it receives the first packet. Second, the re-encoding in LL-SNC helps the sink to receive K degrees of freedom and complete the decoding process in fewer time slots than LL-FEC. The overall delay includes the inherent transmission delay of 250 ms of the satellite systems.

VII. Network coding in satellite independent layers

In the previous sections, we have focussed on the application of the network coding in the satellite-dependent layers, specifically in the link layer of the satellite systems. However, the use of network coding is not limited only to the satellite-dependent layers, the same network coding framework can be used in the satellite-independent layers to guarantee reliability. In this section, we will focus on the protection of application layer data units (ADUs) for better and efficient internet communication in the satellite systems.

In the previous sections, we have shown the benefits of LL-SNC to protect network layer IP packets in the lower layers of the protocol stack. Similarly, SNC can be used to protect ADUs in the upper layers of the protocol stack. The encapsulation process is one of the main factors influencing the efficient implementation of network coding in the networking protocol stack. In this section, we outline two encapsulation processes which can be used for the network coding implementation to protect ADUs for reliable internet communication.

The first encapsulation process (encapsulation process A) is shown in the Figure 6a. This way of encapsulation was used for the protection of ADUs using RS coding [14] over real-time transport protocol (RTP). In Figure 6a, we present the modified encapsulation process to be used for the network coding. A source block (ADT) consists of K ADUs in K columns. The number of rows in the source block is $M = E + 2$ where E is the length of the largest ADU. The columns, which do not have the largest ADU, are filled with zeros to be completely filled. Each column can be considered as a data packet. The first two bytes of each column in the source block contain the length of the corresponding ADU. ADUs are then encapsulated into RTP packets. The first two bytes and the zero paddings are not sent over the network. The FEC block (NCDT) contains $N-K$ columns with $N-K$ coded packets and the coefficient block (CDT) contains $N-K$ columns with $N-K$ set of coding coefficients. FEC packets and coefficients are then encapsulated into RTP packets. Each RTP packet contains RTP payload, RTP header and FEC payload ID. This FEC payload ID is used for signaling the coding parameters like source block ID, FEC packet ID, values of K and N etc. The CRC-32 is added with every RTP packet to detect errors in RTP packets at the receiving end. At the receiver, the values of coding parameters are extracted from the FEC payload ID. Now, if ADUs are lost then the complete columns are lost. So, if FEC decoding succeeds, the receiver recovers ADUs by filling the erased columns. The initial two bytes are used to remove zero padding from the data packets to recover the ADUs.

The second encapsulation process (encapsulation process B) is shown in the Figure 6b. This way of encapsulation was used for the protection of IP packets using RS coding over GSE [12]. In Figure 6b, we present the modified encapsulation process to be used for the network coding to protect ADUs. A source block (ADT) consists of K columns and stores ADUs. Now, ADUs are arranged column wise starting from the upper left corner. If an ADU does not fit in one column, it continues at the top of the following column and so on. If the ADT is not completely filled then the zero-padding bytes are inserted in last column to fill it completely. Each ADU is then encapsulated in a single or multiple RTP packets. The FEC block (NCDT) contains $N-K$ columns with $N-K$ coded packets and the coefficient block (CDT) contains $N-K$ columns with $N-K$ set of coding coefficients. Each coded packet from NCDT and the corresponding coding coefficients from CDT are encapsulated in one RTP packet. The first K bytes of RTP payload contain K coding coefficients followed

 ISBN: 978-1-61208-397-1

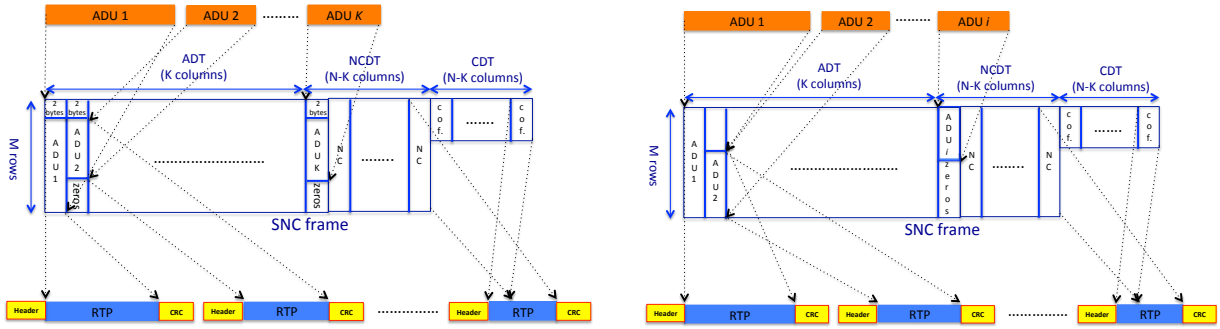

(a) Encapsulation process A

(b) Encapsulation process B

Figure. 6: The two encapsulation processes for encapsulation of application layer data units over RTP

by the corresponding NCDT column. The value of K is signaled through the RTP header of the RTP packet. Finally, the CRC-32 is added with every RTP packet to detect errors in RTP packets at the receiving end. Now, if an ADU is lost, then the corresponding part of the column or the complete column is also lost. The progressive decoding is performed and lost columns (or lost part of columns) in ADT are filled with the recovered data. The implementation efficiency of the encapsulation process based on the overhead due to headers, payload ID's, etc. Both of the above encapsulation processes inlcude filling of data tables in different ways. Specifically, the encapsulation process B does not include adding of zero bytes for each unfilled column. Therefore, the overhead due to the extra padding bytes could be reduced and higher throughput could be achieved by using encapsulation process B for network coding implementation.

VIII. Conclusions

In this paper, we have focussed on the use of SNC for multicast and multi-unicast over satellite. We have identified the transmission regions for multicast and multi-unicast over satellite by characterizing the reliability and achievable rates offered by SNC in these two different regions. We have derived the theoretical expressions for the average reliability and the average achievable rate of the considered topology. Our theoretical and simulation analysis present the benefits of SNC over end-to-end coding for both multicast and multi-unicast. Our results have shown that a higher rate is achievable for the multi-unicast however not all the users in multi-unicast can recover all the data packets. Therefore, based on the requirements from different users, the transmission region can be chosen for the optimal usage of available bandwidth. Finally, we have explored the benefits of network coding at different layers of the satellite network protocol stack. We have shown the encapsulation and architecture feasibility of network coding application in the satellite-dependent layers and we have proposed two encapsulation processes for the network coding application in the satellite-independent layers. Future work includes the investigation of SNC on more complex networks such as network with multiple sources. Furthermore, the implementation efficiency of the two proposed encapsulation processes should be compared numerically using realistic values of coding parameters, packet sizes, etc for different standards.

References

[1] J. Heide, M. Pedersen, F. H. P. Fitzek, and T. Larsen, "Network coding for mobile devices - systematic binary random rateless codes," in Communications Workshops, 2009. ICC Workshops 2009. IEEE International Conference on, June 2009, pp. 1–6.

[2] Y. Li, P. Vingelmann, M. Pedersen, and E. Soljanin, "Round-robin streaming with generations," in Network Coding (NetCod), 2012 International Symposium on, June 2012, pp. 143–148.

[3] B. Shrader and N. Jones, "Systematic wireless network coding," in Military Communications Conference, 2009. MILCOM 2009. IEEE, Oct 2009, pp. 1–7.

[4] D. Vukobratovic, C. Khirallah, V. Stankovic, and J. Thompson, "Random network coding for multimedia delivery services in LTE/LTE-Advanced," Multimedia, IEEE Transactions on, vol. 16, Jan 2014, pp. 277–282.

[5] S. Teerapittayanon et al., "Network Coding as a WiMAX Link Reliability Mechanism," in Multiple Access Communications, vol. 7642 of Lecture Notes in Computer Science, , Springer Berlin Heidelberg, 2012, pp. 1–12.

[6] P. Saxena and M. A. Vázquez-Castro, "Network coding advantage over MDS codes for multimedia transmission via erasure satellite channels," in lecture notes of the institute for computer sciences, social informatics and telecommunications engineering, (Springer 2013), Volume 123, 2013, pp. 199-210.

[7] T. Ho et al., "A random linear network coding approach to multicast," Information Theory, IEEE Transactions on, vol. 52, no. 10, 2006, pp. 4413– 4430.

[8] D. S. Lun, M. Medard, R. Koetter, and M. Effros,"On coding for reliable communication over packet networks," Physical Communication, vol. 1, no. 1, 2008, pp. 3 – 20.

[9] S. Yang and R. Yeung, "Coding for a network coded fountain," in Information Theory Proceedings (ISIT), 2011 IEEE International Symposium on, July 2011, pp. 2647–2651.

[10] O. Trullols-Cruces, J. Barcelo-Ordinas, and M. Fiore, "Exact decoding probability under random linear network coding," IEEE communications letters, vol. 15, Jan 2011, pp. 67–69.

[11] "ETSI TS 102 606 V1.1.1, Digital Video Broadcasting (DVB); Generic Stream Encapsulation (GSE) Protocol," 2007.

[12] "DVB BlueBook a155-2, Digital Video Broadcasting (DVB); Second Generation DVB Interactive Satellite System (DVB-RCS2); Part 2: Lower Layers for Satellite standard," 2013.

[13] F. de Belleville, L. Dairaine, J. Lacan, and C. Fraboul, "Reliable multicast transport by satellite: A hybrid satellite/terrestrial solution with erasure codes," in High Speed Networks and Multimedia Communications, vol. 3079, Springer Berlin Heidelberg, 2004, pp. 436–445.

[14] S.Galanos, O.Peck, and V.Roca, "RTP payload format for Reed Solomon FEC," Internet-Draft, March 14, 2011.

 ISBN: 978-1-61208-397-1

Terrestrial to Satellite Communications Using Multi-antenna Relays Nodes

Styliani Fassoi*, Dimitrios Christopoulos†, Symeon Chatzinotas†,
Emmanouel T. Michailidis*, Athanasios G. Kanatas* and Bjorn Ottersten†
* Department of Digital Systems, Telecommunication Systems Laboratory,University of Piraeus, Piraeus, Greece
Email: {sfassoi, emichail, kanatas}@unipi.gr
† Interdisciplinary Centre for Security, Reliability and Trust (SnT), University of Luxemburg, Luxemburg
Email: {dimitrios.christopoulos, Symeon.Chatzinotas, bjorn.ottersten}@uni.lu

***Abstract*—Satellite communications and relaying techniques have been receiving the attention of the research community over the last years. This paper proposes a terrestrial to satellite communication system aided by terrestrial relay nodes to facilitate a robust, reliable, and efficient communication link and improve the spectral efficiency. In particular, this paper concentrates on evaluating the spectral efficiency and bit error rate (BER) performance of terrestrial to satellite multiple-input multiple-output (MIMO) amplify and forward (AF) relay links. Zero Forcing (ZF) and Minimum Mean Square Error (MMSE) multi-antenna decoding techniques are employed, which have been well established in terrestrial wireless communications. Numerical results are provided to quantify the performance gain of the proposed communication system.**

Keywords–Amplify and forward (AF) relaying; Loo distribution; minimum mean square error (MMSE; multiple-input multiple output (MIMO) techniques; satellite communications; Zero Forcing (ZF).

I. INTRODUCTION

The satellite communications play a crucial role in wireless and mobile communications [1] [2]. There are many practical cases where the terrestrial communications are not able to provide a link between the communicated parties due to troublesome propagation conditions or extremely high link distance. Satellite communications are able to overcome these constraints and provide a reliable wireless link to the communicated parties. In order to improve system capacity and link reliability, Multiple-Input Multiple-Output (MIMO) technology is the dominant candidate for both terrestrial [3]–[8] and satellite [9]–[11] use. However, multiple antenna systems are not directly applicable to the satellites due to some special features of such communication systems. The key concept of MIMO technology is to take the advantage of multipath components of the propagation channel which produce multiple uncorrelated channels at the destination. So, in order to achieve uncorrelated channels there is a constraint regarding the inter-element distance at both the transmitter and receiver antennas. The propagation channel between the satellite and the earth station is characterized by its high propagation loss and the small number of existing scatterers. Therefore, so as to achieve uncorrelated channels, the desired inter-element distance is increased. Satellites refrain thousands of kilometers from the earth and there is no power supply apart from the solar power and the stored batteries energy and therefore, the multiple Radio-Frequency (RF) chains could reduce the life of a satellite.

Since there is not enough space to place many antenna elements in the satellites, additional techniques were investigated to maximize the capacity and reliability gain. Initially, polarization techniques were proposed in order to maximize the available MIMO channels using co-located antennas. However, the terrestrial to satellite communications may benefit from some new emerging technologies. Wireless relay systems [12] [13] are widely adopted in the new wireless standards of 4G and beyond. The role of a relay varies from scenario to scenario, depending on the needs and the specifications of the communication. The use of relay nodes may assist to the coverage extension, link reliability and/or capacity improvement. The most usual and well-defined types of relay modes are the Amplify and Forward (AF) and the Decode and Forward (DF) modes. In the first case the relay is a conventional repeater which just amplifies the received signal and forwards it to the destination. In the second mode, the relay has an active role being able to decode the received signal, perform baseband signal processing and retransmit the signal to the final destination. Despite the fact that relay systems are able to offer more degrees of freedom, their adoption in satellite communications is not duly considered.

In this paper, we present a novel system model for terrestrial to satellite communications with the combination of terrestrial relay systems and MIMO technology [14]–[17]. The performance evaluation and the benefits of such a system are analytically described. The main purpose of this paper is to determine the advantages of the aforementioned technologies in as more realistic scenarios as possible. For that reason, we modeled the terrestrial to satellite wireless channel using the Loo distribution [18] which describes in the most effective way the space conditions. In addition, we used the widely adopted Rician or Rayleigh distribution in order to model the terrestrial channel and some practical detection schemes to the receiver. The rest of the paper is organized as follows: in Section II, we present the system model, while in Section III, we analyze all the detected schemes applied in the model. The main results of the paper are presented in Section IV, where the advantages of such a system are analytically discussed. Finally, in Section V, we conclude the paper.

II. SYSTEM MODEL

We consider an AF, single user MIMO system with multiple full-duplex relays. A system model is given in Figure 1.

The system comprises R intermediate relay nodes which lie between source and destination nodes that have N_t and N_r antennas respectively. Each relay node has M_r transmit/receive antennas (assuming that $M_r = M_t$). The source node transmits

 ISBN: 978-1-61208-397-1

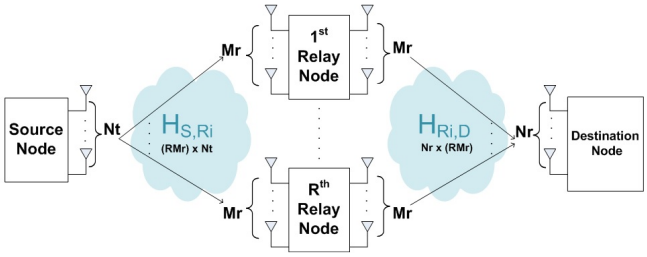

Figure 1. System Model

to the relay nodes and the relay nodes amplify and forward their received signals to the destination. In the described model, we focus in the uplink communication where the connection between source and relay nodes illustrate the terrestrial link, while the communication link between relay nodes and destination represents the satellite link. The destination node is represented by a satellite. The $(M_r R) \times 1$ received signal at the relays is given by

$$\mathbf{y}_{R_i} = \mathbf{H}_{S,R_i}\mathbf{x} + \mathbf{n}_{R_i}. \tag{1}$$

The matrix $\mathbf{H}_{S,R_i}$ is the $(M_r R) \times N_t$ source-relays channel matrix which is presented analytically in Section IV-A. The quantity $\mathbf{n}_{R_i}$ is a vector of zero mean additive white Gaussian noise with the same dimensions as the corresponding received signal. $\mathbf{x}$ is the $N_t \times 1$ input data vector.

The $N_r \times 1$ received signal at the destination from the relays is given by

$$\mathbf{y}_D = \mathrm{a}\mathbf{H}_{R_i,D}\mathbf{y}_{R_i} + \mathbf{n}_D, \tag{2}$$

where a is the amplification factor with constant values, the matrix $\mathbf{H}_{R_i,D}$ is the $N_r \times (M_r R)$ channel matrix which is analytically described in Section IV-B, $\mathbf{y}_{S,R_i}$ is the received signal at the relays and $\mathbf{n}_D$ is a vector of zero mean additive white Gaussian noise with the same dimensions as the corresponding received signal.

Using (1) in (2):

$$\begin{aligned}\mathbf{y}_D &= \mathrm{a}\mathbf{H}_{R_i,D}\mathbf{y}_{R_i} + \mathbf{n}_D \\ &= \mathrm{a}\mathbf{H}_{R_i,D}\left(\mathbf{H}_{S,R_i}\mathbf{x} + \mathbf{n}_{R_i}\right) + \mathbf{n}_D \\ &= \mathrm{a}\mathbf{H}_{R_i,D}\mathbf{H}_{S,R_i}\mathbf{x} + \mathbf{H}_{R_i,D}\mathrm{a}\mathbf{n}_{R_i} + \mathbf{n}_D.\end{aligned} \tag{3}$$

So, the received signal at the destination will be:

$$\mathbf{y}_D = \mathbf{H}\mathbf{x} + \mathbf{n} \tag{4}$$

where $\mathbf{H} = \mathrm{a}\mathbf{H}_{R_i,D}\mathbf{H}_{S,R_i}$ and $\mathbf{n} = \mathrm{a}\mathbf{H}_{R_i,D}\mathrm{a}\mathbf{n}_{R_i} + \mathbf{n}_D$.

The overall end-to-end received signal-to-noise-ratio (SNR) at each destination receiver antenna element γ is given by [19]–[22]

$$\gamma = \frac{\gamma_1\gamma_2}{\gamma_1 + \gamma_2 + 1} \tag{5}$$

,

where $\gamma_j = |\mathbf{H}_j|^2 \Big/ N_0$, $j = 1, 2$ represents the per-hop received SNR.

III. Signal detection schemes

In the following, we are going to use linear detection schemes. To detect the signals from each antenna element, the estimated symbols derive by applying a weight matrix $\mathbf{W}$ to the channel matrix in order to invert its effect [23] :

$$\tilde{\mathbf{x}} = [\tilde{x}_1\ \tilde{x}_2\ \ldots\ \tilde{x}_{N_t}]^T = \mathbf{W}\mathbf{y}_D. \tag{6}$$

The standard linear detection methods include the well-defined techniques of the Zero-Forcing (ZF) and the Minimum Mean Square Error (MMSE) techniques. The weight matrix of the zero-forcing technique for $N_r \geq N_t$ is given by:

$$\mathbf{W}_{ZF} = \left(\mathbf{H}^H\mathbf{H}\right)^{-1}\mathbf{H}^H, \tag{7}$$

where $(\cdot)^H$ is the Hermitian transpose operation. So, the estimated result will be:

$$\begin{aligned}\tilde{\mathbf{x}}_{ZF} &= \mathbf{W}_{ZF}\mathbf{y}_D \\ &= \left(\mathbf{H}^H\mathbf{H}\right)^{-1}\mathbf{H}^H\left(\mathbf{H}\mathbf{x} + \mathbf{n}\right) \\ &= \mathbf{x} + \left(\mathbf{H}^H\mathbf{H}\right)^{-1}\mathbf{H}^H\mathbf{n}.\end{aligned} \tag{8}$$

In order to maximize the post-detection Signal to Interference plus Noise Ratio (SINR), the MMSE weight matrix for $N_r \geq N_t$ is given as:

$$\mathbf{W}_{MMSE} = \left(\mathbf{H}^H\mathbf{H} + \sigma^2\mathbf{I}\right)^{-1}\mathbf{H}^H. \tag{9}$$

As we can see the MMSE receiver uses the statistical information of noise σ^2 . Using the MMSE weight matrix in (6), we have the following relationship:

$$\begin{aligned}\tilde{\mathbf{x}}_{MMSE} &= \mathbf{W}_{MMSE}\mathbf{y}_D \\ &= \left(\mathbf{H}^H\mathbf{H} + \sigma^2\mathbf{I}\right)^{-1}\mathbf{H}^H\left(\mathbf{H}\mathbf{x} + \mathbf{n}\right) \\ &= \mathbf{x} + \left(\mathbf{H}^H\mathbf{H} + \sigma^2\mathbf{I}\right)^{-1}\mathbf{H}^H\mathbf{n}.\end{aligned} \tag{10}$$

In order to improve the performance of linear detection techniques, the ordered Successive Interference Cancellation (SIC) was initially proposed in [24] [25]. In this technique, the receiver estimates the first symbol, using a linear detector (i.e., ZF, MMSE). More specifically, the best transmitted signal is determined using the minimum norm, as long as its weight vector resulting from the transformed channel matrix depending on the reception technique. So, for the SIC-ZF technique the effect based on (8) will be:

$$\tilde{\mathbf{x}}_{SIC-ZF} = \mathbf{W}_{ZF}\tilde{\mathbf{y}}_i, \tag{11}$$

where $\tilde{\mathbf{y}}_i = \mathbf{y}_D - h_i\tilde{\mathbf{x}}_{ZF}$ for the i^{th} stream estimation.

 ISBN: 978-1-61208-397-1

Likewise for the SIC-MMSE technique will be:

$$\tilde{\mathbf{x}}_{SIC-MMSE} = \mathbf{W}_{MMSE}\tilde{\mathbf{y}}_i, \quad (12)$$

where $\tilde{\mathbf{y}}_i = \mathbf{y}_D - h_i\tilde{\mathbf{x}}_{MMSE}$ for the i^{th} stream estimation.

IV. Performance Evaluation

This Section is based on the system model which is described in Section II. More specifically, we focus in the next two scenarios. In the first scenario, as illustrated in Figure 2, we use a single relay MIMO system with two transmit, receive and relay antennas.

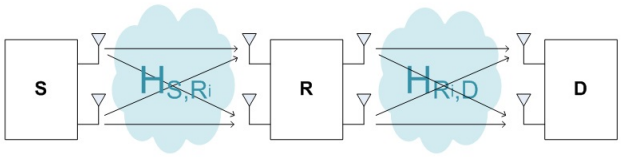

Figure 2. First Scenario

The second scenario, presented in Figure 3, demonstrates the case with two synchronized relay nodes equipped with a single antenna each one, in contrast to the first one that there is only one relay with two antenna elements.

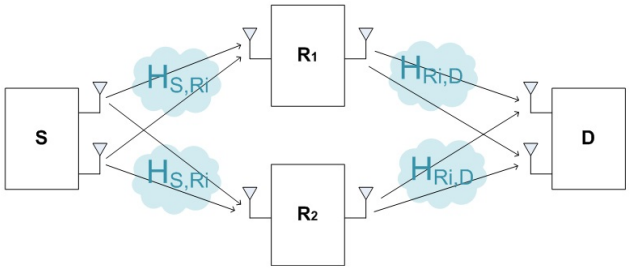

Figure 3. Second Scenario

We will demonstrate the performance of the proposed MIMO architecture in terms of bit error rate (BER) and systems capacity. In order to retrieve more realistic results, a lot of attention was paid on the appropriate wireless propagation channel model selection due to the particular properties of satellite communications.

A. Terrestrial Wireless Channel

The adopted scenarios, previously described, consist of terrestrial and satellite transceivers which consequently lead to two different propagation channel environments. The terrestrial wireless channel is mostly characterized by the existing scatterers which produce multiple signal components. This environment within a simulation study could be emulated using the Rician distribution as [26]:

$$\mathbf{H}_{S,R_i} = \sqrt{\frac{K}{K+1}}\bar{\mathbf{H}}_{S,R_i} + \sqrt{\frac{1}{K+1}}\tilde{\mathbf{H}}_{S,R_i}, \quad (13)$$

where K is the Rician factor, $\bar{\mathbf{H}}$ is a deterministic unit rank matrix which represent the direct component and $\tilde{\mathbf{H}}$ is the channel matrix of the multipath components. Most of work done so far in MIMO performance evaluation is based on the assumption that the involved parties communicate in a rich scattering environment. This means that there is no Line-of-sight (LOS) component and so the gain of MIMO is maximized due to the uncorrelated channel in the input of the multiple antenna elements. This ideal environment for the MIMO performance is totally described using the Rayleigh distribution, resulting from the Rician distribution by applying a zero K factor due to the no existence of a LOS component.

B. Satellite Wireless Channel

For the link between the land mobile and the satellite we have to use a statistical model being able to take into account all the propagation channels characteristics. A well-defined model developed for that case is the Loo distribution [18]. The channel matrix $\mathbf{H}$ of the satellite link using the Loo distribution for the envelope h_{ij} is then given by [18]

$$\mathbf{H}_{R_i,D} = [h_{ij}] = [\bar{h}_{ij}] + [\tilde{h}_{ij}] = \bar{\mathbf{H}}_{R_i,D} + \tilde{\mathbf{H}}_{R_i,D}, \quad (14)$$

where

$$\begin{aligned} h_{ij} &= |h_{ij}| \exp(j\varphi_{i,j}) \\ &= \left|\bar{h}_{ij}\right| \exp(j\bar{\varphi}_{i,j}) + \left|\tilde{h}_{ij}\right| \exp(j\tilde{\varphi}_{i,j}), \end{aligned} \quad (15)$$

and $\bar{\phi}_{ij}$, $\widetilde{\phi}_{ij}$ are uniformly distributed over $[0, 2\pi]$.

The first factor represents the Lognormal fading while the second one describes the Rayleigh fading. Therefore, the Loo distribution as extracted from the previous equation is the superposition of the lognormal distribution to model the large-scale fading and Rayleigh distribution for the modeling of small-scale fading. So, the Loo probability density function is given by

$$\begin{aligned} p(|h_{ij}|) = &\frac{|h_{ij}|}{b_0\sqrt{2\pi\sigma^2}} \times \\ &\int_0^\infty \frac{1}{\bar{h}_{ij}} \exp\left[-\frac{\left(\ln \bar{h}_{ij} - \mu\right)^2}{2\sigma^2} - \frac{|h_{ij}|^2 + \bar{h}_{ij}^2}{2b_0}\right] \\ &I_0\left(\frac{|h_{ij}|\,\bar{h}_{ij}}{b_0}\right) d\bar{h}_{ij} \end{aligned} \quad (16)$$

where b_0 is the average scattered power resulting from the multipath components while σ and μ are the standard deviation and mean respectively and finally $I_0(\cdot)$ is the zero order modified Bessel function of the first kind.

In Figure 4, the different terrestrial channel distributions are compared in terms of bit error rate. Both of them use the same parameters, $N_t = N_r = 2$ and $R = 1$ with $M_r = 2$ in the ZF signal detection. As expected similar to the terrestrial links [27] the Rician is worse than Rayleigh in this detection scheme.

 ISBN: 978-1-61208-397-1

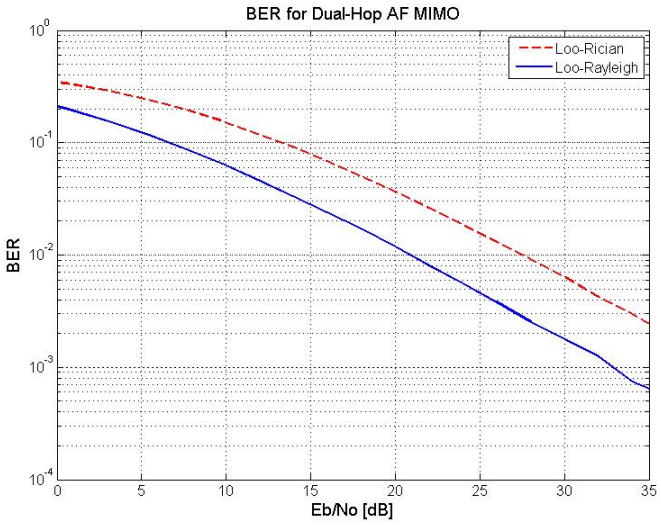

Figure 4. Comparison of terrestrial channel with Rician and Rayleigh distribution ($\gamma_2 = 2\gamma_1$)

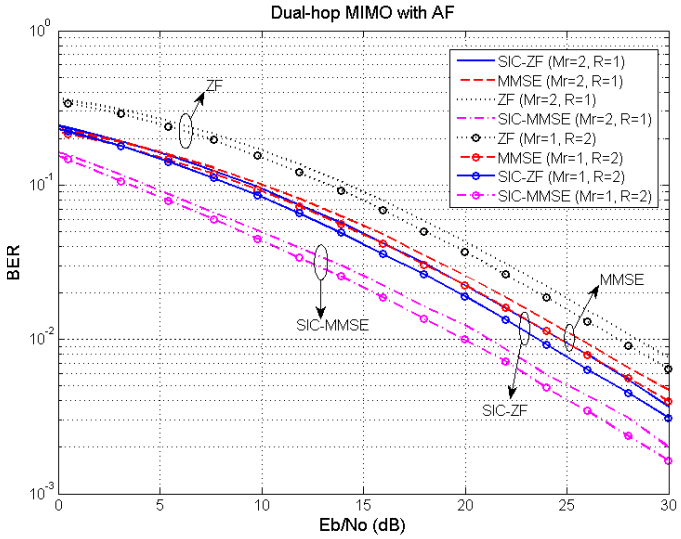

Figure 5. End-to-end BER performance($\gamma_2 = 2\gamma_1$)

C. BER Results

The main scope within this work is to define the performance of land to satellite communication using relay nodes. As previously analyzed, in order to model the terrestrial link between the transmitter and the relay station, Rician distribution is applied with different K factors in order to achieve a realistic simulation environment. The only difference between the two scenarios described in Section II is the number of antenna elements in the relay stations. In our first scenario as illustrated in Figure 2, transmitter, receiver and one relay station are equipped with two antennas each one and Rician factor $K = 10dB$, while in the second scenario depicted in Figure 3, two relays are used with one antenna each one and Rician factor 8dB and 10dB, respectively. In any case, the signal reaches the destination through the relay/relays station/stations. In Figure 5, we present the end-to-end BER performance for quadrature phase-shift keying (QPSK) modulation which is crucial for all the wireless systems and especially the satellite communications which are sensitive to data loss due to the limited resources.

As expected the best signal detection is achieved with the SIC-MMSE while the worst with the ZF for both scenarios. In addition, when the case with more single-antenna relays outperforms the case where a single relay is adopted with more antenna elements. Whereas, one would expect the same bit error rate results for both scenarios, there is a difference around 1-1.5 dB, due to different Rician factor in the channel distribution when more than one relay are used.

D. Capacity Results

The ergodic capacity (bits/sec/Hz) of the AF MIMO dual-hop system described above can be written [28]:

$$C(\gamma) = E\{\log_2 \det(\mathbf{I}_{N_t} + \gamma \mathbf{H}\mathbf{H}^H \mathbf{R}_n^{-1})\}, \qquad (17)$$

where $\mathbf{R}_n$ matrix is also given by :

$$\mathbf{R}_n = \mathbf{I}_{Nr} + \mathrm{a}\mathbf{H}_{R_i,D}\mathbf{H}_{R_i,D}^H, \qquad (18)$$

where a is the constant value of amplification factor. In our system model, we consider an M-ary Phase Shift Keying (M-PSK) , AF, multirelay MIMO system with full-duplex relays. Whereas, in a more realistic scenario, the capacity of a channel in a MIMO system using Linear Detector (LD) can be written as:

$$C_{LD} = \sum_{i=1}^{k} \log_2 (1 + SINR_k), \qquad (19)$$

where $SINR_k$ for each receiver is different. The SINR for the MMSE receiver in MIMO wireless communications on the $k-th$ spatial stream can be expressed as [29]–[34]:

$$SINR_k^{MMSE} = \frac{1}{\left[\left(\mathbf{I}_{Nt} + SNR\mathbf{H}^H(\mathbf{R}_n)^{-1}\mathbf{H}\right)^{-1}\right]_{kk}} - 1, \qquad (20)$$

where $\mathbf{I}$ is a $N_t \times N_t$ identity matrix and $\mathbf{H}^H$ is the Hermitian transpose of $\mathbf{H}$. The SINR for the ZF receiver, denoted by $SINR_k^{ZF}$, which conditional on $\mathbf{H}$, can be expressed as [32] [35]:

$$SINR_k^{ZF} = \frac{SNR}{\left[\left(\mathbf{H}^H(\mathbf{R}_n)^{-1}\mathbf{H}\right)^{-1}\right]_{kk}}. \qquad (21)$$

So, Figure 6, illustrates the system capacity the case of MMSE and ZF receiver for the two different scenarios, as well as the ideal MIMO capacity.

Similarly to Figure 5, we observe that the best signal detection scheme is the MMSE scheme, while ZF is the one with the poorest performance. Moreover, the achievable

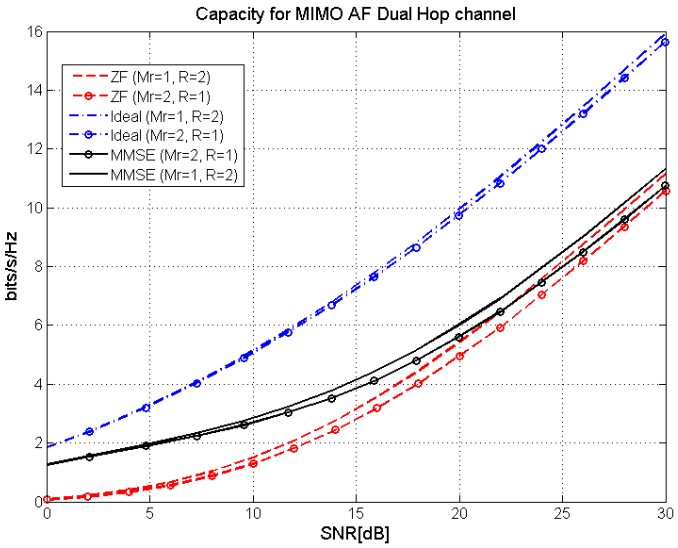

Figure 6. System capacity ($\gamma_2 = 2\gamma_1$)

capacity in all detection schemes of the second scenario is slightly better than in the cases of first scenario.

V. Conclusion

In this paper, we have investigated the benefits of MIMO terrestrial to satellite communication using relay nodes. Multiple simulations have been performed in order to evaluate the system in different scenarios by adopting and applying well-known techniques already applied in terrestrial communications. The results show the gain in the bit error rate performance as well as the gain in the achievable capacity by applying different detection schemes in different environment conditions. So, such a communication seems quite promising for the future wireless networks in order to establish a reliable communication even in difficult terrains and/or high distances.

Acknowledgment

This work has been co-financed by the European Union (European Social Fund - ESF) and Greek national funds through the Operational Program Education and Lifelong Learning of the National Strategic Reference Framework (NSRF) - Research Funding Program THALES MIMOSA (MIS: 380041). Investing in knowledge society through the European Social Fund. This work was also supported by the National Research Fund, Luxembourg under the project "CO^{2}SAT: Cooperative & Cognitive Architectures for Satellite Networks".

References

[1] P. Arapoglou, K. Liolis, M. Bertinelli, A. Panagopoulos, P. Cottis, and R. De Gaudenzi, "Mimo over satellite: A review," Communications Surveys Tutorials, IEEE, vol. 13, no. 1, 2011, pp. 27–51.

[2] D. Bem, T. Wieckowski, and R. Zielinski, "Broadband satellite systems," Communications Surveys Tutorials, IEEE, vol. 3, no. 1, 2000, pp. 2–15.

[3] A. Paulraj, D. Gore, R. Nabar, and H. Bolcskei, "An overview of mimo communications - a key to gigabit wireless," Proceedings of the IEEE, vol. 92, no. 2, 2004, pp. 198–218.

[4] A. Paulraj, R. Nabar, and D. Gore, Introduction to Space-Time Wireless Communications, 1st ed. The Pitt Building, Trumpington Street, Cambridge, United Kingdom: Cambridge University Press, 2003.

[5] E. Biglieri, R. Calderbank, A. Constantinides, A. Goldsmith, A. Paulraj, and H. V. Poor, MIMO Wireless Communications, 1st ed. The Pitt Building, Trumpington Street, Cambridge, United Kingdom: Cambridge University Press, 2007.

[6] D. Gesbert, M. Shafi, D. shan Shiu, P. Smith, and A. Naguib, "From theory to practice: an overview of mimo space-time coded wireless systems," Selected Areas in Communications, IEEE Journal on, vol. 21, no. 3, 2003, pp. 281–302.

[7] D. Gesbert, M. Kountouris, R. Heath, C.-B. Chae, and T. Salzer, "Shifting the mimo paradigm," Signal Processing Magazine, IEEE, vol. 24, no. 5, 2007, pp. 36–46.

[8] J. Mietzner, R. Schober, L. Lampe, W. Gerstacker, and P. Hoeher, "Multiple-antenna techniques for wireless communications - a comprehensive literature survey," Communications Surveys Tutorials, IEEE, vol. 11, no. 2, 2009, pp. 87–105.

[9] ESA Contract No. 18070/04/NL/US, "Novel intra-system interference mitigation techniques and technologies for next generations broadband satellite systems," 2005.

[10] ESA Contract No. AO/1-5146/06/NL/JD, "Mimo applicability to satellite networks," 2007.

[11] ESA Contract No. 21591/08/NL/AT, "Mimo technology in satellite communications for interference exploitation and capacity enhancement," 2008.

[12] X. Tao, X. Xu, and Q. Cui, "An overview of cooperative communications," Communications Magazine, IEEE, vol. 50, no. 6, 2012, pp. 65–71.

[13] C.-X. Wang, X. Hong, X. Ge, X. Cheng, G. Zhang, and J. Thompson, "Cooperative mimo channel models: A survey," Communications Magazine, IEEE, vol. 48, no. 2, 2010, pp. 80–87.

[14] A. Vanelli-Coralli et al., "Satellite communications: Research trends and open issues," in Satellite and Space Communications, 2007. IWSSC '07. International Workshop on, 2007, pp. 71–75.

[15] B. Paillassa, B. Escrig, M.-L. Dhaou, R.and Boucheret, and C. Bes, "Improving satellite services with cooperative communications," International Journal of Satellite Communications and Networking, vol. 29, no. 6, 2011, pp. 479–500.

[16] Y. Labrador, M. Karimi, D. Pan, and J. Miller, "An approach to cooperative satellite communications in 4g mobile systems," Journal Communications, vol. 4, no. 10, 2009, pp. 815–826.

[17] Y. Dhungana, N. Rajatheva, and C. Tellambura, "Performance analysis of antenna correlation on lms-based dual-hop af mimo systems," Vehicular Technology, IEEE Transactions on, vol. 61, no. 8, 2012, pp. 3590–3602.

[18] C. Loo, "A statistical model for a land mobile satellite link," Vehicular Technology, IEEE Transactions on, vol. 34, no. 3, 1985, pp. 122–127.

[19] D. Zogas, G. Karagiannidis, N. Sagias, T. Tsiftsis, P. Mathiopoulos, and S. Kotsopoulos, "Dual hop wireless communications over nakagami fading," in Vehicular Technology Conference, 2004. VTC 2004-Spring. 2004 IEEE 59th, vol. 4, 2004, pp. 2200–2204 Vol.4.

[20] S. Soliman and N. Beaulieu, "Exact analysis of dual-hop af maximum end-to-end snr relay selection," Communications, IEEE Transactions on, vol. 60, no. 8, 2012, pp. 2135–2145.

[21] H. Suraweera, G. Karagiannidis, Y. Li, H. Garg, A. Nallanathan, and B. Vucetic, "Amplify-and-forward relay transmission with end-to-end antenna selection," in Wireless Communications and Networking Conference (WCNC), 2010 IEEE, 2010, pp. 1–6.

[22] T. Tsiftsis, G. Karagiannidis, and S. Kotsopoulos, "Dual-hop wireless communications with combined gain relays," Communications, IEE Proceedings-, vol. 152, no. 5, 2005, pp. 528–532.

[23] Y. S. Cho, J. Kim, W. Y. Yang, and C. G. Kang, MIMO-OFDM Wireless Communications with Matlab. Wiley, 2010.

[24] G. Golden, C. J. Foschini, R. Valenzuela, and P. Wolniansky, "Detection algorithm and initial laboratory results using v-blast space-time communication architecture," Electronics Letters, vol. 35, no. 1, 1999, pp. 14–16.

[25] P. Wolniansky, G. Foschini, G. Golden, and R. Valenzuela, "V-blast: an architecture for realizing very high data rates over the rich-scattering wireless channel," in Signals, Systems, and Electronics, 1998. ISSSE 98. 1998 URSI International Symposium on, 1998, pp. 295–300.

 ISBN: 978-1-61208-397-1

[26] D. Christopoulos, S. Chatzinotas, M. Matthaiou, and B. Ottersten, "Capacity analysis of multibeam joint decoding over composite satellite channels," in Signals, Systems and Computers (ASILOMAR), 2011 Conference Record of the Forty Fifth Asilomar Conference on, 2011, pp. 1795–1799.

[27] R. Xu and F. Lau, "Performance analysis for mimo systems using zero forcing detector over rice fading channel," in Circuits and Systems, 2005. ISCAS 2005. IEEE International Symposium on, 2005, pp. 4955–4958 Vol. 5.

[28] S. Jin, M. McKay, C. Zhong, and K.-K. Wong, "Ergodic capacity analysis of amplify-and-forward mimo dual-hop systems," in Information Theory, 2008. ISIT 2008. IEEE International Symposium on, 2008, pp. 1903–1907.

[29] A. Moustakas, "Sinr distribution of mimo mmse receiver," in Information Theory Proceedings (ISIT), 2011 IEEE International Symposium on, 2011, pp. 938–942.

[30] N. Kim, Y. Lee, and H. Park, "Performance analysis of mimo system with linear mmse receiver," Wireless Communications, IEEE Transactions on, vol. 7, no. 11, 2008, pp. 4474–4478.

[31] P. Li, D. Paul, R. Narasimhan, and J. Cioffi, "On the distribution of sinr for the mmse mimo receiver and performance analysis," Information Theory, IEEE Transactions on, vol. 52, no. 1, 2006, pp. 271–286.

[32] J. Ma, Y. Zhang, X. Su, and Y. Yao, "On capacity of wireless ad hoc networks with mimo mmse receivers," Wireless Communications, IEEE Transactions on, vol. 7, no. 12, 2008, pp. 5493–5503.

[33] H. Poor and S. Verdu, "Probability of error in mmse multiuser detection," Information Theory, IEEE Transactions on, vol. 43, no. 3, 1997, pp. 858–871.

[34] W. Zhang and K. Ben Letaief, "Opportunistic relaying for dual-hop wireless mimo channels," in Global Telecommunications Conference, 2008. IEEE GLOBECOM 2008. IEEE, 2008, pp. 1–5.

[35] R. Xu and F. Lau, "Performance analysis for mimo systems using zero forcing detector over fading channels," Communications, IEE Proceedings, vol. 153, no. 1, 2006, pp. 74–80.

 ISBN: 978-1-61208-397-1

Performance of HAPs Communication Systems in DUSA Storm: Analysis and Modeling

Kamal Harb
Electrical Engineering Department
KFUPM University, Saudi Arabia
Email: kharb@kfupm.edu.sa

Abstract – **High Altitude Platform Station (HAPS) systems are currently under improvement and development. Technology is advancing towards the reliability and creative performance under reasonable fee for service providers and customers. HAPS technology represents one of the most revolutionary way of communication that appears to be convincing and effective under different weather conditions for any location in the world. For desert areas, such as Saudi Arabia, the main impact factor of HAPS is Dust and Sand (DUSA) storms. This attenuation varies with the operational satellite parameters such as frequency, location and other factors. This paper proposes some modifications to an existing DUSA storms model presented by a 3-D mesh model having different visibilities. This model for visibility depends on horizontal and vertical layers with reference to variations in altitude and space along with probabilistic dust particle size distributions in each layer. Such strategies help in conducting reasonable impairment estimates and in providing an optimal design for the HAPS system. As a result, an appropriate enhanced attenuation mitigation model is suggested.**

***Keywords*–*High Altitude Platform Stations*; *Permittivity indices*; *Quality of Service*; *Dust and Sand*; *Signal to Noise Ratio*.**

I. INTRODUCTION

Satellite communications are going toward High Altitude Platform (HAP) technology to cover specific locations such as crowded areas. This system uses an emerging wireless access technology represented by balloons or aircrafts for altitudes ranging between 15 and 25 Km above sea level. This system provides wireless communication networks for different users with the help of aircraft controlled or uncontrolled systems [1][2].

Some advantages of HAPS systems are represented by replacement of terrestrial mobile networks that is quite expensive, has potential health hazards and associated environmental impacts. On the other hand, besides the advantages of satellite systems, unequivocal disadvantages include building and launching them being reasonably expensive, the time interval efficiency associated with geostationary (GEO) satellites and movement requirements for other satellite systems [3]–[8].

Terrestrial systems, on the contrary, have also some difficulties, such as tower implementation for wireless networks, which is quite expensive, and safety problems. Therefore, implementing HAPS technology has became superior.

HAPS is the technology for providing wireless narrow band, broadband telecommunication and broadcasting services, particularly in remote rural areas where the deployment of terrestrial network infrastructure is not only difficult, but costly as well. The HAPS technology attempts to present a new concepts and has several advantages in comparison to the implemented systems such as satellite and terrestrial. The maintenance of HAPS is also easy and can be relocated as needed. Besides that, HAPS maintenance is easy, not expensive, and can be reallocated as needed. Note that, a round-trip delay is less than 0.5 ms and satisfies human safety [1][2][9]–[12]. Moreover, HAPS can be easily integrated with the existing satellite and terrestrial systems, as depicted in Figure 1.

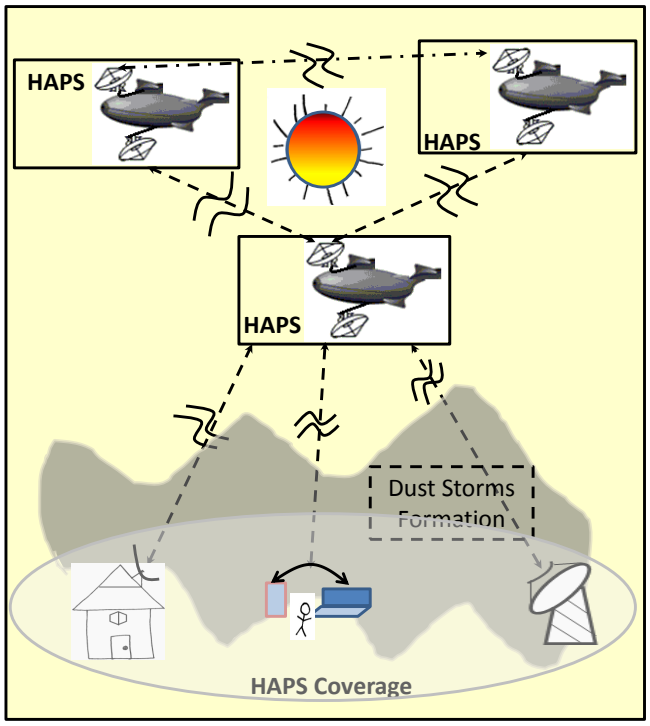

Figure 1. Effects of DUSA storms on HAPs communications.

For arid and semi-arid areas such as Saudi Arabia and its surrounding countries, which are affected with extreme DUSA storms for almost six months per year, the microwave signals are impaired by different weather parameters including dust particle size distributions, visibility and humidity level within DUSA storms [13]. Since DUSA particles from different regions have different characteristics, such as relative permittivity and average sizes, it has hitherto remained a challenge in creating a generic storm model. This paper proposes visibility variations inside DUSA storm represented by four layers or

 ISBN: 978-1-61208-397-1

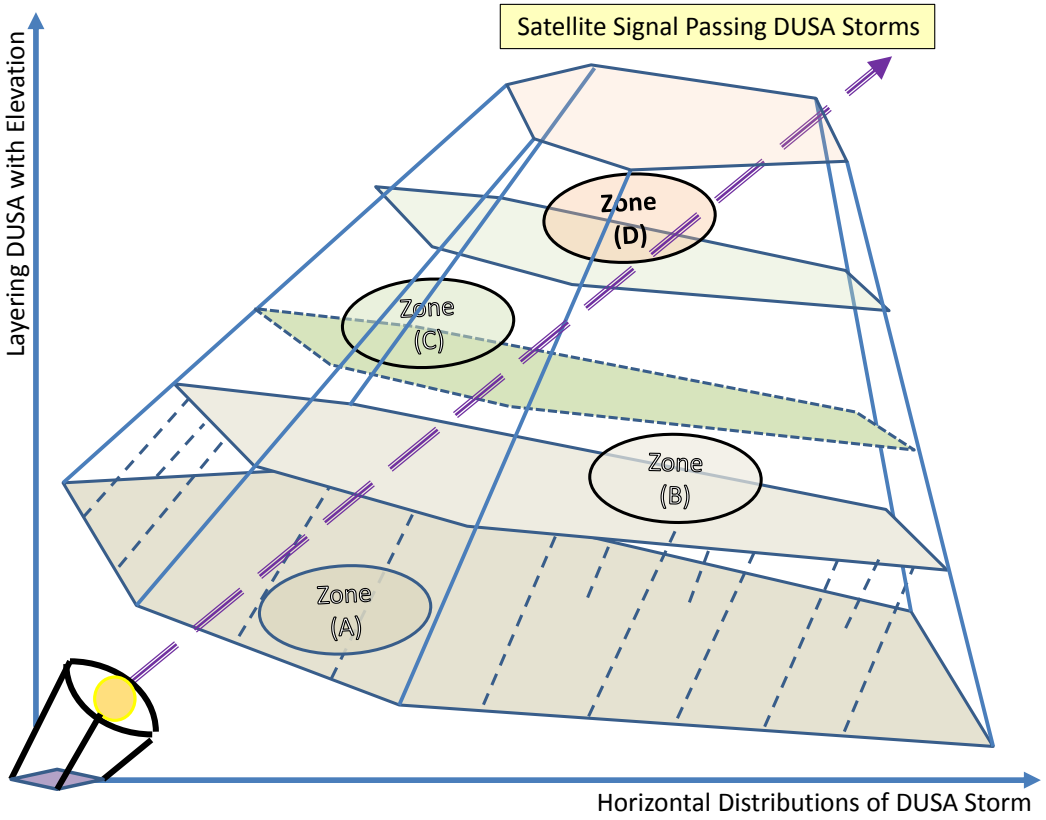

Figure 2. Visibility distribution model within DUSA storm according to different heights.

zones A, B, C, and D, as shown in Figure 2. Also, it presents wireless signal penetrations through multiple layers along the storm that contained different visibilities and particle sizes, etc. According to DUSA storm behavior such as location, intensity, and height, designers have the ability to select the number starting at two up to ten layers. Note that, increasing the number of layers in some cases might not be necessary, especially at high visibility form, as it may not lead to a better system performance and improvement.

This paper is presented in six sections. Section II describes the modeling of DUSA storm in the presence of layering. Section III presents the methodology of DUSA storm variation with visibility level. Section IV discusses different research methods for HAPS systems. Also, it presents analysis and modeling for DUSA storm, propagation effects and link budget calculation. Section V presents SNR results and discussion for HAPS behavior under heavy storm conditions. Finally, we conclude this study in Section VI.

II. DUSA Storm Modeling

The visibility, in desert areas, is usually regarded as a measure for the severity of DUSA storms, and is considered to be severe storm if visibility is below 500 m [14]. A low value of visibility implies that the wireless signal has to pass through a heavy concentration of DUSA particles, which have a particular size distribution depending upon the region of study. DUSA mechanics terms the particles below 60 μm as dust particles otherwise it is sand [15]. Accurate quantification of DUSA attenuation highly depends upon particle sizes, permittivity indices and maximum attenuation that occurs when the particles are of the order of the wavelength of transmitted signal. Most of the DUSA storm prediction models assumed uniform distribution and then neglected the different particle size distributions within DUSA storm [16], which is a most likely reason for slight inaccuracy between real and expected impairments.

In most cases, DUSA storms extend up to 5 Km above the satellite ground station [9], making it almost impossible to recover or immunize the satellite signals against its impairments. Reasonable information of expected impairments due to several factors leads to better satellite link utilization and effective radio resource management. The overall systems' Signal to Noise Ratio (SNR), which is also referred to in terms of Quality of Service (QoS) can be increased by weather adaptive variations in modulation, power, antenna beam shape, site diversity, etc. [7][17]–[21]. From engineering's perspective, the goal is to optimally utilize all radio resources including channel bandwidth, computational complexity, etc. Furthermore, parameters of such communications must also abide by the imposed limitations concerning to human health.

Chu's model for DUSA prediction was implemented based on Rayleigh approximation in [22]. This model presents an enhanced method for the measurement of dust attenuation, by introducing vertical path adjustment factor (r_v). This factor is dependent upon earth station's reference height (h_0), overall DUSA storm elevation (h_l), propagation angle (θ), and the

 ISBN: 978-1-61208-397-1

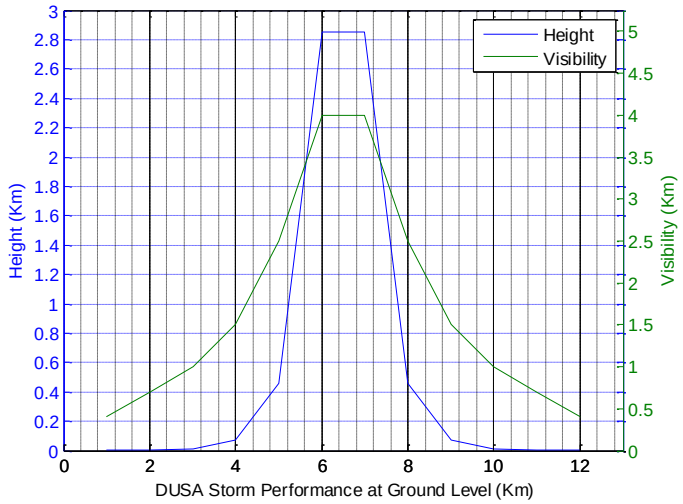

Figure 3. DUSA storm mirrored model for HAPS with visibility and height variations.

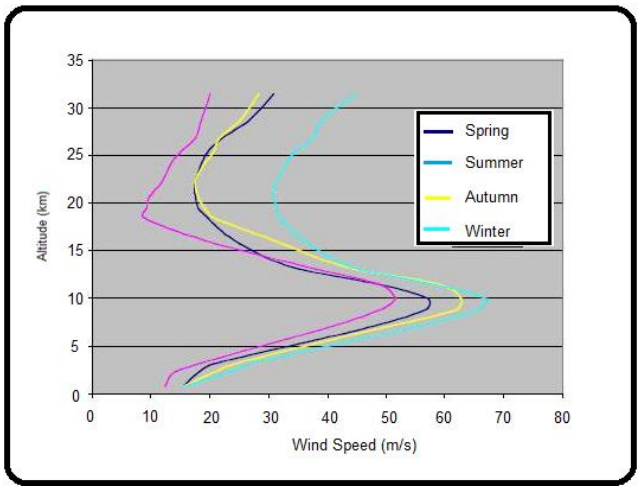

Figure 4. Variation of wind speed with altitude at Spokane, Washington [2].

slant path (L) where the radio wave traverses in dust filled regions.

Weather predictions can be used to dynamically reconfigure the radio resources for better link performance as well to keep the required level of QoS for the most important network components. A generalization of this concept is to utilize minimal resources during clear weather conditions whereas optimally manage resources based on weather predictions. Weather attenuation estimates have been presented by accounting for the variations in the probability distribution of DUSA particles.

III. Methodology

Visibility level keeps on increasing in a monotonic fashion while moving in a vertical direction as shown in Figure 2. This model is developed in an attempt to improve the existing one considering uniform duststorm distribution. Also, the simulation outcomes of this model is presented in Figure 3. The horizontal axis of this figure showed the DUSA performance at ground level with both vertical axes presented by height in blue color from the left side and visibility in red color on the right side. The results depict almost 100 m visibility at the ground station, i.e., the base layer which keeps on increasing to reach 5 Km elevation, at which transmitted signal gets out of the dust influenced region. Based on this fact, this paper presents a strategy to divide the whole DUSA storm into several layers according to visibility level.

$$h_i = h_{i-1}\left[\frac{V_i}{V_{i-1}}\right]^{3.85} \quad (1)$$

Equation (1) is being recursively used to obtain DUSA storm height layering or partition in accordance to visibility variations at several altitudes.

IV. Research Methods

A. HAPS System Geometry

HAP is intended to provide different wireless communications of services such as mobile, TV, and internet, which are located in a fixed point according to earth station and belong to the stratosphere ranges of around $15 - 25$ Km of altitude [1][12]. The footprint, and hence the coverage area of the HAPS communication system is uniquely defined by the accepted minimum elevation angle and its height.

In this paper, the height of the platforms were defined to be 22 Km taking into account the ITU-R recommendations and the wind behavior. From the mathematical calculation of the coverage areas either urban, suburban, or rural areas were determined by the subscriber, the corresponding slant path is 64.324 Km and the coverage radius is 60.445 Km [12].

B. HAP Location and Wind Behavior

The wireless channel between satellite hub and transponder consists of several layers starting with the troposphere above 10 Km in altitude. Within this layer, air temperature and pressure decrease with elevation. Going forward, the stratosphere is the next layer, up to 50 Km in altitude. Much research has been done to conclude that this layer is stable, i.e. slightly windy, and temperature increase with elevation. Also, there is no effect for clouds that help using the solar energy in an efficient manner [1][2]. Therefore, Figure 4 presents useful data for designers to select the ultimate location for HAPS transponder in the space at different areas with relatively low wind, minimum demanding power, high stability which located between 15 and 25 Km. Note that, wind speed variations with height at different location is presented by different researchers [23][24].

C. Propagation Effects

The propagation losses along the fuzzy path connected between ground station and HAPS can be attributed to rain,

 ISBN: 978-1-61208-397-1

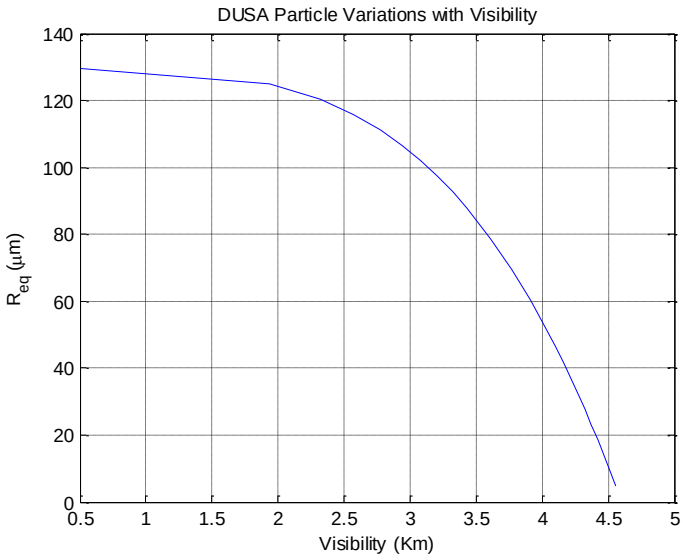

Figure 5. Visibility and DUSA size variations.

DUSA, gases, free space and other attenuations. The existing free space loss is calculated in (2). Our main concern in this paper; related to desert area, is DUSA attenuation as calculated in (4).

1) Free-Space Loss: The free space path loss (L_f) is:

$$L_f = 10 \cdot log(4\pi d/\lambda)^2, \tag{2}$$

where $\lambda(wavelength) = c/f$,
d is the distance between the satellite ground station and the HAP transponder with propagation angle (θ) is:

$$d = h/sin\theta, \tag{3}$$

where h represents the HAPS height above sea level.

2) DUSA Attenuation: DUSA storms can potentially result in serious impairments by increasing losses and destroying transmit signal especially at higher frequency of operation. Mostly, DUSA storms are considerable meteorological phenomenon characterized by strong winds and dust-filled air and water vapor over a wide area such as Saudi Arabia, Nevada, USA, etc. [9][16][25].

There is a number of different models that have been proposed for dust attenuation estimation, taking into account the variation of visibility, particle size, and concentration of the dust particles. An attractive model for the attenuation was proposed by [9][11][16] and is updated in this paper as:

$$A_{Pl} = \left[\frac{5.67 \cdot 10^2}{V_l \cdot r_{el} \cdot \lambda}\right] \left[\frac{\varepsilon''}{(\varepsilon' + 2)^2 + \varepsilon''^2}\right] \sum_i^N p_{il} \cdot r_{il}^3 \; dB/Km, \tag{4}$$

where point attenuation for each layer A_{pl}, ε' and ε'' are real and imaginary dielectric constant, r_{el} is the equivalent particle size corresponding to each layer, and V_l is the visibility of different layers along the signal path is given by:

$$V_l = V_{0l} \left[\frac{h_l}{h_0}\right]^{0.26}, \tag{5}$$

where V_{0l} is the visibility at the reference height h_0 that is dependent on the selected point within the storm. h_l is the height of one layer where each layer has different values. Usually, this height should be small while facing low visibility at low level and increase exponentially with elevation. Therefore, the variations of the visibility (V_l) inside DUSA storm according to travel distance (h) and radius particle size (R_{eq}) are illustrated in Figure 5. This figure shows the variation of visibility with dust particle radius, i.e., particle size decreases, visibility increases.

TABLE I. LINK SPECIFICATIONS AND INPUT PARAMETERS FOR HAPS.

Downlink Operating Frequency [GHz]	32
Transmitted Power [W]	0.5
Transmitting Antenna Gain [dBi]	5 (Minimum available)
Diameter of the Parabolic Antenna (Ground station)	1.3m
Aperture efficiency of Parabolic Reflector	0.55 (Minimum available)
Distance between Satellite and Ground Station (Km)	22
Ground Station Receiver Noise [K]	$\sim$ 119
Ground Station Antenna Noise [K]	$\sim$ 35
Ground Station Amplifier Noise [K]	$\sim$ 60
Bit Rate of the data (Mbps)	1
Bit Error Rate (BER)	10^{-6}
Modulation	QPSK

Therefore, the updated total attenuation based on DUSA layering, A_{DUSA}, can be obtained from the following expression:

$$A_{DUSA} = r_v \times d \times A_{pl}, \tag{6}$$

where r_v is the vertical path adjustment factor and all other symbols carry their usual meanings. The vertical path adjustment is estimated using the following relation [16] as:

$$r_v = \frac{h_0^{0.26} \times h_l^{0.74}}{0.74 \times \; d \; \times (\sin\theta)^{1.74}} \tag{7}$$

It is clear from the expression that, r_v is a function of the inclination angle (θ), height of the storm (h_l), reference height (h_0) and the slant path (d). Then, the values for DUSA attenuation were obtained, using the proposed model, by going through (2) to (7) for existing model, and for varying dust particle sizes with different heights (h_l), is presented in Figure 6.

D. Algorithmic for SNR Calculation

In satellite communications related to desert area, the most prominent contributors to noise, beside rain, is the DUSA storm. Start SNR calculation by the thermal noise power spectral density as: $N_0 = K \cdot T$, where Boltzmann constant $K = 1.38 \cdot 10^{-23}\; Ws/K = -228.6$ dBWs/K and effective noise temperature $T = T_a + T_r$, T_a is noise temperature of the antenna, and T_r is noise temperature for the receiver represented as $\mathrm{T_r} = (10^{N_r/10} - 1) \cdot 290$, with noise figure of low-noise amplifier, $N_r \approx 0.7 \sim 2$ dB. Thus, the ratio between signal and noise power spectral density is:

$$\frac{C}{N_0} = \frac{C}{K \cdot T} = \frac{P_r}{K \cdot T} = \frac{P_t \cdot G_t}{A_T} \cdot \frac{G_r}{K \cdot T}, \tag{8}$$

where total attenuation A_T is:

$$A_T = A_{DUSA} + L_f \tag{9}$$

TABLE II. ASSUME MAXIMUM VALUES FOR HAPS LOSSES.

Atmospheric Loss (dB)	1
Rain Attenuation (dB)	1.3
Fog Attenuation (dB)	0.03
Atmospheric Reflection (dB)	0.2
Ionospheric Loss (dB)	0.6
Polarization Loss (dB)	0.3
Miscellaneous Attenuation (dB)	0.27
DUSA Attenuation (dB)	**0.92**
Total Atmospheric Losses (dB)	**5.12**

Therefore, SNR is presented as:

$$SNR(A_T, f) = P_t + G_t - A_T + G_r - R_s - T - K \quad dB, \tag{10}$$

where P_t and P_r are transmitter and receiver power, and G_t and G_r are antenna gain at transmitter and receiver sides respectively. It should be noted that the SNR estimation of (9) will be optimized by the virtue of having better estimation of A_T through (10), SNR result is presented in Figure 7.

E. Fading Mitigation Techniques

Some researchers including [9][11] proposed the use of intelligent mitigation schemes for SNR improvement. The mitigation techniques that were applied to compensate the attenuation impairment during heavy attenuation period, including Skillful Atmospheric Aware Model (SAAM) for satellite systems, and space diversity such that whenever a heavy DUSA storm condition is experienced, the traffic can be rerouted via the second back haul link. The latter is ineffective as far as mobile HAPS communication system is concerned [11]. SAAM algorithm does not only serve as mitigation technique during a heavy storm, but it provides cost effectiveness as well. The system will be transmitting power according to the demand. By knowing the required performance such as weather prediction, the system will maintain appropriate SNR level by changing the transmitted power according to the demand. The automatic power control mechanism is used whereby the transmit power changes as the dust attenuation changes and it transmits the minimum power during the clear air conditions. However, once weather attenuation increases and power factor reaches its limits, other parameters should be updated to maintain SNR values above minimum signal level that is needed for costumer's satisfaction and acceptable communication performance.

F. An Effective Downlink Budget

This section will introduce a unique calculation for the HAPS downlink operated at 32 GHz. Other parameters are defined from Table I and are used as input parameters to the simulation. Several other losses have been considered with their maximum values at HAPS to ensure an efficacious link margin. In this paper, we introduce DUSA attenuation in the downlink budget specifications. The value was extracted from the simulations in the previous section. A maximum estimated value of 0.92 dB is shown in Table II along with all other losses.

Finally, the link budget is re-estimated with DUSA attenuation considered. The output parameters are shown in Table III. The link margin is an important parameter in satellite links and represents the difference between the available and the required values of the energy-to-noise ratio. It can be viewed as the amount by which the received power exceeds the receiver sensitivity. According to the ITU-R recommendations, practical satellite-earth links must maintain a healthy link margin above 2 dB in order to have effective communication links with acceptable QoS. As can be inferred from the output parameters, the presented satellite link margin is found to be 2.07 dB, which is sufficient for a reliable satellite communication link.

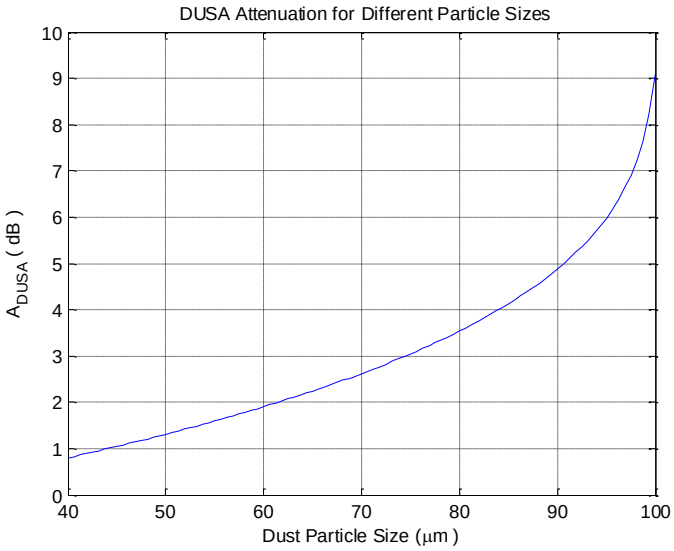

Figure 6. DUSA attenuation for variety of particle sizes at frequency = 30 Ghz and propagation angle = 45 degree.

TABLE III. SUMMARY OF DOWNLINK OUTPUT PARAMETERS FOR HAPS.

Effective Isotropic Radiated Power (dBW)	1.99
Free Space Path Loss (dB)	149.4
Atmospheric losses	5.12
Total Losses (dB)	151.39
Received Power (dB)	-132.23
Noise Density (dB)	-207.14
Received Power to Noise Ratio (dB)	57.01
Energy to Noise Ration (Available) (dB)	14.37
Energy to Noise Ration (Required) (dB)	10.29
Link Margin (dB)	**2.07**

V. RESULTS DISCUSSION

From the output result, the performance of the system was promising under dusty conditions. In case of clear weather, the only degrading component was the path loss. The available SNR ratios were ranging between (-14.0 and -4.0 dB). However, during the DUSA storm, the SNR were drastically reduced to be between (-12.0 and -23.0 dB), keeping other parameters constant, as shown in Figure 7. With the increasing of transmit power, during the heavy storm conditions, the system can provide the required services with relatively reasonable QoS. In this paper, the transmitted power was assumed to be 0 dBm and the results were satisfactory. Thus, a much better result is expected if the transmit power can be raised.

 ISBN: 978-1-61208-397-1

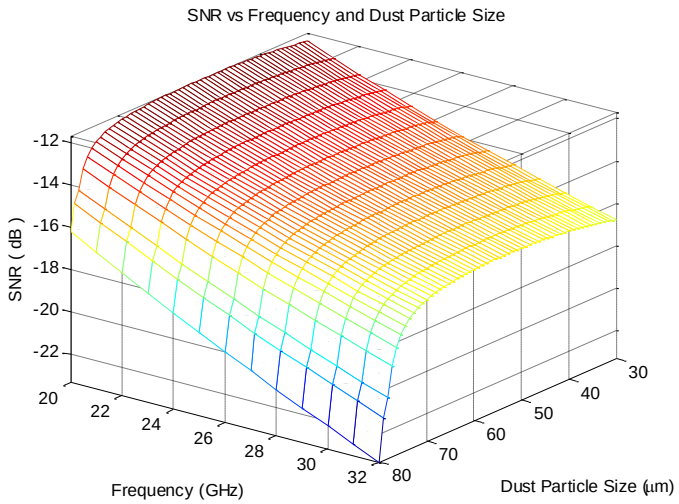

Figure 7. SNR for different DUSA particle size and frequency.

VI. Conclusion and Future work

This paper investigated the link reliability during the DUSA storm scenario. By implementing DUSA layering in order to estimate DUSA attenuation, it was found that the link margin dropped due to the fading effect of the DUSA storm that might destroy the signal at certain levels. Though, the system at this level can be considered operational, only an extra attenuation of around 2.1 dB is enough to make the system unreliable. Therefore, with the application of automatic power transmission and adaptive coding and modulation, the required QoS can be maintained.

Future work is in progress to consider real DUSA measurements at different locations, and to compare it with our simulation. Also, the study of hurricanes and other atmospheric phenomena, as well as proposing enhanced strategies to better present satellite systems.

ACKNOWLEDGMENT

The authors wish to thank King Fahd University of Petroleum & Minerals (KFUPM) and Hafr Al-Batin University, Electrical Engineering department. This work is supported by the Deanship of Scientific Research (DSR) at KFUPM through project No. FT121013.

References

[1] M. Vzquez-Castro, F. Prez-Fontn, and B. Arbesser-Rastburg, "Channel modeling for satellite and haps system design," Wireless Communications and mobile computing, 2002, vol. 2, no. 3, pp. 285–300.

[2] A. Arago'n-Zavala, J. L. Cuevas-Ru'z, and J. A. Delgado-Pen'n, High-Altitude Platforms for Wireless Communications. First edition, John Wiley & Sons, 2008.

[3] R. E. Hushcke, Ed., Glossary of Meteorology. Boston, MA: Amer. Meteorological Soc., 1995.

[4] F. Haidara, A. Dissanayake, and J. Allnutt, "A prediction model that combines rain attenuation and other propagation impairments along Earth-satellite paths," IEEE Trans. on Antennas & Propagation, Oct. 1997, vol. 45, no. 10, pp. 1546–1558.

[5] K. Harb, F. R. Yu, and S. H. Abdul-Jauwad, "Performance evolution in satellite communication networks along with markovian channel prediction," Journal of Wireless Networking and Communications, 2012, vol. 2, no. 5, pp. 143–157.

[6] K. Harb, B. Omair, S. H. Abdul-Jauwad, A. Al-Yami, and A. Al-Yami, "A proposed method for dust and sand storms effect on satellite communication networks," in Innovations on Communication Theory (INCT), Oct. 2012, pp. 33–37.

[7] K. Harb, F. R. Yu, P. Dakhal, and A. Srinivasan, "An intelligent QoS control system for satellite networks based on markovian weather," in Proc. IEEE VTC, Sept. 2010, pp. 1–5.

[8] ITU-R, "Specific attenuation model for rain for use in prediction methods," Radio wave propagation, International Telecommunication Union Recommendation ITU-R P.838-3, 2003.

[9] Z. Elabdin and M. R. Islam, "Duststorm measurements for the prediction of attenuation on microwave signals in Sudan," in International Conference on Computer and Communication Engineering (ICCCE), May 2008, pp. 1181–1185.

[10] K. Harb, O. Butt, A. Al-Yami, and S. H. Abdul-Jauwad, "Probabilistic dust storm layers impacting satellite communications," in Proc. of the IEEE International Conference on Space Science and Communication (IconSpace), July 2013, pp. 407–411.

[11] K. Harb, B. Omair, S. H. Abdul-Jauwad, and A. Al-Yami, "Systems adaptation for satellite signal under dust, sand and gaseous attenuations," Journal of Wireless Networking and Communications, Nov. 2013, vol. 3, no. 3, pp. 39–49.

[12] K. Harb, A. Talib, M. Mohamed, and S. H. Abdul-Jauwad, "Haps communication in Saudi Arabia under dusty weather conditions," in International Conference 11th Malaysia International Conference on Communication (MICC), Nov. 2013, pp. 379–384.

[13] K. Afzaal, T. K. Bandopadhyaya, and S. Poonam, "Effect of soil textural class and relative humidity of regions in accurate prediction of attenuation of millimeter waves during sand and dust storms," in Physics and Engineering of Millimeter and Sub-Millimeter Waves. The Fourth International Kharkov Symposium on, June 2001, vol. 1, pp. 393–395.

[14] J. Goldhirsh, "Attenuation and backscatter from a derived two-dimensional duststorm model," IEEE Transactions Antennas Propagation, Dec. 2001, vol. 49, no. 12, pp. 1703–1711.

[15] S. I. Ghobrial and J. A. Jervase, "Microwave propagation in dust storms at 10.5 GHz-A case study in Khartoum, Sudan," IEICE Trans. Commun., Nov. 1997, vol. E80-B, no. 11, pp. 1722–1727.

[16] E. A. Elsheikh, M. R. Islam, K. Al-Khateeb, A. Z. Alam, and Z. Elshaikh, "A proposed vertical path adjustment factor for dust storm attenuation prediction," in 4th International Conference on Mechatronics (ICOM), May 2011, pp. 1–3.

[17] W. J. Vogel and J. Goldhirsh, "Multipath fading at L band for low elevation angle, land mobile satellite scenarios," IEEE J. on Selected Areas in Communications, Feb. 1995, vol. 13, no. 2, pp. 197–204.

[18] A. Safaai-Jazi, H. Ajaz, and W. L. Stutzman, "Empirical models for rain fade time on Ku and Ka-band satellite links," IEEE Trans. on Antennas & Propagation, Dec. 1995, vol. 43, no. 12, pp. 1411–1415.

[19] ITU-R, Characteristics of precipitation for propagation modeling. Radio wave propagation, International Telecommunication Union. Rec. P.837-4, ITU-R, Fascicle,Geneva, 2001.

[20] T. P. Mao, D. F. Zhou, and Z. X. Niu, "The calculation model of the attenuation due to clouds or fog and the analysis of its characteristic," Proc. of Asia-Pacific, Aug. 2004, pp. 332–334.

[21] Telesat Canada, "ISS (Intelligent Satellite Service) Research and Development." website: http://www.telesat.ca, last accessed date March 2015.

[22] T. S. Chu, "Effects of sandstorms on microwave propagation," Bell System Technology Journal, Feb. 1979, vol. 58, no. 2, pp. 549–555.

[23] R. Struzak, "Mobile telecommunications via stratosphere." website: http://www.intercomms.net/AUG03/content/struzak1.php, last accessed date March 2015.

[24] T. King and E. Bell and James R. Thieman, "Space physics archive search and extract (spase)." website: http://nssdc.gsfc.nasa.gov/space/, last accessed date Feb. 2015.

[25] A. Arun and T. Sreeja, "An effective downlink budget for 2.24 GHz s-band LEO satellites," in IEEE Conference on Information & Communication Technologies (ICT), 2013, pp. 342–345.

 ISBN: 978-1-61208-397-1

Downlink Energy Efficiency Power Allocation for OFDM-based Aerial Systems with Limited Satellite Backhaul

Ruijin Sun, Ying Wang, Yichun Xu
State Key Laboratory of Networking and Switching Technology
Beijing University of Posts and Telecommunications, Beijing 100876, P.R. China
Email: 601341194@qq.com, wangying@bupt.edu.cn, cathy_xyc@163.com

***Abstract*—Emergency communications can benefit from the integrated aerial-satellite systems due to the frequent Line Of Sight (LOS) access for User Equipments (UEs) and the robust satellite backhaul. This paper addresses an energy efficiency power allocation problem for a OFDM-based aerial system with limited satellite backhaul. Due to the non-convex backhaul capacity limit, the optimization problem is solved in two steps. Firstly, a non-negative parameter is introduced to convert the objective function to an equivalent convex form according to the fractional programming. Then, the optimal parameter for maximum Energy Efficiency (EE) without total power and backhaul capacity constraints is obtained. Secondly, by proving that the derivative of $R(P_{tot})$ is equal to the above introduced parameter, which is decreasing in total power limit, P_{tot}, these two constraints can be transformed into a lower bound on the parameter through geometric interpretation. Thus, an energy efficiency power allocation algorithm is proposed. Finally, numerical results show that the circuit power, total power limit and backhaul capacity limit have effect on the system EE.**

Keywords–energy efficiency; backhaul limit; power allocation.

I. INTRODUCTION

Large-scale disaster or unexpected emergency may overload or totally paralyze the existing terrestrial network in severe cases. Therefore, an effective Public Protection and Disaster Relief (PPDR) system is crucial to meet the requirements of victims and first responders, which is characterized by rapid deployment, large capacity-coverage, flexibility and scalability [1].

In this regard, ABSOLUTE project is working at establishing an integrated satellite-aerial-terrestrial architecture to guarantee reliable communication in the aftermath of natural disaster [2]. An important element of the integrated architecture is aerial station which is an air balloon or aircraft based Low Attitude Platform (LAP). The LAP goes from 100 meters to 1000 meters height, lifting with a low-complexity Long Term Evolution (LTE) eNB, named Aerial eNodeB (AeNB), and filling the gaps of destroyed LTE base stations. The lower altitude of aerial station compared to that of satellite makes it easier for LAP to support frequent Line Of Sight (LOS) with User Equipments (UEs), which explains the advantage of LAPs for the public safety network.

Emergency communications can greatly benefit from the integrated aerial-satellite systems which could provide UEs with high capacity-coverage thanks to low delay aerial links, while reliable backhauling links to remote networks (headquarters) can be supplied by the satellite segment [3]. On the other hand, due to the limited overload, LAPs are unable to carry enough battery and AeNB thus may face stiff constraints regarding its total energy consumption. Therefore, the Energy Efficiency (EE) is demonstrated as a significant metric to evaluate the power allocation performance of AeNB.

In this paper, we consider a subset of aerial-satellite systems. As illustrated in Figure 1, the system consists of a single air balloon based LAP, keeping a quasi-stationary position over a predefined area and serving a set of UEs. The AeNB is connected to its Evolved Packet Core (EPC) through optical link. The satellite serves as a backhaul to connect aerial system with Headquarter. We assume that aerial system is OFDM-based and design a downlink energy efficiency power allocation algorithm for a OFDM-based aerial system.

Different from previous work on downlink EE maximization for OFDM-based systems under only convex constraints, such as total power limit [4], minimal overall system throughput limit [5] and interference limit [6], we maximize the system EE with the total power constraint, peak power limit, QoS requirement of each UE, as well as non-convex backhaul capacity constraint. The problem is solved in two steps owing to this non-convex constraint. Firstly, according to the properties of fractional programming, a non-negative parameter is introduced to convert the objective function to an equivalent convex form. Then, the optimal parameter for maximum EE without total power and backhaul capacity constraints is obtained. Secondly, by proving that the derivative of $R(P_{tot})$ is the above introduced parameter, which is decreasing in total power limit, P_{tot}, this paper transform these two constraints into a lower bound on the parameter through geometric interpretation. Finally, theoretical analysis is corroborated by numerical experiments.

The remainder of the paper is organized as follows. In Section II, system description and channel model are introduced. In Section III, we present the energy efficiency power allocation algorithm. The simulation results are presented and discussed in Section IV. Finally, Section V concludes the paper.

II. SYSTEM DESCRIPTION AND CHANNEL MODEL

In this section, we present our system model in detail. Also, a practical channel model is given here.

A. System Description

As illustrated in Figure 1, information is transmitted from the headquarter ground station to the AeNB through the satellite link L_1, L_2, Internet and optical link. In this paper, we omit the detailed signal transmission of these links and see them as a whole backhaul, the capacity of which is denoted as $C_{backhaul}$. We focus on the downlink transmission of the aerial system. We consider a single OFDM-based aerial network with K active UEs. The total bandwidth, B, is divided into B subcarriers, each with $W = \frac{B}{K}$.

 ISBN: 978-1-61208-397-1

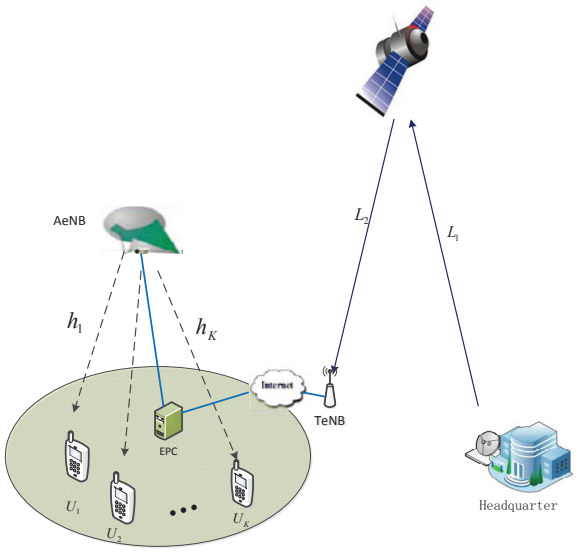

Figure 1. System Model in Integrated Aerial-Satellite Network

Assume that the kth subcarrier is assigned to the kth UE to avoid interference among different UEs. Then, the maximum achievable data rate at the kth UE is accordingly

$$r_k = W\log_2(1+\frac{|h_k|^2 p_k}{\sigma^2}) = W\log_2(1+g_k p_k), \quad (1)$$

where h_k and p_k denote the channel fading factor and transmit power from AeNB to the kth UE, respectively. σ^2 is the received noise power and $g_k = \frac{|h_k|^2}{\sigma^2}$ is the Carrier-to-Noise Ratio (CNR) of the kth subcarrier. Then, the overall throughput of the OFDM-based aerial system is given by $R = \sum_{k\in\mathcal{K}} r_k$, where $\mathcal{K} = \{1, 2, ..., K\}$ denotes the set of all UEs.

The total power consumption at AeNB is modeled as [6]

$$P_{tot} = \zeta P + P_c, \quad (2)$$

where ζ is the reciprocal of drain efficiency of power amplifier. $P = \sum_{k\in\mathcal{K}} p_k$ and P_c represent the transmit power consumption and the circuit power consumption incurred active circuit block, respectively.

We use the throughput for unit-energy consumption to measure the system EE, i.e.,

$$\eta_{EE} = \frac{\sum_{k\in\mathcal{K}} W\log_2(1+g_k p_k)}{\zeta\sum_{k\in\mathcal{K}} p_k + P_c}. \quad (3)$$

The energy efficient power allocation problem considering each UE's QoS, total power limit as well as backhaul capacity constraint can be written as $\mathcal{P}1$:

$$\mathcal{P}1: \max_{p_k, k\in\mathcal{K}} \frac{\sum_{k\in\mathcal{K}} W\log_2(1+g_k p_k)}{\zeta\sum_{k\in\mathcal{K}} p_k + P_c} \quad (4a)$$

$$\text{s.t.} \quad W\log_2(1+g_k p_k) \geqslant r_{k,\min}, \forall k\in\mathcal{K}, \quad (4b)$$

$$\zeta\sum_{k\in\mathcal{K}} p_k + P_c \leqslant P_{Tot}, \quad (4c)$$

$$\sum_{k\in\mathcal{K}} W\log_2(1+g_k p_k) \leqslant C_{backhaul}, \quad (4d)$$

$$0 \leqslant p_k \leqslant p_{peak}, \forall k\in\mathcal{K}, \quad (4e)$$

where $r_{k,\min}$ is the traffic-related minimum rate requirement of the kth UE; P_{Tot} and $C_{backhaul}$ denote the maximal total power consumption and backhaul capacity, respectively. The allowed peak power at each subcarrier, p_{peak}, is also considered in this paper.

For simplicity, we assume that $r_{k,\min}, \forall k\in\mathcal{K}$ is achievable under the constraint (4c) and (4d), i.e.,

$$\zeta\sum_{k\in\mathcal{K}} p_{k,\min} + P_c \leqslant P_{Tot} \quad (5)$$

$$\text{and} \sum_{k\in\mathcal{K}} r_{k.\min} \leqslant C_{backhaul} \quad (6)$$

should be satisfied simultaneously, where $p_{k,\min} = \frac{2^{\frac{r_{k,\min}}{W}}-1}{g_k}$ is the minimum required transmit power to meet the kth UE's QoS. If not, optimization problem $\mathcal{P}1$ is unfeasible.

B. Channel Model

An existing empirical propagation channel model [7] between the AeNB and UEs is adopted in this paper. The large-scale fading taking path loss and shadow fading into account is given as

$$L = \begin{cases} L_{FSL} + \xi_{LOS}, & LOS \\ L_{FSL} + L_s + \xi_{NLOS}, & NLOS, \end{cases} \quad (7)$$

where L_{FSL} is the free space loss in dB as follows:

$$L_{FSL} = 20\log(d_{km}) + 20\log(f_{GHz}) + 92.4, \quad (8)$$

where d_{km} is the propagation distance between transmitter and receiver. f_{GHz} denotes the carrier frequency in GHz. An elevation angel dependent shadowing L_s is a normal distributed random variable. The location variability components ξ_{LOS} and ξ_{NLOS} both follow Log-normal distribution with zero mean.

With respect to the small-scale fading, Rayleigh distribution is added to NLOS link and Rician distribution LOS link.

III. Energy Efficiency Power Allocation

$\mathcal{P}1$ is obviously a non-convex problem since the objective function (4a) and the backhaul capacity constraint (4d) is non-convex [8]. The objective of a fractional programming, as we observed in $\mathcal{P}1$, takes the form of a ratio of two functions which is very challenging to solve directly. According to Isheden et al. [9], a non-negative parametric can be introduced to formulate a parametric optimization $\mathcal{P}2$ which is closely related with $\mathcal{P}1$.

 ISBN: 978-1-61208-397-1

$$\mathcal{P}2: \max_{p_k \in \mathcal{S}} \sum_{k\in\mathcal{K}} W\log_2(1+g_k p_k) - \lambda\left(\zeta \sum_{k\in\mathcal{K}} p_k + P_c\right) \quad (9a)$$

$$\text{s.t.} \quad (4c)(4d), \quad (9b)$$

where $\mathcal{S} = \{p_k, \forall k \in \mathcal{K} \mid p_{k,\min} \leq p_k \leq p_{peak}\}$ is the set of individual powers and each has a box constraint. Note that (9a) is convex for a given λ since its formulated as the difference between a convex function and a concave function (linear function for more strictly). But, $\mathcal{P}2$ is still a non-convex optimization problem due to the constraint (4d).

In order to solve problem $\mathcal{P}2$ effectively, we first leave out the constraint (4c) and (4d) and consider the optimal system EE only under the individual power set, which is formulated as

$$\mathcal{P}3: \max_{p_k \in \mathcal{S}} \sum_{k\in\mathcal{K}} W\log_2(1+g_k p_k) - \lambda\left(\zeta \sum_{k\in\mathcal{K}} p_k + P_c\right). \quad (10)$$

For convenience, we define the optimal value of $\mathcal{P}3$ as a function of λ, denoting as $F(\lambda)$.

The optimal power allocation is achieved at the stationary point for a given λ since (10) is convex, i.e.,

$$\left.\frac{d\sum_{k\in\mathcal{K}} W\log_2(1+g_k p_k) - \lambda\left(\zeta\sum_{k\in\mathcal{K}} p_k + P_c\right)}{dp_k}\right|_{p_k = p_k^*} = 0, \quad \forall k \in \mathcal{K}. \quad (11)$$

Taking the box constraints into account, the optimal power allocation is given as

$$p_k^*(\lambda) = \left[\frac{W\log_2 e}{\lambda\zeta} - \frac{1}{g_k}\right]_{p_{k,\min}}^{p_{peak}}, \forall k \in K. \quad (12)$$

It is obvious that the maximum system energy efficiency without constraints (4c) and (4d) can be achieved by finding the optimal λ^* of $\mathcal{P}3$. According to Isheden et al. [9], the optimal power allocation to obtain the maximum energy efficiency only under the individual power set $\mathcal{S}$ is the same as that of $\mathcal{P}3$ for $\lambda = \lambda^*$, where λ^* satisfies $F(\lambda^*) = \max_{p_k\in\mathcal{S}} \sum_{k\in\mathcal{K}} W\log_2(1+g_k p_k) - \lambda^*\left(\zeta\sum_{k\in\mathcal{K}} p_k + P_c\right) = 0$. In addition, λ^* is the optimal bit-per-joule, i.e.,

$$\lambda^* = \frac{\sum_{k\in\mathcal{K}} W\log_2(1+g_k p_k^*)}{\zeta\sum_{k\in\mathcal{K}} p_k^* + P_c}. \quad (13)$$

Since the power allocation has been expressed in (12) for a given λ, we need to determine λ^* with $F(\lambda^*) = 0$. The Dinkelbachs method [9], as described in Algorithm 1, is adopted in this paper to find it.

Until now, the problem $\mathcal{P}3$ without constraints (4c) and (4d) has been solved. In order to solve problem $\mathcal{P}2$, we explore some properties of $R(P_{tot})$, which are described in following Lemma 1. Define $R(P_{tot})$ as the maximum overall system throughput under the given total power consumption P_{tot} and individual power constraint, which is given as

$$R(P_{tot}) \triangleq \max_{p_k\in\mathcal{S}, P_c+\zeta\sum_{k\in\mathcal{K}} p_k \leqslant P_{tot}} \sum_{k\in\mathcal{K}} W\log_2(1+g_k p_k). \quad (14)$$

Due to the individual power constraint in $\mathcal{S}$, $P_{tot} \in [P_{Tot,\min}, P_{Tot,\max}]$, in which $P_{Tot,\min} = \zeta\sum_{k\in\mathcal{K}} p_{k,\min} + P_c$ and $P_{Tot,\max} = \zeta K p_{peak} + P_c$. Since the right hand side of (14) is a convex optimization problem with fixed P_{tot}, $R(P_{tot})$ has a unique value for all allowed P_{tot}. According to the constraint $P_c + \zeta\sum_{k\in\mathcal{K}} p_k \leqslant P_{tot}$, it is obvious that $R(P_{tot})$ is an increasing function in P_{tot}. The curve of $R(P_{tot})$ is plotted in Figure 2.

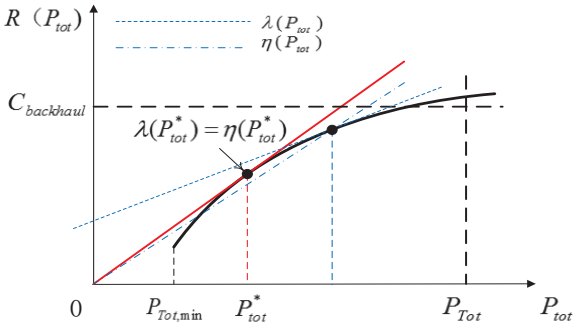

Figure 2. Simple Intuitive Illustration of $R(P_{tot})$

Lemma 1: $R(P_{tot})$ is continuously differentiable in P_{tot} and $R'(P_{tot}) = \lambda(P_{tot})$ is decreasing in P_{tot}, where $P_{tot} \in (P_{Tot,\min}, P_{Tot,\max})$.

Proof: please refer to Appendix for a proof of Lemma 1.

As illustrated in Figure 2, the slope of the origin-to-$(P_{tot}, R(P_{tot}))$ is $\eta(P_{tot}) = \frac{R(P_{tot})}{P_{tot}}$, which represents the maximum system EE at P_{tot}. By Lemma 1, we have that the tangent at $(P_{tot}, R(P_{tot}))$ is $\lambda(P_{tot})$. It is obvious to see that the slope $\eta(P_{tot})$ first increases and then decreases with growing of P_{tot} as well as the optimal EE is achieved when $\eta(P_{tot}^*) = \lambda(P_{tot}^*)$. When taking the constraints (4c) and (4d) into consideration, it is straightforward that (4c) and (4d) correspond to an upper lower bound on λ, say $\lambda_{P_{T,\min}}$ and $\lambda_{C_{b,\min}}$, respectively. This is because that $\lambda(P_{tot})$ is decreasing in P_{tot} which is described in Lemma 1. Obviously, the system lower bound $\lambda_{\min} = \max(\lambda_{P_T,\min}, \lambda_{C_b,\min})$ and $\lambda_{\max}$ is determined by $P_{Tot,\min}$. Therefore, if the optimal λ^* of $\mathcal{P}3$ falls into the interval $[\lambda_{\min}, \lambda_{\max}]$, it is also the optimal λ^* of $\mathcal{P}2$. If not, $\lambda^* < \lambda_{\min}$ must be satisfied and optimal λ^* of $\mathcal{P}2$ is replaced by $\lambda_{\min}$. $\lambda^* > \lambda_{\max}$ would not occur due to the lower bound of total power consumption.

According to the above analysis, we design an energy efficiency power allocation algorithm in the following Algorithm 1, which is based on Dinkelbachs method.

IV. Numerical Results

In this section, simulation results and discussions are presented to evaluate the effectiveness of our proposed energy

Algorithm 1 Energy Efficiency Power Allocation Algorithm

Initialize λ satisfying $F(\lambda) \geqslant 0$ and tolerance ε;
while $(|F(\lambda)| > \varepsilon)$ **do**
  Determine $p_k^*(\lambda)$ in (12) and $F(\lambda)$ in (10);
  $\lambda \leftarrow \frac{\sum_{k\in\mathcal{K}} W\log_2(1+g_k p_k^*(\lambda))}{\zeta \sum_{k\in\mathcal{K}} p_k^*(\lambda)+P_c}$;
end while
Calculate $\lambda_{\min} = \max(\lambda_{P_T,\min}, \lambda_{C_b,\min})$;
if $\lambda \geqslant \lambda_{\min}$ **then**
  $\lambda^* = \lambda$;
else
  $\lambda^* = \lambda_{\min}$;
end if
return $p_k^*(\lambda^*)$;

Figure 3. Energy Efficiency Power Allocation Algorithm

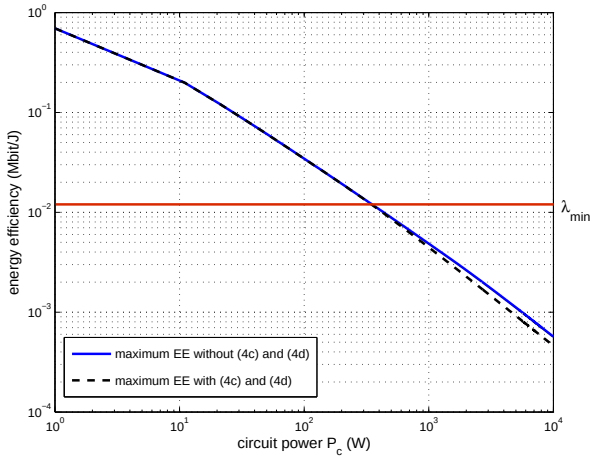

Figure 4. Energy Efficiency versus the circuit power for $\mathcal{P}3$ and $\mathcal{P}2$

efficiency power allocation algorithm. We use Matlab for the simulation. In our simulation, the total bandwidth, 0.5MHz, is equally divided into 20 orthogonal subcarriers and assigned to 20 users, as well as the carrier frequency is selected to 2GHz. The requirement of each user is 100kbit and the peak power at each subcarrier is set to 10W. For simplicity, we set the drain efficiency of power amplifier as 1. The AeNB is assumed to $500m$ high, all users are uniformly distributed in a circle around the AeNB and the radius of which is $3km$. The practical channel factor has been described in (7)(8). According to Holis et al. [7], we choose the Dense Urban environment for our simulation and the probability of LOS is then determined. The power spectrum of the noise equals to -110dBm/Hz.

Figure 4 depicts the impact of static circuit power on the energy efficiency for the problem of $\mathcal{P}3$ and $\mathcal{P}2$, i.e., without and with the consideration of total power and backhaul capacity constraints. The maximum total power and the backhaul capacity are set to 40W and 5Mbit, respectively. Note that the energy efficiency is decreasing with the increase of static circuit power. λ_{min} here is co-determined by the total power and backhaul capacity. When the circuit power is small,

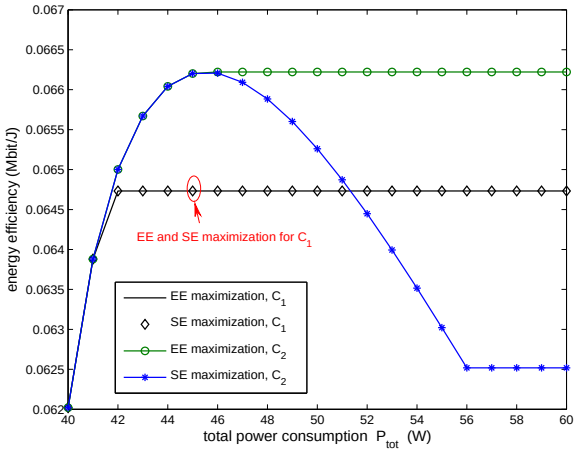

Figure 5. Energy Efficiency versus the total power consumption for different backhaul capacity

these two constraints has no effect on the energy efficiency and this case corresponds to the optimal λ^* of $\mathcal{P}3$ falls into $[\lambda_{\min}, \lambda_{\max}]$. However, when circuit power goes large, the energy efficiency is limited by these two constraints since the optimal λ^* of $\mathcal{P}3$ is less than λ_{min}.

Figure 5 illustrates the energy efficiency versus the total power consumption for different backhaul capacity. The static power is fixed to 35W, so the increase of total power is caused by transmit power only. The backhaul capacity C_1 and C_2 are set to 2.7Mbit and 3.5Mbit, respectively. In Figure 5, EE maximization is our proposed algorithm and SE maximization is achieved by maximizing the system throughput under the same constraints. It can be observed that when the total power is large enough, the energy efficiency of each algorithm approaches a constant value. However, for EE maximization and $C_{backaul} = C_2$ case, this is because that the maximum energy efficiency is obtained and thus resource allocator is not willing to consume more power. For other three cases, the constant value is caused by limited backhaul capacity.

V. Conclusion and Future Work

In this paper, we consider the downlink energy efficiency power allocation for a single OFDM-based aerial system with limited satellite backhaul. Due to the non-convex backhaul capacity limit, the problem is solved in two steps by exploring the properties of fractional programming and the derivative of $R(P_{tot})$. Then, an energy efficiency power allocation algorithm is proposed. Finally, theoretical analysis is corroborated by numerical experiments. The cooperation between multiple aerial systems can be considered in our future work.

Acknowledgment

This work is supported by National 863 Project (2012AA01A50604) and National Nature Science Foundation of China (61421061, 61431003).

Appendix
Proof of Lemma 1

In Xiong et al. [5], $R(P_{tot})$ with the individual power constraint $p_k \geq 0$ is proved to be differentiable. In this

$$
\begin{aligned}
R'_{+}(P_{tot}) &= \lim_{\Delta P^{+}_{tot}\to 0} \frac{R(P_{tot}+\Delta P_{tot})-R(P_{tot})}{\Delta P_{tot}} \\
&= \lim_{\Delta P^{+}_{tot}\to 0} \frac{\left(\max\limits_{\Delta p_k \geqslant 0} \sum\limits_{k\in K} W\log_2(1+g_k(\hat{p}_k+\Delta p_k))\right) - \sum\limits_{k\in K} W\log_2(1+g_k\hat{p}_k)}{\Delta P_{tot}} \\
&= \lim_{\Delta P^{+}_{tot}\to 0} \frac{\max\limits_{\Delta p_k \geqslant 0} \sum\limits_{k\in \mathcal{K}} W\log_2 e \ln\left(1+\frac{g_k\Delta p_k}{1+g_k\hat{p}_k}\right)}{\Delta P_{tot}} \approx \lim_{\Delta P^{+}_{tot}\to 0} \frac{\max\limits_{\Delta p_k \geqslant 0} \sum\limits_{k\in \mathcal{K}} \frac{Wg_k\log_2 e}{1+g_k\hat{p}_k}\Delta p_k}{\Delta P_{tot}} \\
&= \lim_{\Delta P^{+}_{tot}\to 0} \frac{\max\limits_{\Delta p_k > 0} \sum\limits_{k\in \mathcal{K}-\mathcal{K}'} \frac{Wg_k\log_2 e}{1+g_k\hat{p}_k}\Delta p_k}{\Delta P_{tot}} \overset{(a)}{=} \max_{k\in\mathcal{K}-\mathcal{K}'} \frac{Wg_k\log_2 e}{\zeta(1+g_k\hat{p}_k)}. \qquad (15)
\end{aligned}
$$

$$
\begin{aligned}
R'_{-}(P_{tot}) &= \lim_{\Delta P^{-}_{tot}\to 0} \frac{R(P_{tot}+\Delta P_{tot})-R(P_{tot})}{\Delta P_{tot}} \approx \lim_{\Delta P^{-}_{tot}\to 0} \frac{\max\limits_{\Delta p_k < 0} \sum\limits_{k\in \mathcal{K}-\mathcal{K}'} \frac{Wg_k\log_2 e}{1+g_k\hat{p}_k}\Delta p_k}{\Delta P_{tot}} \\
&= \min_{k\in\mathcal{K}-\mathcal{K}'} \frac{Wg_k\log_2 e}{\zeta(1+g_k\hat{p}_k)}. \qquad (16)
\end{aligned}
$$

paper, we further prove that $R(P_{tot})$ is differentiable and the derivative of $R(P_{tot})$ is continuous and decreasing. We consider the limit under the constraint $\sum\limits_{k\in\mathcal{K}} \Delta p_k = \Delta P_{tot}$ and let $\hat{p}_k$ denote the optimal power allocation at the kth subcarrier under the total power consumption P_{tot}.

According to the definition of derivative, we derive that (15) is satisfied, in which $\mathcal{K}' = \{k|\Delta p_k = 0, k \in \mathcal{K}\}$. We have $\Delta p_k = 0$ if either of the following two cases occurs, i.e., (a) $\hat{p}_k = p_{\min}$ and $\exists k' \in \mathcal{K}$, $\hat{p}_{k'} > p_{k',\min}$ and the water level at the k'th subcarrier is lower than that of kth subcarrier; (b) $\hat{p}_k = p_{peak}$. $\overset{(a)}{=}$ is obtained since $\max\limits_{\Delta p_k>0} \sum\limits_{k\in\mathcal{K}-\mathcal{K}'} \frac{Wg_k\log_2 e}{1+g_k\hat{p}_k}\Delta p_k = \left(\max\limits_{k\in\mathcal{K}-\mathcal{K}'} \frac{Wg_k\log_2 e}{\zeta(1+g_k\hat{p}_k)}\right)\left(\sum\limits_{k\in\mathcal{K}-\mathcal{K}'} \Delta p_k\right)$.

If $\mathcal{K}' = \phi$, $\max\limits_{k\in\mathcal{K}} \frac{Wg_k\log_2 e}{\zeta(1+g_k\hat{p}_k)}$ is equivalent to $\min\limits_{k\in\mathcal{K}} \frac{1}{g_k} + \hat{p}_k$. According to $\hat{p}_k = \frac{W\log_2 e}{\lambda_+(P_{tot})\zeta} - \frac{1}{g_k}$, we know that $\min\limits_{k\in\mathcal{K}} \frac{1}{g_k} + \hat{p}_k = \frac{W\log_2 e}{\lambda_+(P_{tot})\zeta}$, where $\frac{W\log_2 e}{\lambda_+(P_{tot})\zeta}$ is the water level under P_{tot}. Hence, we have $R'_{+}(P_{tot}) = \lambda_+(P_{tot})$. If case (a) or (b) occurs, $\mathcal{K}' \neq \phi$. In this case, $\min\limits_{k\in\mathcal{K}-\mathcal{K}'} \frac{1}{g_k} + \hat{p}_k = \frac{W\log_2 e}{\lambda_+(P_{tot})\zeta}$ is also satisfied. However, $\frac{W\log_2 e}{\lambda_+(P_{tot})\zeta}$ here denotes the water level without regard to the kth ($k \in \mathcal{K}'$) subcarrier. As a whole, $\frac{W\log_2 e}{\lambda_+(P_{tot})\zeta}$ denotes the water level at the kth ($k \in \mathcal{K} - \mathcal{K}'$) subcarrier which would increase if the value of P_{tot} grows ΔP_{tot}.

Similarly, (16) is derived. In this case, we have $\Delta p_k = 0$ if either of the following two cases occurs, i.e., (c) $\hat{p}_k = p_{peak}$ and $\exists k' \in \mathcal{K}$, $\hat{p}_{k'} < p_{peak}$ and the water level at the k'th subcarrier is higher than that of kth subcarrier; (d) $\hat{p}_k = p_{k,min}$. Analogously, $R'_{-}(P_{tot}) = \lambda_-(P_{tot})$ is satisfied and $\frac{W\log_2 e}{\lambda_-(P_{tot})\zeta}$ here represents the water level at the kth ($k \in \mathcal{K}'$) subcarrier which would decrease if the value of P_{tot} reduces ΔP_{tot}.

Obviously, water level $\frac{W\log_2 e}{\lambda_+(P_{tot})\zeta} = \frac{W\log_2 e}{\lambda_-(P_{tot})\zeta}$ holds for any given $P_{tot} \in (P_{Tot,\min}, P_{Tot,\max})$. Then, we have $R'_{+}(P_{tot}) = R'_{-}(P_{tot}) = \lambda(P_{tot})$. The existence of the limit indicates that $R(P_{tot})$ is differentiable in P_{tot}. Clearly, the growing of water level is continuous as the value of P_{tot} gets larger. Therefore, $\lambda(P_{tot})$ is continuously decreasing since its inversely proportional with water level. This completes the proof of lemma 1.

REFERENCES

[1] K. Gomez, T. Rasheed, L. Reynaud and I. Bucaille, "Realistic deployments of LTE-based Hybrid Aerial-Terrestrial Networks for public safety", Computer Aided Modeling and Design of Communication Links and Networks (CAMAD)2013 IEEE 18th International Workshop on, Sep 2013, pp.233-237.

[2] I. Bucaille, S. Hethuin, A. Munari, R. Hermenier and S. Allsopp, "Rapidly Deployable Network for Tactical Applications: Aerial Base Station with Opportunistic Links for Unattended and Temporary Events ABSOLUTE Example", Military Communications Conference, MILCOM 2013-2013 IEEE, Nov 2013, pp. 1116-1120.

[3] S. Kandeepan, K. Gomez, T. Rasheed and L. Reynaud, "Aerial-Terrestrial Communications: Terrestrial Cooperation and Energy-Efficient Transmissions to Aerial-Base Stations", IEEE Transactions on Aerospace and Electronic Systems, vol.50, no.4, Oct 2014, pp. 2715-2735.

[4] T. Wang, "Energy-efficiency maximization for OFDMA networks with total power constraint", Communications in China (ICCC), 2013 IEEE/CIC International Conference on, Aug 2013, pp. 357-361.

[5] C. Xiong, G. Y. Li, S. Zhang, Y. Chen and S. Xu, "Energy-efficient resource allocation in OFDMA networks", IEEE Transactions on Communications, vol.60, no.12, Dec 2012, pp. 3767-3778.

[6] J. Mao, G. Xie, J. Gao and Y. Liu, "Energy efficiency optimization for OFDM-based cognitive radio systems: a water-filling factor aided search method", IEEE Transaction on Wireless Communications, vol.12, no.5, May 2013, pp. 2366-2375.

[7] J. Holis and P. Pechac, "Elevation dependent shadowing model for mobile communications via high altitude platforms in built-up areas", IEEE Transactions on Antennas and Propagation, vol.56, no.4, Apr 2008, pp. 1078-1084.

[8] S. Boyd and L. Vandenberghe, Convex optimization. Cambridge University Press, 2004.

[9] C. Isheden, Z. Chong, E. Jorswieck and G. Fetttweis, "Framework for link-level energy efficiency optimization with informed transmitter", IEEE Transaction on Wireless Communications, vol.11, no.8, Jun 2012, pp. 2946-2957.

 ISBN: 978-1-61208-397-1

Preliminary Performance Analysis of Space-based AIS Payload for KOMPSAT-6

Yong-Min Lee, Byoung-Sun Lee
Satellite & Wireless Convergence Research Dept.
Electronics and Telecommunications Research Institute
Daejeon, Republic of Korea
ymlee01@etri.re.kr,

***Abstract*—Space-based automatic identification system (AIS) payload has been designed conceptually to provide a platform for AIS signal collection, down conversion, and demodulation of the AIS burst signals operating at VHF band. AIS receiver uses a reconfigurable Software Defined Radio (SDR) technology, which has digital filtering and cross-correlation functions within field programmable gate array (FPGA) device and demodulation of Gaussian minimum-shift keying (GMSK) waveform by a general purpose processor. AIS receiver is able to operate in either or both on-board processing (OBP) mode and on-ground-processing (OGP) mode depending on the availability of communications links, on-board resources and the user preference. In this paper, the link budget analysis and detection probability have carried out as a basic performance analysis of AIS payload for KOMPSAT-6.**

Keywords-space-based AIS; software defined radio; GMSK; on-board processing; on-ground processing; KOMPSAT-6.

I. INTRODUCTION

With greater emphasis being placed on global situational awareness, global asset monitoring, environmental monitoring, maritime and terrestrial sensor, and data acquisition systems are critical enabling capabilities that are becoming more ubiquitous [1].

A space-based AIS payload makes use of AIS system beyond the intended 4S (Ship-to-Ship and Ship-to-Shore) communications. A satellite even microsatellite equipped with an AIS receiver can provide reliable services in widely trafficked area.

The Korean government had started to develop a multi-purpose low earth orbit satellite named KOMPSAT-6. KOMPSAT-6 satellite will accommodate Synthetic Aperture Radar (SAR) as a primary payload and Automatic Identification System (AIS) as a secondary payload.

The focus on this paper is to develop a conceptual design for a space-based AIS payload for KOMPSAT-6 with special emphasis on the performance analysis of ship-to-satellite link budget and detection probability versus the number of ships.

II. SDR BASED AIS RECEIVER

AIS payload for KOMPSAT-6 was designed to collect, down-convert, detect and demodulate the AIS burst signals from vessels. AIS receiver processes two groups of AIS messages in terms of dynamic messages every 2~10 seconds and static messages every 6 minutes.

Software defined radio architecture for AIS receiver includes the digital filtering and cross-correlation function within a field programmable gate array (FPGA) device and demodulation of Gaussian minimum-shift keying (GMSK) waveform within a general purpose microprocessor. Store and forward architecture is also allowed for autonomous data collection and archiving from vessels. Figure 1 shows the operational concept of AIS payload for KOMPSAT-6.

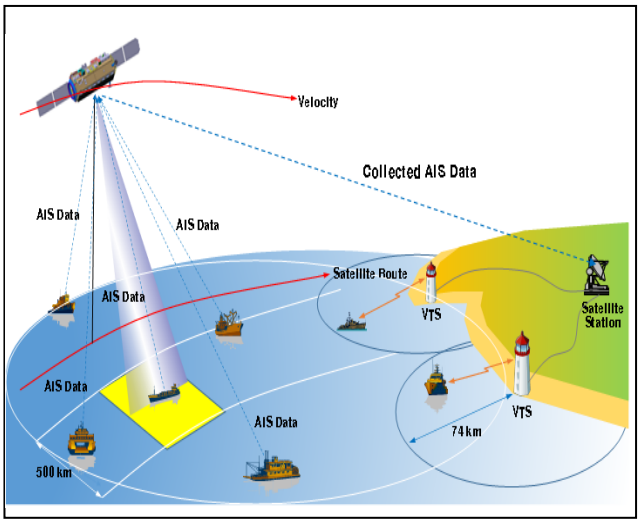

Figure 1. Operational Concept of AIS Payload for KOMPSAT-6

III. OPERATION MODES

The in-flight reconfigurable AIS payload is going to operate in either/both on-board processing mode or/and on-ground processing mode depending on the shipping traffic conditions of the field-of-view.

A. On-Board Procesing (OBP) Mode

The OBP mode leads to a reduced downlink bandwidth requirement but requires more powerful processing capability on-board AIS receiver. In areas with very high traffic density, it is not possible to successfully decode all AIS signals using this mode due to the high number of signal collisions. The OBP mode must not be confused with de-collision which is the process of applying de-collision algorithms to detangle the collided signals. Signal de-collision is only available with OGP.

 ISBN: 978-1-61208-397-1

B. On-Ground Processing (OGP) Mode

In OGP mode, the receivers take snapshot information of the RF environment and downlink the raw data to ground for processing by the very powerful ground processing equipment to apply the de-collision algorithms. This mode requires a lot of data handling and a larger downlink bandwidth to ground due to the amount of raw data generated (~20MB/s).

IV. PERFORMANCE ANALYSIS

The detection of AIS transmissions was recently improved by the introduction of satellite sensors, which enables the collection of AIS over wide areas in the open ocean. However, space-based AIS payload has its own challenges due to the fact that AIS is primarily intended for sea-level reception and therefore leads to performance degradation when observed over large areas from space. It is therefore critical to understand how the performance of these new sensors, and to identify the condition under which the performance is acceptable for operational use.

Another issue is the message collision and the message loss. All exchanged messages transmitted from ships on the sea are synchronized and guaranteed the functions of the system without any message loss. On the other hand, AIS messages received at satellite from lots of vessels at the same time with the same frequency cause a message collision and lead to message loss [2].

In this paper, the link budget and detection probability analysis have carried out as the main factors impacting the performance.

A. Link Budget Anlysis

A substantial part of the AIS payload design is to evaluate the received power from the ships compared to the noise power in term of carrier-to-noise (C/N) ratio.

Table I shows a rough link budget calculated for ships near the edge of the satellite swath. The received power at satellite is -107.1 dBm and the link margin is about 4.8 dB. If we take into account some potential losses due to Doppler shift and ionosphere effects, the margin may go down a few but more sensitive receiver will help to increase the margin.

B. Dectection Probability

Basically AIS is designed as a ship collision avoidance system for terrestrial use and used a multiple access scheme called self-organized time domain multiple access (SOTDMA) that assigns approximately 2,000 time slots, automatically and dynamically, to ships in local “cells”, that is, ships within VHF range of each other [3]. This communication protocols make sure that interferences cannot occur with normal traffic density.

However, a space-based AIS payload receives signals from a number of cells over the antenna footprint and a time slot is not coordinated properly. It means that signal collisions occur from other ships outside its self-organizing cell.

TABLE I. RESULTS OF AIS LINK BUDGET ANLAYSIS

AIS Transmission Parameter	Value
AIS-1 Frequency (MHz)	161.975
AIS-2 Frequency (MHz)	162.025
Data Rate (bits/sec)	9600
Line code	NRZI
Modulation	GMSK
Number of Training Bits	24
Transmit Bandwidth Time Product	0.4
Receive Bandwidth Time Product	0.5
Class A Transmit Power (W)	12.5
Channel Bandwidth (kHz)	25
Geometry	
Range (km)	530
MinTransmit Elevation Angle (Deg)	0
Satellite Antenna Off-axis Angle (Deg)	67.5
Maximum Slant Range (km)	2183
Maximum Surface Range (km)	2018
Power	
AIS Transmit Power (dBm)	41.0
Ship Antenna Gain (dBi)	2.0
Transmit Cable & Other Loss (dB)	3.0
Free Space Loss at Max Range (dB)	143.2
Polarization Mismatch Loss (dB)	3.0
Satellite Antenna Gain at Horizon (dBi)	1.6
Satellite RF Cable & Filter Loss (dB)	2.4
Satellite Received Power (dBm)	-107.1
Receiver Sensitivity (dBm) @ 20% PER	-112.0
Link Margin (dB)	4.8

The probability of detection of an uncorrupted ship’s AIS message for KOMPSAT-6 has calculated with the different observation time shown in Figure 2 [4].

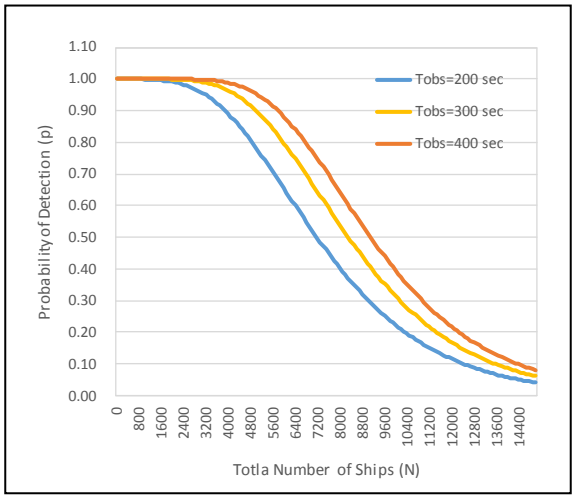

Figure 2. Probability of detection vursus total number of ships

 ISBN: 978-1-61208-397-1

V. CONCLUSIONS

In this paper, we have looked at general considerations around AIS payload and evaluated the feasibility for a space-based AIS receiver for KOMPSAT-6 conceptual design with respect to a basic link budget and detection probability. It can be concluded that there is sufficient margin about 4.8 dB to receive messages from ships and interferences between AIS messages will depend upon the number of vessels in the field-of-view. In order to improve the performances of AIS payload, there are ways to implement the interference cancellation schemes by using antenna diversity methods and de-collision algorithms on the ground.

REFERENCES

[1] Marion “Rick” Earles and CANEUS Shared Small Satellites CSSP Workshop Committee, “International Space-Based AIS and Data Extraction Backbone - High Level Requirements”, CANEUS International, 2010.

[2] Rob Goldsmith, “Preparatory Action for Assessment of the Capacity of Spaceborne Automatic Identification System Receivers to Support EU Maritime Policy : The PASTA MARE Project”, Maritime forum, October 2010.

[3] James K.E. Tunaley, “Space-Based AIS Performance”, LRDC, May 2011.

[4] Yong-Min Lee and Byoung-Sun Lee, “Conceptual Design of Space-Based AIS System”, KSAS fall conference, November 2014.

 ISBN: 978-1-61208-397-1

Tactically Extensible and Modular Communications - X-Band

TEMCOM-X

William Herbert Sims
National Aeronautics and Space Administration
NASA / MSFC / ES63
Huntsville, USA
Herb.sims@nasa.gov

Kosta A. Varnavas
National Aeronautics and Space Administration
NASA / MSFC / ES33
Huntsville, USA
Kosta.A.Varnavas@nasa.gov

Joseph Casas
Science and Space Technology Projects Office
NASA Marshall Space Flight Center
Huntsville, USA
joseph.casas@nasa.gov

Stephen L. Spehn
Deputy Science Advisor
U.S. European Command
Stuttgart, Germany
stephen.l.spehn.civ@mail.mil

Neal Kendrick
Dynetics, Inc.
Huntsville, USA
Neal.Kendrick@dynetics.com

Stephen Cross
Dynetics, Inc.
Huntsville, USA
Steve.Cross@dynetics.com

Paul Sanderson
Dynetics, Inc.
Huntsville, USA
Paul.Sanderson@dynetics.com

Janice C. Booth
U.S. Army Aviation and Missile Research,
Development, and Engineering Center (AMRDEC)
Huntsville, USA

***Abstract*— This paper will discuss a proposed CubeSat size (3U) telemetry system concept being developed at Marshall Space Flight Center (MSFC) in cooperation with the U.S. Department of the Army and Dynetics Corporation. This telemetry system incorporates efficient, high-bandwidth communications by developing flight-ready, low-cost, Proto-flight software defined radio (SDR) and Electronically Steerable Patch Array (ESPA) antenna subsystems for use on platforms as small as CubeSats and unmanned aircraft systems (UASs). The current telemetry system is slightly larger in dimension of footprint than required to fit within a 0.5U CubeSat volume. Extensible and modular communications for CubeSat technologies will partially mitigate current capability gaps between traditional strategic space platforms and lower-cost small satellite solutions. Higher bandwidth capacity will enable high-volume, low error-rate data transfer to and from tactical forces or sensors operating in austere locations (e.g., direct imagery download, unattended ground sensor data exfiltration, interlink communications), while also providing additional bandwidth and error correction margin to accommodate more complex encryption algorithms and higher user volume.**

Keywords-Software Defined Radio, Tactically Extensible, Electronically Steerable Phased Array, unattended ground sensors.

I. INTRODUCTION

This paper provides information on the Marshall Space Flight Center (MSFC) SDR Low-Cost Transponder as well as the Army/Dynetics Electronically Steerable Phased Array - X-Band (ESPA-X) that contributes to advancing the state-of-the-art in telemetry system design – directly applicable to the SmallSat and CubeSat communities. The SDR, called PULSAR – Programmable Ultra Lightweight System Adaptable Radio – as well as the ESPA-X can be incorporated into orbital and suborbital platforms. In doing so, Tactically Extensible and Modular Communications - X-Band (TEMCOM-X) will allow project/programs to perform remote commanding capabilities, as well as real-time payload(s) and science instruments telemetry, all of which are self-supporting infrastructures requiring both component and system level work to complete.

Current CubeSats do not have sufficient bandwidth for transmit and receive to support innovative payload designs and complex encryption schemes being developed by the CubeSat community (academic, military, civil, industry) to support increasing bandwidth with low error-rate demands on the tactical edge[1]. The leap ahead technology is the low-cost space / high-altitude qualified reconfigurable SDR transponder for simultaneous X-band transmit and receive communications at a minimum of 110 Mbps. In addition, the SDR has a highly efficient SWaP (less than 50% of traditional Size, Weight and supply Power), which achieves higher bits per input supply watt (at ~10 Mbits per input

 ISBN: 978-1-61208-397-1

watt) than traditional communication SDR systems (at ~300Kbits per input watt). [2]

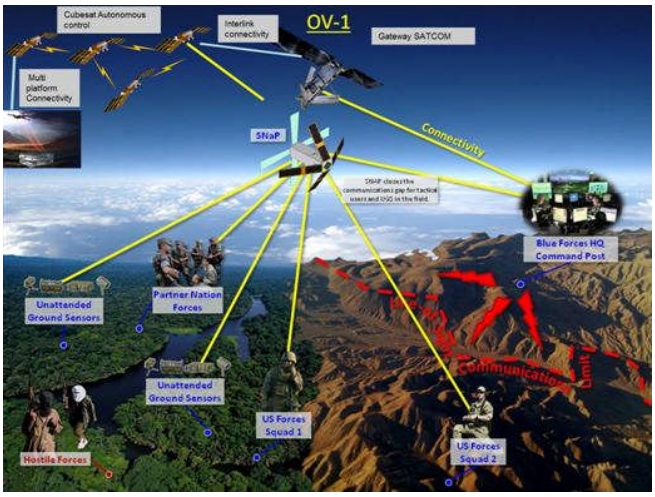

Figure 1. Tactically Extensible and Modular Communications - X-Band (TEMCOM-X)

Due to the SDR technology flexibility, TEMCOM-X can be used on any type of aircraft, UAV, orbital, or sub-orbital platforms and tailored to each mission's requirements. TEMCOM-X low cost and size, weight, and power (SWaP) makes it attractive for CubeSat and micro satellite missions.

The matched low profile form factor electronically steerable array antenna provides mission adaptive beam forming for optimizing signal to noise ratios with extensibility in the design approach for future multiple independently steerable beams from the same antenna array.[3]

This paper will discuss the technical approach being proposed showing the extensibility of the system. Further the performance of the overall system will be discussed. TEMCOM-X will be shown to align with current NASA Strategic Space Technology Investment Plan.[4] The discussion will then migrate to the Electronically Steerable Patch Array – X-Band (ESPA-X). The final area of discussion will show one possible operational scenario.

II. TECHNICAL APPROACH

The proposed TEMCOM-X Project leverages the lessons learned during the PULSAR telemetry system (First Generation) development, which used NASA funds from FY2012-13. The project objective is to advance the TEMCOM-X design to a proto-flight unit, which will be accomplished by reducing the overall size of PULSAR to fit within a 1U form factor. PULSAR currently uses non-radiation tolerant hardware to keep costs low, with a clearly defined path to radiation tolerance.

The TEMCOM-X base design will have up to four selectable decks – power deck, processor deck, X-Band receiver deck, and X-Band telemetry transmitter deck. The application determines the configuration, thus the number of decks used.

The current PULSAR power deck will be reduced in overall footprint to meet the 1U CubeSat dimensions. The operating voltage of TEMCOM-X is proposed to be from 16VDC to 50VDC (the same as PULSAR).

The current PULSAR Processor deck has been proposed to provide beam-forming control for the ESPA-X antenna. Having a processor deck dedicated to a transponder communication system was a first in industry.

The proposed X-Band Receiver deck will leverage the IP and lessons learned from the PULSAR S-Band Receiver. Command and Data (uplink) capabilities will be on the order of 150Mbps.

The transmitter deck will produce up to 2 W of radio frequency (RF) output. The RF output power can be tailored to any particular mission. The telemetry transmitter deck streams data with OQPSK modulation at a maximum data rate of 110 Mega-bits per second (Mbps).

Exemplifying flexibility, PULSAR currently transmits using Reed-Solomon (223/255) Forward Error Correction (FEC). Future enhancements will include Low Density Parity Check (LDPC, rate 7/8), or convolutional (Rate ½) based on mission requirements. Currently the LDPC encoding algorithm has been verified in simulation at MSFC as well as in independent external testing. TEMOCOM-X can incorporate other error correction algorithms, as necessary.

The antenna array (front-end) will incorporate a planar design consisting of multiple board layers with integrated array circuitry to reduce the array depth.

III. PERFORMANCE

Table shows a market analysis of industry transponders and differentiates their features compared to PULSAR.[5] In comparison, the NASA-MSFC SDR incorporates the latest in Forward Error Correcting (FEC) codes and utilizes State-of-the-Art electronic components which give PULSAR the capability to achieve much higher Bits-per-Watt (the industry standard benchmark showing data rate versus power).

TABLE I. 2012 MARKET ANALYSIS OF TYPICAL INDUSTRY TELEMETRY TRANSPONDERS

Maker	Unit	Freq. Band	Downlink Data Rate, Mbps	Mass, kg	Bench-mark, b/W
NASA-MSFC	PULSAR	S-, X-	150	2.1	10e6
L3 Comm	Cadet	S-	100	0.215	8.3e6
Innoflight	SCR-100	S-	4.5	0.25	3e6
L-3 TW	CTX-886	X-	400	3.85	5.3e6
Space Micro	µSTDN-100	S-	4	2.1	0.7e6
Harris Corporation	SCaN	Ka	100	19.2	2.5e6
General Dynamics	SCaN	S-	10	-	1.0e6
Jet Propulsion Laboratory	SCaN	S-	10	6.6	1.0e6

 ISBN: 978-1-61208-397-1

PULSAR exceeds most of the other units in term of the industry benchmark. The L-3 TW CTX-886 exceeds PULSAR in data rate, but PULSAR has less mass (2.1 versus 3.85 kg) and uses less power (15 versus 75 watts – not shown in table).

The system contains sufficient RF link capacity to achieve the desired performance while maintaining the goal Bit Error Probability (BEP) assuming that the design goal gain (19.76dBi) can be met.

Table 2 lists the RF link margin assumptions. The calculation was performed using the IRIG 119 method.

$$SNR = P_T - L_{C(T)} + G_T - L_P - L_M - L_{Pol} - L_A + G/T - kB$$

P_T = Transmitter Power
$L_{C(T)}$ = Transmitter Cable Loss
G_T = Transmitter Antenna Gain
L_P = Path Loss
L_M = Multipath Loss
L_{Pol} = Polarization Mismatch Loss
L_A = Atmospheric Attenuation
G/T = Receiving System Figure of Merit
kB = Boltzmann's constant x Bandwidth

Results were correlated using an Error Bit/Noise calculation method.

TABLE II. LINK MARGIN ASSUMPTIONS/CALCULATIONS

	Uplink		Downlink	
Frequency	8.2GHz		8.2GHz	
P_T	50W	47dBm	1W	30dBm
$L_{C(T)}$	1dB		1dB	
G_T	43.9dBi[1]		19.76dBi[2]	
L_P	2448km[3]	178.5dB	2448km[3]	178.5dB
L_M	0dB		0dB	
L_{Pol}	0.25dB		0.25dB	
L_A	1.0dB		1.0dB	
G/T	-4.91dB/K[4]		22.5dB/K[1]	
Data Rate	150Mbps		150Mbps	
kB	-116.84dB		-116.84	
SNR	22.08dB		8.35dB	
Threshold	No FEC	12.0dB[5]	FEC	5.0dB[6]
Margin	**+10.08dB**		**+3.35dB**	

1 – Documented performance of GATR 2.4m X-band antenna system.

2 – Design goal performance of Dynetics Phased Array Antenna.

3 – Max slant range calculated from satellite to ground station for 650km orbit and 5° elevation.

4 – Calculated assuming design goal Gain with low loss feed system and LNA noise figure of 2.5dB maximum.

5 – Required SNR for BEP of $1x10^{-5}$

6 – Required SNR for BEP of $1x10^{-12}$ using LDPC FEC

IV. ALIGNMENT

NASA is called, at the direction of the President and Congress, to maintain an enterprise of technology that aligns with missions and contributes to the Nation's innovative economy. NASA has been and should be at the forefront of scientific and technological innovation. In response to these calls, NASA generated a plan (NASA Strategic Space Technology Investment Plan) to advance technologies and nurture new innovation that will feed into future missions. PULSAR aligns primarily with the Technology Area (TA) 5 – Communication & Navigation – but has connections to other TAs in which lightweight structures, power efficiency, and communication reliability and throughput are the focus.[6]

V. ESPA-X

The current proposed design of the ESPA-X includes a radiating element that is a circularly polarized patch antenna with +8dBi gain with a maximum 11 dB return loss (1.78 VSWR) in the band of interest. The T/R module will transmit in horizontal polarization and receive in vertical. This design decision prevents the need for a second circulator adjacent to the antenna element, and it should provide sufficient isolation between the two paths.

In order to achieve the desired 100 W (+50dBm) Effective Radiative Power (ERP) on transmit, each of the 15 patch antenna elements' input power must be approximately 18.5 dBm. The transmit gain profile assumes that the +36 dBm from the diplexer will arrive at each element after a series of four two-way power dividers, with each divider incurring an approximate loss of 4 dB (hence the +20 dBm input power to the TR module transmit chain.) The transmit chain is quite simple, with a phase shifter (nominal 7 dB loss), an amplifier, and a harmonic reject filter (nominal 1.5 dB loss).

The receive chain gain distribution assumes a 0.4 dB loss through the patch antenna and a 1.2 dB loss through the front-end bandpass filter. The LNA's noise figure of 0.6 dB is sufficient to insure that the overall transmit chain's noise figure will remain below the required 2.5 dB.

VI. OPERATIONAL SCENARIO

The operational scenario in the graphic shown in the Introduction depicts U.S. and Partner nation (PN) small-unit forces operating beyond line-of-sight communications with their command center, and in close proximity to hostile forces. The U.S. and PN units have deployed unattended ground sensors (UGS) in key location for remote reconnaissance, and are supported by low-earth-orbit (LEO) assets that incorporate both PULSAR and ESPA-X. The communications requirements of the U.S. and PN forces include:

– Encrypted voice between the small units and the command center;

– Imagery and other map-based data between the small units and the command center;

 ISBN: 978-1-61208-397-1

– Frequent, periodic polling of UGS with forwarding of trigger information from the UGS to the small units and the command center; and

– Relay of imagery, full-motion video (FMV), and other near-real-time data from airborne and orbital sensor platforms to the small units and the command center.

These communications requirements are individually serviceable through existing systems, and collectively serviceable through combinations of existing systems, but TEMCOM-X provides unique advantages, to include:

– Increased bandwidth to service larger data demands with fewer assets;

– Multiple beam-forming to provide simultaneous access to frequency bands with reduced error rates;

– Provides high rate bandwidth for satellite interlink communications;

– Full duplex transmit and receive for maximizing communication opportunities;

– Tailored spot beams for prioritized service to critical assets; and

– Dynamically adaptable waveforms to support multiple disparate systems simultaneously.

VII. CONCLUSION

The TEMCOM-X concept is currently in the late formulation stages and has been proposed for full implementation to develop and test a protoflight unit of the integrated PULSAR-X and ESPA-X technologies to support X band communication systems for cubesat and small aircraft platform compatibility.

TEMCOM-X leverages existing Marshall Space Flight Center SDR designs and commercially enhanced capabilities. Innovations will

(1) Reduce the cost of Low Earth Orbit (LEO) and Deep Space transponders,

(2) Increase data through-put,

(3) Decrease power requirements, and

(4) Reduce volume.

Also, TEMCOM-X concept increases flexibility to implement multiple transponder types by utilizing the same hardware with altered logic – no hardware change required – all of which will eventually be accomplished in orbit. The flexibility permits CubeSat and SmallSat programs to select only what they need for their mission.

TEMCOM-X offers high capability, low cost, transponders to programs of all sizes. The final project outcome will be the introduction of a low-cost CubeSat to SmallSat telemetry system.

The potential future TEMCOM-X Roadmap includes adaptation into options such as C-Band and Ka-Band. These technologies are proposed for continued development.

ACKNOWLEDGEMENTS

I cannot express enough thanks to my supervisors for their continued support and encouragement: Mr. Mark James and Mr. Tim Ezell. To Maegan and Maeson – thank you for allowing me time away from you to complete the research and writing of this paper. Thanks to my parents as well, Mr. and Mrs. William H. Sims, who instilled the work ethics that I have today – it has not gone unnoticed, and is very much appreciated. Finally, to my caring, loving, and supportive wife, Beverly, your encouragement when the research and writing times got rough is much appreciated. It was a great comfort and relief to know that you were willing to provide management of our household activities while I completed this work.

REFERENCES

[1] Klofas, Bryan, and Anderson, Jason; “A Survey of CubeSat Communication Systems,” California Polytechnic State University, November 2008.

[2] Internal NASA email correspondence, 2013-2014.

[3] National Aeronautical and Space Administration, “NASA Strategic Space Technology Investment Plan” NASA Washington, DC, 2013. pp. 1 – 92 , December 2012, retrieved: January,2015

[4] Internal NASA email correspondence, 2013-2014.

[5] Internal NASA email correspondence, 2013-2014.

[6] National Aeronautical and Space Administration, “Draft Communication and Navigation Systems Roadmap – Technology Area 05” NASA Washington, DC, 2010. pp. 1 – 28 , November 2010 , retrieved: January, 2015.

 ISBN: 978-1-61208-397-1

Interference Study in a Proposed Integrated Multi-beam Active Phased Antenna Array Transmission System for Satellite Communications

Victor Ivanovich Nefedov
Department: Telecommunication systems
Governmental Technical University MIREA
Moscow, Russia
Email: nefedov@mirea.ru

Mohamed Atta Aboelazm
Department: Telecommunication systems
Governmental Technical University MIREA
Moscow, Russia
Email: mmziadatta@yahoo.com

***Abstract*— In this paper, an integrated active phased array multi-beam antenna system model including a nonlinear model of the amplifier and a digital pre-distortion linearizer is introduced and validated by simulation. To investigate nonlinearity effects in a phased-array antenna, a two-beam, three-beam, and five-beam S-band arrays are simulated and the results of the proposed system model are analyzed. The presented model is able to precisely predict the inter-modulation products with an accuracy of 1 dB in power with small fraction of a degree in direction. The effect of integrating a digital pre-distortion linearizer is to enhance the efficiency of antenna array transmission power amplifiers. Therefore, the model can be used as a tool to accurately predict the inter-modulation patterns for multi-beam satellite array applications, avoiding excessive system margin and reducing DC power consumption.**

Keywords- SSP; IM; DSP; DPD; LMS; RLS; IBO.

I. INTRODUCTION

Modern satellite communication payloads require high directivity and multiple beams with large signal bandwidth to satisfy broad-band applications, such as multimedia and voice conferences. Therefore, an active phased array is ideal for such applications, since they can be configured in orbit to provide the bandwidth in demand and increase overall system utilization [1]-[3].

The total transmission quality of a communication satellite using a multi-beam phased-array antenna system is most dependent upon the nonlinear distortion of the Solid State Power Amplifier (SSPA) modules [2]. This distortion brings about Inter-Modulation (IM) interferences. The closer to the compression point in order to have the most power efficiency means more IM product levels that degrade Carrier-to-Interference ratio (C/I) associated with beam steering direction. So, accurate modeling of these IM beams helps to control the IM interference, thus allowing the SSPAs to be operated with minimum back-off since fewer margins are needed. This results in a more efficient array that requires a lower system DC power with reduced mass and cost of the satellite [3].

Inter-Modulation Products (IMPs) in an active antenna array have characteristics that are different from those in lumped active circuits and systems. For multi-beam satellite digital communication systems, signal suppression and IMP interference in amplifiers may degrade the bit-error rate 1 to 5 dB in comparison to passive antennas. The presence of interfering signals may result in an increase of the array beam width, sidelobe level, null depth degradation, as well as changing the null positions [2]. Sandrin [4] previously analyzed the radiating patterns of third and fifth orders IM products of active antenna arrays. In his analysis, he derived the phase gradient for the *m*-th order intermodes and used generic transfer functions for modeling nonlinear characteristics of the power amplifier. His analysis incorporates approximations appropriate for limited field of view arrays (as in the case of an earth-looking antenna on a geosynchronous satellite) and for small percentage bandwidth. Kohls [2] presented simulation and experimental results for KU band arrays. Bessel series function approximation is used to fit the above-mentioned model of a KU-band array for predicting third-order IM product beam patterns. Meanwhile, Maalouf et al. [3] studied IM estimation in an active phased-array theoretically and experimentally.

All of these studies involved narrow band signals. This implies that the amplifier characteristics are frequency independent over the frequency band of interest. However, while having broadband input signals, or systems including wide-band amplifiers and relatively narrow-band components, a frequency-dependent quadrature model is required [5]. Johari et al. [6] introduced an amplifier model with considering frequency-dependent parameters to investigate nonlinearity effects in a phased-array antenna and validate the model by experimental data.

For base stations, the major issue is linearity, as the down-link signal must be highly-linear in order to achieve a small error rate and a good quality of reception in mobile terminals. Power amplification of RF signals faces a problem of achieving high linearity and efficiency at the same time. Efficiency is maximized when a PA operates with a small back-off, i.e., close to the saturation region. However, in this mode of operation, nonlinear distortions are produced, which degrade the system linearity. It means that efficiency and linearity are mutually exclusive requirements. A trade-off between them is usually sought for each particular application [7][8].

Linearization techniques for nonlinear microwave power amplifiers have been around for decades, ranging from analog techniques such as feed forward linearization [8][9] and Cartesian loop feedback correction [8], to digital

 ISBN: 978-1-61208-397-1

techniques such as digital pre-distortion linearization [8]-[10].

This paper consists of eight sections. In Section II, the used power amplifier model in the integration process is introduced. Then, the mathematical modeling of IM products is calculated in Section III. Next, the model of radiation farfield pattern is considered in Section IV; a digital pre-distortion linearizer is explained in Section V, and finally the functionality of the proposed integrated system is introduced in section VI. The simulated results are presented in Section VII, and conclusions are given in Section VIII.

II. NONLINEAR SSPA MODEL

Using a complex envelope instead of real narrow band signals; thus, there is no carrier information in the complex envelope except the modulation information is the main idea of quadrature modeling technique. This point is important from the viewpoint of computational efficiency. In the SSPA model, its characteristics are modeled with series of Bessel function coefficients [4] because of their ability to quickly converge to the nonlinear characteristics of the amplifier and model the IM products at the output of the amplifier. The mathematical model provides the gain and phase insertion of each carrier and IM component at the output of the SSPA; therefore, it is suitable to incorporate into the antenna phased-array model. Therefore, this method can achieve the necessary accuracy for active phased array systems [4][7].

The nonlinear behavior of the amplifier can be expressed by the following Bessel function series [7]:

$$g(\rho)e^{j\,\varphi(\rho)} = \sum_{s=1}^{L} \beta_s J_1(\alpha\, s\, \rho) \quad (1)$$

where ρ, g(ρ), and $\varphi(\rho)$ denote the amplitude of the input tone and measured AM/AM and AM/PM single-tone characteristics, respectively. J_1 is the Bessel function of the first kind with order 1; β_s, α, and s are the complex number, the real number, and an integer, respectively. The appendix in [7] shows in detail how the parameters s and α are chosen to evaluate β_s, by a linear search method. Once s and α are selected, β_s is calculated to separately satisfy the real and imaginary parts of (1). In particular, the solution to the following two equations uses the least-squares method [7] as:

$$\sum_{k=1}^{z}\left[g_k\cos\varphi_k - \sum_{s=1}^{L} b_{gs} J_L(\alpha s\rho)\right]^2 = \min,$$
$$\sum_{k=1}^{z}\left[g_k\sin\varphi_k - \sum_{s=1}^{L} b_{ms} J_L(\alpha s\rho)\right]^2 = \min \quad (2)$$

where, z is the number of measured sample points during the characterization of the AM/AM and AM/PM behavior of the amplifier. A typical value for the integer z is less than 20, while α is selected such that $1 < \alpha$. $A_{sat} < 2$, where A_{sat} is the saturation voltage of the amplifier. With s and α are fixed, both equations in (2) are quadratic minimization problems in $\beta_{real}(s)$and $\beta_{imag}(s)$ with known analytical solutions. Equation (2) is solved for several (s, α) pairs, and the solution with the lowest residual error is kept. The final model coefficients are given by $\beta(s) = \beta_{real}(s) + \beta_{imag}(s)$

III. IM MODELING

This section investigates the effects of IM upon the performance of a *K*-element planar phased-array antenna satellite communication system. In an array, the input single of the *k*-th amplifier of the array can be represented by [6]:

$$e(k,t) = \sum_{n=1}^{N} A_{nk}\, e^{-j(2\pi f_n t + \varphi_{nk})} \quad (3)$$

where A_{nk} is the amplitude of the *n*-th channel at the *k*-th element, which, in this work, is assumed constant over time, φ_{nk} is the corresponding phase, and f_n is the carrier frequency at the given channel. At the output of the amplifier, the signal is composed of the amplified carriers and IM components that are introduced by the nonlinear amplifier characteristics. The output signal is expressed as [3][6]:

$$e_o(k,t) = \sum_{n=1}^{N} M(L_p) e^{j\sum_{n=1}^{N} l_n(2\pi f_n t + \varphi_{nk})} \quad (4)$$

where L_P is a vector member of the set

$$L = \{[l_1, l_2, \ldots\ldots, l_N],\ \sum_{n=1}^{N}|l_n| = 1, or\ 3\ or\ 5\ldots.\} \quad (5)$$

where the components that correspond to $\sum_{n=1}^{N}|l_n| = 1$ are carriers, the components that correspond to $\sum_{n=1}^{N}|l_n| = 3$ are third order IM products, and $\sum_{n=1}^{N}|l_n| = 5$ are fifth order IM products. For each index *p*, there is a unique set of integer number l_1 to l_n. In addition, higher order products are ignored because they are lower than the third order, at least 6 dB [3]. Furthermore, the voltage gain of the *p*-th component is derived in, and can be expressed as [7]:

$$M(L_p) = \sum_{s=1}^{S} \beta_s \prod_{n=1}^{N} J_{l_n}(\alpha\, A_{nk}\, s) \quad (6)$$

IV. RADIATING ARRAY MODEL

The radiation pattern of the array is modeled analytically as the product of the element pattern and the array factor, assuming identical element patterns over the array and no mutual coupling. These assumptions are relatively accurate for patch elements with distances of 1.5 times greater than lambda, which are considered in the modeling. Furthermore, it is assumed that the fundamental TM10 mode is propagating in the microstrip patch antenna. Here, the radiating elements are modeled in an array environment, and the array factor's farfield radiation patterns are calculated for both the carriers and IM products based on excitation coefficients generated by the IM algorithm. The farfield array factor radiation pattern $P_p(\theta)$ for each component in any spatial direction is given by the coherent sum of the corresponding SSPA output component given in (7), expressed as[6]:

 ISBN: 978-1-61208-397-1

$$P_p(\theta) = M(L_p)\sum_{k=1}^{K}\left\{\exp j\,\frac{2\pi}{\lambda_p}(\cos\varphi_n x_k + \sin\varphi_n y_k)\sin\theta_n \cdot \exp j\,\sum_{n=1}^{N} l_n \varphi_{nk}\right\} \quad (7)$$

where λ_p is the wavelength of the *p*-th component whose frequency is given by $\sum_{n=1}^{N} l_n f_n$, (x_k, y_k) are the Cartesian coordinates of the array elements, and (θ_n , φ_n) defines the spatial beam directions in spherical coordinates for the *n*-th beam [3].

V. LINEARIZER MODEL

As processing power has become cheaper and more powerful over the last two decades, mainly due to the great advances in Digital Signal Processing (DSP), digital pre-distortion linearization has become one of, if not the most cost efficient linearization technique available for microwave power amplifiers [8]-[10]. The overall goal is to design a block which compensates for nonlinear effects present in the power amplifier in digital baseband, allowing to utilize digital signal processing techniques to achieve great precision [9]. Prior to designing a digital pre-distorter, a model of the nonlinear microwave power amplifier is often required in order to estimate its inverse. the next step is to estimate the model parameters, either by an direct approach with least squares methods, or by an adaptive or iterative approach, i.e., using an adaptive filter such as the Least Mean Square (LMS) filter [10], or the Recursive Least Square (RLS) filter [10].

The Digital Pre-Distortion technique (DPD) has high efficiency, adaptability and good inter-modulation suppression as it is operated before the power amplifier, which means the signal processing does not consume large power [8]-[10].

The best way to solve this problem is to use the discrete time form of Horison model which takes the following mathematical model [10]:

$$y_n = \sum_{k=0}^{N} f_k(x_{n-k}) \quad (8)$$

To compensate for the distortions introduced by the amplifier in the amplified baseband signal, it can be shown that according to Horison model (8), there exists an exact inversion [10]. Indeed, from (8), it follows that [10]:

$$f_0(x_n) = y_n - \sum_{k=0}^{N} f_k(x_{n-k}) \quad (9)$$

It is easy to obtain the inversion system equation as [10]:

$$x_n = \frac{1}{f_0}\left(y_n - \sum_{k=0}^{N} f_k(x_{n-k})\right) \quad (10)$$

Thus, if there is a reversible function f_0, the analytical model of the form (8), which implies its precise handling (9). These functions can be used to implement the nonlinear characteristics of the linearizer as an inverse of PA model.

In the proposed model the basic functions f_0, f_1, f_2, have been chosen to be spline functions, in particular, piecewise linear splines and the cubic parabola (third degree polynomial).

VI. INTEGRATED SYSTEM MODEL

A functional block diagram of the proposed integrated active phased antenna array transmission system is shown in Figure 1. It consists of *M* radiating elements, *M* Solid State Power Amplifiers (SSPAs), and *N* independent beamformer channels and *M* attenuators and phase shifters for each beamformer. The proposed integrated model functionality can be described briefly as following:

- Antenna array radiating elements: form the antenna aperture and consist of a set of identical near-omni-directional radiators (dipole, slot, horn, waveguide), usually located in the form of right-angled or skew-angled nodes;
- Power amplifier modules: are usually implemented in the form of electric vacuum or solid-state devices, which are connected directly to the antenna elements in order to eliminate the need for RF feeder line at a high power level, and thereby significantly reduce the high-frequency loss;
- Linearizer module: is responsible for the transmission factor adjustment (the gain and the phase) of each power amplifier module via linearization of PA characteristics, which in turns achieves a higher efficiency performance due to the enhancement of power losses, which are generated by IM signals;
- The central microprocessor: determines the complex coefficients of transmission channels in accordance with a predetermined shape and position of the antenna array pattern in the space, which are determined by beam pattern control unit and simultaneously an adaptive monitoring of PAs outputs is achieved via a command control program within the linearizer module. The output signals are multiplied with the vector of coefficients that take into account the internal state of the system (failures, amplitude and phase calibration) for correction of antenna array pattern;
- Modulator: adaptive phased antenna array emitted signals can be modulated in the excitation stage or at PA elements;

 ISBN: 978-1-61208-397-1

- Beam pattern control unit: generates the necessary distribution of amplitudes and phases of the input signals to the array radiation elements. This system comprises a set of power amplifiers, a set of phase shifters and a set of matching circuits. Each radiator element is connected in series with the matching circuit, power amplifier and phase shifter to form a single adaptive phased array channel. Usually, all channel elements are combined into a unitary structure which is called a module;
- In addition, the construction of any adaptive phased array systems may include some other units such as; power supply, functional check control and cooling units, where the construction of adaptive phased antenna array system are mainly based on three factors: the location of the phase shifters in each transmitter sub-channel, the number of distribution systems, and the presence of cascaded PA conversion (frequency multiplication stages).

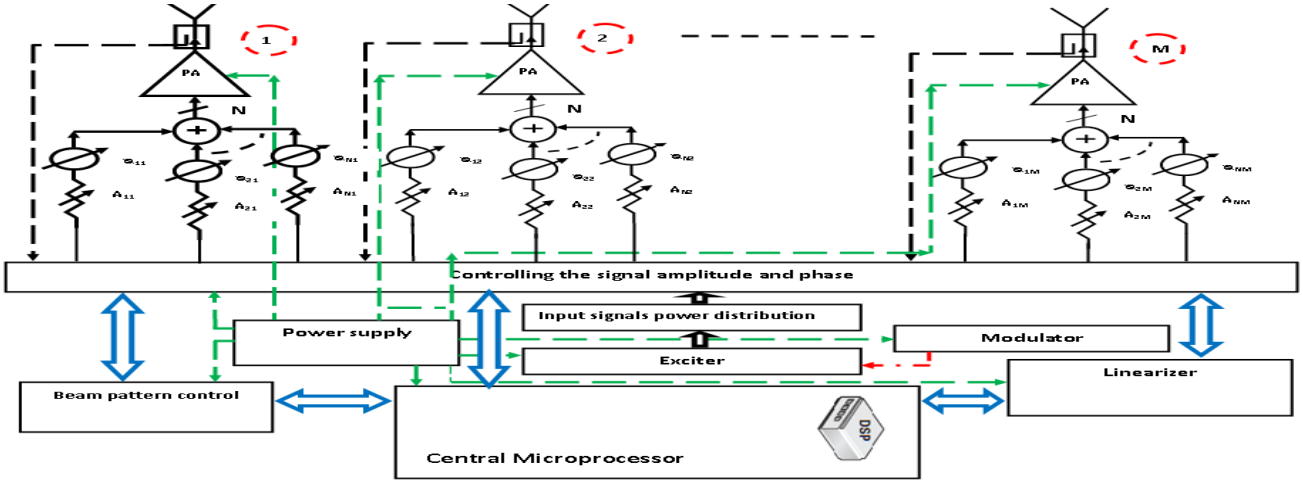

Figure 1. Scheme for the construction of transmission channels of digital active phased antenna array (DAPAA) systems

- Amplitude and phase control unit: generates the required phase and amplitude distribution of excitation signals. Usually it consists of a set of controlled delay lines or phase shifters, and attenuators;
- Input power distribution unit: can be implemented in a passive or active forms. Passive type is based on the parallel, serial, or other multilevel scheme by using different types of power dividers (feeder excitation) or by the optical system (spatial excitation). Active type is intended to be included at different levels (stages) of cascaded amplifiers. Active types are used in cases when the excitation power is not sufficient to excite all PAs of adaptive phased array system, or when it is required to build an array by using the same active devices, i.e., unifying or standardizing them;
- Matching devices, such as impedance transformers and non-dissipative stubs, which have been installed to reduce the reflection losses from the antenna array radiators in the scan mode (or changing the array radiation pattern) and providing stable operating conditions at PAs outputs;
- Non-reciprocal devices - valves or circulators can be installed for isolation PAs and radiators;

VII. SIMULATION RESULTS

In this paper, a five-beam S-band array has been studied, which is comprised of sixteen patch antenna elements in a *1x16* configuration. The amplifier characterization is described by measuring the single tone AM/AM and AM/PM of a subset of the SSPAs with frequency *3.5* GHz to represent the nonlinear response of the PA element. Then, the amplifier is modeled as described in Section II with ten terms of Bessel function series. The agreement between the measured and predicted amplitude and phase characteristics is shown in Figure 2.

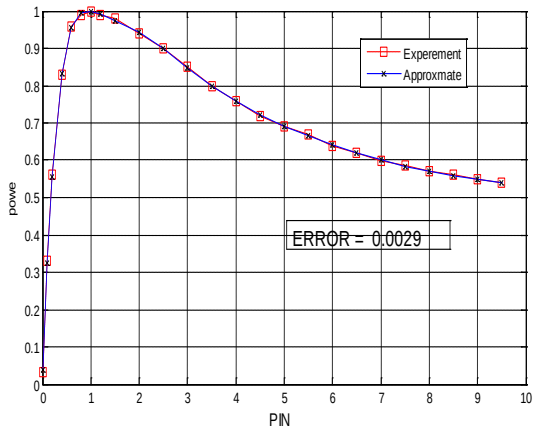

(a)

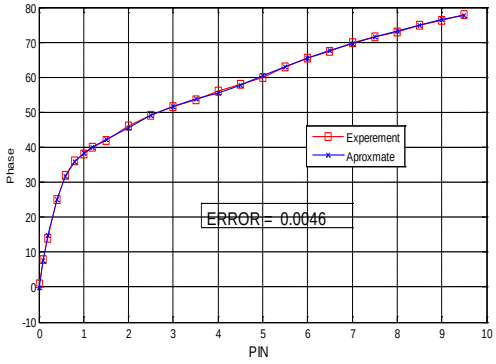

(b)

Figure 2. Predicted and measured power amplifier characteristics
(a) AM / AM characteristics (b) AM / PM characteristics

After PA modeling, the array is fed by five different tones 3500 MHz, 3450 MHz, 3475 MHz 3525 MHz, and 3550 MHz, which are steered in directions [-50°, -25°, 0°, 25°, 50°], such that each PA excitation power is set at 0 dB total power Input Back-Off (IBO) to represent the nonlinear operation of predicted frequency components in the compressed region. Figure 3 shows the predicted two components on the same graph (carrier component as well as the third order IM-32 component) when the array is fed to be operated at 0 dB IBO in Cartesian diagram and Figure 4 represents them in polar diagram.

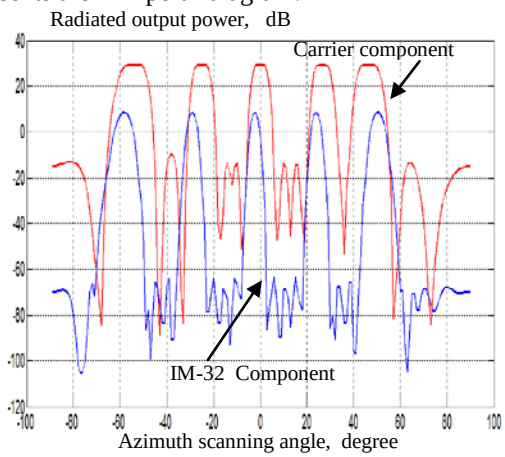

Figure 3. Five beams antenna array patterns of both carrier component and IM-32 component in cartesian diagram

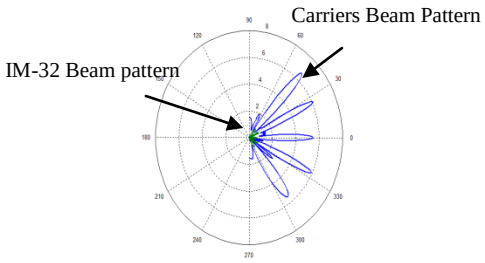

Figure 4. Five beams antenna array patterns of both carrier component and IM-32 component in polar diagram

The linearizer characteristics based on having the inverse of the predicted PA model by using Horison model is shown in Figure 5. Both distorted carrier component and the linearized one are shown in Figure 6 to represent models integration output.

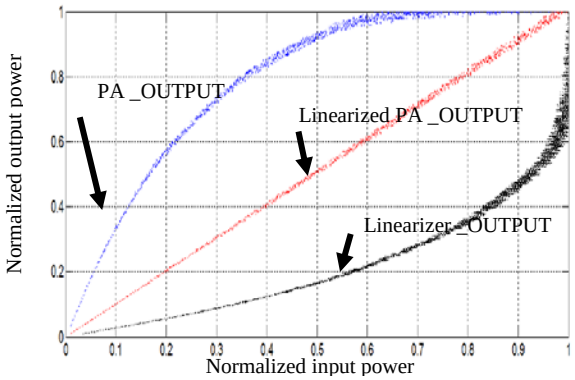

Figure 5. Linearizer effect on power amplifier response

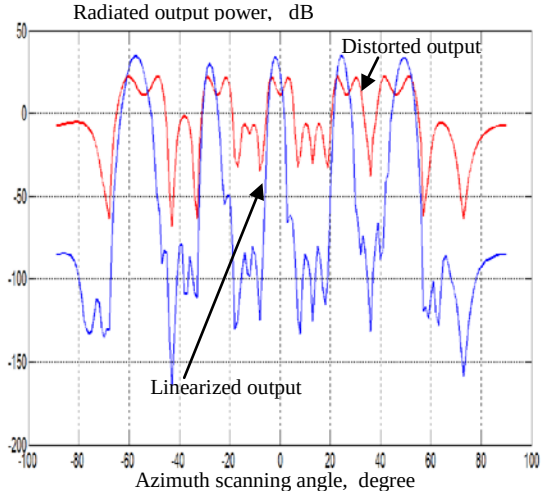

Figure 6. Model integration (distorted carrier component as PA output and its linearized form as linearizer output)

VIII. CONCLUSIONS

A main goal in an active transmitter array is to drive the amplifiers to be as saturated as possible (for optimal efficiency). In this paper, an sixteen-element integrated S-band phase array system is simulated by the Shimbo

 ISBN: 978-1-61208-397-1

nonlinear amplifier model [7] and digital pre-distortion linearizer model based on getting PA inverse by using Horison model. Also, the array farfield parameters, side lobe, and IM patterns are considered in the proposed integrated model. This analysis presents that IM interference can be predicted accurately, which enable controlling its effects in multi-beam phased-array satellite system. Hence, it reduces the necessary excessive margin. Therefore, with this reduction, the transmission power consumption will be decreased, and consequently, satellite power consumption and mass will be reduced.

REFERENCES

[1] C. Hemmi, "Pattern characteristics of harmonic and intermodulation products in broad-band active transmit arrays," IEEE Trans. Antennas Propagat., vol. 50, 2002, pp. 858–865.

[2] E. C. Kohls, E. P. Ekelman, A. I.Zaghloul, and F. T. Assal, "Intermodulation and bit-error ratio performance of KU-band multi-beam high-power phased array," Proc. Antennas Propagat. Soc.Int. , Symp. Dig. 3, 1995, pp. 1404–1408.

[3] K. J. Maalouf, and E. Lier, "Theoretical and experimental study of interference in multi beam active phased array transmit antenna for satellite communications," IEEE Trans. Antennas Propagat., AP-52, 2004, pp. 587–592.

[4] W. A. Sandrin, "Spatial distribution of intermodulation products in active phased array antennas," IEEE Trans. Antennas Propagat., AP-21, 1973, pp. 864–868.

[5] M. T. Abuelma'atti, "Frequency dependent nonlinear quadrature model for TWT amplifiers," IEEE Trans. Commun., COM-32, 1973, pp. 982–986.

[6] J. Ehsan, H. Karkhaneh, and A. Ghorbani, "Theoretical approach to estimate intermodulations in wideband active transmit phase-array antennas," Electromagnetics, vol. 32, 2012, pp. 50-59 .

[7] X. T. Vuong, and M. A. Henchey, "On the accuracy of the Shimbo approach to intermodulation and crosstalk calculations," IEEE Trans. Commun., COM-29, 1981, pp. 1076–1082 .

[8] P. B. Kenington, "High linearity RF amplifier design," ser. Artech House MicrowaveLibrary. Artech House, 2000.

[9] E. Aschbacher, M. Y. Cheong, P. Brunmayr, and V. Laakso , "Prototype implementation of two efficient low-complexity digital predistortion algorithms," EURASIP Journal on Advances in Signal Processing, vol. 2008, january 2008, article No.56.

[10] S. Haykin, "Adaptive filter theory," 4th ed. Prentice Hall, 2002.

 ISBN: 978-1-61208-397-1

A Database Approach to Extending the Usable Ka Band Spectrum for FSS Satellite Systems

Wuchen Tang, Paul Thompson and Barry Evans

Institute for Communication Systems (ICS), University of Surrey,
Guildford GU2 7XH, Surrey, United Kingdom
Email: {w.tang, p.thompson, b.evans}@surrey.ac.uk

***Abstract*—Broadband access by satellite in Ka band will become constrained by spectrum availability. In this context, the EU FP7 project CoRaSat is examining the possible spectrum extension opportunities that could be exploited by a database approach in Ka band via the use of cognitive mechanisms. The database approach utilising spectrum scenarios between Fixed Satellite Services (FSS), Fixed Services (FS) and Broadcast Satellite Service (BSS) feeder links are considered. Database statistics for several EU countries are also provided for database analysis. Interference in the downlink scenarios are evaluated by the database approach using real databases and propagation models. The importance of using correct terrain profiles and accurate propagation models is shown. For the case of BSS interference to the FSS downlink (17.3-17.7GHz), it is demonstrated that in the UK, an area of less than 2% is adversely affected. FS interference into the FSS downlink 17.7-19.7GHz is shown for the UK to only affect a small percentage of the band at any location. Thus, using a database approach to allocate frequencies, it is possible to use most of the band across different locations.**

Keywords–Database approach; frequency sharing; propagation model; area analysis; spectrum analysis.

I. INTRODUCTION

The demand for higher rate and reliable broadband communications is accelerating all over the world. Within Europe the Digital Agenda sets a target for universal broadband coverage of at least 30 Mbps across the whole of Europe by 2020 and 100 Mbps to at least 50% of the households [1]. Fixed connections and cellular cannot alone meet this target, particularly in the rural and remote areas but also in some black spots across the coverage. In these latter regions, satellite broadband delivery is the only practical answer as satellite will cover the whole territory. Some recent studies of the roll out of broadband have shown that up to 50% of households in some regions will only have satellite available as a means of accessing broadband and thus 5-10 million households are potential satellite customers [2]. Current Ku band satellites do not have the capacity to deliver such services at a cost per bit that makes a business case and thus the satellite community has turned to High Throughput Satellites (HTS) operating at Ka band and above. Examples of early HTS Ka band satellites dedicated to such services are Eutelsats KaSat [3] and VIASAT 1 [4]. These satellites employ multiple (around 100) beams using four- fold frequency reuse over the coverage area to achieve capacity of the order of 100 Gbps per satellite. The latter is limited by the exclusive spectrum available to satellite (FSS) of 500 MHz in both the up and downlinks and this limits the feasible user rates to 10-20 Mbps. Thus, looking ahead to the increased user demands we have to look to larger satellites (maybe up to a Terabit/s [5], [6]) and to more spectrum. Moving up to Q/V bands has already been suggested for feeder links but, for user terminals, the additional expense is not considered desirable. So we return to the problem of getting more usable spectrum at Ka band.

The Ka-Band exclusive bands for satellite are 19.7 to 20.2 GHz in the downlink and 29.5 to 30 GHz on the uplink. In these bands FSS terminals can operate in an uncoordinated manner, which means that they do not have to apply for and be granted a licence by the national regulators, provided they meet set performance characteristics. The issue in other parts of the Ka band is that the spectrum is allocated, not just to FSS but also to fixed links (FS) and to BSS (uplinks for broadcast satellites) as well as mobile services (MS). This spectrum is allocated by the ITU in three regions of the world as shown in Table 1 for Ka band (Europe is Region 1). In these so-called 'shared bands', the different services need to co-exist and this is usually done by the process of coordination. For example, a larger gateway or feeder link may use this band but is coordinated and then licensed to operate and receives protection from interference from other service users.

Within Europe the CEPT [7] have adopted decisions that expand those of the ITU and produce tighter regulation as follows;

- 17.3-17.7 GHz: the BSS feeder links are determined as the incumbent links but uncoordinated FSS links are also permitted in this band.
- 17.7-19.7 GHz: FS links are considered incumbent but FSS terminals may be deployed anywhere but without right of protection.
- 27.5-29.5 GHz: CEPT provide a segmentation of the band between FSS and FS portions as shown in Figure 1. Within each segment there is a specified incumbent but for instance FSS terminals can operate in FS portions provided they do not interfere with the incumbent FS.

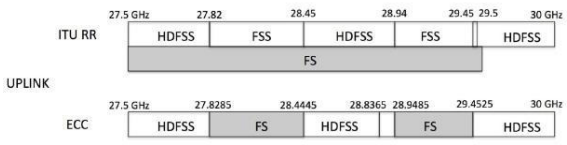

Figure 1. CEPT 27.5-29.5 GHz Segmentation.

The work reported in this paper has been conducted within the EU FP7 project CoRaSat [8]–[11], which examines ways in which FSS satellite terminals in the Ka band can co-exist with FS and BSS links given the regulatory regime discussed above.

 ISBN: 978-1-61208-397-1

TABLE I. ITU-R TABLE OF ALLOCATION

Frequency bands	ITU Region 1	ITU Region 2	ITU Region 3
17.3-17.7 GHz (Scenario A)	FSS (space-Earth) BSS (feeder links) Radiolocation	FSS (space-Earth) BSS (feeder links) Radiolocation	FSS (space-Earth) BSS (feeder links) Radiolocation
17.7-19.7 GHz (Scenario B)	FSS (space-Earth) BSS (feeder links up 18.1 GHz) FS	FSS (space-Earth) FS	FSS (space-Earth) BSS (feeder links up 18.1 GHz) FS
27.5-29.5 GHz (Scenario C)	FSS (Earth-space) FS MS (Mobile Services)	FSS (Earth-space) FS MS	FSS (Earth-space) FS MS

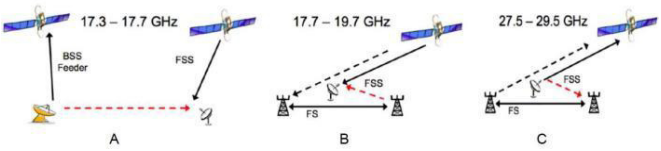

Figure 2. Scenarios in CoRaSat.

Specifically, a database approach for such coexistence schemes is investigated and demonstrated to exploit the frequency sharing opportunities for uncoordinated FSS terminals and verify its applicability. The aim is to show that future satellite systems can access additional spectrum beyond the exclusive bands that is needed to deliver cost effective broadband services.

This paper is organised as follows. In Section II, we describe the scenarios and the database approach for each. In Section III we provide analysis of various databases, and in Section IV, the applications of the databases to scenario A and B and the results of additional bandwidth availability. Finally, we provide conclusions in Section V.

II. SCENARIOS AND DATABASE APPROACH

Within the CoRaSat project, three scenarios have been investigated that reflect the three spectrum components detailed in the previous section. In Figure 2, we illustrate the interference paths in these scenarios. Two of the scenarios are downlink for the FSS; scenario A, 17.3-17.7 GHz where the potential interference is from BSS uplinks and scenario B, 17.7-19.7 GHz where the potential interference is from incumbent FS transmitters. In both of these cases the FSS is permitted to operate but is not protected by the regulatory regime and thus it is important to ascertain the level of the interference and its effect on the FSS received signal. The third scenario C, is in the transmit band of the FSS from 27.5-29.5 GHz and the interference is from the FSS transmitting earth station into the FS receivers which are protected. The latter is more critical in that we need to demonstrate that the FSS does not contravene interference limits imposed by the regulatory regime. The forward link, e.g. the downlink, can be considered more important in that the ratio of downlink broadband to uplink broadband as operated via satellite is currently at around 6:1 and thus the acquisition of more spectrum here is key. In addition to this, operation in the downlink bands does not require regulatory changes but merely a reassurance to FSS users that services need not be impaired.

The calculation of interference can be performed if the corresponding accurate database had been obtained, which includes that the characteristics and locations of the potential interferers are known by using accurate models of the equipment, propagation and the path details.

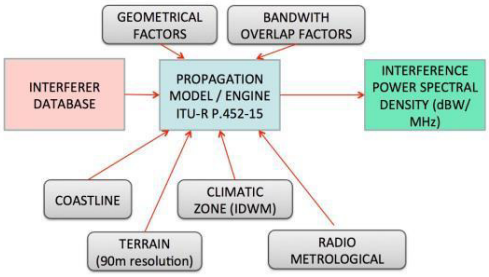

Figure 3. Interference modelling by ITU-R P.452-15

Similar ideas have been employed in TVWS systems [12] to allow UHF frequencies to be used in the gaps between TV transmission regions. For scenario A, the number of BSS uplinks in Europe is small and thus a database system is similar in magnitude to that of TVWS. However, for scenario B and C, the number of FS links runs into the tens of thousands and the database is much more complex. The data on the positions and the characteristics of the BSS and FS are generally held by national regulators and these need to be available for a database system to work.

The information of a real interferer database is interfaced to an interference modelling engine which uses ITU- Recommendation P.452-15 [13] procedures plus terrain databases. This is the latest version of this ITU Recommendation that contains a prediction method for the evaluation of path loss between stations. ITU-R P.452-15 includes all the propagation effects on the surface of the Earth at frequencies from 0.1 GHz to 50 GHz. In addition, other factors which affect interference calculation, such as terrain height, bandwidth overlapping are also considered in the proposed database approach, which is illustrated in Figure 3. The typical interference threshold we determine is based on the long term interference which can be expected to be present for at least 20% of the average year and it is set at 10 dB below the noise floor. The interference thresholds for FSS reception and for FS reception are therefore -154 dBW/MHz and -146 dBW/MHz, respectively as given in [14] and [15].

Having determined the interference level at the FSS (in scenarios A or B) it can be compared with the regulatory threshold. The action is then taken in the resource allocation at the gateway where a new carrier can be assigned either in another part of the 'shared band' where interference is

 ISBN: 978-1-61208-397-1

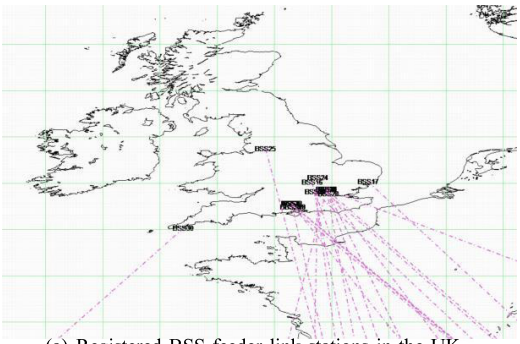

(a) Registered BSS feeder link stations in the UK.

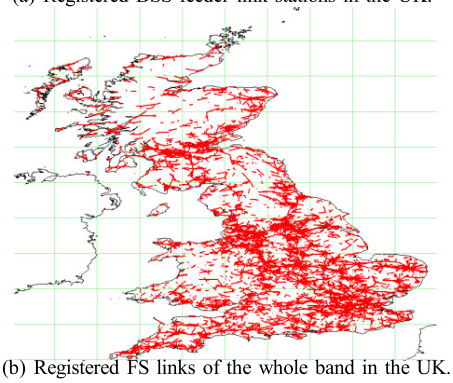

(b) Registered FS links of the whole band in the UK.

Figure 4. Registered BSS and FS links in the UK.

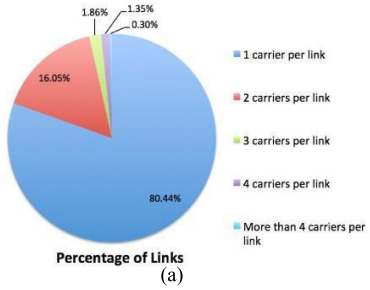

(a)

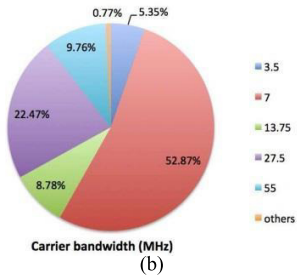

(b)

Figure 5. Pie chart of (a) FS carrier number of each link and (b) carrier bandwidth (MHz).

acceptable or in the exclusive band. For scenario C the situation is different as the interference is caused by the FSS into the FS. Here, the database is used to calculate the maximum permissible power that can be transmitted from the FSS in the vicinity in order to retain the threshold condition at the FS receivers. More details of the database approach are given in

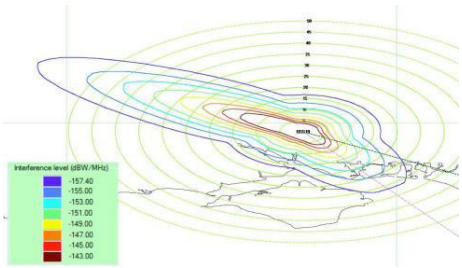

(a)

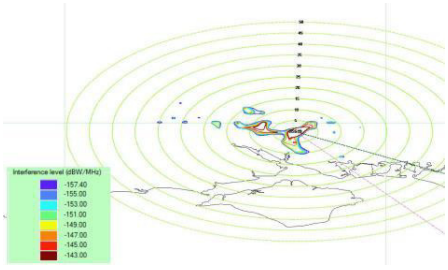

(b)

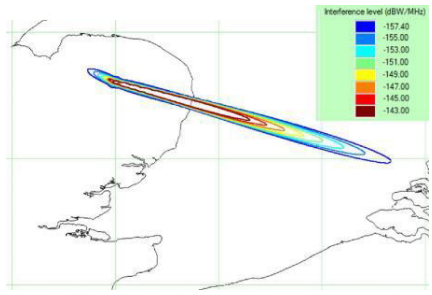

(c)

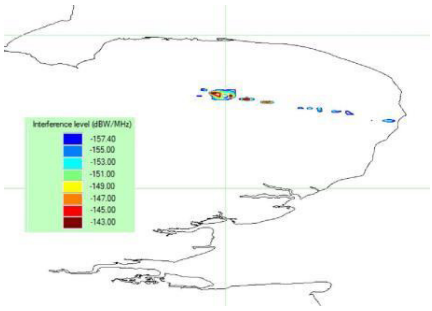

(d)

Figure 6. Example of cognitive zone for (a) BSS with free space loss model (b) BSS with full ITU model (c) FS with free space loss model (b) FS with full ITU model.

the following sections.

III. DATABASE ANALYSIS

The information in a database is normally listed on a carrier by carrier basis for a frequency band of interest. All carriers are usually detailed with their frequencies and channel bandwidths. When the database relates to satellite terminals the database should also contain details on the associated satellite in terms of satellite longitude and the earth stations azimuth and elevation angles. Polarization and antenna gain are also required along with the antenna radiation patterns as

 ISBN: 978-1-61208-397-1

TABLE II. AREA ANALYSIS (sqkm) OF THE BAND 17.3-17.7 GHz

17.7−17.3GHz	*SB1*	*SB2*	*SB3*	*SB4*	*SB5*
−155 dBW/MHz	2, 420.9 (1.06%)	1, 692.4 (0.74%)	1, 692.4 (0.74%)	1, 683.3 (0.73%)	3, 570.9 (1.56%)
−145 dBW/MHz	683.0 (0.30%)	544.8 (0.24%)	544.8 (0.24%)	541.8 (0.24%)	926.0 (0.40%)
17.7−17.3GHz	*SB6*	*SB7*	*SB8*	*SB9*	*SB10*
−155 dBW/MHz	1, 683.3 (0.73%)	2, 411.0 (1.05%)	2, 535.6 (1.11%)	2, 367.6 (1.03%)	2, 936.4 (1.28%)
−145 dBW/MHz	541.8 (0.24%)	741.3 (0.32%)	774.2 (0.34%)	697.5 (0.30%)	928.6 (0.40%)

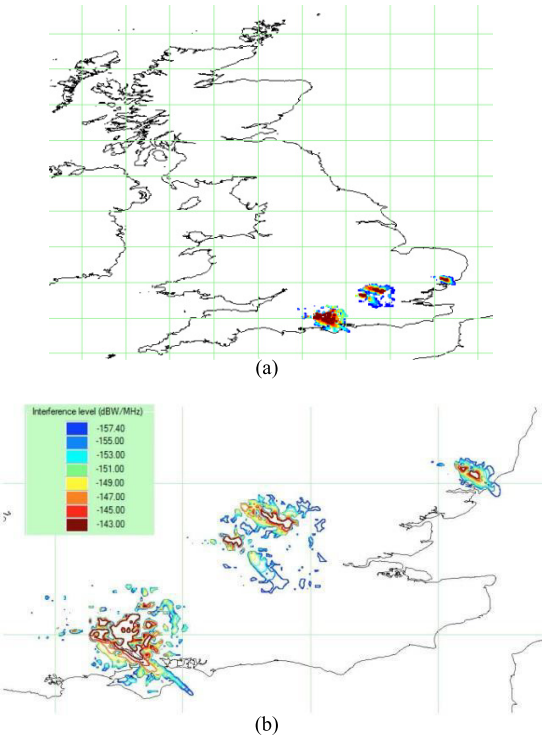

(a)

(b)

Figure 7. Example of cognitive zones for the sub-band 1 (17.3-17.34 GHz) based on full ITU model.

defined in ITU Recommendations for use in regulatory work or ETSI standards. In addition, transmission power and equivalent isotropic radiated power (EIRP) may also be included.

A UK BSS database made available for this study is used for scenario A and contains 442 carriers from a total of 31 BSS uplink earth stations at 8 physical sites, to 12 different satellites, which is shown as Figure 4(a). The locations of all these 31 BSS earth stations are marked with an indication of the direction of the beam to the satellite. The number of carriers of each BSS earth station ranges from 1 to 42. The carriers span the range 17.3 GHz to 18.35 GHz. The bandwidths of the carriers that belong to the same BSS earth station are the same while those that belong to different earth stations might be different and are typically 26 MHz, 33 MHz, 36 MHz or 66 MHz. The EIRP of these earth station antennas ranges from 69 dBW-84 dBW and all antenna radiation patterns are as defined in ITU-Recommendation S.465 [16] or S.580 [17].

FS databases at 18 GHz are required to evaluate scenario B. Again, an FS database was made available to this project (under the UK Freedom of Information Act). This database for the UK FS in the band 17.7 to 19.7 GHz is much larger than that for the UK BSS and contains 12,712 links with 15,970 carrier recorded in the UK. A French database has also been examined at 18 GHz and is based on the latest ITU-R terrestrial services BR IFIC database [18], which contains 11,548 links with 17,384 carriers recorded. Figure 4(b) illustrates the FS links in the band 17.7 to 19.7 GHz in the UK and it can be seen that the FS links are much denser than for the BSS.

Figure 5 provides pie charts of numbers of carriers per link and carrier bandwidths based on the UK FS database in (a) and (b), respectively. It is indicated that more than 80% of links have only one carrier and more than 96% of links have up to 2 carriers. The majority of carriers have a bandwidth from 3.5 to 55 MHz. As a consequence, it can be deduced that at a particular location in the UK, little spectrum resource from the available 2 GHz band is used by the FS at a specific location. Thus, we are optimistic that spectrum available for FSS on a micro scale geographical basis is significant and can be exploited if the information of spectrum occupancy is known from the analysis of the database or is detectable by other mechanisms. A similar situation also exists for France.

We have implemented the ITU-R.P452-15 propagation and interference modelling to provide cognitive zones around incumbent terminals based on the available database. A cognitive zone here is defined as the geographical area around an incumbent user station where cognitive radio techniques such as spectrum sensing and beamforming should be employed to mitigate the interference to an acceptable level. In other words, the interference outside of this area is below the acceptable interference threshold thus cognitive radio techniques are not necessary.

Figures 6(a) and 6(b) show plots of cognitive zones around a BSS Station under scenario A case based on a free space loss model and the full ITU-R P.452-15 model, respectively. Similarly, Figures 6(c) and 6(d) show plots of cognitive zones around a FS Station under scenario B case based on these two models. For the BSS cognitive zone the FSS terminal evaluated points to a satellite at 53 degrees E longitude and the BSS transmitting terminal points to a satellite at 28.2 degree while for the FS cognitive zone the FSS terminal is pointing to a satellite at 20 degrees E longitude and the FS transmitting terminal is pointing at a receive terminal on a bearing of 110 degrees (ETN). Clearly for both cases, the cognitive zones from the full model are much smaller and differently shaped compared with the ones under free space model. On the average the areas are 9 times smaller at the -155 dBW/MHz and 3.5 times smaller at the -145 dBW/MHz thresholds. This is mainly because the diffraction effect based on the terrain data is considered in the full model while the free space loss model only includes line of sight propagation loss, which reflects the fact that the terrain data based diffraction effect is extremely

 ISBN: 978-1-61208-397-1

significant in cognitive zone determination.

IV. DATABASE APPLICATIONS FOR SCENARIOS

In this section, we analyse for scenario A the areas that are affected by interference from BSS uplinks and for scenario B the availability of spectrum at FSS locations as a result of FS interference. Typical examples are provided to demonstrate the additional spectrum that could be available.

A. Scenario A: Area Analysis

Using the BSS database, area analysis for scenario A in the UK is provided to investigate how much area would be affected by interference from the BSS feeder links. The band of interest is split into 10 x 40 MHz sub-bands (*SB1*−*SB10*) and the analysis is then conducted in each sub-band to determine the area of the contours at different cognitive zone thresholds. These mirror the usual 40 MHz channel spacing adopted for BSS satellites. Area analysis is based on a BSS database with the full ITU-R P.452-15 model employing the terrain and climatic zones and the FSS terminal evaluated points to a satellite at 53 degrees E longitude. The results are for long term interference (normally 20%).

One example of affected area at difference cognitive zone thresholds is shown in Figure 7, which represents *SB1*. Full data on the areas are given in the Table II. It can be seen that in general across the sub-bands at a -155 dBW/MHz threshold less than for 2% of the area of the UK is affected by BSS feeder links and thus more than 98% of the area of the UK can be used by an FSS terminal without the need for any further action. Some mitigation of excess interference may be required in these affected areas. Such mitigation could be achieved by suitable site shielding, beam-forming or reallocation to another frequency that is clear at the specific location. If such mitigation measures result in 10 dB suppression (a very conservative figure) then the remaining affected area would be of the order of 0.4% of the area of the UK. Re-farming the spectrum of such a small amount of traffic should not represent much of a challenge. This is very promising for future FSS deployment as the additional 400 MHz identified in scenario A (17.3-17.7 GHz) represents an 80% increase over the current exclusive band allocation (19.7-20.2 GHz).

Although we have presented results herein for an FSS terminal pointed at a specific orbit location we have examined a range of orbit locations from the UK and the results are very similar.

B. Scenario B: spectrum analysis

Unlike the situation in scenario A, the UK 18 GHz FS database comprises many more carrier records (15,036 records) over the 2 GHz band from 17.7 to 19.7 GHz. For scenario B we perform spectrum analysis for a particular location in the UK instead of geographical area analysis across the whole of the UK to determine which carrier(s) can be used by an FSS at a specific location. This information could then be integrated with a resource allocation algorithm in the satellite network to assign the carriers.

Spectrum analysis results for the UK FS links at 18GHz at a specified location with latitude 52.5 degrees, longitude -0.1 degree is shown here as an example. The analysis results of the location with both LOS and full model (ITU-R P.452-15) are shown as Figures 8 and 9, respectively. The FSS terminal evaluated points to the same satellite as the previous examples which is located at 53 degrees E longitude. In each figure, a map of the links that exceed an interference level of -160 dBW/MHz is presented along with spectrum analysis as a plot of the interference power spectral density (PSD). Interference PSD is shown per MHz from 17.7 to 19.7 GHz. At this location, it can be seen that with the LOS model

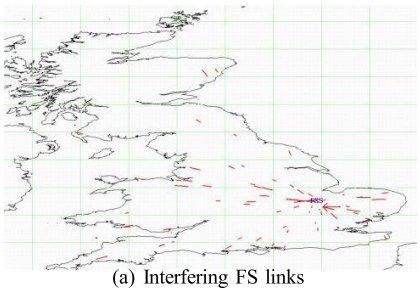

(a) Interfering FS links

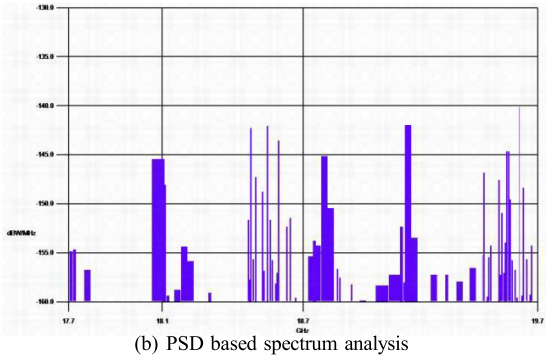

(b) PSD based spectrum analysis

Figure 8. LOS result of all UK FS links, interfering to FSS terminal at latitude of 52.5 degs and longitude of -0.1 degs.

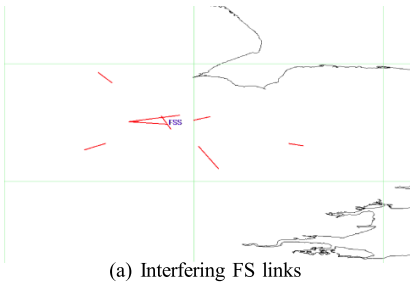

(a) Interfering FS links

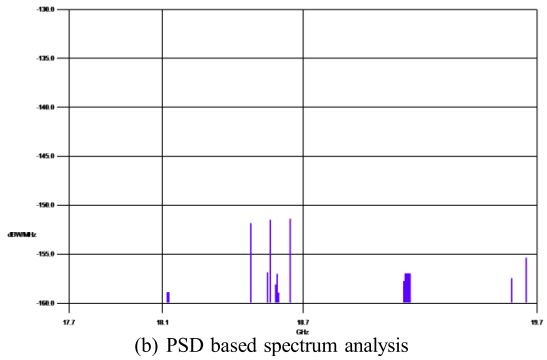

(b) PSD based spectrum analysis

Figure 9. Full terrain model Results result of all UK FS links, interfering to FSS terminal at latitude of 52.5 degs and longitude of -0.1 degs.

the interference can arise from FS links much further from the location of interest and these links are ones pointing directly at the location. Only a few point with some offset and these are located very close so that interference is from their side lobes. From the interference PSD in Figure 8, it can be seen that more than half of spectrum resource from 17.7 GHz to 19.7 GHz is available (with interference below the threshold) at this location under LOS model. However, if the full terrain model is considered as in Figure 9, the number of interfering FS links dramatically decreases to less than ten, which means less than 0.1% of total FS links would cause problem at the location. Therefore the majority of the 2 GHz band can be used by an uncoordinated FSS VSAT terminal site. The comparison of the increased spectrum available is shown in Figure 9.

A complete map of the locations in the UK has been produced and this can be used as input to a resource allocation scheme which would then optimize the carrier allocation on the basis of the extra spectrum available. It was noted that although the number of FS links in the data base was large those that actually caused interference at a specific location and in a particular frequency band were quite small. It should also be noted that the available spectrum is not the same at each location and thus the data base analysis can be used to optimize the carrier allocation as a function of FSS location.

C. Scenario C

Cognitive zones for scenario C are around FS stations and interference is from FSS terminals to FS links. This is a much more difficult case to address if we plan to use the whole of the shared band because we do not have access to an adequate 28 GHz database on which to operate. The techniques and software developed for scenario A and B can be used in a similar manner for scenario C if we have access to such a database. The results would be presented in a slightly different format as they would give the maximum allowable EIRP for the FSS at a given point. However, the HDFSS uplink band has been agreed for uncoordinated earth stations in all except 5 of the EU countries thus perhaps the uplink increase in spectrum is not so urgent at this time. Some preliminary evaluation of scenario C was performed in [19] and the results of this indicated that only very close FS links would be affected and the density of FSS terminals would not cause a problem in the multi interference case. Further evaluation will be done within CoRaSat.

V. Conclusion

To meet future broadband access targets, in this paper we have described how the increased spectrum opportunities can be exploited by the proposed database approach together with interference mitigation techniques. We have demonstrated that in 17.3-17.7 GHz spectrum band 400 MHz of additional bandwidth is available across 98% of the UK which houses the densest BSS network in Europe, and similar results were obtained for Luxembourg. The evaluation needs to be repeated in other EU countries, but a similar if not better performance would be expected due to the lower density of BSS. If the FSS is required to be closer to a BSS, then cognitive means can be used to mitigate the interference. We also have explored the availability of the 2 GHz spectrum band between 17.7 to 19.7 GHz downlink and the results have shown that the number of actual interfering FS links are limited due to terrain diffraction effects so that at a particular location substantial parts of the 17.7 to 19.7 GHz are available, but not the same frequencies at all locations. This indicates that a data base interfaced with a resource allocation scheme could give access to the increased spectrum. This was demonstrated for the UK but needs to be validated in other European countries. In the case of the uplink 27.5-29.5 GHz we are still evaluating the potential but early signs look promising.

Acknowledgement

The authors would like to acknowledge the EU FP7 project CoRaSat which has supported the work herein.

References

[1] “A Digital Agenda for Europe, FCC 02-155,” European Commission COM 245, Brussels, Tech. Rep., 2010.

[2] “EU FP7 Project BATS,” Vodafone Chair, Available: http://www.batsproject.eu/. , February 2015.

[3] H. Fenech, E. Lance, and M. Kalama, “KA-SAT and the way forward,” Ka-Band Conference, Palermo, Italy., Tech. Rep., 2011.

[4] “Highest-capacity communications satellite,” http://www.guinnessworldrecords.com/records-1/highest-capacity-communications-satellite/., November 2014.

[5] P. Thompson, B. Evans, L. Castenet, M. Bousquet, and T. Mathiopoulos, “Concepts and technologies for a terabit/s satellite,” in Proceedings of SPACOMM-2011 (best paper award in 2011), April 2011, Budapest, Hungary.

[6] A. Kyrgiazos, B. Evans, P. Thompson, P. T. Mathiopoulos, and S. Papaharalabos, “A terabit/second satellite system for european broadband access: a feasibility study,” International Journal of Satellite Communications and Networking, vol. 32, no. 2, 2014, pp. 63–92.

[7] “The European conference of postal and telecommunications administrations,” avaliable: http://www.cept.org/cept., February 2014

[8] “EU FP7 Project CoRaSat,” available: http://www.ict-corasat.eu.

[9] K. Liolis, G. Schlueter, J. Krause, F. Zimmer, L. Combelles, J. Grotz, S. Chatzinotas, B. Evans, A. Guidotti, D. Tarchi, and A. Vanelli-Coralli, “Cognitive radio scenarios for satellite communications: The corasat approach,” in Future Network and Mobile Summit (FutureNetworkSummit), 2013, July 2013, pp. 1–10.

[10] S. Maleki, S. Chatzinotas, B. Evans, K. Liolis, J. Grotz, A. Vanelli-Coralli, and N. Chuberre, “Cognitive spectrum utilization in ka band multibeam satellite communications,” IEEE Communication Magazine, accepted, to be published in 2015.

[11] “Cognitive radio techniques for satellite communications operating in Ka band,” Tech. Rep., ETSI System Reference document, available: http://webapp.etsi.org.

[12] “Standardization of TV white space systems,” available: http://www.ict-crsi.eu/index.php/standardization-streams/tv-white-spaces.

[13] “Recommendation P.452-15: Prediction procedure for the evaluation of interference between stations on the surface of the earth at frequencies above about 0.1 GHz,” International Telecommunication Union, Tech. Rep., 2013.

[14] “Methods for the determination of the coordination area around an earth station in frequency bands between 100 MHz and 105 GHz,” ITU Radio Regulation Appendix 7, International Telecommunication Union, Tech. Rep., 2012.

[15] “Recommendation F.758-5: System parameters and considerations in the development of criteria for sharing or compatibility between digital fixed wireless systems in the fixed service and systems in other services and other sources of interference,” International Telecommunication Union, Tech. Rep., 2012.

[16] “Recommendation ITU-R S.465: Reference radiation pattern for earth station antennas in the fixed- satellite service for use in coordination and interference assessment in the frequency range from 2 to 31 GHz,” International Telecommunication Union, Tech. Rep., 2010.

[17] “Recommendation ITU-R S.580: Radiation diagrams for use as design objectives for antennas of earth stations operating with geostationary satellites,” International Telecommunication Union, Tech. Rep., 2004.

[18] ITU-R Terrestrial BRIFIC, available: http://www.itu.int/ITU-R/index.asp?category=terrestrial&rlink=terrestrial-%brific&lang=en.

[19] A. Mohamed, M. Lopez-Benitez, and B. Evans, “Ka band satellite terrestrial co-existence: A statistical modelling approach,” in Proceedings of 20th Ka and Broadband Communications, Navigation and Earth Observation Conference, October 2014.

 ISBN: 978-1-61208-397-1

Self-calibration of Spaceborne Membrane Phased Array

Yang Bo, Liu Ning , Zhang Zhaolin
UAV Lab, ASN technology, Northwestern Polytechnical University
Xi'an, China
email:rvdyang@126.com

Chang Cuiyan
Xi'an Peihua University
Xi'an, China
ccyrock@126.com

***Abstract*—Spaceborne membrane phased array is prone to distortion due to lack of mechanical rigidity. Distortion introduces phase errors between array elements which will significantly degrade antenna performance, such as directivity and sidelobe level. An innovative self-calibration method was invented to compensate phase errors with minimum equipment involved. Using the un-calibrated array itself to transmit and receive ground reflective signal, the phase errors between elements can be estimated and then be compensated. Simulation demonstrated the principle of the algorithm and show promising results for further investigation.**

Keywords—membrane phased array; spaceborne antenna; calibration

I. INTRODUCTION

Future space missions need low mass, low cost and high packaging efficiency structures to reduce launch cost, stow volume and production costs. The innovation of highly deployable membrane phased array antenna satisfies the requirements and promise wide application in future space missions.

Spaceborne membrane phased array antenna (Figure 1) is manufactured on light weight membrane structures. This technology enables the use of larger antennas for high speed space communication and low frequency earth observation. Some earth remote sensing applications, such as soil moisture and ocean salinity, need the antenna to be physically large in order to obtain the necessary resolution at the frequencies of interest (low frequency). Membrane antenna also makes it possible to place huge Synthesized Aperture Radar (SAR) systems on Medium or Geosynchronous Earth Orbits (MEO or GEO) to compensate signal space loss and improve the field of view for earth observation which would lead to much shorter revisit times in comparison to satellites in a Low Earth Orbit (LEO). Moreover, membrane antenna is a key enabling technology for miniaturized satellite, for example, CubeSat, for its super light weight and high stow efficiency.

The forerunner in this research field is Jet Propulsion Laboratory (JPL) where a membrane phased array demonstrator has been built including structure, radiator and electronics design. The primitive demonstrator has shown huge reduction of mass in comparison with traditional phased array antenna [1][2].

When applying membrane phased array to real system, there are many technical problems need to be solved. One of them is as the result of lack of mechanical rigidity; membrane structure is prone to distortion. Such distortion may be introduced during launch vibration, during folding and expending or caused by long term thermal effect. Besides, as fabricated on such highly elastic structure, antenna array will vibrate when spacecraft maneuvers, as happened in dual side looking SAR operations. Both of mechanical distortion and structure vibration generate relative displacements between array elements which will significantly degrade radiation performance of the array as a whole. Therefore, these displacements need to be calibrated, that is, to estimate and compensate the relative phase differences of antenna elements.

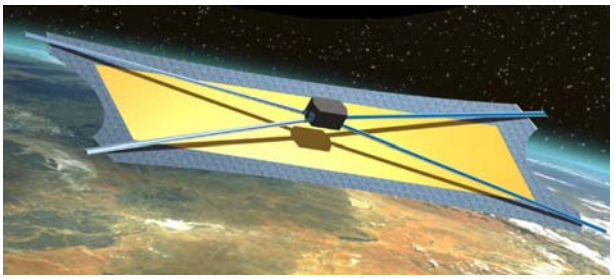

Figure. 1. membrane phased array in space (imaginery picture)

There are some existing technologies to calibrate array element displacement and radiation pattern. As introduced in [3][4], the phase differences between array elements can be accurately measured by near field probe antenna attached on the spacecraft. The advantage of this technology is it can correct the phase errors with high accuracy. The major disadvantage is extra mass and cost, increased inherent technical risk to the spacecraft as the near field probe requires more mechanical structure.

Another method measure the phase differences between array elements with pre-installed ground transmitters, receivers or corner reflectors [5][6]. The process is time consuming and costs a lot of labor.

A more convenient scheme use reflective signal from illuminated patch to calibrate the antenna [7]. This kind of technology is more convenient because no ground facilities are needed. It processes signal reflected from noncoherent ground scatterers and takes advantage of the statistical properties of the backscattered clutter signal to estimate phase errors in the array [8]. The key idea is that a homogeneous clutter scene will make the phase of the ensemble correlation between signals received

 ISBN: 978-1-61208-397-1

by adjacent array elements equal to zero. Thus, any variation from this zero phase correlation attributes to relative phase error between the two elements and therefore can be used to calibrate the array.

A large number of nonrigid scatterers, which are uniformly distributed and with random relative motions, can provide the required noncoherence, for example, sea waves and rainforest. And a well calibrated transmitting antenna installed on the spacecraft is also needed to illuminate the patch for the required homogeneous clutter scene.

Our algorithm is based on such noncoherent scatterer algorithms, the difference from former ones is that the independent well calibrated transmitting antenna has been removed to reduce support structure complexity. Although adding some computation complexity, our method minimized the structure demand, reduced cost, and achieved real self-calibration by using uncalibrated antenna array to calibrate itself. Since the transmitting antenna and the receiving antenna is the same array. This algorithm can calibrate transmit channel and receive channel at the same time. Theoretical description of the algorithm is in Section II, followed by simulation demonstration in Section III, and finally concluded in Section IV.

II. ALGORITHM

Unlike the well calibrated illuminating antenna, transmitting signal with the uncalibrated antenna array can't generate the homogeneous clutter scene we need. But when randomize transmitting phase in each pulse and accumulate different pulses, we can achieve equivalent result as required from homogeneous clutter scene. The underlying principle of our algorithm is presented here.

The signal received by i th element is:

$$\begin{aligned} e_i^{'}(n) &= e_i(n)e^{j(\phi_i+\frac{2\pi}{\lambda}d_i)} + \eta_i(n) \\ &= e_i(n)e^{j\delta_i} + \eta_i(n) \end{aligned} \tag{1}$$

where $e_i(n)$ is the received signal at each sampling time when there is no phase error between adjacent elements. Since phase errors exist, the signal phase will change. ϕ_i is for electronics delay of different channel, d_i is physical displacement of the array element deviated from its nominal position and η_i is measurement noise. Since λ is the wavelength, $2\pi d_i / \lambda$ is the phase difference from displacement. The phase delay from electronics and displacement can be added together to δ_i. As it will be showed in following description, our algorithm can actually estimate electronics and displacement phase change at the same time which is favorable for real system application. If we set the phase of one element as reference phase, then we only need to estimate the phase difference between reference element and other elements $\Delta\delta_{ij} = \delta_i - \delta_j$. Conjugate multiply can achieve the phase difference as

$$e_i^{'}(n)e_j^{'*}(n) = e_i(n)e_j^{*}(n)e^{j(\delta_i-\delta_j)} + noise\ term \tag{2}$$

In order to reduce the noise, we need to average the signal

$$E\left[e_i^{'}(n)e_j^{'*}(n)\right] = E\left[e_i(n)e_j^{*}(n)\right]e^{j(\delta_i-\delta_j)} \tag{3}$$

let $\psi_{ij} = \arg\left\{E(e_i^{'}e_j^{'*})\right\}$, $\beta_{ij} = \arg\left\{E\left(e_i e_j^{*}\right)\right\}$, then $\psi_{ij} = \left(\delta_i - \delta_j\right) + \beta_{ij}$. If β_{ij} is 0, then $\Delta\delta_{ij} = \psi_{ij}$, thus phase difference can be estimated from measured signal $e_i^{'}(n)$, $e_j^{'}(n)$. The condition of $\beta_{ij} = 0$ can only be satisfied when $E\left[e_i(n)e_j^{*}(n)\right]$ is real.

For convenience, we give the theoretical analysis of one-dimensional situation to explain our algorithm. In this situation, e_i can be modeled as:

$$e_i = \int_{-\infty}^{+\infty} f(x)e^{-j\frac{4\pi}{\lambda}r_i} w_T(x)w_R(x)dx \tag{4}$$

where $f(x)$ is radar backscattering coefficient. r_i is distance from array element to ground scatterers as show in Figure 2. Figure 2 visualized the one-dimensional situation, where two array element are showed in this figure, among them, one will be taken as reference. The vertical distance from antenna array to ground is h. $w_T(x)$ is ground project of antenna array transmitting pattern and $w_R(x)$ is the receiving pattern of individual element. 4π is for two-way distance delay include both transmitting and receiving path. Since the unknown array element displacement, we have no idea of the radiation pattern of the transmitting array. Nevertheless, we can randomize the transmitting array phase at each pulse and average the receiving signal from pulse to pulse. As draw in Figure 2, transmitting beam pattern is completely randomized.

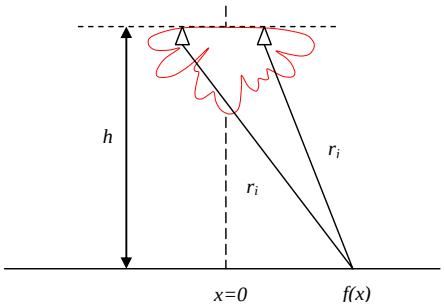

Figure. 2. visualization of randomised radiation pattern

From (4). The conjugate correlation of received signal is:

$$\begin{aligned} E\left[e_i e_j^{*}\right] = E\{\int_{-\infty}^{+\infty}\int_{-\infty}^{+\infty} f(x)f^{*}(x)e^{-j\frac{4\pi}{\lambda}(r_i-r_j)} \\ w_T(x)w_T(x^{'})w_R(x)w_R(x^{'})dxdx^{'}\} \end{aligned} \tag{5}$$

where $E\{f(x)f^{*}(x')\} = E\{|f(x)|^2\delta(x-x')\} = \sigma_0\delta(x-x')$

for noncoherent ground scatterers. $w_T(x)$ is a random process. Notice in (5), $r_i - r_j$ can be simplified by binomial expansion:

 ISBN: 978-1-61208-397-1

$$r_i - r_j = \sqrt{h^2 + (x + D/2)^2} - \sqrt{h^2 + (x - D/2)^2}$$
$$\approx h\left(1 + \frac{(x + D/2)^2}{2h^2} - 1 - \frac{(x - D/2)^2}{2h^2}\right) = \frac{Dx}{h}$$

Then, (5) reduced to:

$$E\left[e_i e_j^*\right] = \sigma_0 \int_{-\infty}^{+\infty} e^{-j\frac{4\pi D}{\lambda h}x} p(x)q(x)dx \qquad (6)$$

where $p(x) = E\left[w_T(x + D/2)w_T(x - D/2)\right]$, $q(x) = E\left[w_R(x + D/2)w_R(x - D/2)\right]$. Let $\omega = \frac{4\pi D}{\lambda h}$, we got:

$$E\left[e_i e_j^*\right] = \sigma_0 \int_{-\infty}^{+\infty} e^{-j\omega x} p(x)q(x)dx \qquad (7)$$

which is in the form of Fourier transform. According to the properties of Fourier transform, if $p(x)q(x)$ is a real and even function, then $E[e_i e_j^*]$ will be real. Therefore $\beta_{ij} = \arg\left\{E(e_i e_j^*)\right\}$ will be zero and phase difference can be estimated $\Delta\delta_{ij} = \psi_{ij}$. Since $p(x)$ is the expectation of completely randomized radiation pattern, which can be taken as a random process, $p(x)$ will be even as the expectation will show symmetry pattern around central axis. $q(x)$, as the function related to array radiation element, will submit to the property of element radiation pattern. Here, we take a typical radiation pattern, microstrip patch antenna element to analyze. The pattern can be described through approximation as:

$$w_R'(\theta) = \frac{\sin\left(\frac{kh_e}{2}\sin\theta\right)}{\frac{kh_e}{2}} \frac{\sin\left(\frac{kw}{2}\cos\theta\right)}{\frac{kw}{2}} \qquad (8)$$

which is showed in Figure 3. Figure 3 present the definition of θ and the pattern for a patch antenna element. In (8), $k = 2\pi/\lambda$, h_e is patch height, w is width of the patch.

With some substitutes, $w_R'(\theta)$ can be transformed to

$$w_R(\theta) = \frac{\sin\left(\frac{kh_e}{2}\frac{x}{\sqrt{x^2 + h^2}}\right)}{\frac{kh_e}{2}} \frac{\sin\left(\frac{kw}{2}\frac{h}{\sqrt{x^2 + h^2}}\right)}{\frac{kw}{2}\frac{h}{\sqrt{x^2 + h^2}}} \qquad (9)$$

according to (9), $q(x) = w_R(x + D/2)w_R(x - D/2)$ is an even function. Then in (7), $p(x)q(x)$ will be even, therefore, $E\left[e_i e_j^*\right]$ will be a real function $\beta_{ij} = \arg\left\{E\left[e_i e_j^*\right]\right\} = 0$. This means if antenna array elements are microstrip patches, our algorithm will guarantee the phase difference between reference element and uncalibrated element can be estimated. In fact, the analysis above also guarantee that as long as array element radiation pattern is symmetric which is real for most applications, the algorithm will work well.

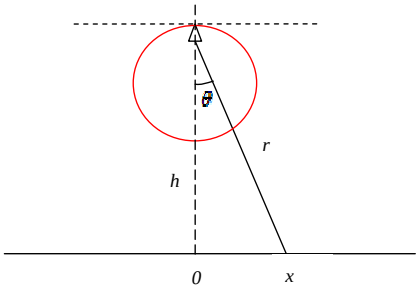

Figure. 3. approximate radiation pattern of a patch antenna element

III. SIMULATION

We need some simulation to demonstrate the algorithm and first to model the received signal. Assume the radar transmits signal pulse $s_T(t)$

$$s_T(t) = g(t)\exp(j2\pi f_0 t) \qquad (10)$$

where $g(t)$ is the complex envelop and f_0 is carrier frequency. The received signal from scatterer i will be:

$$s_i(t) = f_i(\theta,\beta)w_T(\theta,\beta)g\left(t - \frac{2r}{c}\right) \exp\left(j2\pi f_0\left(t - \frac{2r}{c}\right)\right) \qquad (11)$$

c represents the speed of light, r is distance between radar and a scatterer, then the round-trip time delay is $2r/c$. The received signal is multiplied by factor $f(\theta,\beta)$, determined by the scatterer reflectivity as well as the elevation angle θ and azimuth angle β, and w_T, the beampattern. When striped off the carrier frequency, the echo from scatterer i would be:

$$s_i(t) = f_i(\theta,\beta)w_T(\theta,\beta)g\left(t - \frac{2r}{c}\right)\exp\left(-j\frac{4\pi r}{\lambda}\right) \qquad (12)$$

where λ is the wavelength. By combining echoes from each scatterers, the composite signal is given by

$$e(t) = \sum_{i=1}^{N} s_i(t) \qquad (13)$$

where N is the number of scatterers.

The i th element delivers measured field value of $e_i'(n)$ to the signal processor. In order to get $E\left[e_i' e_j'^*\right]$, time sample average is applied to approach the assembly expectation. $E_T = \frac{1}{M}\sum_{m=1}^{M} e_i'(m)e_j'^*(m)$. There are two strategies to realize the sample average. One is just averaging echoes from multiple pulses; the other is averaging from both different pulses and

 ISBN: 978-1-61208-397-1

successive range bins. The latter will work when the geometrical features are statistically homogeneous over the whole area, thus echoes from different range bins can be treated as sample function drawn from the same random process.

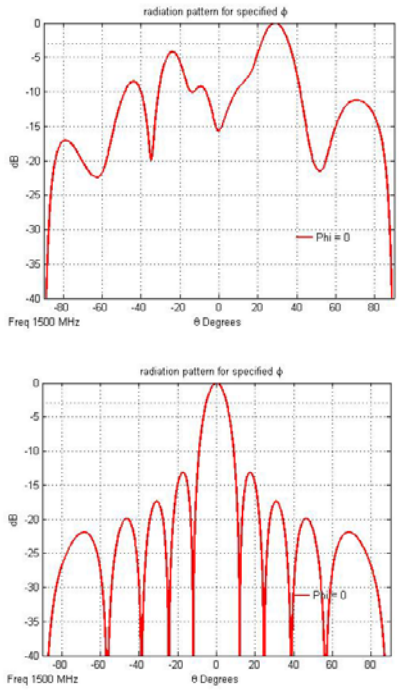

Figure. 4. radiation pattern before (up) and after (down) compensation 2D

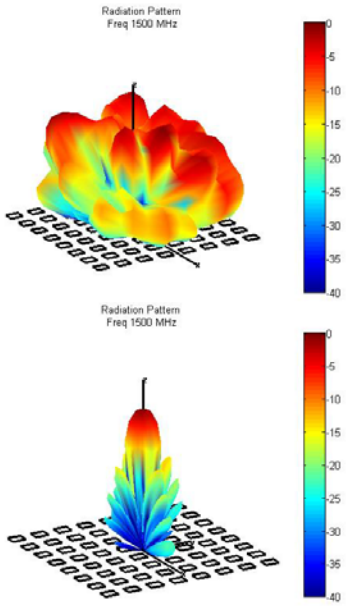

Figure. 5. radiation pattern before (up) and after (down) compensation 3D

Figures 4 and 5 showed the simulation results. The array was constructed by 64 elements. Given working frequency 1.5GHz, we design the patch firstly. The up sides of Figure 4 and 5 is the radiation pattern before calibration, the down sides are after calibration.

Simulation results proved the efficiency of the algorithm. Phase errors between elements can be estimated and calibrated with high accuracy.

IV. CONCLUSION

A problem when applying membrane phased array to real system is that the light weighted non-rigid membrane structure is prone to distortion. As the result of distortion, relative position of array radiation element will change and cause relative phase errors which dramatically degrade antenna performance and imaging capability. Therefore, these phase errors need to be calibrated and compensated. By measuring the correlation of backscattered clutter signal from noncoherent ground homogeneous scatterers, unknown phase errors between array elements can be estimated. The problem of non-uniform illumination arise from unfocused array can be tackled by average pulses with randomized transmitting phase. Simulation result showed even when the array is completely unfocused, the algorithm can still work.

Randomized radiation pattern will reduce imaging power in real system which may generate some other problems. Since the array will not completely unfocused at the first time, the decrease of transmitting power will not affect the efficiency of our algorithm, however, phase error estimation accuracy may be affected which need further investigation.

ACKNOWLEDGMENT

The research is supported by Northwestern Polytechnical University Research Fund, grant No. 3102014KYJD014, and Key Laboratory Fund, grant No. 9140C390601140C39002.

REFERENCES

[1] A. Moussessian, et al., “Transmit/Receive Membranes for Large Aperture Scanning Phase Arrays,” NASA ESTO Workshop, 2002.

[2] M. Leipold, H. Runge, C. Sickinger, “Large Sar Membrane Antennas With Lightweight Deployable Booms,” 28th ESA Antenna Workshop on Space Antenna Systems and Technologies, ESA/ESTEC, 2005.

[3] T. Takahshi, N. Nakamoto, M. Ohtsuka, T. Aoki, Y. Konishi, and M. Yajima, “A simple on-board calibration method and its accuracy for mechanical distortions of satellite phased array antennas,” in 3rd European Conference on Antennas and Propagation, EuCAP 2009, 2009, pp. 1573 –1577.

[4] T. Takahashi, et al., “On-Board Calibration Methods for Mechanical Distortions of Satellite Phased Array Antennas,” IEEE Transactions on Antennas and Propagation, vol. 60, no. 3, Mar. 2012, pp. 1362 –1372.

[5] A. A. Thompson, D. Racine, and A. P. Luscombe, “RADARSAT-2 antenna calibration using Ground Receivers/Transmitters,” in Geoscience and Remote Sensing Symposium, IGARSS ’02. IEEE International, 2002, vol. 3, pp. 1465 – 1467.

[6] M. Bachmann, M. Schwerdt, and B. Brautigam, “TerraSAR-X Antenna Calibration and Monitoring Based on a Precise Antenna Model,” IEEE Transactions on Geoscience and Remote Sensing, vol. 48, no. 2, Feb. 2010, pp. 690 –701.

[7] D. L. Goeckel and J. B. Mead, “Linear filtering approaches for phase calibration of airborne arrays,” IEEE Transactions on Aerospace and Electronic Systems, vol. 42, no. 3, Jul. 2006, pp. 806 –824.

[8] E. H. Attia and B. D. Steinberg, “Self-cohering large antenna arrays using the spatial correlation properties of radar clutter,” IEEE Transactions on Antennas and Propagation, vol. 37, no. 1, Jan. 1989, pp. 30–38.

 ISBN: 978-1-61208-397-1

The Use of Field Programmable Gate Arrays (FPGA) in Small Satellite Communication Systems

Kosta Varnavas, William Herbert Sims, Joseph Casas
National Aeronautics and Space Administration , NASA / MSFC / ES33, Huntsville, USA
Kosta.varnavs@nasa.gov , Herb.sims@nasa.gov, joseph.casas@nasa.gov

***Abstract*— This paper will describe the use of digital Field Programmable Gate Arrays (FPGA) to contribute to advancing the state-of-the-art in software defined radio (SDR) transponder design for the emerging SmallSat and CubeSat industry and to provide advances for NASA as described in the TAO5 Communication and Navigation Roadmap. The use of software defined radios (SDR) has been around for a long time. A typical implementation of the SDR is to use a processor and write software to implement all the functions of filtering, carrier recovery, error correction, framing etc. Even with modern high speed and low power digital signal processors, high speed memories , and efficient coding , the compute intensive nature of digital filters, error correcting and other algorithms is too much for modern processors to get efficient use of the available bandwidth to the ground. By using FPGAs, these compute intensive tasks can be done in parallel, pipelined fashion and more efficiently use every clock cycle to significantly increase throughput while maintaining low power. These methods will implement digital radios with significant data rates in the X and Ka bands. Using these state-of-the-art technologies, unprecedented uplink and downlink capabilities can be achieved in a ½ U sized telemetry system. Additionally, modern FPGAs have embedded processing systems, such as ARM cores, integrated inside the FPGA allowing mundane tasks such as parameter commanding to occur easily and flexibly. Potential partners include other NASA centers, industry and the DOD. These assets are associated with small satellite demonstration flights, LEO and deep space applications. MSFC currently has an SDR transponder test-bed using Hardware-in-the-Loop techniques to evaluate and improve SDR technologies.**

Keywords - Software Defined Radio; Field Programmable Gate Arrays; Programmable Lightweight System Adaptable Radio, PULSAR; Finite Impulse Response Filter; microprocessor; digital signal processor; parallel processing.

I. INTRODUCTION

Marshall Space Flight Center (MSFC) has been developing a low-cost software defined radio transponder which contributes to advancing the state-of-the-art in telemetry system design which is directly applicable to the Small Sat and CubeSat communities. The SDR, called PULSAR – Programmable Ultra Lightweight System Adaptable Radio, can be incorporated into orbital and suborbital platforms.

By examining a number of the systems available for current CubeSats, they do not have sufficient bandwidth or processing capability for transmitters and receivers to support new error correcting protocols as well as innovative payload designs with complex encryption schemes being developed by the CubeSat community (academic, military, civil, industry). The PULSAR SDR has a highly efficient

Figure 1. Ground Station Antennas

SWaP, (Size, Weight and Power), which achieves higher bits per input supply watt (at ~10 Mbits per input watt) than traditional communication SDR systems (at ~300Kbits per input watt) requirements.

The paper will go into the details of a technical approach to implement high speed flexible satellite radios. It will then compare the differences between implementing these techniques using processors or FPGAs, and then it will look at how this work aligns with the NASA roadmap.

II. TECHNICAL APPROACH

A basic SDR block diagram is shown in figure 2 [1]. As is typical, the concept of the SDR is to minimize the analog / radio frequency (RF) components and do as much as possible in the digital domain.

 ISBN: 978-1-61208-397-1

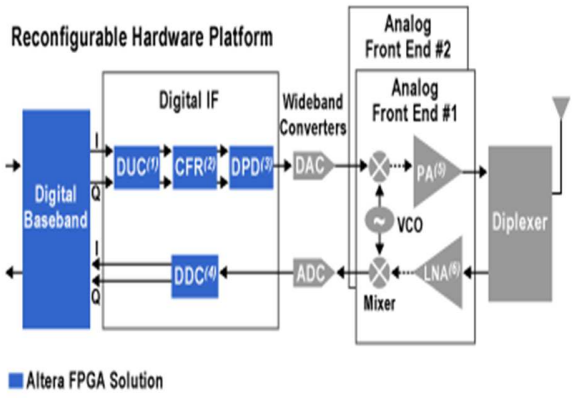

Figure 2. Typical Software Defined Radio [1]

Many traditional software defined radios actually use processors to accomplish these tasks. With low bandwidth requirements and frequency bands below the L-Band range, 1-GHz processors can handle the workload. Even with minor forward error correction coding, the processors can still handle the load. However, as the frequencies climb into and above S-band, 2.0 GHz, and data rates increase significantly, even fast digital signal processors will have trouble keeping up with executing all the code necessary to do filtering, digital up converting and down converting, as well as forward error correction schemes such as Reed-Solomon, Low Density Parity Check and others. Add encryption of any type to the mix, and the processor will get bogged down quickly. Utilizing multiple processors or even multi-core processors are all advanced means of achieving the throughput necessary. However, the complexity of these systems grows as will the cost, size and power.

Because of the above problems with utilizing digital signal processors, Marshall Space Flight Center's SDR, PULSAR, chose to use Field Programmable Gate Arrays such as the Actel ProAsic3 Flash devices. All signal processing algorithms are done inside the FPGA and designed using Hardware Description Language (HDL).

The PULSAR radio is divided up into a series of stackable decks. This can be seen in Figure 3. Each one stacks on top of the other to make a very modular system that can be customized for each mission's requirements. Each deck is designed to be stand-alone with the exception of the power deck, for any configuration. However, even the power deck can be eliminated if filtered, isolated power of the right voltages are provided. Of the stackable decks available, the S-band transmitter will transmit Quadrature Phase Shift Keyed (QPSK) data at 5-10 Mbps. The X-band transmitter will transmit one channel of QPSK data at 110 Mbps, and the S-band receiver will receive data at 300 kbps. Although, maximum data rates on the uplink have not been tested, it is believed that at least 1 Mbps could be uploaded in the current hardware and FPGA algorithmic configurations.

These data rates are not the limit of the hardware or of the algorithms inside the FPGA. They are the constraints placed on the satellite transceivers by the NASA Near Earth Network (NEN)[5]. In addition to these radio component decks, there is a power deck to provide isolated power to the entire stack. Also, there is a processor deck that utilizes an embedded ARM processor inside of the FPGA. This can be used for additional algorithms or as the flight computer itself. With an embedded ARM processor [6]and external ram, the processor deck has enough computational power to be a flight controller for many applications.

Because each deck can be stand alone, each deck has its own FPGA and performs all signal processing inside of the FPGA. This provides plenty of extensibility to allow additional functions and algorithms to be added to each deck's. The FPGA chosen for this version of the PULSAR is the Actel ProAsic3 [7]. It is a flash based FPGA which means it is live at power up and does not need a configuration memory like SRAM based FPGAs such as Xilinx.

Exemplifying the flexibility of PULSAR, transmission can occur using Low Density Parity Check (LDPC), Reed-Solomon (255/223), or convolutional (Rate ½) Forward Error Correction (FEC) codes based on mission requirements. Each of these codes, except the Rate ½ convolutional encoding, is very compute intensive. The intensity of computations necessary to implement these FECs limit a digital signal processors ability to perform these functions and maintain a high data rate to the ground.

A unique feature of the power deck is its ability to monitor current draw on each of the power rails going to each of the decks. The power deck is programmed for a maximum current draw per deck and when it is exceeded, the power rail is turned off until the fault is cleared. This is designed in as a radiation mitigation method to prevent radiation induced latch-up.

Each of the radio decks, transmitters and receiver, have a number of digital algorithms it has to perform. The S-band receiver has algorithms it has to perform to recover the signal and strip the data of headers and error correction to get to the actual message / commands sent. The transmitter decks have algorithms to perform Forward Error Correction (FEC), and NEN compatible packetization. This is typical of SDRs and is what provides their small size and low power and flexibility. However, the amount of processing involved becomes more difficult to do in a processor the higher the data rates and frequency. Filters, carrier recovery loops, error correcting decoding are all very compute intensive.

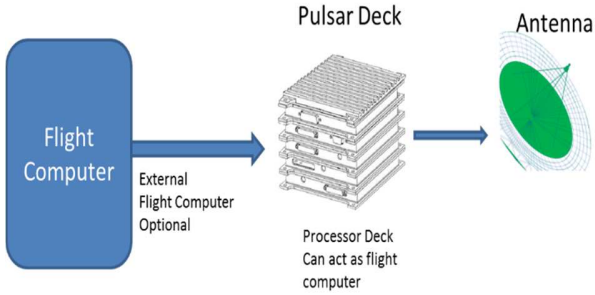

Figure 3. PULSAR stack in system. Flight computer optional.

 ISBN: 978-1-61208-397-1

III. PERFORMANCE

Computations take so much more time in a processor versus an FPGA. Processors of any kind, even those designed specifically for signal processing, can only perform one instruction per clock cycle. And that is for the fast and well-designed processors. But even so, some computations require more than one, maybe many clock cycles to achieve one action. For a receiver, if a processor is reading the analog to digital (A/D) converter it may take several instructions to point to the A/D, read the data and store it in a register. Cache and direct memory access will help, but it gets worse. Now that you have the data, you may want to down convert it again which uses a numerically controlled oscillator and digital mixers which are multiplier heavy. Then it will need to be filtered. Filters have numerous multiplies and adds. All this has to be done in a seamless, continuous manner to get the data to come through correctly. A Finite Impulse Response Filter (FIR) is a typical type of filter for signal processing of all types. A typical digital signal processor (DSP) such as the TI TMS320C55x at 300 MHz built for signal processing, has direct memory access, cache and embedded hardware multipliers. These features enhance data throughput. Memory is treated as a circular buffer with pointers that automatically update. Due to a high amount of parallelism and pipelining, the whole - fetch data, perform MAC, return data - process is usually done in one clock cycle.

Loop X times:

- Move (2) input samples from memory to MAC
- Move coefficient from memory to MAC
- Perform MAC operation

Retrieve output from MAC and store in memory
Send output sample to interface.

The higher order the filter, the higher number of taps are necessary and the number of loops, X, goes up significantly.

Using the features of the above processor, a 422 tap FIR filter could be implemented up to ~ 628 kbps. But this will come at a cost of ~ 200mW of power! Additionally, processors and clock rates are not linearly correlated. Just because one DSP had a higher clock rate, it doesn't mean it will perform better on a benchmark.

So with the above example, there is a lot of overhead for circuit design, and power to achieve less than 1 Mbps on just one FIR filter. In a typical SDR there will be numerous filters as well as other digital algorithms and multiple data paths in the case of mPSK modulations schemes. So why do we not just run to faster DSPs? There is a limit to the speed and the power hit goes up linearly! See Figure 4 [2].

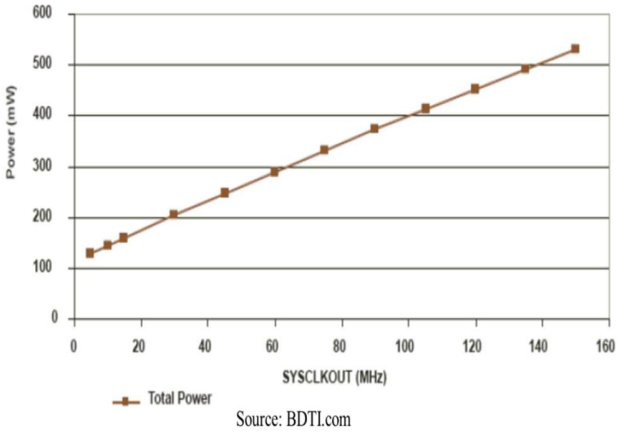

Figure 4. Power Consumption vs. Clock Frequency [2]

In an FPGA, all of these functions are performed in a pipeline manner. In addition, each step of the pipeline has all the adders, multipliers necessary to accomplish the task. The data is presented to the next stage on every clock cycle, eliminating the need to fetch data and instructions as to what to do with the data, on every iteration. There are still numerous functions that require numerous iterations, but with the pipelined structure and some parallelism, the main clock does not have to be as high to achieve the same data rates. Additionally, some of the newer FPGAs have numerous dedicated hardware multipliers. This speeds up the multiplication process itself, which can be an iterative implementation.

Figure 5 [3] shows a graphic explaining the problem using a general-purpose digital signal processor.

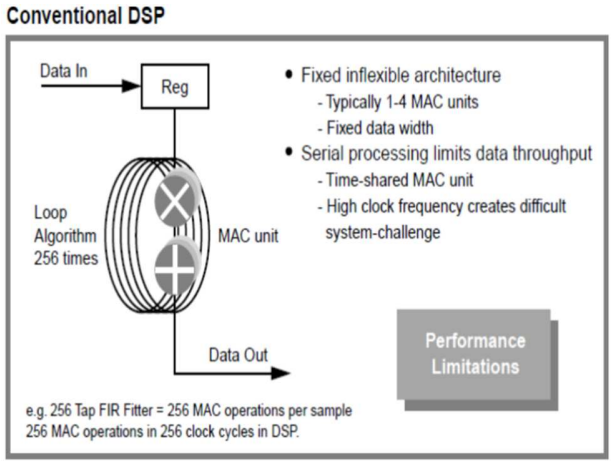

Figure 5. Conventional DSP Implementation [3]

 ISBN: 978-1-61208-397-1

Even the latest processors still have the above limitations. However, as Figure 6 [3] shows, an FPGA clearly has the ability to perform, parallel, pipelined functions with local dedicated hardware, from multipliers to block rams, enabling a much more efficient use of the clock and at a much lower overall clock speed.

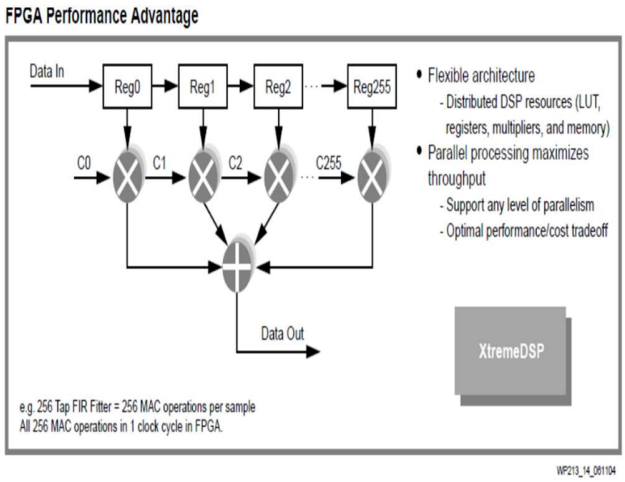

Figure 6. FPGA Performance advantage. [3]

IV. ALIGNMENT

NASA is called, at the direction of the President and Congress, to maintain an enterprise of technology that aligns with missions and contributes to the Nation's innovative economy. NASA has been and should be at the forefront of scientific and technological innovation. In response to these calls, NASA generated a plan (NASA Strategic Space Technology Investment Plan [4] to advance technologies and nurture new innovation that will feed into future missions. PULSAR aligns primarily with the Technology Area (TA) 5 – Communication & Navigation – but has connections to other areas in which lightweight structures, power efficiency, and communication reliability and throughput are the focus.

V. CONCLUSION AND FUTURE WORK

Currently PULSAR implements an S-band transmitter, S-band receiver and X-band transmitter utilizing advanced FPGA technology and digital signal processing techniques inside the FPGA. As a complete integrated unit, PULSAR has been tested in a lab environment with typical NEN ground station equipment, procedures and operational scenarios. Upcoming builds of this system are planned for full environmental testing. This includes Electromagnetic Interference/compatibility tests, Thermal/ Vacuum tests, as well as vibration tests. A variety of potential upcoming flights will allow PULSAR to fly as a payload to prove its capability as a flight read instrument. An upcoming ground demonstration with the Space Launch System could be its first relevant environment testing. This test will interface numerous development flight instrumentation (DFI) sensors with the PULSAR to transmit to the remote test station. This will eliminate significant amounts of long run cabling.

Depending on funding levels, future developments of the next generation of software defined radios on the roadmap, include a C-band transceiver, an X-band receiver to complement the current X-band transmitter, and at some point Ka-band transponders. The PULSAR team is constantly applying the latest innovations to provide cutting edge systems for small satellite communications systems.

REFERENCES

[1] http://www.google.com/url?sa=t&rct=j&q=&esrc=s&source=web&cd=2&ved=0CCQQFjAB&url=http%3A%2F%2Fweb.cecs.pdx.edu%2F~mperkows%2FCAPSTONES%2FDSP1%2FPresentation%2520of%2520Software%2520Defined%2520Radio.ppt&ei=GNG2VKzdAcbksATJgYLoBA&usg=AFQjCNHRWPr0IcC8NJnra5rQocs5HSiB1A&sig2=XQw0-5wjEJ_qg3HbHQY7fAL-3 Communication Systems-West, "Cadet Nanosat Radio," Product specification sheet, pp. 6, 2011 , retrieved: January, 2015

[2] QuickfilterTechnologies,, Inc., "Digital Filtering Alternatives for Embedded Designs" http://www.quickfiltertech.com/files/Digital%20Filtering%20Alternatives%20for%20Embedded%20Designs.pdf pp. 16, September 2006 , retrieved: January,2015

[3] Xilinx, http://www.xilinx.com/support/documentation/white_papers/wp213.pdf , Xilinx White Papert, pp. 18, July 2004 , retrieved: January,2015

[4] National Aeronautical and Space Administration, "NASA Strategic Space Technology Investment Plan" NASA Washington, DC, 2013. pp. 1 – 92 , December 2012 , retrieved: January,2015

[5] Nasa Near Earth Network, https://www.nasa.gov/directorates/heo/scan/services/networks/txt_nen.html

[6] ARM Processors, http://www.arm.com/products/processors/cortex-m/index.php

[7] ActelProAsic3, http://www.microsemi.com/products/fpga-soc/fpga/proasic3-overview

 ISBN: 978-1-61208-397-1

Experimental X-Band Automotive SAR System for Land Observation Application

Chul H. Jung, Jung-Hwan Song
Wireless Technology Laboratory
SOLiD Systems
Seoul, Korea
email: chjung@solid.co.kr, jhsong@solid.co.kr

Hyeon-Cheol Lee
Payload Electronics Team
Korea Aerospace Research Institute
Daejeon, Korea
email: hlee@kari.re.kr

***Abstract*— In this paper, an experimental X-band automotive-Synthetic Aperture Radar (SAR) system for land observation application is proposed with the obtained SAR images. In order to develop and validate simply, Commercial Off-The-Shelf (COTS) technology is partially employed especially for standard horn antenna, arbitrary waveform generator, and digital signal processor. In order to validate the system performance, SAR image quality is evaluated by using corner reflector. In this paper, the feasibility of the automotive-SAR system for land application is demonstrated by presenting the SAR images of several kinds of ground areas.**

Keywords-Synthetic aperture radar (SAR); Ground-based SAR system; land application; system development.

I. INTRODUCTION

Recently, ground-based Synthetic Aperture Radar (SAR) systems have been proposed as observation and monitoring tool for land application such as landslides monitoring, terrain elevation mapping, and environmental study of vegetation cover. Because a ground-based SAR system has great advantage of stable motion effect, SAR formation processing can be very simple. Therefore many researchers employ the ground-based SAR system for its research purpose [1]-[7]. Pieraccini et al. [2][3] suggest simple interferometric system based on ground rail system for topographic mapping application. And Luzi et al. [4] demonstrate the potential of ground-based SAR system for landslides monitoring. Recently, Lingua el al. [5] employ the Terrestrial Laser Scanning (TLS) technique to improve the ground-based interferometric SAR system for remote sensing of landslide monitoring. Recently, Zhou, et al. [6] and Sato et al. [7] suggest ground-based SAR systems for ground-truth validation in polarimetric SAR remote sensing of vegetation cover. Most of a ground-based SAR system is based on rail system, so its observation area is very limited. We have developed a high resolution experimental automotive-SAR system for land application. Unlike rail-based SAR systems, an automotive-SAR system provides large observation area of ground cover and can be used in various kinds of land applications.

This paper is organized as follows. In Section II, the automotive-SAR system is described. Section III describes the development and the evaluation of the system. Section IV addresses the SAR image results which are conducted during SAR data acquisition campaign to show the feasibility for land application.

II. SYSTEM DESCRIPTION

The system described in Figure 1 consists of arbitrary waveform generator (AWG) module, amplifier (AMP) module, receiver (RCV) module, signal processor (PRC) module, antenna module, and power module.

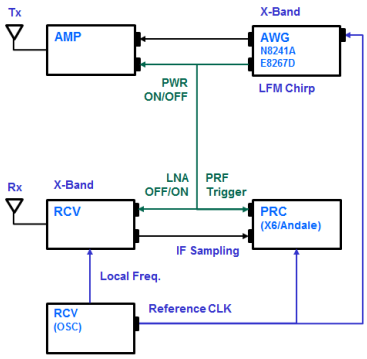

Figure 1. Block diagram of automotive-SAR system.

We employ an arbitrary waveform generator (N8241A) for the generation of baseband I/Q signal and the baseband signal is up-converted by vector signal generator (E8267D). Utilizing commercial off-the-shelf technology, operating frequency can be easily varied for other applications. The signal waveform of this system is Linear Frequency Modulation (LFM) chirp pulse with wide bandwidth. Therefore, very high resolution SAR image of sub-meter in range direction can be obtained. AWG also provides stable trigger signal for ON/OFF control of AMP and RCV module and for sampling timing of PRC. Because of low power level of AWG module, we develop an AMP module with the high power level to extend the maximum detection range. As mentioned earlier, the AMP module is controlled by ON/OFF trigger signal to avoid amplification of noise level during the receiving window time.

In order to avoid I/Q imbalance problem, we adapt Intermediate Frequency (IF) sampling, and Digital Down Conversion (DDC) scheme is used to obtain I/Q signals. The

 ISBN: 978-1-61208-397-1

sampling rate is more than gigahertz with high bit resolution, and as a result, the recorded data rate is also gigahertz.

Figure 2 shows the overall SAR system. In order to avoid internal leakage, bi-static type is considered. Due to the short period of time for development and validation, we need to make use of standard horn type antenna with the high gain and the feed and adaptor type provides linear polarization.

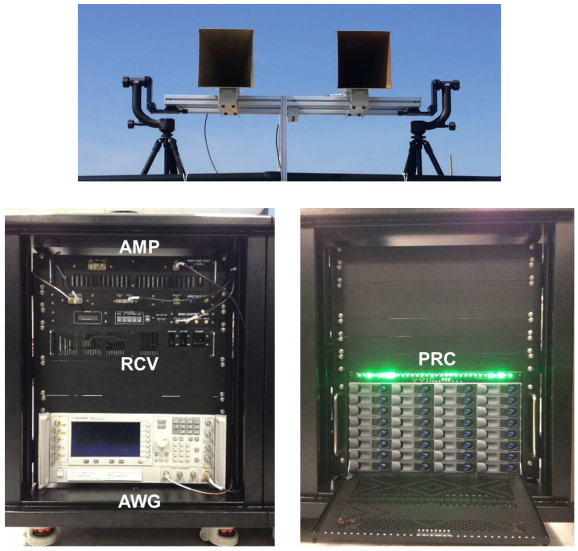

Figure 2. Automotive-SAR system.

By change of feed direction, dual or quad polarization can be supported. The receiving channel can be expanded up to 4 channels by additional ADC board in PRC module. Therefore, this system can be used for interferometric SAR (InSAR) and/or polarimetric SAR (PolSAR) application.

III. DEVELOPMENT AND VALIDATION OF AUTOMOTIVE-SAR SYSTEM

The SAR system, as shown in Figure 3, is installed in vehicle which provides power supply utilizing vehicle battery and invertor. Antenna module is mounted on top of vehicle. The elevation of antenna can be easily controlled by using tripod. The system is controlled by laptop notebook which means that the system could be operated in the moving vehicle.

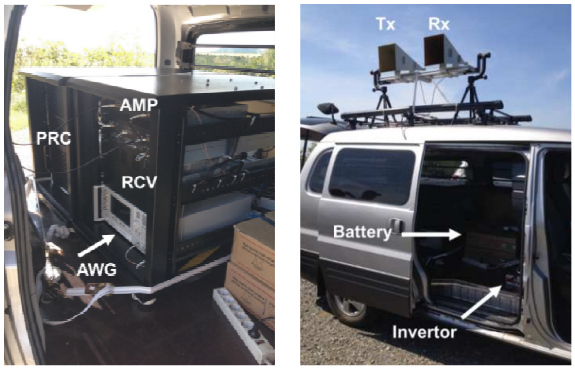

Figure 3. Installation of automotive-SAR system.

The system operation frequency in the experiment is 10 GHz. The bandwidth of LFM chirp is 500 MHz, so the ideal range resolution of 0.3 meter can be expected. The velocity of vehicle is about 80 km/h, and the antenna beam width is approximately 4 deg. Therefore, Doppler bandwidth can be obtained about 104 Hz and the expected resolution is 0.2 m in azimuth. The PRF is set to 1 KHz so that the processing gain in azimuth direction can be very high after aperture synthesizing.

In order to validate the system performance, some of experiment results are presented. The height of the road is normally more than 20 m. Also, the road condition is very important. The road should be flat and straight. The SAR image from first field work is described in Figure 4. The system has no squint angle and beam width is narrow. Therefore, Doppler centroid is close to zero and Doppler estimation can be very simple. Because the road condition is very flat and straight, the motion factor of automotive-SAR system is very stable. Therefore, a motion compensation process can be relatively simple compared to airborne SAR case. Contrast-based autofocusing is used for velocity estimation.

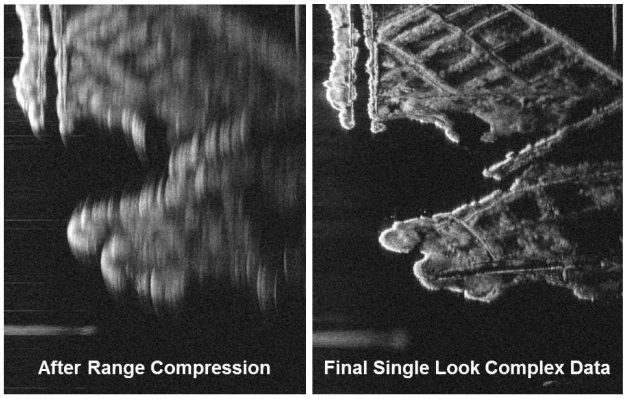

Figure 4. First SAR image.

In order to verify the system performance, we do calibration field work using passive calibrator as shown in Figure 5 and Figure 6.

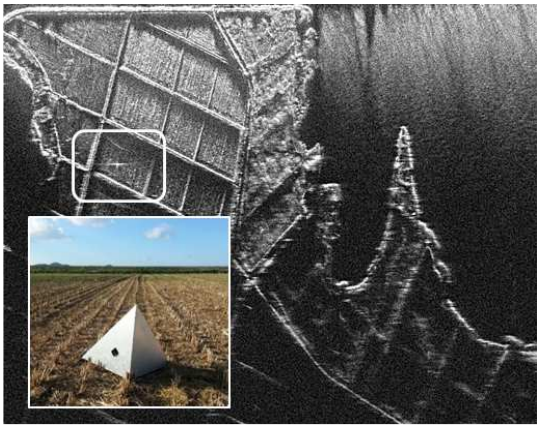

Figure 5. SAR image of calibration field.

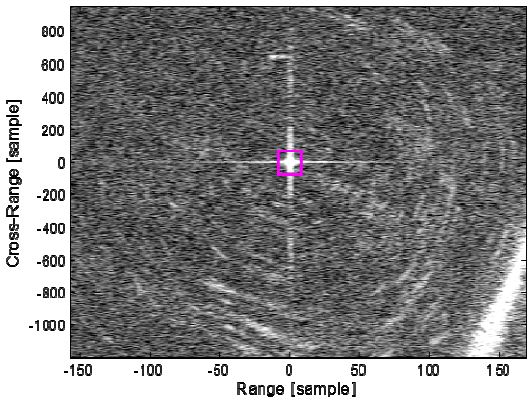

Figure 6. Response of passive calibrator.

Several corner reflectors with diameter of 1 m and 0.5 m are used as passive calibrator. These are located in rice field with very low backscattering. Figure 7 shows the profile of the corner reflector response in range and azimuth direction.

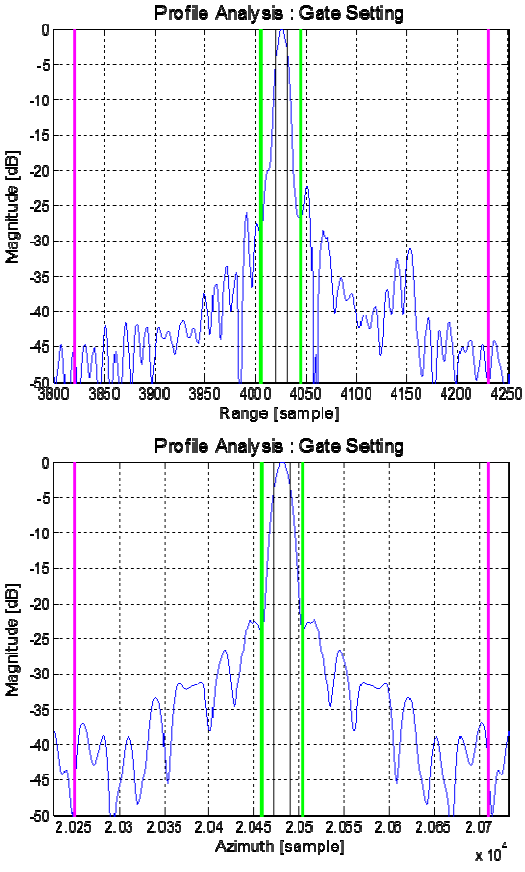

Figure 7. IRF Profile in range and azimuth direction.

Because of wide bandwidth LFM chirp waveform, slant range resolution can be 0.3 m in theory. Actual resolution of 0.4 m can be obtained. Azimuth resolution of 0.2 m, depending on Doppler bandwidth, can be also obtained.

TABLE I. IRF PERFORMANCE

Range Profile	Resolution	0.4	[m]
	PSLR	-22.1	[dB]
	ISLR	-20.2	[dB]
Azimuth Profile	Resolution	0.2	[m]
	PSLR	-22.3	[dB]
	ISLR	.17.1	[dB]

For evaluation of SAR systems, Impulse Response Function (IRF) is recognized as the basic and most representative performance parameter in SAR community. The experiment result of IRF performance, consisting of resolution, peak to sidelobe ratio (PSLR), and integrated sidelobe ratio (ISLR), is shown in Table 1.

IV. SAR IMAGES FOR LAND APPLICATION

For land observation application, several SAR images were obtained during SAR data acquisition campaign. The first SAR image obtained by the automotive-SAR system is depicted in Figure 8. By changing the horn antenna, we can get the full polarization SAR images. The image scene area is nearby seawall area. There are various kinds of scatterer scene such as water area, rice field, wet land and reed grass. Scene size is 4 km x 1.5 km.

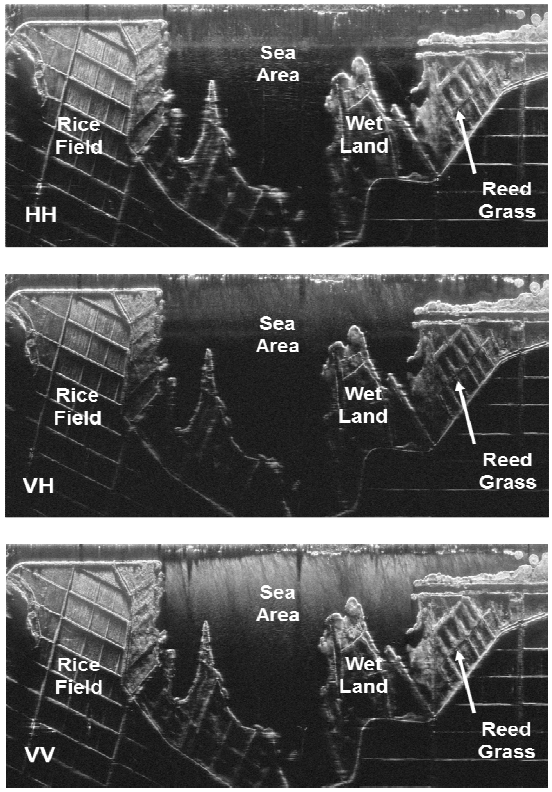

Figure 8. Polarization SAR image.

For land observation, another SAR image of rice field is presented in Figure 9. Image scene size is 1 km x 400 m and polarization is VV. The vehicle is moving up on the left of image scene. As shown in Figure 9, some of rice field is

already under cultivation and the cultivated direction is well described in SAR image. In this image, radar shadow is visible because the data is acquired with low altitude. In right middle of image, there is very bright object nearby dark scene because of man-made object and water bank for fish hatchery.

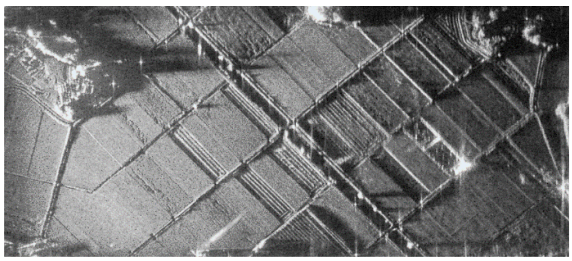

Figure 9. SAR image – rice field.

For another image, Figure 10 shows the rice field and image scene size is 500 m x 1 km. In this image, radar shadow is visible because of rice terrace. In this case, the test site is middle of mountain and the vehicle is moving right on the top of the image scene. The ground based SAR system is near range system so there is no offset from imaging vehicle.

Figure 10. SAR image – rice terrace area.

The last SAR image is acquired from mudflats area, as shown in Figure 11. This image can be used for biomass study.

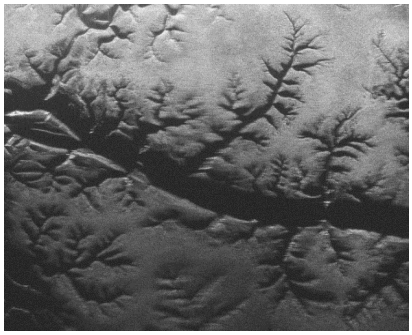

Figure 11. SAR Image - mudflats.

As mentioned in the introduction, almost all ground-based systems are based on rail system. Therefore, the observation area, such as Swath width and detection range, is very limited. In rail system, the synthetic aperture is realized by moving the antenna system along a linear rail. So, image size in azimuth is limited by physical length of rail. Tarchi et al. [1] suggest the ground-based InSAR system for landslide monitoring. But, its resolution is 4 x 4 meter and observation length is 2.8 meter in azimuth. Sato et al. [7] propose a ground-based SAR system with resolution of 1 x 5 meter. But, its observation area is still limited in 500 x 500 meter. We developed an automotive-SAR system which is installed on the top of vehicle, so we could take the image of wide area by moving the long distance up to 4 km. The resolution performance is also better than the previous ground-based SAR systems.

V. CONCLUSION

In this paper, an automotive-SAR system for land observation was proposed with various scenes of SAR image. The system is equipped in a vehicle, so motion effect is very stable compared to airborne SAR system. Unlike most of the other ground-based SAR systems, the proposed automotive-SAR system takes advantage of large observation coverage. In order to validate the system performance, calibration field work is performed using passive corner reflector. Finally, various kinds of scenes are presented to verify the possibility for land applications.

Because receiving channel can be easily expanded up to 4 channels, this system could be used for along-track and across-track interferometry SAR applications. Furthermore, PolSAR and PolInSAR applications can be also possible with a minor modification of antenna module.

REFERENCES

[1] D. Tarchi, D. Leval, and A. J. Sieber, "SAR interferometric techniques from ground based system for the monitoring of landslides", IEEE Proceedings of International Geoscience and Remote Sensing Symposium, IGARSS 2000, vol. 6, 2000, pp. 2756-2758.

[2] M. Pieraccini, G. Luzi, and C. Atzeni, "Ground-based interferometric SAR for terrain elevation mapping", IET Electronics Letters, vol. 36, no. 16, 2000, pp. 1416-1417.

[3] M. Pieraccini, G. Luzi, and C. Atzeni. "Terrain mapping by ground-based interferometric radar", IEEE Transactions on Geoscience and Remote Sensing, vol. 39, no. 10, 2001, pp. 2176-2181.

[4] G. Luzi, et al., "Ground-based radar interferometry for landslides monitoring: atmospheric and instrumental decorrelation sources on experimental data", IEEE Transactions on Geoscience and Remote Sensing, vol. 42, no. 11, 2004, pp. 2454-2466.

[5] A. Lingua, D. Piatti, and F. Rinaudo, "Remote monitoring of a landslide using an integration of GB-INSAR and LIDAR techniques", The International Archives of the Photogrammetry, Remote Sensing and Spatial Information Sciences, vol. 37, 2008, pp. 133-139.

[6] Z. S. Zhou, W. M. Boerner, and M. Sato, "Development of a ground-based polarimetric broadband SAR system for noninvasive ground-truth validation in vegetation monitoring", IEEE Transactions on Geoscience and Remote Sensing, vol. 42, no. 9, 2004, pp. 1803-1810.

[7] M. Sato, Z. S. Zhou, T. Hamasaki, and W. M. Boerner, "Development of a ground-based synthetic aperture radar (GB-SAR) system and its applications to environment monitoring and disaster prevention", POLINSAR 2005 Workshop, European Space Agency (ESA) Special Publication, vol. 586, 2005.

 ISBN: 978-1-61208-397-1

Very High Resolution SAR Speckle and CCD

Daniel Andre and Keith Morrison
Centre for Electronic Warfare, CDS,
The Defence Academy of the United Kingdom,
Cranfield University,
Shrivenham, UK
e-mail: d.andre@cranfield.ac.uk

David Blacknell, Darren Muff, Matthew Nottingham and Claire Stevenson
Defence Science and Technology Laboratory,
Porton Down, Salisbury, UK

***Abstract*—Synthetic Aperture Radar (SAR) Coherent Change Detection (CCD) has been found to be of great utility in detecting changes that occur on the ground. Detectable changes of interest include vehicle tracks, water flow, and small scale subsidence. The CCD procedure involves performing repeat pass radar collections to form a coherence product, where ground disturbances can induce detectable incoherence. Currently, SAR imagery of between 10cm and 30cm resolution is considered to be a high resolution, allowing the detection of subtle changes on the ground, however it is of interest to examine SAR image speckle characteristics and corresponding CCD images resulting from very high resolution SAR down to 1cm resolution, which in principle could be collected through airborne or spaceborne radar platforms. To perform this study, laboratory data was generated with a ground-based SAR system.**

Keywords — Radar; SAR; speckle; CCD; coherent change detection; UWB

I. INTRODUCTION

Synthetic Aperture Radar (SAR) Coherent Change Detection (CCD) has been found to be of great utility in detecting changes that occur on the ground. Detectable changes of interest include vehicle tracks, water flow, and small scale subsidence. The CCD procedure involves performing repeat pass radar collections to form a coherence product, where ground disturbances can induce detectable incoherence [1]-[5].

Currently, SAR imagery of between 10cm and 30cm resolution is considered to be a high resolution, allowing the detection of subtle changes on the ground, however it is of interest to examine CCD images resulting from very high resolution SAR down to 1cm resolution, which in principle could be collected through airborne or spaceborne radar platforms [6]. To perform this study, laboratory data was generated with the Cranfield University Ground-Based SAR system (GB-SAR) [7][8].

The laboratory SAR system is first described, and the requirements for SAR imagery of different resolution are presented. Pyramidal antenna horns, nominally calibrated for X-band 8-12GHz were employed in this study, and first results within this band are presented. However for the 15GHz bandwidth collection, calibration proved difficult, so a filtering process was employed instead, resulting in the very high resolution SAR and CCD images presented.

II. GB-SAR MEASUREMENTS

The GB-SAR system is a portable stepped frequency CW imaging radar which has been employed both indoors and outdoors [7][8]. For the experiments reported here, the system was deployed indoors at a laboratory within Cranfield University, UK, as seen in Fig.1. The antenna horn was mounted on a SAR rail 1.60m above the floor and incrementally stepped across different imaging apertures, up to 3.50m wide, with a predefined step size interval. A band between 5GHz and 20GHz was employed, thus providing up to 15GHz bandwidth. The slant range to scene center was approximately 3.75m, so that the 2.4m x 3.6m rectangular gravel scene was effectively imaged in the SAR near-field. Monostatic SAR measurements were conducted by attaching the receiver horn to the moving rail, however bistatic and multistatic SAR and CCD measurements can also be conducted with the system [4]. A calibration was conducted for the X-band pyramidal horns between 8GHz and 12GHz, providing initial results of resolution down to 4cm. Metal spheres of diameter 3cm and 5cm were arranged to either side of the gravel scene to allow for image alignment and resolution estimation. The changes made to the gravel to evaluate the level of CCD were implemented by gently moving a stick over the gravel. The gravel stones were nominally 1cm in diameter.

Figure 1. The GB-SAR system set up indoors with a gravel scene to be imaged. The X-band antenna horns are mounted on a SAR rail, which is mounted on the Green “Niftylift120” trailer. Metal spheres, with both 3cm and 5cm diameter are setup on either side (left and right) to aid in image alignment and resolution estimation.

 ISBN: 978-1-61208-397-1

Throughout, image formation was performed with the SAR back-projection algorithm, which is suitable for the SAR near-field scenario [1].

III. RESOLUTION

Because the scene center is only 3.75m from the SAR rail, and the aperture length can be as much as 3.5m wide, the scene is in the SAR near-field. This has the effect that different points within the scene can have different radar azimuth angle apertures as well as radar grazing / elevation angles, which in its turn implies that the SAR image resolution is spatially variant. Additionally, the point spread function will be irregular and will also vary in form from place to place. The resolution quoted in the following however, is always that estimated at the scene centre. It is noted that in principle the back-projection imaging algorithm can be modified to compensate for the spatial variation in resolution [4][5], however this was not implemented for this study. It would be difficult to compensate for the variation in the form of the point spread function however.

The ground range resolution is given by [1]

$$r_r = \frac{c}{2B\cos(e)} \tag{1}$$

Where c is the speed of light, B is the frequency bandwidth employed, and e is the radar grazing angle, evaluated as 27.3°. The cross range resolution is given by [1]

$$r_{cr} = \frac{c}{2f_c 2\sin(\theta/2)\cos(e)} \tag{2}$$

Where f_c is the centre frequency transmitted, and θ is the azimuth angle aperture, given by

$$\theta = 2\,\mathrm{atan}\left(\frac{L_{ap}}{2R}\right) \tag{3}$$

Where L_{ap} is the azimuth SAR aperture length and R is the closest range to scene center.

With a minimum frequency of 5GHz and maximum aperture length of 3.5m, for a given bandwidth B, the centre frequency is given by

$$f_c = \frac{5 + (B + 5)}{2} \tag{4}$$

Hence one may plot SAR resolution as a function of frequency bandwidth, as shown in Fig.2, where the solid curve is the range resolution and the dashed curve is the cross-range resolution. In the figure it can be seen that as the bandwidth increases, the range and cross-range resolution curves improve, coming closer together and eventually crossing in the bandwidth region between 12GHz and 15GHz where a resolution just over 1cm is achieved.

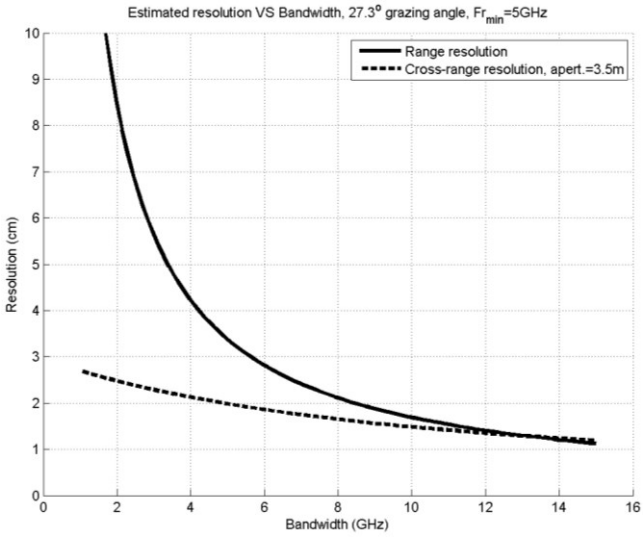

Figure 2. Graph showing range and cross-range SAR resolution as a function of frequency bandwidth, with minimum frequency set at 5GHz. Range resolution is given by the solid black curve and cross-range resolution, for the 3.5m aperture length is given by the dashed curve. The finest resolution achievable is just over 1cm.

IV. HIGH RESOLUTION SAR SPECKLE AND CCD

Initial high resolution SAR images were formed within the calibration range of the pyramidal horns. The X-band calibration frequency range was from 8GHz to 12GHz, allowing a maximal bandwidth of 4GHz.

Generally, SAR resolutions within the range of 30cm to 10cm are already considered to be of high resolution [1]. However a bandwidth of 4GHz allows resolutions down to 4.2cm. For comparison with later *very high resolution* images, in this section SAR image and speckle characteristics results are presented for 10cm resolution in Fig.3 and 4.2cm resolution in Fig.4. In both cases, SAR aperture length is set so that the cross-range resolution matches the range resolution.

Verifying that the SAR images satisfy theoretical predictions for speckle would indicate that the SAR system and near-field geometry employed allow a well-controlled CCD experiment to be undertaken. The theoretical intensity probability distribution for speckle is given by

$$P(I) = \frac{1}{\langle I \rangle}\exp\left(\frac{-I}{\langle I \rangle}\right) \tag{5}$$

where I is the intensity and $\langle I \rangle$ is the mean intensity [1].

In order to measure the SAR intensity distribution at a given nominal resolution, a central portion of the various SAR images was extracted. This is necessary because SAR resolution is spatially variant in the SAR near-field geometry. Then for easier cross comparison of results across the SAR image extracts, pixel intensity was normalized by division by the mean intensity. The resulting intensity histograms were also normalized for easier cross comparison – the normalization was by total pixel number, and the bin widths were normalized due to varying maximum pixel intensity.

 ISBN: 978-1-61208-397-1

For 10cm SAR resolution, the full SAR images, the SAR image extracts and the corresponding normalized intensity histogram plots are shown in Fig.3(a), (b) and (c) respectively. The theoretical speckle distribution is shown as the red curve overlaid on the histogram plot. The corresponding plots for 4.2cm SAR resolution are shown in Fig.4(a), (b) and (c) respectively.

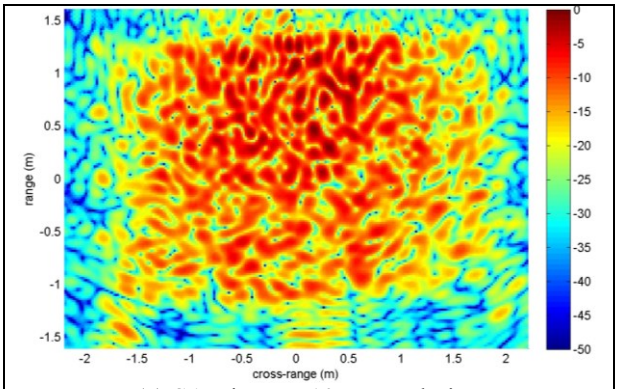

(a) SAR image, 10cm resolution

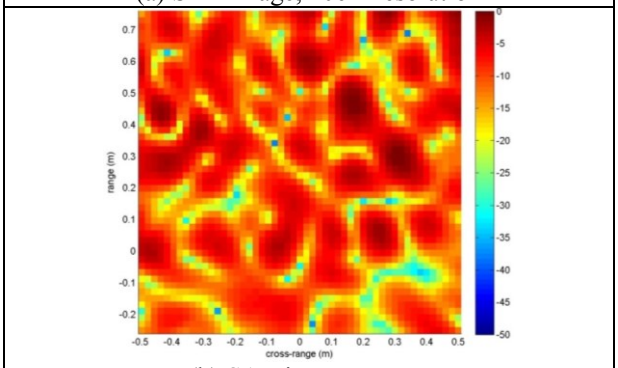

(b) SAR image extract

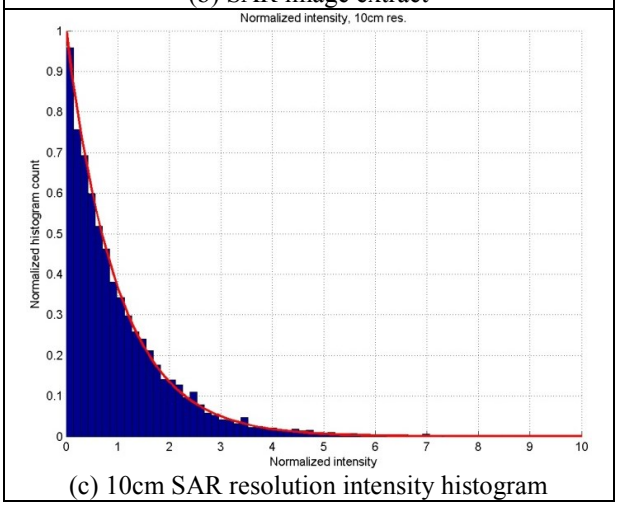

(c) 10cm SAR resolution intensity histogram

Figure 3. SAR image (a), approximately **10cm resolution**, of gravel scene with metal spheres arranged on left and right. The frequency bandwidth is **1.7GHz (10GHz centre frequency)**; (b) extract from center of SAR image for speckle analysis, (c) normalised intensity histogram overlaid by the theoretical speckle intensity probability distribution.

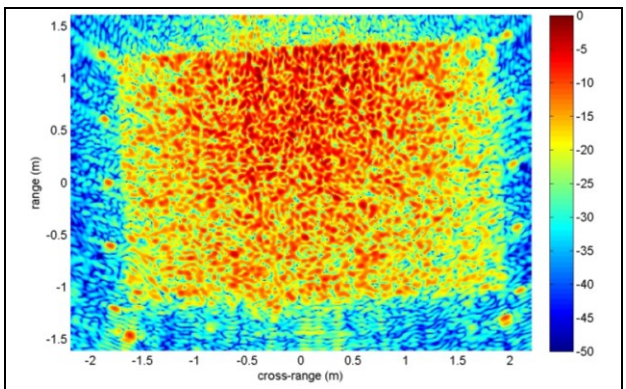

(a) SAR image, 4.2cm resolution

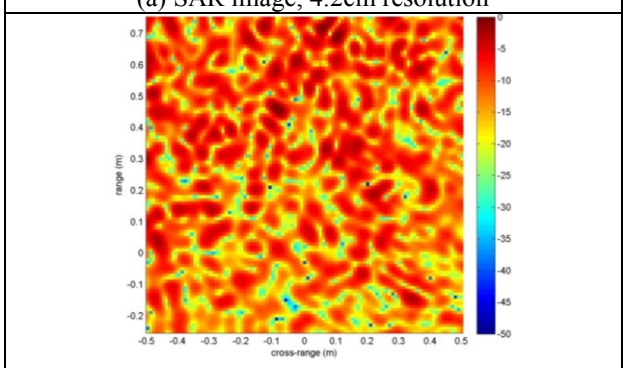

(b) SAR image extract

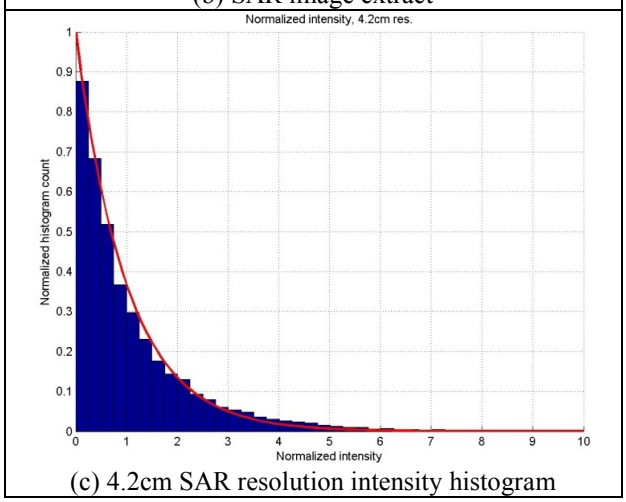

(c) 4.2cm SAR resolution intensity histogram

Figure 4. SAR image (a), approximately **4.2cm resolution**, of gravel scene scene with metal spheres arranged on left and right. The frequency bandwidth is **4GHz (8-12GHz)**; (b) extract from center of SAR image for speckle analysis, (c) normalized intensity histogram overlaid by the theoretical speckle intensity probability distribution.

 ISBN: 978-1-61208-397-1

For both resolutions, it can be seen that the histogram bar charts follow the theoretical curves very closely, indicating that the SAR images have well developed speckle characteristics, which will allow for a controlled CCD experiment.

Light disturbances were made to the gravel scene by gently scraping a stick over the gravel, allowing the formation of CCD products. The 10cm and 4.2cm SAR image resolution CCD products are shown in Fig.5(a) and (b) respectively.

The disturbances were neither evident directly to the eye, nor evident in the corresponding individual SAR images, but they are evident in the CCD images of Fig.5. However, the exact nature of the disturbances is difficult to determine at these resolutions (they should spell out some words).

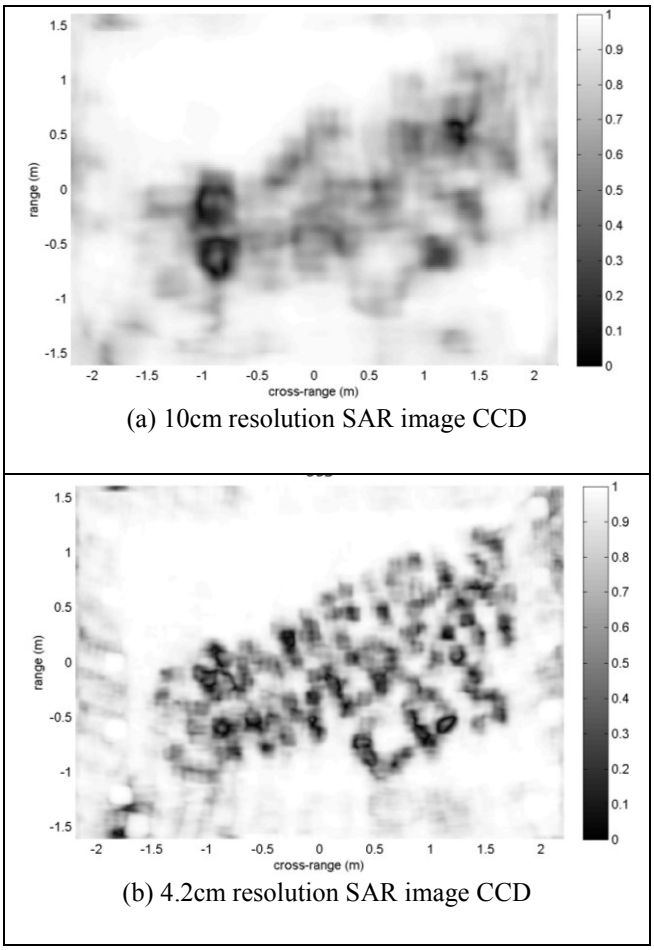

(a) 10cm resolution SAR image CCD

(b) 4.2cm resolution SAR image CCD

Figure 5. CCD images showing some disturbance to the gravel. One of the 10cm resolution SAR images used to form CCD a) can be seen in Fig.3(a). One of the 4.2cm resolution SAR images used to form CCD b) can be seen in Fig.4(a).

V. VERY HIGH RESOLUTION SAR AND CCD

In section IV, SAR and CCD images formed within the calibrated range of the antenna horns were presented. There, a bandwidth of 4GHz was employed, achieving a resolution down to 4.2cm. The system however, is capable of larger bandwidths up to 15GHz, potentially achieving very high range resolution down to 1cm, as can be predicted in Fig.2. Additionally the full aperture length of 3.5m can be employed, which will also potentially achieve very high cross-range resolution down to 1cm at these frequencies, as predicted in Fig.2.

For the purposes of the evaluation of SAR and CCD quality at very high resolutions and given the stable behavior of pyramidal horns over wide bandwidths, it was determined that it would likely be sufficient to employ signal processing filters, instead of a full calibration, which proved difficult over the full 15GHz bandwidth range.

The raw pulse amplitudes in the frequency domain are presented in Fig.6(a). It can be seen that there is a very large variation in amplitude in the recorded signal, which cannot be due to the scene. Hence for the purposes of SAR image formation, two successive filters were employed, resulting in a cleaner and more uniform amplitude signal in the frequency domain, where some underlying scene structure is made visible, as seen in Fig.6(b).

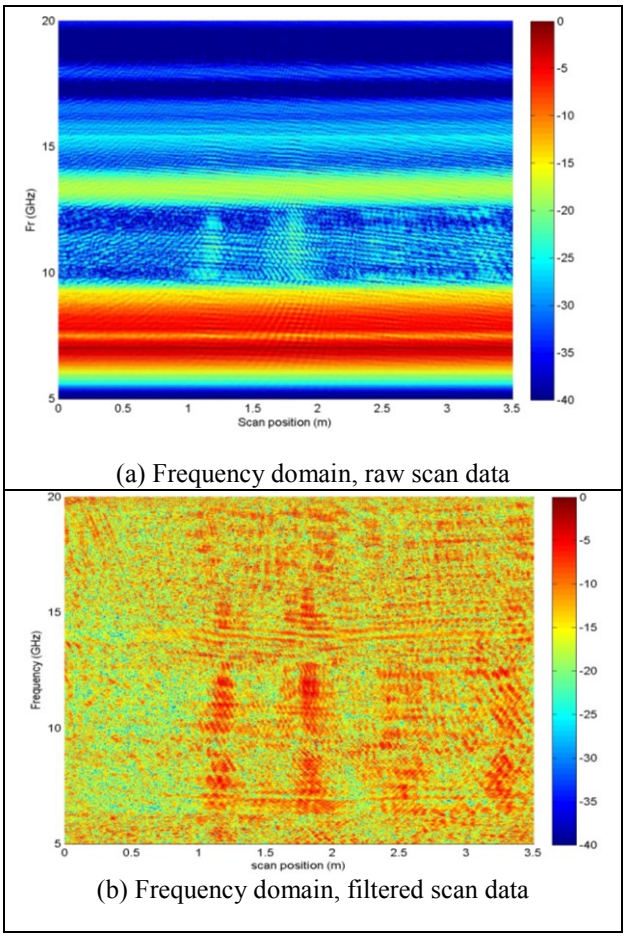

(a) Frequency domain, raw scan data

(b) Frequency domain, filtered scan data

Figure 6. raw frequency domain scan data (a) (frequency VS scan position on rail), showing large variation in recorded intensity; (b) filtered frequency domain scan data.

 ISBN: 978-1-61208-397-1

The two successive filters are as follows:

1. The first is the subtraction of system noise: The average complex pulse signal is determined over all of the pulses and is then subtracted from the raw dataset;
2. The second filter to be employed is a normalization filter: The mean absolute pulse is determined and divided through all of the pulses, thus normalizing the overall amplitude, whilst leaving the underlying structure in the data

After having filtered the raw data (from the state in Fig.6(a) to that in Fig.6(b), image formation is performed, providing SAR images such as that seen in Fig.7(a). A close inspection of features within the image confirms that a resolution of approximately 1cm has been obtained: Examination of the metal sphere signatures supports this, as well as examination of the speckle structure over the gravel scene in the SAR image extract in Fig.7(b), which should be of the same size as the image resolution [1].

The normalized intensity histogram for the SAR image extract, shown in Fig.7(c), shows very close agreement with the theoretical intensity distribution for speckle shown as the overlaid red curve.

The corresponding CCD image shown in Fig.8 can be seen to be of high quality, and now at the very high SAR resolution the nature of the disturbance is clearly evident, and can be seen to spell out “Cranfield University CDS”.

The additional disturbance evident on the bottom left of the CCD image is mostly outside of the gravel area, and was found to be due to a change in the articulation of a window at the far end of the laboratory. The window was open during the reference image collection, producing some sidelobes in that region, but it had been closed during the second SAR scan, so that the sidelobes were absent. The result thus became apparent in the CCD product.

VI. CONCLUSION

This work has examined very high resolution SAR images down to 1cm resolution, and corresponding CCD images, collected in a laboratory environment by a ground-based SAR system. The SAR image intensity distributions closely matched theoretical intensity probability distributions for speckle.

The resulting CCD images showed subtle change detections to a scale that was not possible with conventional high resolution SAR images of resolution down to 10cm.

In principle, these techniques can be applied to remote sensing at these very fine resolutions if desired.

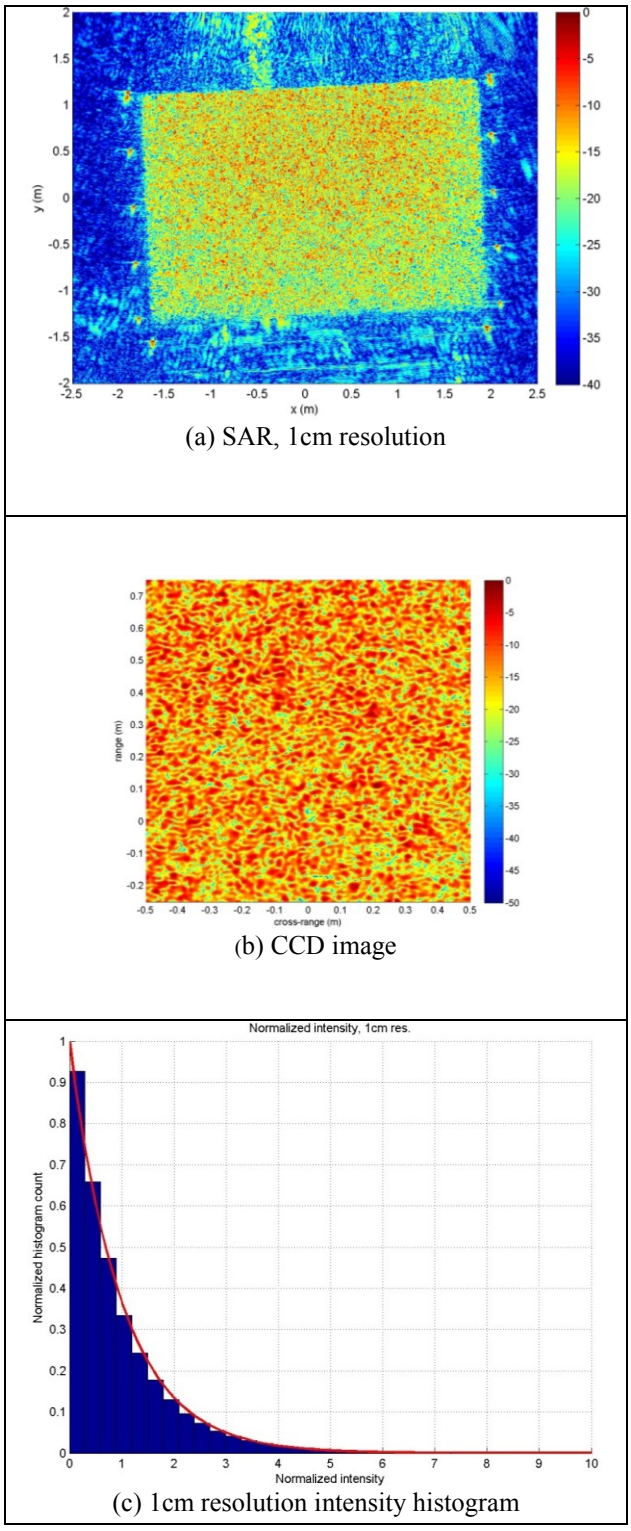

(a) SAR, 1cm resolution

(b) CCD image

(c) 1cm resolution intensity histogram

Figure 7. SAR image, approximately **1cm resolution**, of gravel scene with metal spheres arranged on left and right (a). The frequency bandwidth is **15GHz (5-20GHz)**, and the SAR rail aperture is **3.5m**; (b) extract from center of SAR image for speckle analysis, (c) normalised intensity histogram overlaid by the theoretical speckle intensity probability distribution.

 ISBN: 978-1-61208-397-1

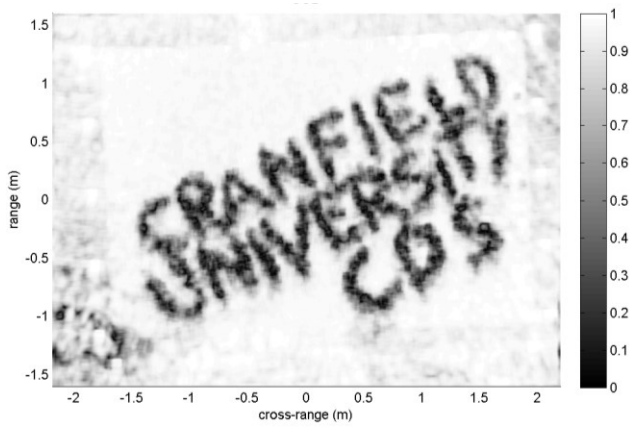

Figure 8. CCD image showing the disturbance to the gravel, spelling out "Cranfield University CDS". One of the 1cm resolution SAR images used to form this CCD can be seen in Fig.7(a).

ACKNOWLEDGMENT

This work was funded by the Defence Science and Technology Laboratory, UK.

REFERENCES

[1] C. V. Jakowatz Jr., D. E. Wahl, P. H. Eichel, D. C. Ghiglia, P. A. Thompson, "Spotlight-Mode Synthetic Aperture Radar: A Signal Processing Approach", Kluwer Academic Publishers, 1999.

[2] M. Preiss and N. J. S. Stacy, "Coherent Change Detection: Theoretical Description and Experimental Results", Technical Report, Defence Science and Technology Office, Australia, DSTO-TR-1851, August 2006.

[3] D. Blacknell, D. B. Andre and C. M. Finch, "SAR coherent change detection (CCD) over mountainous regions", International conference on synthetic aperture sonar and synthetic aperture radar (SAS/SAR), 13th-14th September 2010.

[4] D. B. André, D. Blacknell and K. Morrison, "Spatially variant incoherence trimming for improved SAR CCD", SPIE DSS 2013, April 2013.

[5] D. B. André, D. Blacknell. and K. Morrison, "Spatially variant incoherence trimming for improved bistatic SAR CCD", IEEE Radar Conference 2013, 1st -5th April 2013.

[6] D. G. Muff, D. Blacknell and M. R. Nottingham, "Pharos – a SAR concept to accelerate advanced exploitation", IET International Conference on Radar Systems, October 2012.

[7] K. Morrison, J. C. Bennett, G. Cookmartin, A. J. McDonald, A. Race and S. Quegan "Three-dimensional X-band SAR imaging of a small conifer tree", Int. J. Remote Sens., 22, p705 (2001).

[8] S. C. M. Brown, S. Quegan, K. Morrison, J. C. Bennett and G. Cookmartin, "High resolution measurements of scattering in wheat canopies – implications for crop retrieval." IEEE Transactions of Geoscience and Remote Sensing, 41, p1602-1610 (2003).

 ISBN: 978-1-61208-397-1